Long-Term Monitoring of Lakes in the Northern Central European Lowlands Using Optical and Radar Remote Sensing Imagery

vorgelegt von
Diplom-Geoökologin
Iris Elisabeth Heine
geb. in Stuttgart

Von der Fakultät VI – Planen Bauen Umwelt
der Technischen Universität Berlin
zur Erlangung des akademischen Grades

Doktor der Naturwissenschaften
Dr. rer. nat.

genehmigte Dissertation

Promotionsausschuss:
Vorsitzende: Prof. Dr. Eva Nora Paton
Gutachterin: Prof. Dr. Birgit Kleinschmit
Gutachter: Prof. Dr. Luis Guanter
Gutachter: Prof. Dr. Achim Brauer

Tag der wissenschaftlichen Aussprache: 13. September 2017

Berlin 2017

Abstract

The glacial landscape of the northern Central European lowlands in Germany and Poland is characterized by a large number of lakes. These lakes fulfill important ecosystem services, however, they are sensitive to climate change, land use changes, and human impact. Very few of them are regularly monitored in situ. This thesis tests the potential of remote sensing imagery for the long-term monitoring of lakes in northern Central European lowlands, because remote sensing imagery enables an area wide monitoring with the possibility of multi-temporal observations. The thesis comprises the results of four scientific papers aiming at the development and evaluation of new remotely-sensed lake monitoring methods, in combination with instrument and proxy-based monitoring. The monitoring is focused on 1) the reconstruction of lake levels and the monitoring of 2) shoreline vegetation and 3) calcite precipitation as part of the Helmholtz Virtual Institute for Integrated Climate and Landscape Evolution Analyses (ICLEA).

The lakes are characterized by seasonal and long-term lake level changes, which affect the shoreline vegetation (reed belts). In this thesis, lake levels are reconstructed by intersecting water-land borders that were derived from remote sensing imagery together with topographic data. Aerial photos are tested for a long-term monitoring approach. High-resolution multi-spectral satellite imagery is utilized for the monitoring of short-term lake level changes. The accuracy of the reconstructed levels is high. However, there are very strict prerequisites that need to be met by the image data and the lakes to achieve this accuracy. The greatest challenge is vegetation at the shorelines that covers the water-land border. The optical images are also affected by low solar angles or clouds.

Synthetic aperture radar (SAR) imagery enables a regular lake monitoring: thus, high-resolution dual-co-polarized SAR imagery is used for the monitoring of reed belts. Polarimetric decomposition techniques allow the discrimination of different scattering scenarios and show the phenological changes in the reed belts: in summer dense leaves cause volume scattering, whereas in winter, the deciduous reed stems cause predominately double-bounce scattering. Thus, double-bounce-sensitive polarimetric parameters and winter images are preferred for a classification of reed. However, the application of this method for long-term lake monitoring is limited, because of a lack of polarimetric archive data and its geocoding. The third monitoring subject is calcite precipitation. Calcite precipitation is an extensive limnological process that dyes the lake water a milky turquoise. This allows the use of medium-resolution optical satellite images: the Landsat archives and new Sentinel-2 imagery enable a long-term and large scale monitoring of calcite precipitation. The most accurate classification is hereby based on a ratio of the blue, green, and red spectral bands, because calcite precipitation enhances the reflectance in the green band. The approach is evaluated with field measurements and then propagated to 21 lakes to monitor frequency and duration of calcite precipitation events.

The monitoring results of this thesis emphasizes the temporal heterogeneity within lakes and the spatial heterogeneity between the lakes. They confirm the importance of remotely-sensed monitoring for large scale monitoring. It is shown that the success of the developed monitoring approaches is limited by their demands on remote sensing data: long time series, and high temporal and spatial resolution. The main limitations are spatial and temporal resolution, specifically in the beginning of Earth observation with data from very few satellites. Thus, the potential of remote sensing archives for the long-term monitoring of lakes is best exploited if the lake parameter is detectable in medium-resolution imagery, as in case of the monitoring of calcite precipitation.

Zusammenfassung

Die Seenlandschaft Nordostdeutschlands und Polens ist Teil des eiszeitlich geprägten mitteleuropäischen Tieflandes. Die Seen sind wichtig für das Ökosystem, sie sind allerdings auch gefährdet durch menschliche Eingriffe und beeinflusst durch Landnutzung- und Klimaänderungen. Hier besteht Forschungsbedarf, denn bisher wurden nur vereinzelt Seen wissenschaftlich untersucht. Dieser Dissertation prüft, inwiefern Fernerkundung (FE) das Monitoring von Seen unterstützen kann, denn FE-Daten erfassen große Gebiete und Archivbilder dokumentieren vergangene Zustände. Ziel der Arbeit ist die Entwicklung und Bewertung neuer fernerkundlicher Monitoringverfahren für Seen in Kombination mit in situ Untersuchungen. Das Monitoring der Seen zielt dabei speziell auf 1) die Rekonstruktion von Seespiegeln sowie das Monitoring von 2) Ufervegetation und 3) Kalzitfällungen ab. Die Arbeit umfasst dabei die Ergebnisse von vier wissenschaftlichen Veröffentlichungen und ist Teil des Virtuellen Instituts zur Integrierten Klima- und Landschaftsentwicklungsanalyse (ICLEA).

Langfristige und saisonale Seespiegeländerungen sind typisch für die Seen, aber schnelle oder starke Veränderungen beeinträchtigen beispielsweise die Vegetation an den Ufern und in den Flachwasserbereichen. Mithilfe hochaufgelöster Luftbilder und optischer Satellitenbilder können frühere Uferlinien der Seen bestimmt werden. Verknüpft man diese Uferlinien nun mit topographischen Daten, ergeben sich die dazugehörigen Seespiegel. Luftbilder reichen dabei weit länger in die Vergangenheit als Satellitenbilder. Sie haben dafür aber eine viel geringere zeitliche Auflösung. Trotz guter Ergebnisse ist die Übertragbarkeit der Methode schwierig, da die Anforderungen an die FE-Daten und die Seen sehr hoch sind. Problematisch ist zum Beispiel Vegetation, die die Uferlinie in den Bildern verdeckt. Regelmäßige Aufnahmen sind bei optischen Satellitenbildern aufgrund von Wolken oder niedrigem Sonnenstand ebenfalls nicht möglich. Hier helfen Synthetic Aperture Radar (SAR) Zeitreihen: In dieser Arbeit werden hochaufgelöste, dual-co-polarimetrische SAR Bilder für die Beobachtung von Schilf herangezogen. Durch polarimetrische Entmischung können verschiedene Streuungsmechanismen unterschieden werden und es zeigen sich phänologische Unterschiede des Schilfes: Im Sommer, wenn das Schilf dichte Blätter hat, überwiegt Volumenstreuung, wohingegen es im Winter, ohne Laub, zwischen der Wasserfläche und den Schilfstängeln vermehrt zu Zweifachreflektionen kommt. Eine Kombination aus Winterbildern und polarimetrischen Parametern, die diese Zweifachreflektionen anzeigen, eignet sich daher am besten für die Klassifizierung von Schilf. Leider ist auch hier die großflächige Anwendung der Methode eingeschränkt, da polarimetrische Bilder noch recht selten sind. Kalzitfällungen färben den See trüb Türkis. Diese Färbung ist auch in optischen Satellitenbildern mit mittlerer Auflösung zu sehen. Das bedeutet, dass das Landsat-Archiv und Bilder vom neuen Sentinel-2 Satelliten hier eine langfristige und großflächige Beobachtung erlauben. Die Türkisfärbung geht mit einem Anstieg der Reflexion im grünen Wellenlängenbereich einher, wobei die neuentwickelte Klassifikation die Reflexionen im blauen, grünen und roten Wellenlängenbereich nutzt. Die Übertragbarkeit der Methode wurde nach gründlichen Vergleichen mit Feldmessungen an weiteren 21 Seen getestet.

Die Ergebnisse dieser Arbeit zeigen die zeitlichen und räumlichen Unterschiede von Seen und verdeutlichen, wie wichtig FE für ein langfristiges und großflächiges Seenmonitoring ist. Ob die neuen Monitoringverfahren dabei erfolgreich sind, liegt an ihren Voraussetzungen an die FE: Welche räumliche und zeitliche Auflösung ist nötig und welcher Zeitraum muss abgedeckt werden? Hohe räumliche und zeitliche Auflösung ist aber vor allem zu Beginn der FE selten, das heißt das Potential von FE-Archiven wird dann am besten ausgeschöpft, wenn eine mittlere räumliche Auflösung der Daten genügt, wie hier im Falle der Kalzitfällung.

Table of Contents

List of Figures

List of Tables

List of Abbreviations

A_{dual}	Anisotropy
Area BGR	"Area Blue Green Red"
asc	Ascending
ATKIS-DGM1	Digital surface model with 1 m resolution
BL	Breiter Luzin
BS	Bergsee
CDI	Cross-Date-Index
CDOM	Colored dissolved organic matter
Chl-a	Chlorophyll-a
CIR	Color-infrared
dB	Decibel
DEM	Digital elevation model
desc	Descending
DGPS	Differential Global Positioning System
DLR	Deutsches Zentrum für Luft- und Raumfahrt
DOP	Digital orthophotos
DSM	Digital surface model
DWD	Deutscher Wetter Dienst (German Weather Service)
ENL	Equivalent number of looks
ESA	European Space Agency
FH	Feldberger Haussee
FN	False negative
FP	False positive
FS	Fürstenseer See (Chapter 4), Flacher See (Chapter 5)
GCP	Ground control point
GIS	Geographic information system
GLK	Gleichläufigkeit
GPS	Global Positioning System
H_{dual}	Entropy
H	Horizontal
HS	Hofsee
ICLEA	Helmholtz Virtual Institute for Integrated Climate and Landscape Evolution Analyses
IDL	Interactive Data Language
IGB	Leibniz-Institute of Freshwater Ecology & Inland Fisheries
IQR	Interquartile range
JS	Jakobsdorfer See
KS	Krummer See
LAWA	Bund/Länder-Arbeitsgemeinschaft Wasser
LF	Fürstenseer See (Chapter 3)
LGB	Landesvermessung und Geobasisinformation Brandenburg
LIDAR	Light detection and ranging
LUCC	Land-use/land-cover change
m1	*H-A*-combination 1
m2	*H-A*-combination 2
m3	*H-A*-combination 3
m4	*H-A*-combination 4

MDWI	Modified normalized difference water index
MODIS	Moderate-resolution imaging spectroradiometer
MS	Mecklenburgische Seenplatte
M-V	Mecklenburg-Vorpommern
NA	Not available, not applicable
NAFD	Normalized absorption feature depth of red
NDWI	Normalized difference water index
NESZ	Noise equivalent sigma zero
NHN	Normalhöhennull
NIR	Near-infrared
NISAR	NASA-ISRO SAR Mission
OSM	OpenStreetMap
PIK	Potsdam Institute for Climate Impact Research
PolSAR	Synthetic aperture radar polarimetry
PZ	Poratz
Ratio RG	Ratio of the reflectance values of band red and green
Ratio RL	Ratio of bands of an unknown lake and a dark reference lake
RE	RapidEye
Ref	Reflectance
RF	Random forest
RG	Rohrhahngrund
RGB	Red Green Blue
ROI	Regions of interest
RS	Redernswalder See
RMSE	Root mean square error
SAR	Synthetic aperture radar
SEA	Sun elevation angle
SI	$CaCO_3$ saturation index
SL	Schmaler Luzin
SNR	Signal-to-noise ratio
SSC	Single Look Slant Range Complex
SWIR	Shortwave-infrared
T_{2x2}	2 × 2 coherency matrix
TIN	Triangulated Irregular Network
TN	True negative
TOAR	Top of atmosphere reflectance
TP	True positive
TS	Tiefer See
TSAP	Time Series Analysis Program
TSX	TerraSAR-X
USGS	United States Geological Survey
V	Vertical
VIS	Visible light
WRRL	Europäische Wasserrahmenrichtlinie (European Water Framework)
δ_{HH}	Intensity of HH channel
$\delta_{HH/VV}$	Intensity ratio HH/VV
δ_{HH+VV}	Intensity of HH plus Intensity of VV
δ_{HH-VV}	Intensity of HH minus Intensity of VV
δ_{VV}	Intensity of VV channel
$\lvert\gamma_{HHVV}\rvert$	Coherence HHVV amplitude

$\angle\gamma_{HHVV}$	Coherence HHVV phase
$\delta_{XX,pseudo}$	Intensity XX (pseudo)
$\overline{\propto}_{dual}$	Dual-polarimetric mean alpha angle
$\propto_{dual}$	Dual-polarimetric dominant alpha angle

1 Introduction

1.1 Motivation and Structure

The glacial landscape of the northern Central European lowlands in Germany and Poland is characterized by a large number of lakes. Those lakes fulfill important ecosystem services such as e.g. water storage, groundwater recharge and discharge, water quality maintenance, habitat for flora and fauna, biodiversity, and carbon storage. They have also an important recreational value for, e.g. tourism (Kaiser, Koch, et al. 2014; Tiner et al. 2015). However, the lakes are sensitive to climate and land use changes and human impact (Germer et al. 2011; Kaiser, Koch, et al. 2014; Palmer et al. 2015; Heinonen et al. 2000). In times of changing climate it is essential to understand the past to make assumptions for the future to be able to adapt to coming environmental changes. We all depend on complex Earth system processes and past climate and environmental changes had major impacts on human society and economy.

This thesis analyzes the potential of remote sensing for the long-term monitoring of lakes in the northern Central European lowlands. It is part of the framework of the Helmholtz Virtual Institute for Integrated Climate and Landscape Evolution Analyses (ICLEA). The international ICLEA project combines research in hydrology, dendrochronology, lake sediments, geomorphology, and remote sensing for the reconstruction and analysis of long- and short-term environmental and climate changes since the last ice age. The reconstruction and analysis of long- and short-term changes is hereby focused on lakes, because they show climate and land use changes, but also regulate climate (Williamson et al. 2009). Fundamental for ICLEA is the compilation of a database of instrumental monitoring, remote sensing, and proxy data, their chronological synchronization, and the integration of different time scales. This database will provide information on natural background variability and is essential for the understanding of the impact and interaction of different landscape forming processes.

Whereas instrumental and proxy-based lake monitoring are very time-consuming and limited to few selected lakes and small spatial scales (point data), remote sensing enables an extensive monitoring of large areas. Additionally, archived Earth observation data enable the analysis of past changes of a lake system. Therefore, the objectives of this thesis are **the monitoring of lakes in the recent past using remote sensing archives, aiming at linking the different temporal scales from in situ measurements to long-term proxy-based monitoring, and the expansion of the monitoring on larger spatial scales** (cf. **Figure 1-1**) **as lakes are important climate archives.**

The monitoring of lakes in this thesis is focused on three important lake parameters: 1) lake level variation, 2) shoreline vegetation, and 3) calcite precipitation, which have the potential to be mapped and monitored with remote sensing data. Those lake parameters are all monitored in situ or proxy-based within ICLEA.

Proxy-based (Kaiser 1996) and instrumental monitoring at selected lakes showed lake level fluctuations in the last century as a reaction to land use, hydromelioration, and climate change (Kaiser, Koch, et al. 2014; Germer et al. 2011). Those lake level variations influence the aquatic and shoreline vegetation: rapid level fluctuations that exceed the capacity of the vegetation to adapt or move can cause desiccating or drowning. This is a problem for shoreline vegetation, e.g. the common reed (Phragmites australis) (Schmieder et al. 2004) that is widespread at the shallow water areas of the lakes in the northern Central European lowlands. The reed belts are important for lakes as they protect the shorelines from erosion, filter the lake water, are an

important habitat for animals (Bogenrieder 1990; Schmieder et al. 2004). They are a sink for greenhouse gases in the long term (Brix et al. 2001). The phenology of the deciduous reed belts, are also of interest for hydrological measurements, because it changes the density and total surface area of the vegetation.

Calcite precipitation is a bio-geochemical process that induces the precipitation of calcium carbonate particles due to a shift in the carbonate equilibria in the open water of hardwater lakes. The precipitation dyes the lake a water milky turquoise (Strong & Eadie 1978; Koschel et al. 1987; Kelts & Hsü 1978) until the calcite particles settle and are deposited in the lake sediment. Those calcite layers are well preserved in drilled sediment cores of selected, varved lakes and provide long-term climate records of lake changes with seasonal temporal resolution (Kienel et al. 2013). Calcite precipitation additional has a high climate relevance as the sedimentation process represents a carbon sink (Koschel et al. 1997; Koschel et al. 1987).

This thesis aims at the development of new remotely-sensed monitoring methods for level changes, shoreline vegetation (reed), and calcite precipitation in the northern Central European lowlands and their application to large-scale areas.

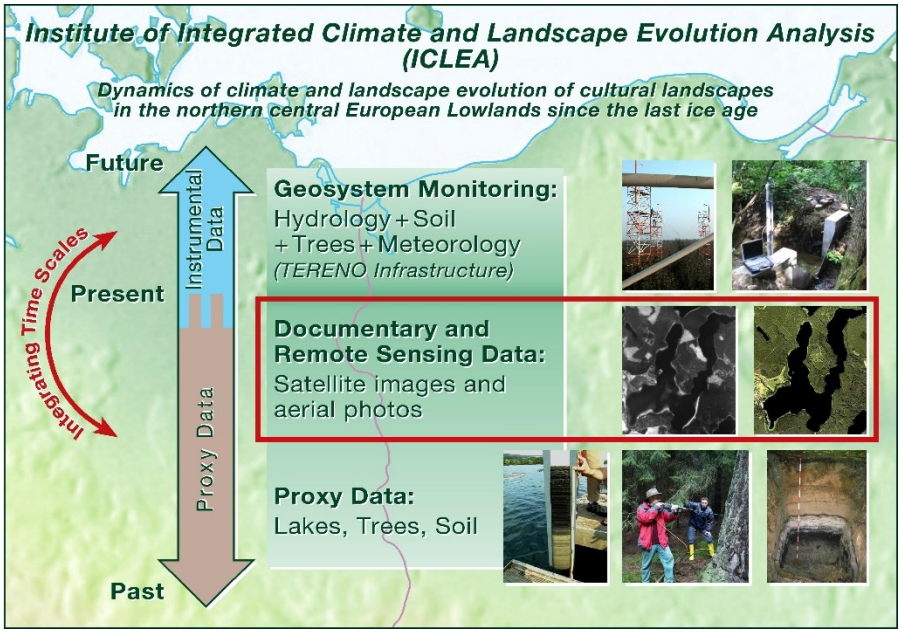

Figure 1-1: Schematic description of the ICLEA project structure and its research concept with integrating data sources at various time scales (modified after Grafik ICLEA, Gerd Helle, GFZ, www.iclea.de).

The thesis comprises five main chapters (**Figure 1-2**). **Chapter 1** gives an overview of the general research topic and the specific research framework. Here, the main research objectives and research questions are introduced. **Chapters 2** to **5** present consecutive stand-alone manuscripts on new methods of remotely-sensed lake monitoring and their application in northern the Central European lowlands. **Chapter 2** introduces the method of remotely-sensed lake level retrieval and tests the long-term monitoring approach of using optical aerial photos. **Chapter 3** elaborates the topic of lake level retrieval using satellite imagery for a higher temporal resolution and the monitoring of seasonal lake level changes. **Chapter 4** introduces a new method for short-term reed monitoring and considers the measurement of the lake area below vegetation using polarimetric synthetic aperture radar (PolSAR). **Chapter 5** focuses is the long-term monitoring of calcite precipitation as a recurring seasonal event. Finally,

Chapter 6 discusses the overall research questions, considering the insights of **Chapters 2** to **5**.

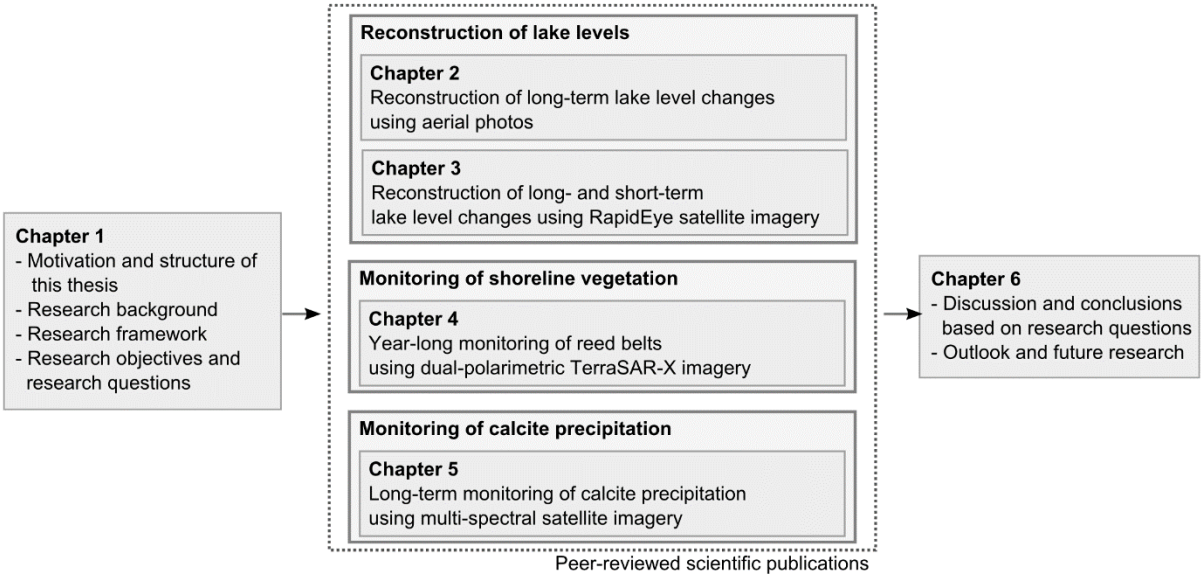

Figure 1-2: Structure of the thesis. The monitoring of lakes is focused on three monitoring subjects: lake levels, shoreline vegetation and calcite precipitation. The objectives on method and application of **Chapters 2** to **5** are presented in detail in **Chapter 1.4**.

1.2 Research Background

The research background provides an overview of natural lakes in the northern Central European lowlands (**Chapter 1.2.1**) and of remote sensing monitoring of lakes (**Chapter 1.2.2**). This includes aerial photos, optical and synthetic aperture radar (SAR) satellite imagery.

1.2.1 Natural Lakes in Northern Central European Lowlands

Most of the natural lakes in Europe are located in Northern Europe, the Nordic Countries and the Karelo-Kola part of the Russian Federation. Those lakes were formed or reshaped during the last glacial period and their lake surface area may reach 5-10 % of the total surface area (Heinonen et al. 2000).

The lakes in the northern Central European lowlands have been classified by Mauersberger (2006) based on their inflow and outflow dynamics. The inflow to the lakes consists of surface inflow by runoff, precipitation and groundwater inflow. The outflow can be surface outflow, groundwater seepage, and evapotranspiration. Whereas river lakes, flow lakes, spring lakes, and endorheic lakes have at least periodical inflow by running water. Groundwater-fed lakes and kettle hole lakes are solely fed by precipitation and/or groundwater (cf. **Table 1-1)**. As a consequence the lake levels of the lakes vary on short-term and long-term scales: endorheic, groundwater-fed, and kettle hole lakes show significant long-term changes (decades, centuries), whereas river and flow lakes, if non-regulated, show mostly seasonal short-term variation. Spring lakes hardly fluctuate at all (Mauersberger 2006). The natural lake level changes include small seasonal fluctuations and large perennial lake level changes, resulting from the precipitation-evapotranspiration balance and groundwater changes (Mauersberger 2006; Kaiser, Friedrich, et al. 2012). Thus, the monitoring of lake level changes in this study is focused on three endorheic and groundwater-fed lakes in the northern Central European lowlands. However, it must be considered that natural fluctuations of the lakes are often

overprinted by human interference through land use and hydromelioration (Germer et al. 2011; Kaiser, Koch, et al. 2014).

Table 1-1: Overview of lake types in northern Central European lowlands (modified after (Mauersberger 2006)). The lake types are characterized by their catchment size, the inflow and outflow dynamics. The intensities are abbreviated as followed: huge ++++, strong/very large +++, moderate/moderately large ++, weak/small +, very weak/very small (+), non-existing -, exists E, and exists, but insignificant in relation to other inflow (E). Lakes, whose lake level changes are monitored within this thesis, are in bold characters.

	River lake	Flow lake	Spring lake	**Endorheic lake**	**Groundwater lake**	Kettle hole lake
Distribution	Flood plains or within canal systems	In flow valleys and flow mires or part of melioration systems	At the feet of moraine tracts, in sinks of outwash plains	Alongside of river and stream valleys, in outwash plains and ground moraines	Alongside of river and stream valleys, in outwash plains and ground moraines	In sinks with cohesive soil, dead ice holes in end/ground moraines
Frequency	Rare	Most frequent	Rare	Very rare	Frequent	Rare
Catchment size	++++	+ to +++	++	+ to ++	+ to ++	(+)
Surface inflow by running water	+++ (river)	+ to ++ (stream, trench, flow mire)	+ to ++ (spring mire, many small streams)	+ (often just periodical)	-	-
Surface inflow by precipitation	(E)	(E)	(E)	E	E	E
Groundwater inflow	+++	E	+++	E	E	-
Surface outflow	+++	+ to ++	+ to ++	-	-	-
Groundwater seepage	(E)	E	-	E	E	-
Lake level variation	Strongly irregular yearly hydro-graphs (if non-regulated)	Significant yearly hydrographs, but with long-term stability	Hardly fluctuating	Irregular yearly hydrographs with extreme long-term changes	Groundwater level	Climatic water balance of the kettle hole
Example	Potsdamer Havelseen; Oderberger See	Scharmü-tzelsee, Welletzsee	Aalgastsee (Stegelitz)	Briesensee (Poratz), **Redernswalder See**	**Krummer See (Melzow), Fürstenseer See**	Schwarzer See (Granitz, Rügen)

The inflow and outflow of the catchment also influences the trophic state of the lakes as nutrients are transported with the water flow. The input of phosphorus and nitrogen determines the productivity (chlorophyll-a (chl-a) concentration), the oxygen concentration in the water, and the water transparency (secchi depth) (Schlungbaum & Krech 1999; Wetzel 2001). The trophic state of lakes is important in the monitoring of lakes in this thesis, because the trophic state and calcite precipitation affect each other (Koschel 1997; House 1987; Gal et al. 1996; Proft 1984; Koschel et al. 1987). Oligotrophic lakes have a small productivity and low plankton concentration due to low availability of nutrients. Mesotrophic lakes have a higher nutrients

concentration and higher productivity with medium phytoplankton concentration, resulting in lower secchi depth and occasional oxygen deficiency. Eutrophic lakes have a high availability of nutrients and consequently a high productivity and high phytoplankton concentration. This high phytoplankton concentration generally causes low secchi depths and at the end of August frequently a strong oxygen deficiency. Thus, the trophic index is an important parameter for water quality evaluations and it is used for the classification of lakes. The state-of-the-art classification in Germany is based on the work of the Bund/Länder-Arbeitsgemeinschaft Wasser (LAWA): the LAWA trophic index (Riedmüller et al. 2014). It was devised as consequence of the European Water Framework (in German "Europäische Wasserrahmenrichtlinie (WRRL)") that came into force in 2000. The lakes are classified by their current and potential trophic levels into oligotrophic, mesotrophic, and eutrophic lakes.

Another lake characterization is also important: the concentration of alkaline elements in the water. Whereas soft water lakes have low salinity, hardwater lakes contain large concentrations of alkaline elements such as magnesium or calcium. The northeast German Plain, and probably also the entire northern Central European lowlands,are dominated by hardwater lakes (Koschel et al. 1987), caused by the drainage of calcareous deposits (Wetzel 2001). Calcium-rich hardwater is a precondition for calcite precipitation in lakes. Additionally, the alkaline content determines the acid neutralization capacity (=alkalinity) of the lake, in interaction with the pH value (Wetzel 2001).

1.2.2 Remote Sensing for Lake Monitoring

Remote sensing imagery enables large scale monitoring, whilst image archives allow the construction of a time-series. Thus, remote sensing is a valuable tool for a long-term lake monitoring. The following chapters give an overview of the development of lake monitoring using optical (**Chapter 1.2.2.1**) and radar (**Chapter 1.2.2.2**) data. The chapters introduce different remote sensing data, aerial photos, and satellite missions that have been used for lake monitoring. It illustrates their potential and limitations for water monitoring.

1.2.2.1 Optical Remote Sensing of Lakes

Optical remote sensing is carried out by passive systems that use the sunlight as source to image the Earth's surface. Thus, low solar angles and the atmosphere, especially cloud coverage, hamper useful data acquisitions. The spectral acquisition ranges between visible light (VIS) (400 - 700 nm) and near-infrared (NIR) (700 - 1300 nm) or short-wavelength infrared (SWIR) (1300 – 3000 nm) (Lillesand et al. 2008). The acquisition geometry is ideally close to nadir to avoid radiometric and geometric distortions. A prerequisite for long-term monitoring is the geometric and radiometric normalization of the remote sensing images (Behling 2016; Hill & Mehl 2003). The atmospheric correction of the optical images is important for water quality measurements (Lillesand et al. 2008; Gholizadeh et al. 2016).

Aerial photography is the oldest remote sensing data source with a consistent very high spatial resolution from the 1930s until the present. Therefore, aerial imagery is ideal for long-term monitoring of landscape dynamics (Gens 2010; Gerard et al. 2010). Since the 1950s panchromatic and color aerial imagery has been used regularly for the mapping of water level and shoreline changes at coastlines (McCurdy 1950; Stafford 1971; Fisher & Overton 1994; Boak & Turner 2005; Lipakis & Chrysoulakis 2008; Gens 2010) and lakes (Schumann et al. 2009; Lyon & Drobney 1984; Lyon & Greene 1992; Williams & Lyon 1997; Muster et al. 2013; Klein et al. 2005; Papastergiadou et al. 2007; Shapley et al. 2005). Aerial photos have also proved useful for long-term monitoring of vegetation, e.g. reed, at lake shorelines

(Papastergiadou et al. 2007; Ritchie et al. 2003; Klein et al. 2005; Kowalski & Wilcox 1999; Csaplovics 1984; Schmieder et al. 2004).

The quality differences between historical aerial images and digital orthophotos are challenging for the analysis of aerial photos for long-term monitoring of shorelines and vegetation. Orthophotos provide high spatial accuracy, whilst historic images require time consuming geo-referencing and are spatially less accurate. Lens distortions of historic cameras aggravate this problem. The analysis of aerial photos is often based on manual photointerpretation, thus, the results depend on the experience of the interpreter and the image quality (Barrette et al. 2000; Anders & Byrnes 1991; Crowell et al. 1991).

For the monitoring of vegetation and for better distinction of water and land color-infrared (CIR) images are preferred: whereas green vegetation has a significant increase in its reflectance at approximately 700 nm (red edge) (Weichelt et al. 2014), clear water absorbs wavelengths larger than 800 nm (Bochow et al. 2012; Thiemann & Koschel 2001; Moore 1980) (cf. Figure 1-3). Turbid water, e.g. through high concentration of suspended material increases the reflectance in the NIR (Moore 1980; Schultz & Engman 2000; Mertes et al. 2004). Thus, the classification of water is most robust using the longer SWIR wavelength (Moore 1980; Li et al. 2013).

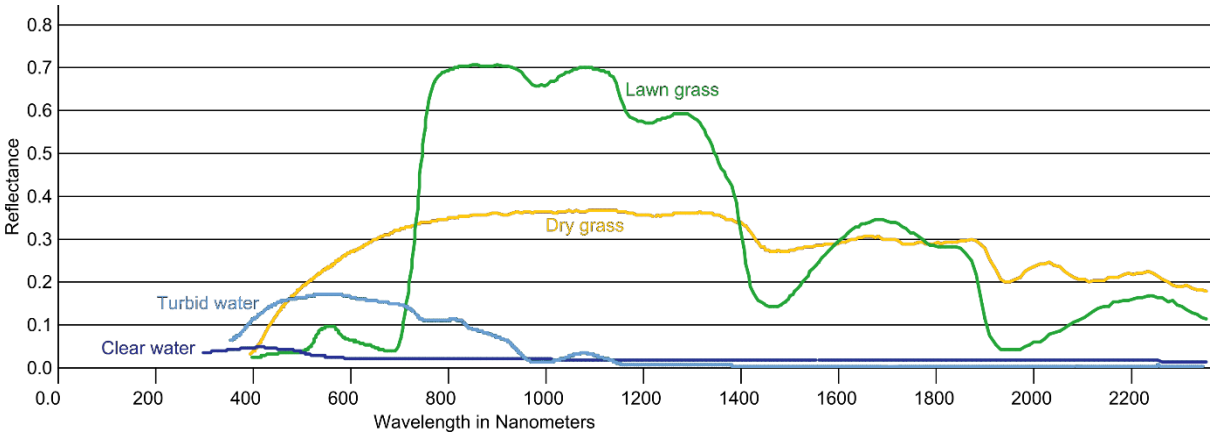

Figure 1-3: Spectra of water and vegetation in optical remote sensing ((USGS 2016), modified)

Earth observation via satellites dates back to the Keyhole-Satellites of the United States (U.S.) Corona-program in the 1960s. After the U.S. government declassified the images from the Corona-program the panchromatic films were digitized and are provided for a small price (Schowengerdt 2007). The historic Corona images are suitable for coastline and lake mapping and change detection (Grosse et al. 2005; Michael Voltersen 2011; Kropáček et al. 2012; Bayram et al. 2004), but their geo-referencing is challenging (Bayram et al. 2004). Clouds during the acquisitions reduce the number of available images significantly as with every optical satellite mission.

Since 1972 the Landsat satellites enable regular multi-spectral acquisition of the Earth's surface. The data base of Landsat archive images is immense and the images are available for free, thus, they have a great potential for long-term lake monitoring (Nath & Deb 2010; Gholizadeh et al. 2016; Smith 1997; Crétaux 2012; Chipman, J.W. 2009). Landsat images acquire only medium-resolution images, as the spatial coverage is negatively correlated to the spatial resolution. Landsat 1 and 2 have a low spatial resolution of 80 m, Landsat 4 to Landsat 8 have a 30 m resolution. The old Landsat satellite missions 1 and 2 acquire VIS and NIR. Since Landsat 4 (launch 1982) the Landsat missions also acquire SWIR and thermal data. The

currently operating Landsat satellites 7 and 8 also provide a panchromatic band with 15 m resolution. The spatial resolution of Landsat images limits their usability for monitoring of small lakes (Muster et al. 2013), but the multi-spectral images have been used successfully at larger lakes and coastal areas. Water mapping using old Landsat images is based on the NIR band (Arbor et al. 1976; Gupta & Banerji 1985; Lu et al. 2013), but since Landsat 4 the SWIR band is preferred for water mapping (Alesheikh et al. 2007; Feyisa et al. 2014; Li et al. 2013; Lu et al. 2013; Roach et al. 2012). The SWIR band is preferred as it enhances the contrast between turbid water and land features (cf. Figure 1-3). The VIS bands of Landsat penetrate the water surface, thus, they are suitable for bathymetric mapping (Philpot 1989; Bierwirth et al. 1993). The VIS bands of Landsat images are generally preferred for water quality mapping (Gholizadeh et al. 2016). Chl-a shows a peak in the red edge band (Schultz & Engman 2000), but Landsat does not acquire the red edge. Nevertheless, band combinations of VIS and NIR show good results for chl-a measurements (Brandão et al. 2016; Gholizadeh et al. 2016; Luoheng Han & Jordan 2005; Oyama et al. 2015). However, those approaches are limited to lakes with low concentrations of suspended minerals (Ritchie et al. 2003; Gholizadeh et al. 2016), because large concentrations of suspended sediments increase the reflectance in NIR (Moore 1980; Schultz & Engman 2000; Mertes et al. 2004) (cf. Figure 1-3). Thus, for the measurement of suspended minerals Landsat wavelengths between 400 nm and 1000 nm are suitable (Pulvermüller et al. 1995; Moore 1980; Strong & Eadie 1978; Gholizadeh et al. 2016; Zhang et al. 2003; Ritchie et al. 2003).

In 1999 the multi-spectral ASTER sensor was launched on board of the Terra satellite, however, the images have only available been free of charge since April 2016 (Tan & NASA 2016). The resolution of the ASTER images is 15 m in red, green and NIR, 30 m in SWIR and 90 m in thermal. A blue band is not acquired. ASTER images have proven useful for the monitoring of lakes (Gholizadeh et al. 2016), but due to their spatial resolution they are also limited in their use for lake monitoring.

In the last two decades several commercial satellite missions with a high spatial resolution were launched, e.g. IKONOS, WorldView-2/3, SPOT 5/6/7, Quickbird, and RapidEye (RE). However, a disadvantage of those satellite missions is the cost of the image data and the limited availability of archive data. The high-resolution satellites generally do not acquire the Earth's surface regularly, but only on-demand. RE images are available freely for German scientists with a data proposal. RE images have been acquired since 2009 by a constellation of five satellites and despite on-demand acquisitions there are many archive images of the study area. The multi-spectral images cover the VIS, red edge, and NIR and the spatial resolution of the images is 6.5 m (resampled to 5 m). RE imagery has been used in different band combinations for water mapping (Tetteh et al. 2015; Leeuwen & Tobak 2014; Maillard et al. 2012) and chlorophyll-a monitoring (Torbick & Corbiere 2015; Wen et al. 2014; Gholizadeh et al. 2016).

A great potential for lake monitoring is the new Copernicus Earth observation program: the first high-resolution optical satellite (Sentinel-2a) was launched in 2015, and will be joined by a second satellite Sentinel-2b in 2017, that is identical in construction (Drusch et al. 2012; European Space Agency (ESA) for Earth observation 2017b)). The Sentinel-2 satellites have a spatial resolution of 10 m to 20 m. The multi-spectral images include VIS, red edge, NIR and SWIR and are provided free of charge. So far, the number of available images is limited, but first tests show a great potential of Sentinel-2 images for water mapping (Du et al. 2016) and monitoring of water quality parameters (Toming et al. 2016).

1.2.2.2 Radar Remote Sensing of Lakes

Imaging radar remote sensing is an active system that acquires Earth's surface in the microwave spectrum from 1 mm to 1 m. The emitted microwave beam is directed sidewards to use the Doppler-effect for the resolution of the otherwise ambiguous signal. This side-looking geometry causes two separate spatial resolutions in radar imagery: the azimuth direction in flight direction of the sensor and the range resolution in the looking direction of the sensor. Because the azimuth resolution is limited by the length of the antenna, long antennas are synthesized in imaging radar remote sensing. Sensors with synthesized antennas are called synthetic aperture radar (SAR) (Lillesand et al. 2008).

The regular monitoring of the Earth's surface via SAR started in 1991 with the European ERS-1 satellite, complemented in 1995 by ERS-2. In 2002 the third European SAR satellite ENVISAT was launched. ERS-1/2 and ENVISAT acquire the Earth's surface in C-band (5.7 cm wavelengths) with 30 m resolution (Rignot & Van Zyl 1993; Louet & Bruzzi 1999). In addition to their imaging radar, those SAR satellite missions are equipped with a radar altimeter that can be used for direct lake level measurements (Baup et al. 2014; Maillard et al. 2015; Da Silva et al. 2012). However, radar altimeters measure point data along the orbital paths of the satellites, thus, they cover only few lakes (Alsdorf et al. 2007).

C-band SAR penetrates the atmosphere undistributed (Lillesand et al. 2008), but cannot penetrate vegetation due to its short wavelength and is scattered on the leaves' surface (Castree et al. 2009). **Figure 1-4** illustrates the imaging principles of an imaging SAR system with short wavelengths: smooth water reflects the microwave beam specularly away from the sensor, thus, no returning signal is received by the sensor and the target appears black. The scattering through waves, vegetation, or rough soil reflects a part of the signal back to the sensor and the target appears in grey tones. Thus, water quality parameters can only be measured if they influence the roughness of the water surface (e.g. oil spills (Topouzelis & N. 2008; Brekke & Solberg 2005). In the case of double-bounce scattering on two smooth surfaces most of the signal is scattered back to the sensor and the target is bright white (Lillesand et al. 2008; Martinis 2010). A higher water content of the target additionally enhances its reflectivity surface scattering (Lillesand et al. 2008; Martinis 2010).

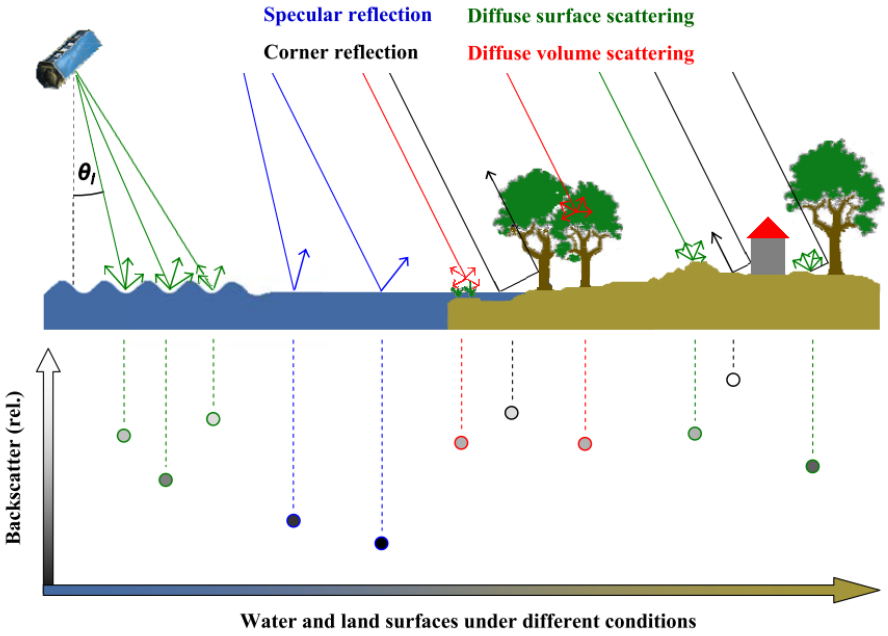

Figure 1-4: Scattering mechanism of an imaging SAR ((Martinis 2010), modified). The microwave beam is emitted sidewards, thus, the scattering depends on the look angle Θl. On the ground, the signal is then scattered or reflected depending on the size of the target, its orientation, and surface roughness in relation to the signals' wavelengths. Short wavelengths like X-band and C-band are mostly scattered on the surface of objects, e.g. vegetation.

ERS (Oberstadler & Ho 1997; Solbo & Pettinato 2004) and ENVISAT imagery (Heremans et al. 2003; Li et al. 2005; Gstaiger et al. 2012) were first used for flood mapping, but ENVISAT imagery has later also been used for lake monitoring (Liebe et al. 2009; Annor et al. 2009), because of their sunlight- and weather-independency.

The advantage of ENVISAT is its capability of polarimetric SAR acquisitions (Liebe et al. 2009): in imaging SAR, the emitted and received microwave signals are always polarized, either horizontally (H), vertically (V), or circularly. ERS acquires single-polarized SAR imagery: the sensor emits a H polarized signal and receives a H polarized signal (notation: HH) (Lillesand et al. 2008). However, for the classification of water surface areas with single-polarimetric SAR images, HH is preferred (Horritt 2003; Herrera-Cruz & Koudogbo 2009; Townsend 2001), because it has the highest contrast between water and land and low sensitivity to waves and ripples (Martinis 2010).

ENVISAT can acquire single-polarized images in all four different modes (HH, VV, HV, and VH) as well as dual-polarimetric images. (Multi-) polarimetric SAR acquisitions enhance the information content of SAR images by the combination of different polarizations, in exchange for a reduced spatial resolution (Lillesand et al. 2008). In quad-polarimetric SAR all four polarizations (HH, VV, HV, and VH) are acquired, in dual-polarimetric SAR only two polarization directions. The possible dual-polarized combinations are dual-co-polarization with HH and VV or dual-cross-polarization with either HH and HV or VV and VH.

The resolution of those first SAR missions is too low for the monitoring of small lakes, especially in multi-polarimetric mode with reduced spatial resolution. Several (very) high-resolution SAR missions were launched in the last decade, with spatial resolutions better than 5 m in single-polarimetric mode. However, as with the high-resolution optical images, the high-resolution SAR images are only acquired on demand.

C-band satellite Radarsat-2 was launched in 2007. It provides SAR images in single-, dual-, or quad-polarimetric mode on demand (Morena et al. 2004). The more polarizations are acquired, the better the physical illustration of the sensor target interaction is, thus, quad-polarimetric SAR can be used for the distinction of different scattering mechanisms and the measurement of physical properties (Lillesand et al. 2008; Mertes et al. 2004). Therefore, the quad-polarimetric images are preferred for the monitoring of wetlands and the discrimination of open water and flooded vegetation (Zhao et al. 2014; White et al. 2014; Yonezawa et al. 2012; Brisco et al. 2011; Hong et al. 2015; Evans & Costa 2013; Schmitt & Brisco 2013; White et al. 2015; Qi et al. 2010).

TerraSAR-X (TSX) and COSMO-SkyMed are two X-band missions (3 cm wavelengths). The German satellite TSX was launched in 2007, joined by its twin satellite TanDEM-X in 2010. COSMO-SkyMed is a constellation of four satellites, launched between 2007 and 2010. X-band and C-band are very similar in their scattering behavior (cf. **Figure 1-4**), but due to its shorter wavelengths X-band can be attenuated by heavy precipitation or hail (Danklmayer et al. 2008). Both missions can acquire single-, dual-, as well as quad-polarimetric images, but the operational use the TSX satellites includes only single- and dual-polarimetric images. Single-polarimetric X-band imagery is frequently used for flood monitoring (Herrera-Cruz & Koudogbo 2009; Gebhardt et al. 2008; Hahmann et al. 2008; Schwarz et al. 2009; Martinis 2010; Martinis et al. 2009; Martinis et al. 2015; Voormansik et al. 2014; Gstaiger et al. 2012; Pulvirenti et al. 2011; Mason et al. 2010; Pulvirenti et al. 2013; Puech & Matgen n.d.; Hung et al. 2012), but can also be used for lake monitoring (Heine et al. 2014; Baup et al. 2014; Strozzi et al. 2012; Yayong et al. 2016). Dual- and quad-polarimetric X-band are preferred for wetland monitoring and the distinction of different vegetation types (Hong et al. 2015; Betbeder et al. 2014; Van Beijma et al. 2014).

Three new high-resolution SAR satellites were launched, during the time of the here presented work: ALOS-2 and Sentinel-1a and -1b. ALOS-2 was launched in 2014 and acquires the Earth's surface in L-band (23 cm wavelengths) (Japan Aerospace Exploration Agency / Public Affairs Department 2014). L-band SAR penetrates the canopy of trees and is only scattered on thick branches and stems (Castree et al. 2009), thus it could be used for the monitoring of water below vegetation. The Copernicus Earth observation program by ESA launched two high-resolution C-band SAR satellites in 2014 (Sentinel-1a) and in 2016 (Sentinel-1b) (European Space Agency (ESA) 2016; European Space Agency (ESA) for Earth observation 2017a). The two satellites acquire the Earth's surface regularly and the data are provided free of charge. However, the satellites can only be used in single-polarimetric or in dual- cross-polarimetric mode (HH and HV or VV and VH). Dual-co-polarized (HH and VV) images and quad-polarimetric images cannot be acquired, but still the new images are useful for regular lake monitoring and first tests proved their potential (Amitrano et al. 2014; Malenovský et al. 2012; Twele et al. 2016).

1.3 Research Framework

The thesis is focused on the lake rich area of northern Central European lowlands. This chapter illustrates the research framework of the thesis, including the study area with case areas used throughout the chapters, and the spatial data for the methodological developments.

1.3.1 Study Area

The northern Central European lowlands, including northeastern Germany and Poland, were formed by the last glaciation 10 000 years ago. The retreat of the glaciers after the last ice age

can be seen as the point “zero” in the landscape formation. Thus, the region provides an ideal “large scale natural laboratory” for landscape evolution analysis. The landscape differs in its land use ranging from quasi-natural national parks to intensively used agricultural land. This setting allows deciphering possible influences of land-use on the landscape evolution. The region has a climate gradient with increasing continentality towards the eastern part of Poland. It has a rather low annual precipitation, which makes it vulnerable to hydrological changes (Deutscher Wetterdienst (DWD) n.d.).

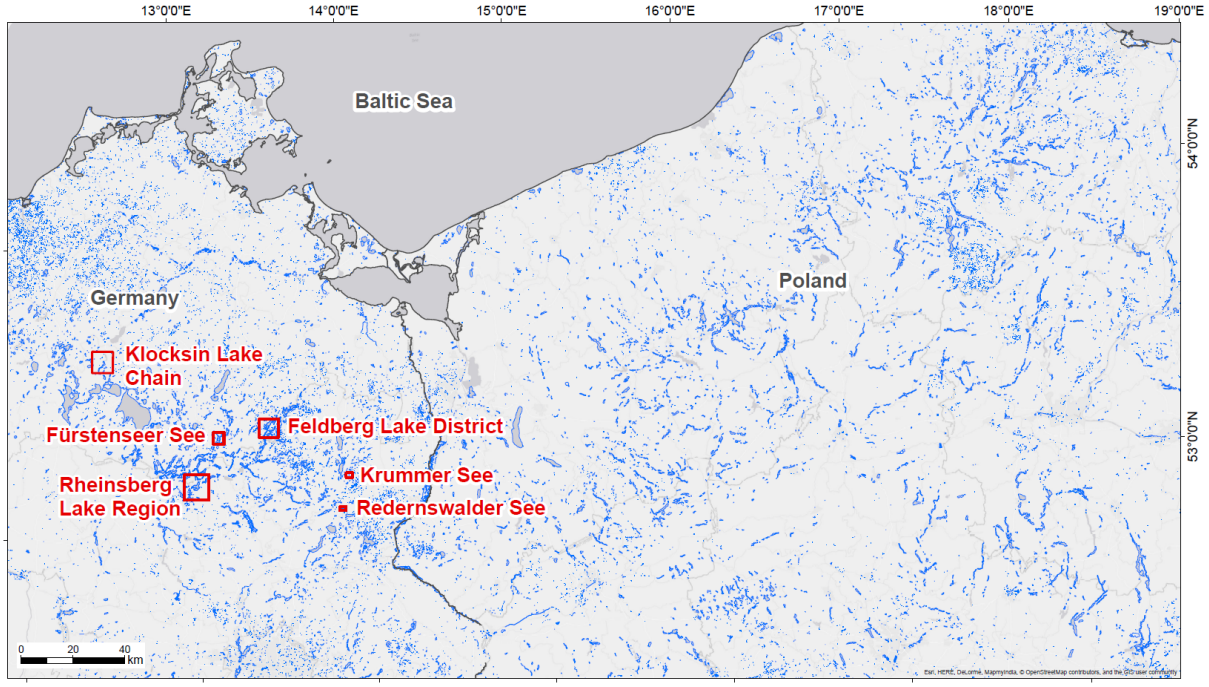

Figure 1-5: The study area – the northern Central European lowlands - with its six case study areas in northeastern Germany. Lakes are outlined with blue color. The lake polygons are provided by OpenStreetMap (OpenStreetMap 2016)

The landscape is defined by a large number of natural lakes (cf. **Figure 1-5**). The lakes are characterized by their inflow and outflow dynamics, their trophic state, and the concentration of alkaline elements (e.g. calcium) in the lake water (cf. **Chapter 1.2.1**). Endorheic, and kettle hole lakes show long-term lake level changes (cf. **Table 1-1**) due to their flow dynamics groundwater-fed. Thus, the monitoring of lake level changes is focused on those lake types: Redernswalder See is an endorheic lake with regular in situ gauging since 1982 (Kaiser, Koch, et al. 2014; Kaiser, Friedrich, et al. 2012). It is used for the validation of the lake level reconstruction using aerial photos, before the method is applied to Lake Krummer See, a groundwater-fed lake without in situ measurements. Lake Fürstenseer See is the case study site for lake reconstruction using satellite images. It is a groundwater-fed lake with regular measurements since 1988 (Kaiser, Germer, et al. 2012). Lake Fürstenseer See is later also used for the development and validation of the reed monitoring.

Calcite precipitation occurs in calcium-rich hardwater lakes only and is linked to their trophic states. Three lakes in the Feldberg Lake District were selected that are well-researched and have documented calcite precipitation events, for the development of a robust classification approach and its valitation: Feldberger Haussee, Breiter Luzin, and Schmaler Luzin. The chemical and physical water parameters of the three lakes have been measured in situ since

1998. The remotely-sensed monitoring of calcite precipitation is applied to four lakes in the Klocksin Lake Chain (Flacher See, Tiefer See, Hofsee, and Bergsee) and 16 lakes in the Rheinsberg Lake Region (Breutzensee, Dagowsee, Gerlinsee, Großer Glietzensee (Ost), Großer Krukowsee, Kleiner Krukowsee, Nehmitzsee, Peetschsee, Plötzensee, Großer Glietzensee (West), Großer Boberowsee, Großer Pälitzsee, Kleiner Glietzensee, Menowsee, Roofensee, and Stechlinsee). Lake Tiefer See was sampled within the framework of ICLEA, including the drilling of a lake sediment core and the collection of solid substances in the open water in sediment traps since 2012. All analyzed lakes are illustrated in **Figure 1-5**.

1.3.2 Database

This thesis combines remote sensing data with terrain and field data. In the **Chapters 1.3.2.1** to **1.3.2.3** the different data sets are described in detail.

1.3.2.1 Remote Sensing Data

Optical and SAR remote sensing images have both proven useful for lake monitoring (cf. **Chapters 1.2.2.1** and **1.2.2.2**). For this thesis, limiting factors for the data selection are a) the availability of the images for the northern Central European lowlands, including spatial coverage and the number of archive images, b) the spatial resolution of the images with respect to the monitoring subject, and c) the cost of the images. The data selection is further discussed in the according **Chapters 2** to **5**.

Overall 35 aerial photos, 242 optical satellite images (RE, Landsat 5/7/8, and Sentinel-2) and 19 SAR satellite images (dual-co-polarimetric TSX) are analyzed within this thesis.

Redernswalder See is covered by eight greyscale aerial photos between 1937 and 1993 and Krummer See by seven between 1959 and 1993. The greyscale aerial photos are provided digitally, but without spatial information. The processing of the aerial photos is described in detail in the **Supplementary Materials on Chapter 2**. Between 2003 and 2012 four additional true-color aerial photos have been acquired of Redernswalder See and Krummer See. Those true-color aerial photos are provided as digital orthophotos by Landesvermessung und Geobasisinformation Brandenburg (LGB). Two further digital orthophotos (true-color, 2011 and 2013) of Lake Füstenseer See were provided by Landesamt für innere Verwaltung Mecklenburg-Vorpommern.

The optical and SAR satellite images are listed in **Table 1-2**. The processing of the 35 RE images for lake level reconstruction is described in detail in **Chapter 3** and illustrated in **Supplementary Materials on Chapter 3**. The processing of the dual-polarimetric TSX images for reed monitoring is described in **Chapter 4** and the processing of Landsat and Sentinel-2 images in **Chapter 5.** All satellite imagery used in this thesis is (with data proposals) free of charge. TSX images were provided by Deutsches Zentrum für Luft- und Raumfahrt (DLR) under the proposal HYD2636 and RE imagery was provided by BlackBridge AG (now: Planet Labs, Inc.) under proposal RESA Projekt-ID A1274. Landsat Surface Reflectance data are provided by USGS and Sentinel-2 by ESA.

Table 1-2: Overview of satellite imagery used in this thesis.

System	Satellite	Spatial resolution (m)	Range of wavelengths (and polarization)	Number of bands	Time period	Number of data sets	Product level
Optical	RapidEye	6.5 x 6.5, resampled to 5 x 5	440 nm - 850 nm	5	Apr 2009 - Oct 2014	37	3A
Optical	Landsat 5	30 x 30	450 nm - 2350 nm	6	Mar 1998 - Oct 2011	60	Surface Reflectance product
Optical	Landsat 7	30 x 30	450 nm - 2350 nm	6	Jul 1999 - Oct 2015	116	Surface Reflectance product
Optical	Landsat 8	30 x 30	450 nm - 2300 nm	8	Apr 2013 - Oct 2015	27	Surface Reflectance product
Optical	Sentinel-2	10 x 10 (20 x 20 resampled to 10 x 10)	458 nm - 900 nm (690 nm - 2280 nm)	4 (6)	Aug 2015	2	L1C
SAR	TerraSAR -X (asc)	1.7 x 6.6, resampled to 3 x 3	3.1 cm (HH + VV)	2	Aug 2014 – Mar 2015	4	Single Look Slant Range Complex (SSC)
SAR	TerraSAR -X (desc)	1.9 x 6.6, resampled to 3 x 3	3.1 cm (HH + VV)	2	Aug 2014 – May 2015	15	Single Look Slant Range Complex (SSC)

1.3.2.2 Terrain Data

Terrain data is required for the reconstruction of lake levels using remote sensing images (**Chapters 2 and 3**).

Terrain data was used in form of digital surface models (DSM) and bathymetric point data of lakes to cover over- and underwater surface. The DSM have 1 m spatial resolution (ATKIS-DGM1) and are acquired using light detection and ranging (LIDAR) measurements in 2010 and 2011. The DSM were provided by Landesvermessung und Geobasisinformation Brandenburg (LGB) and Landesamt für innere Verwaltung Mecklenburg-Vorpommern. The bathymetric point data was measured via sonar.

Bathymetric data of Redernswalder See was provided by Landesamt für Umwelt, Gesundheit und Verbraucherschutz (Brandenburg) and Ministerium für Landwirtschaft, Umwelt und Verbraucherschutz M-V. In the case of Krummer See bathymetric point data was acquired within the framework of ICLEA.

The processing of the data is described in detail in the **Supplementary Materials on Chapter 2** and in **Chapter 3**.

1.3.2.3 Field Data

The linkage of the different temporal scales from in situ measurements to long-term proxy-based monitoring by remote sensing is one of the objectives of this thesis within the framework of ICLEA. However, in situ measurements are also essential for the validation of remote sensing results. This chapter summarizes the field data used in this thesis.

Lake levels have been gauged at Fürstenseer See since 1987 and at Lake Redernswalder See since 1976. Water-land borders have been mapped using handheld (differential) Global Positioning System (GPS) devices at Fürstenseer See on 12 August 2014 and at Krummer See on 14 January 2014. Additionally, photos of the study site have been taken (cf. **Chapters 2** and **3**). The reed vegetation at Fürstenseer See has been documented on photos in June 2014, November 2015, and January 2016 and a camera acquired a time lapse video of the northern part of the lake since 2015 (cf. **Chapter 4**). Drowned trees are used as bioarchives at Redernswalder See and Krummer See. The trees are analyzed dendro-hydrologically within the ICLEA framework and used as a proxy for lake level changes (cf. **Chapter 2**).

For the monitoring of calcite precipitation $CaCO_3$, chl-a, temperature, pH, alkalinity, and ion concentrations (NO_3^-, $SiO3^{2-}$, Cl^-, SO_4^{2-}, Na^+, K^+, Mg^{2+}, and Ca^{2+}) were measured by Leibniz-Institute of Freshwater Ecology & Inland Fisheries (IGB) at the lakes Feldberger Haussee, Breiter Luzin, and Schmaler Luzin. The measurements were conducted on 68 days in the period between March 1998 and October 2015. At Lake Tiefer See a sediment core was drilled and analyzed within the ICLEA framework: This sediment record provides information about calcite precipitations in the lake with yearly resolution (cf. **Chapter 5**).

1.4 Research Objectives and Research Questions

ICLEA aims at the long-term and large scale monitoring of landscape dynamics, specifically lakes. The purpose of the remote sensing imagery is the temporal linkage of in situ measurements and proxy-based monitoring and the expansion of the monitoring to a large scale. Method development in remote sensing is often pursued from a pure remote sensing perspective. In contrast to that, the motivation of this thesis is user driven, anchored in an interdisciplinary context.

This background leads to the following **overarching research questions** of the thesis:

- What are the requirements for remote sensing data for the monitoring of (specific) lake parameters in the northern Central European lowlands?
- What is the greatest potential and what are the limitations of remote sensing imagery for long-term monitoring?
- What new ecological insights can be found for lakes in the northern Central European lowlands by using remote sensing archives?

The specific objectives of the thesis are first the development of new methods for the monitoring of lake level changes, shoreline vegetation and calcite precipitation. The developed methods are then thoroughly validated before the transferability is discussed and/or tested, because the new methods aim at an application on a large-scale areas. The ecological analysis of the newly achieved remotely-sensed monitored results concludes the study.

Based on the objectives the following **specific research questions** will be addressed in this thesis:

Method perspective:

- How accurately can lake level changes be reconstructed based on optical remote sensing data? What are the advantages and disadvantages for the lake level reconstruction of different optical remote sensing data archives?
- Can polarimetric SAR data be used for the short-term and long-term monitoring of reed areas? What are the advantages over optical remote sensing imagery monitoring methods? What are disadvantages? Can polarimetric SAR data be used for the extraction of water-land borders at vegetated shorelines?
- What are efficient and robust methods to monitor calcite precipitation using multi-spectral remote sensing data?

Application perspective:

- What are requirements for the successful application of the developed approaches? What are challenges for the transfer to other lakes?
- Which specific results can be achieved for northern Central European lowlands and how can the new methods complement in situ measurements and proxy-based monitoring?

The specific research questions are first addressed in four stand-alone manuscripts of **Chapters 2 to 5**. Those manuscripts are all published in international peer-reviewed scientific journals. For this purpose, each of these chapters is subdivided into the sections introduction (research background), study area and data base (research framework), method, results, discussion, and conclusions. Consequently, recurring material cannot be avoided completely. The four manuscripts are presented unchanged in the thesis, neglecting adjustments in formatting. Supplements to the manuscripts, which are important for the thesis have been included.

The manuscript of **Chapter 2** is a joint work of researchers in interdisciplinary fields. The remote-sensing monitoring and analysis was performed by Iris Heine. The first author, Knut Kaiser, managed the joint work. **Chapters 3 to 5** were written by the first author, Iris Heine. The co-authors contributed to discussions and revisions to clarify and improve the manuscripts. Further publications within the scope of the thesis are listed in the Appendix.

The next paragraphs briefly introduce the individual manuscripts in the overall context of the thesis by providing their specific objectives and main contributions. For each chapter, the publication information, the overall objective, the relations to the other manuscripts as well as its specific method and application objectives are given.

Chapter 2: Reconstruction of Long-Term Lake Level Changes Using Aerial Photos

published as:

Kaiser, K., Heinrich, I., Heine, I., Natkhin, M., Dannowski, R., Lischeid, G., Schneider, T., Henkel, J., Küster, M., Heussner, K.-U., and Bens, O. (2015). Multi-decadal lake-level dynamics in north-eastern Germany as derived by a combination of gauging, proxy-data and modelling. Journal of Hydrology, 529, 584–599, doi:10.1016/j.jhydrol.2014.12.057.

Only selected lakes have historic hydrological records and the observation periods are rarely longer than fifty years despite an early start of hydrological gauging in central Europe. Thus, other methods of lake level reconstructions are required for lakes without gauging or during

periods without in situ measurements: water-balance modelling may be used to estimate former lake levels of endorheic and groundwater-fed lake. This strongly depends on meteorological data and gauged lake levels. As an alternative, lake levels can be derived from document archives such as historic maps and aerial photos and geo-/bioarchives like drowned and living trees.

Even though aerial photos are ubiquitous and easy to obtain for lakes in the northern Central European lowlands, they have been rarely used for lake-level studies. In this first chapter, aerial photos are used for the reconstructions of lake levels at two lakes (Redernswalder See and Krummer See). The derived lake levels are then, for the first time, jointly analyzed with dendro-hydrological results from geo-/bioarchives and compared to modelled lake levels.

In the framework of this thesis the underlying objectives of this chapter are the evaluation of the potential of aerial photos for the two lakes, Redernswalder See and Krummer See, the development of a semi-automated approach for the extraction of lake levels using aerial photos, and finally the synthesis with other approaches for combined long-term lake level reconstructions.

Method objectives:

- Evaluation of the potential of aerial photos at two lakes (Redernswalder See and Krummer See)
- Development of a semi-automated approach for the extraction of lake levels using aerial photos

Application objectives:

- Reconstruction of the lakes levels of Redernswalder See and Krummer See based on aerial photos
- Synthesis of document archives with geo-/bioarchives, gauged and modelled lake levels for cross-validation of the results and in order to derive continuous long-term level reconstructions

Chapter 3: Reconstruction of Long- and Short-Term Lake Level Changes Using RapidEye Satellite Imagery

published as:

Heine, I., Stüve, P., Kleinschmit, B., & Itzerott, S. (2015). Reconstruction of Lake Level Changes of Groundwater-Fed Lakes in Northeastern Germany Using RapidEye Time Series. Water, 7(8), 4175–4199, doi:10.3390/w7084175.

Aerial photos provide a long time series, but have a sparse temporal resolution. Short-term lake changes are missed. Satellite time series data are shorter, but they do have a much higher coverage frequency. In a second step, the potential of satellite imagery for the monitoring of short-term lake level changes is tested. We chose RE satellite imagery, because of their spatially high resolution, the large data archive with regular acquisitions of the study area since 2009, and their free availability for German scientists with a data proposal.

The objectives of this chapter are the development of an automated approach for the extraction of lake levels based on the experience of **Chapter 2** and the evaluation of RE satellite images for lake level reconstruction and the monitoring of short-term changes.

Method objectives:

- Testing the potential of high-resolution multi-spectral satellite images (RE) for the indirect measurement and reconstruction of small and short-term lake level changes
- Detailed discussion of methodological challenges, such as the influence of shorelines slopes, vegetation, and shadows on the accuracy of lake level reconstruction

Application objectives:

- Examination of the attainable accuracy and defining requirements and limitations to assess the transferability of this lake level reconstruction approach

Chapter 4: Year-Long Monitoring of Reed Belts Using Dual-Polarimetric TerraSAR-X Imagery

published as:

Heine, I., Jagdhuber, T., & Itzerott, S. (2016). Classification and Monitoring of Reed Belts Using Dual-Polarimetric TerraSAR-X Time Series. Remote Sensing, 8(7), 552, doi:10.3390/rs8070552.

Chapter 4 focuses on the monitoring of reed belts at shallow water areas as reed provides important ecosystem functions. This depends on the lake level and is influenced by level changes. Additionally, the monitoring of seasonal changes of reed, specifically the start and duration of leaf-on and leaf-off periods, are of interest for hydrological measurements. Optical imagery is not suitable for operational monitoring with high temporal resolution, because cloud coverage and low sun elevation angles in winter hamper regular monitoring (cf. **Chapter 3)**. Thus, in this chapter the potential of dual-polarimetric TSX imagery for reed monitoring is tested. Additionally, we also try to overcome the limitations of optical imagery for the extraction of precise water-land borders at shorelines with reed vegetation by the use of dual-polarimetric TSX (cf. **Chapter 3**).

Method objectives:

- Gain knowledge about the scattering mechanisms of reed belts during the monitoring period (August 2014 to May 2015) and their exploitation for the phenological monitoring of reeds
- Development of an automatic algorithm for classification of reed areas with recommendations for the best suitable classification input parameters and the most effective acquisition periods for the most suitable classification

Chapter 5: Long-Term Monitoring of Calcite Precipitation using Multi-Spectral Satellite Imagery

published as:

Heine, I., Brauer, A., Heim, B., Itzerott, S., Kasprzak, P., Kienel, U., & Kleinschmit, B. (2017). Monitoring of Calcite Precipitation in Hardwater Lakes with Multi-Spectral Remote Sensing Archives. Water, 9(1), 15, doi:10.3390/w9010015.

The objective of **Chapter 5** is the analysis of calcite precipitation based on medium-resolution optical satellite images. The analysis is based on the Landsat archive. Sentinel-2 data is tested for transferability.

Calcite precipitation is an extensive limnological process, thus, medium-resolution imagery is sufficient for the monitoring from space. However, a high temporal resolution is important as calcite precipitation events are usually limited to a short time period.

The specific objectives of **Chapter 5** are the development of a robust automated classification method for calcite precipitation based on Landsat images, the evaluation of the application to Sentinel-2 imagery, and finally, the application of the classification for long-term monitoring at several lakes.

Method objectives:

- Development of a robust automated remote sensing-based approach for retrospective long-term monitoring of calcite precipitation based on Landsat time series
- Evaluation of the transferability to Sentinel-2 data.

Application objectives:

- Long-term monitoring of calcite precipitation based on the Landsat archive at selected lakes and linking of calcite precipitation to lake restoration measures
- Transfer of the classification approach to two additional regions in the Central European lowlands
- Characterization of calcite precipitation in terms of frequency and duration to deepen the process understanding

2 Reconstruction of Long-Term Lake Level Changes Using Aerial Photos

Kaiser, K., Heinrich, I., Heine, I., Natkhin, M., Dannowski, R., Lischeid, G., Schneider, T., Henkel, J., Küster, M., Heussner, K.-U. and Bens, O. (2015). Multi-decadal lake-level dynamics in north-eastern Germany as derived by a combination of gauging, proxy-data and modelling. Journal of Hydrology, 529, 584–599*, doi:10.1016/j.jhydrol.2014.12.057*.

Available online 7 January 2015.

Abstract

In the glacially formed landscape of north-eastern Germany pronounced hydrological changes have been detected in recent decades, leading to the general question how lake levels and related groundwater levels perform in a long-term perspective, i.e. during the last c. 100 years. But long-term lake-level records are rare; most observations do not start before the late 20th century. Therefore, the potential of historic hydrological data, comprising drowned trees (as a geo-/bioarchive) and aerial as well as map imagery (as a document archive) was tested in order to derive discrete-time lake-level stands. These data are contrasted with lake-level simulations, obtaining a continuous-time series.

Two small glacial lakes without connection to the stream network (i.e. closed lakes) were investigated in the Schorfheide area, c. 70 km north of Berlin. Both are dominantly fed by groundwater and precipitation but differ in their hydrogeological and catchment characteristics. For one lake a c. 40 year-long gauging record is available, showing high lake levels in the 1980s followed by a lowering of c. 3 m till the mid-2000s. In both lakes submerged *in situ* tree remains were discovered and dated by dendrochronology, revealing low lake levels during the first half of the 20th century. One lake was almost completely dry until c. 1960. Aerial photos provided data on lake levels since the 1930s which are corroborated by evidence of topographic mapping. Combining the empiric data with retrograde lake-level modelling, a well-proven lake-level record can be established for one lake that covers the last c. 90 years. The same general lake-level dynamics could be reconstructed by means of proxy data for the other lake. In both cases climate has been the dominant driver of lake-level dynamics. Comparisons with other multi-decadal lake-level records from the region show that these differ, depending on the hydrological lake type which modifies water feeding and water level. The results clearly showed that lake levels exhibited substantial long-term changes that should be taken into account in future hydroclimatic and hydrological studies.

2.1 Introduction

Despite the relatively early commencement of hydrological records in central Europe, monitoring data are often heavily constrained by the length of the observation period. While some gauging stations at large rivers and lakes as well as tidal gauges along the North and Baltic Sea coasts have operated since the 18th and 19th century (e.g. River Elbe/Magdeburg: 1727, River Rhine /Cologne: c. 1770, River Oder/Frankfurt O.: 1810, Lake Constance: 1816, Lake Müritz: 1879; (Strigel et al. 2010); www.undine.bafg.de), gauging of low-order streams and lakes as well as aquifers and peatlands were established very late, i.e. mostly from the last third of the 20th century onwards. Furthermore, most hydrological monitoring sites are located along drainage networks and are thus heavily influenced by discharge regulation and other human impacts (e.g. hydromorphological change, intensive land use). These sites are less suitable for the tracing of long-term hydrological changes driven by climatic impact compared to pristine catchments. While the empirical detection of hydrological changes is an indispensable prerequisite for environmental and climate impact research, the general challenge to develop long time series at suitable sites still remains. Long records generally help to identify trends and to separate short-term (i.e. high frequency) from long-term (i.e. low frequency) dynamics. This in turn is important for the attribution of the changes detected (Lischeid et al. 2012). Not all hydrological phenomena observed in a relatively short period can be unequivocally attributed to global (i.e. climate and land use) change. Some changes may even reflect periodic long-term natural processes (Blöschl & Montanari 2010), basically driven by natural solar and atmospheric dynamics.

For the extension of hydrological time series into the past, a comprehensive bundle of well-developed historic-hydrological and palaeohydrological methods is required (e.g., (Brown 2002; Brázdil et al. 2006; Gregory et al. 2006; Meko 2006; Baker 2008; Benito & Thorndycraft 2005)). This historical or reconstructive perspective on (landscape) hydrology forms a research field usually established in geosciences/geography and palaeoecology including dendrohydrology. But even in central Europe, with its advanced hydrological, climatic and ecologic monitoring systems, a close linkage between observation data on the one hand and reconstruction data on the other is still rarely found (e.g. (Schönfelder & Steinberg 2004; Brázdil et al. 2005; Hilt et al. 2008; Czymzik et al. 2010; Kämpf et al. 2012; Dressler et al. 2007).

In this paper we present a case study on the nexus of observation and reconstruction from north-eastern Germany, where pronounced hydrological changes were observed during the last decades. Declining discharge or drying out of rivers and streams, lowering of groundwater and lake levels as well as shrinking peatlands indicate a period of two to three decades with decreasing water balances in the region, ending about 2010 (e.g. (Germer et al. 2011; Natkhin et al. 2012; Kaiser, Friedrich, et al. 2012)). Some hydrological phenomena are clearly related to direct human impact (e.g. drainage of peatlands; (Merz & Pekdeger 2011)). Other 'drying-up' symptoms concern even near-natural ecosystems (e.g. decreasing lake levels within closed lake basins lying in forested catchments) and point to climatic impact on a large scale (Kaiser, Koch, et al. 2014). Furthermore, north-eastern Germany is one of the regions in central Europe which is most affected by climate change, as projected by model scenario studies (e.g. (Jacob et al. 2008; Huang et al. 2010; Hattermann et al. 2011; Dietrich et al. 2012; IPCC 2014)).

Considering the available empirical database, the long-term hydrological variability on multi-decadal (50 to 100 years) to centennial scale (several hundreds of years) is poorly recorded and understood in that region so far. Knowledge is needed about the long-term dynamics of closed groundwater-fed lakes, which serve as 'sentinels' of the climate and human impact on the regional water balance (e.g. (Mason et al. 1994; Williamson et al. 2008; Adrian et al. 2009; Rinke et al. 2013)).

The focus of our study is on multi-decadal (last c. 100 years) lake-level dynamics of two closed lake basins. For Lake Redernswalder See (RS) a gauging record is available since 1976. Lake Krummer See (KS) is an ungauged lake (**Figure 2-1**). For both lakes proxy data from archives exist (historic maps, aerial photos), potentially reflecting the local water-level history. Generally, these data are ubiquitous and easy to obtain for the lakes in the region, but have been rarely compiled and used for lake-level studies thus far. Drowned tree remains, however, which were discovered in both lakes in 2009 (Supplement 1), are a newly described and rare feature of inland lakes in the region. Furthermore, for RS water-budget and lake-level modelling covering the period 1958-2007 was performed recently (Natkhin et al. 2012; Natkhin 2010), forming the base for retrograde lake-level modelling of the last 90 years. Combining all evidence we are able to establish a robust lake-level record for RS. If climate primarily drives the multi-decadal water-level dynamics of lakes and groundwater aquifers, one can assume that lakes of the same hydrological setting (groundwater-fed closed lakes) may respond in a fairly similar way. This should be true even if the catchment structure (geology, hydrogeology, soils, land-use/land-cover) is somewhat different. For that reason KS was included in our study. Further adjacent lake- and groundwater-level records were used for comparison (**Figure 2-1**, **Table 2-1**).

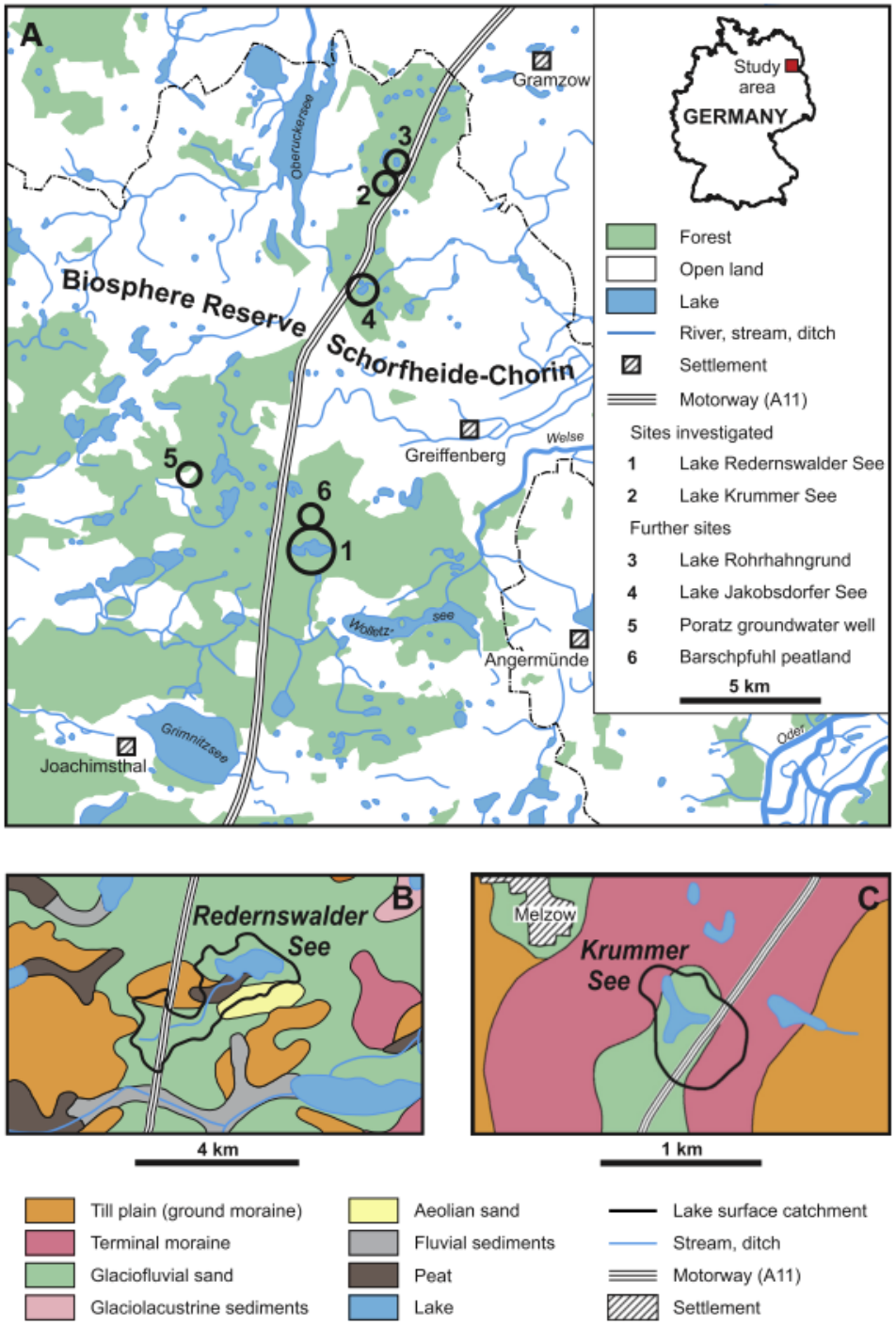

Figure 2-1: Sketch maps with the sites investigated. **A** – Overview on the study area with the main sites investigated and with further sites used for comparison. **B** – Drainage network and geology in the surroundings of Lake Redernswalder See (after LGRB, 1997, modified). **C** – Drainage network and geology in the surroundings of Lake Krummer See (after LGRB, 1997, modified).

Table 2-1: Characterisation of the lakes under study and of further sites and its catchments (data from (Mauersberger & Mauersberger 1996; LGRB 1997; Luthardt et al. 2009) and from own compilation).

Site name	Lake Redernswalder See	Lake Krummer See	Lake Rohrhahngrund	Lake Jakobsdorfer See	Poratz groundwater well
Site ID and data	RS(a,d,c,d,e)	KS(b,c,e)	RG(a)	JS(a)	PZ(a)
Northing (°)	53.046949	53.159979	53.176824	53.131995	53.063524
Easting (°)	13.857089	13.905887	13.917912	13.89259	13.787774
Altitude (m NHN)	55	85	76	60	56
Lake area (ha)	55	4	5	23	-
Max. lake depth (m)	13	7	6	10	-
Hydrologcial lake type (sensu (Mauersberger 2006))	Endorheic lake	Groundwater lake	Groundwater lake	Spring lake	-
Gauging since (year)	1976	-	2006	1996	1968
Max. water-level amplitude (m)	3.2	>5.0	0.6	1.2	4
Trophic state	Mesotrophic	Eutrophic	Eutrophic	Mesotrophic	-
Catchment area (ha)	390	30	30	120	-
Catchment geology (prevailing)	Outwash plain	Terminal moraine	Terminal moraine	Terminal moraine	Outwash plain
Catchment land-cover (prevailing)	Coniferous forest	Decidious forest	Decidious forest	Decidious forest	Arable land

a: Gauging data; b: Dendrochronological data; c: Remote sensing data; d: Modelling data; e: Bathymetric data.

2.2 Study sites

The study area, c. 70 km northeast of Berlin, is situated in the glacially formed north-eastern German lowlands in the Uckermark region, part of the federal state of Brandenburg. Since 1990 the area has been part of the UNESCO Biosphere Reserve Schorfheide-Chorin. This nature conservation status aims at the protection and development of the regional cultural landscape, consisting of typical and well-preserved lowland ecosystems (e.g. lakes, peatlands, flowing waters, deciduous forests).

The landscape is dominated by Pleistocene sandy and loamy sediments of glacial origin. Holocene organic sediments (mostly gyttja and peat) occur in lake basins, riversides and peatlands. Larger peatlands are drained and under agricultural grassland use. The wider study area (**Figure 2-1A**) covers an altitudinal range from c. 1 to 140 m NHN (NHN is the German altitudinal reference system that is nearly equal to m a.s.l.). A prominent terminal zone of the last glacial Weichselian phase stretches through the study area (Gerswalde end moraine north of Angermünde; (LGRB 1997)). The geology in the catchments of our two main study sites is rather diverse. The basin of RS, c. 55 ha in size, is embedded in glaciofluvial and well

permeable sands of a slightly undulating outwash plain with accompanying till, aeolian sand and peat (**Figure 2-1B**). The catchment of KS, with a lake size of c. 4 ha, is dominated by several and partly less permeable sediments of the hilly terminal zone (e.g. tills, glaciofluvial sands, erratic boulders; (LGRB 1997); **Figure 2-1C**). Accordingly, the hydrogeological settings differ. The lake level of RS conforms to the water level of the first unconfined aquifer of the wider surroundings (supralocal aquifer), whereas KS lies in a small groundwater body of a small basin that is sealed by till (a local perched aquifer). Both lake basins, with maximum water depths of c. 13 m (RS) and c. 7 m (KS), were probably formed by the late Pleistocene/early Holocene melting of buried glacial ice (i.e. so-called 'dead ice'; (Kaiser, Lorenz, et al. 2012)). For RS and KS bathymetric data (maps) are available that were obtained in 2002 and 2014, respectively.

RS and KS as well as Lake Rohrhahngrund (RG), whose gauging record is used for comparison, are located in closed basins with interior drainage. By contrast, Lake Jakobsdorfer See (JS), which is also used for comparison, has an artificial outlet. The lakes belong to different hydrological lake types (*sensu* (Mauersberger 2006); **Table 2-1**). But they are all dominantly fed by groundwater and precipitation. The surroundings of the lakes are drained either by the Rivers Welse and Sernitz, and thus to the Oder, or by the Ucker, draining northwards to the Baltic Sea. Additionally, the groundwater-level record of Poratz (PZ) adjacent to RS was used for comparison.

The study area is located in the transition zone between maritime and continental climate. At the Angermünde station of the German Weather Service/DWD a long-term (1958-2007) mean annual precipitation sum of 529 mm, mean annual air temperature of 8.6 °C and mean annual grass reference evapotranspiration sum (after Penman-Monteith) of about 570 mm were recorded (Natkhin et al. 2012).

All lake catchments are forested. The surroundings of RS are dominated by plantations of Scots pine (*Pinus sylvestris*), whereas the surroundings of KS, RG and JS are covered by deciduous forests, dominated by beech (*Fagus sylvatica*) and oak (*Quercus robur*).

All the lake catchments are touched by the motorway A11 (Berlin-Szczecin) that was built in 1935/1936 (Schütz & Gruber 2000). Despite a certain reshaping of the very local relief, no considerable impact of the road on the catchment hydrology is detectable. The rainwater collected on the road's surface is released in a widespread way into the surroundings, not channelled locally into the lakes. According to historical maps all lakes existed as early as the 18th/19th century, i.e. well before the road's construction (see **Chapter 2.4.3**).

Further information on bathymetry, hydrology and limnology of the lakes as well as on geology and land-use of the catchments are given in **Table 2-1**.

2.3 Methods and Data

2.3.1 Gauging

At RS lake-level gauging by an analogous graduated rod was established in January 1976, but there is a large data gap between January 1985 and December 1994. In February 2006, an additional automatic gauge with a data logger was installed. In 1995 and 2003, the location of the gauge was lowered because the water level fell below the measurement range. In June 2006 the gauge was levelled out to a fixed point. As a consequence, the zero point of the rod had to be corrected down by 0.81 m.

The Poratz (PZ) groundwater observation well at 4 km distance from RS is in operation since 1969. It gives an impression of the water-level dynamics of the upper confined aquifer that drives the lake level of RS as well (Lischeid et al. 2010; Natkhin et al. 2012). For KS no gauging record is available. Therefore, the gauging record from nearby RG, established in 2006 and located 2 km to the northeast, was used for comparison. In terms of hydrology, limnology and catchment properties this lake is very similar to KS. Further comparison is conducted with the gauging record of JS, located between KS and RS.

All gauging records are based on monthly readings. As the gauging data refer mostly to different reading dates and showed pronounced autocorrelation, similar to those reported by Lischeid et al. (Lischeid et al. 2010), linear interpolation between the data points was applied.

2.3.2 Dendrochronology

Along the shore of RS nine stumps of black alder (*Alnus glutinosa*) were sampled in December 2009. Due to decreasing lake level the tree stumps had emerged recently. Since the stumps were still standing with their roots in the ground, it can be assumed that the trees grew *in situ* where they were found in 2009 (Supplements 1, 2, 3). A survey of the bottom of the lake did not reveal additional tree stumps.

Twenty-nine tree stumps of beech and oak were sampled at KS in September 2012. Similarly to RS, all samples were taken from *in situ* tree stumps in the lake or just outside of its water body (Supplements 1, 2, 3). It was observed that the deepest location of a tree stump within the lake was 5.1 m below the actual water level (January 2014). Six core samples of beech tree stumps were taken underwater in May 2014. All other samples from RS and KS were taken either with a handsaw or a power saw, cutting entire stem discs or parts thereof. All samples were identified with wood anatomical methods (Schweingruber 1978).

The methods of dendrochronology applied in the current study follow the general methodology described in (Fritts 1976; Schweingruber 1983; Cook & Kairikukstis 1990; Speer 2010).

Details on sample preparation, measuring, cross-dating and statistical sample treatment are given in Supplement 2.

2.3.3 Analysis of Aerial Photos and Topographic Maps

For the reconstruction of historic lake levels of RS and KS 16 maps dating between 1792 and 2008 are available. RS is additionally covered by 12 aerial photos and digital orthophotos (DOPs) since 1937 and KS by 11 aerial photos/DOPs since 1959. All data were provided in digital form. Whereas aerial photos and topographic maps needed pre-processing such as the assignment of coordinates (‘geo-referencing‘), DOPs were already geometrically corrected including topographic relief, lens distortion and camera tilt. Geo-referencing was based on the DOPs of 2007 and 2012, using ground control points (GCPs; cf. (Anders & Byrnes 1991; Hughes et al. 2006). All the topographic and remote sensing data, the metadata and the description of the pre-processing of aerial photos and topographic maps are given in Supplement 3.

Two approaches exist to estimate former lake levels based on aerial photos or topographic maps. The first is based on the reconstructed shoreline position and the second on the shape of the lake area. Both approaches require a high-resolution digital elevation model (DEM) covering the over- and underwater topography of the lake. The DEMs of RS and KS are

mosaics of a laser survey DEM and bathymetric data of the lakes. Detailed descriptions of the DEMs and their pre-processing, e.g. the interpolation of the bathymetric data (cf. (Furnans & Austin 2008; Johnson et al. 2008)), are given in Supplement 3.

For the first approach, we digitised manually former shorelines using the DOPs as well as the pre-processed aerial photos. These shorelines were merged with the DEM (cf. (Hostache, Matgen, Schumann, Member, et al. 2009)) to obtain the topographic heights of the shorelines (i.e. absolute lake levels). In an ideal case the merging of a shoreline with the DEM will return one height value (i.e. one absolute lake level), following the same contour line. However, in practice the merging returns a range of height values due to a number of cumulative inaccuracies (cf. (Fisher & Overton 1994)), such as the geo-position errors of aerial photos, inaccuracies in the manual digitisation (interpretation problems due to e.g. vegetation) and inaccuracies of the DEM (Supplement 3). By averaging those varying height values of each shoreline, we derived as final result one estimated lake level per aerial photo/DOP.

For the second approach, the shapes of the lake areas of the topographic maps were compared with the shapes of modelled lake areas in the DEM (cf. (Grandke 2009)). Different lake levels were simulated until the shape of the mapped and the modelled lake areas were very similar, e.g. concerning their numbers of bays and islands. This approach is suitable for a rough estimation of former lake levels despite geo-position errors (Choiński 2009). The final result is one estimated lake level per topographic map.

2.3.4 Lake-Level Modelling of Lake Redernswalder See

In general, a changing lake level indicates a change of the water storage of a lake. Changing water storage is the outcome of the lake water balance over a given time interval. The lake water balance is driven by meteorological conditions, such as precipitation and evapotranspiration, as well as by surface and subsurface in- and outflow. In addition, these are dependent on catchment properties such as relief, pedologic and geologic conditions, land use or water management. The relationship between lake levels and the water balance is described in equation 1 in Supplement 4.

A total of five precipitation gauges near RS was taken into account for the analysis of the water balance. Three gauges were provided by the German Weather Service (DWD). They are located about 9 km east, 7 km west and 7 km northeast of RS. The time series were harmonised and homogenised. Gaps were filled by data from the Potsdam Institute for Climate Impact Research (PIK). Two of our own rain gauges (within 4 km distance from RS) were used to consider the local heterogeneity of the precipitation field. Linear regression with the Angermünde met station (DWD) was performed to fill the gaps in the precipitation time series. For that reason the mean of the factors from linear kriging from 20 surrounding precipitation stations and the correlation of the measured time series were used (Natkhin et al. 2012). Since precipitation data measured in the field need correction (HAD 2003), we applied the regionally calibrated German standard method (Richter 1995) for the correction of our precipitation time series.

The difference of precipitation and grass reference evapotranspiration (climatic water balance; reference evapotranspiration after Penman-Monteith; cf. (Allen et al. 1998) was applied to consider changing climatic boundary conditions. The climatic water balance considers only meteorological conditions, but not the water-related properties and the water fluxes in the catchment. An empirical approach to model separately the lake-level dynamics was developed

by Richter (Richter 1997) for another lake in the region (Lake Peetschsee). It uses terms of the water balance which are easy to determine (equation 2 in Supplement 4).

In addition to this model, we developed our own empirical approach to recalculate the lake-level fluctuation of RS (equation 3 in Supplement 4). Our approach considers both the changing climatic boundary conditions as well as the dampened and delayed subsurface exchange of water between the lake and its catchment. The subsurface lake outflow is calculated by an exponential function with a pressure gradient based on the lake level and the stable groundwater level of a lower hydraulic boundary. For RS the water level of the nearby Sernitz River (35 m NHN) was taken.

In general, an empirical approach requires information about the actual water balance in the catchment. An acceptable approximation can be obtained by means of the model WaSiM-ETH (Schulla & Jasper 2007). The specific catchment model and the data basis used are described in Natkhin et al. (Natkhin et al. 2012). The modelled time series of the lake level are originally given in daily time steps. These were aggregated to 7-day steps in order to obtain a suitable convergence with the monthly lake-level measurements.

As described by Natkhin et al. (Natkhin et al. 2012), land-use/land-cover change (LUCC) in the forested catchment is important for the water balance. LUCC was considered for the period 1950-2010 as described in Natkhin et al. (Natkhin et al. 2012). Because of the lack of data between 1901 and 1950, no LUCC could be modelled for this time. Thus the conditions of the 1950s were assumed to be consistently valid for the preceding period.

Calibration of the two empirical approaches for RS was undertaken with R-project software (R Development Core Team 2006). To assess the quality of these approaches, the modelled and observed lake levels were compared based on the coefficient of determination (R^2) and Willmott's index of agreement (Willmott 1982).

2.4 Results

2.4.1 Gauging

The recorded lake levels of RS are partly inconsistent with the fact that 70 to 90 year old beeches are growing near the lakeshore. According to the lake-level record, they should have been flooded by c. 0.6 m during maximum water levels in the early 1980s for several months. This indicates that presumably a differing zero point was used at the reinstallation of the gauge board in 1995. To ensure consistency of the time series, the lake levels between 1976 and 1984 were shifted by minus 1 m. Accordingly, between the 1980s and 2007, the maximum decrease of the measured lake level was c. 3 m. Annual maxima occur usually in May, minima in October. The average intra-annual amplitude amounts to 0.3 m.

The gauging records shown in **Figure 2-2** differ with respect to both the length of the observation period (7-45 years until 2013) and to the water-level amplitude in the respective period (0.6-3.0 m; **Figure 2-2**, **Table 2-1**). The correlation coefficients between the records are rather high (0.6-0.9; Supplement 5) except between RS and JS, where a slightly negative coefficient (-0.12) is apparent. RS is the only one that did not exhibit a steep lake-level increase after 2010, whereas JS is the only one without a marked lake-level decrease before 2010. In contrast to the other lakes, lake-level increase at JS started clearly before 2010. Except for JS, the lake-level dynamics of closed lake basins in the region during the last decades were to a large degree synchronous. This can be illustrated by the lake-level dynamics after 2010. After

a period of several decades of sinking or heavily fluctuating water levels, all of them rose again (**Figure 2-2**). Even in the ungauged KS basin the lake-level dynamics clearly followed this regional development. In 2009, as we discovered the submerged tree remains, they partly rose up to c. 0.8 m above the lake level (Supplement 1) and were flooded again thereafter.

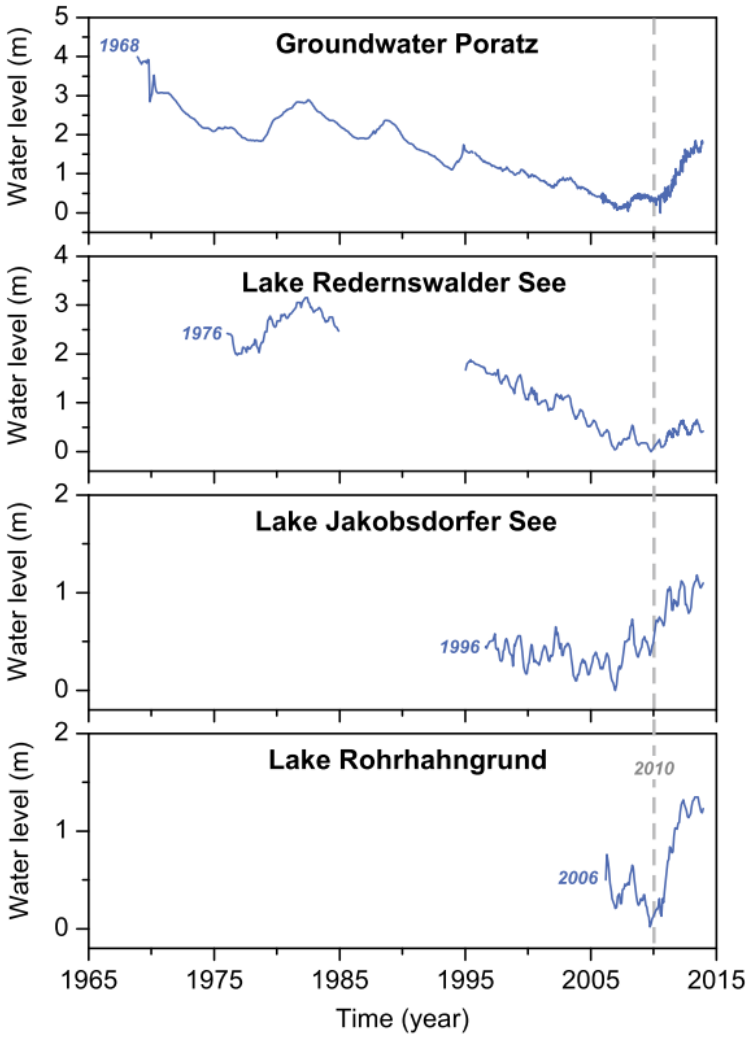

Figure 2-2: Gauging time series of the main sites investigated (Lakes Redernswalder See and Krummer See) and of further sites used for comparison (Lakes Jakobsdorfer See and Rohrhahngrund, groundwater observation well Poratz; data provided by Rüdiger Michels, Angermünde). The diachronous onset of the gauging record is given each by the blue date (year). The onset (2010) of the present period of rising lake and groundwater levels is marked by the grey dashed line.

2.4.2 Dendrochronology

RS site

The tree-ring widths of the nine stumps of black alders could be cross-dated easily, since no false or missing rings were identified. The arithmetic mean of the nine series resulted in a floating site chronology of 30 years length (**Figure 2-3**, Supplement 2). The dating of the otherwise difficult to determine alder samples was eased by the fact that stem discs rather than core samples were used for the analysis.

When the mean chronology was loaded into the Time Series Analysis Program (TSAP) the cross-dating statistics indicated the growth period 1923 to 1952 as the most likely position (Supplement 2). The decision of TSAP for this time period was based primarily on the Cross-Date-Index (CDI) value, which is a combination of the 'Gleichläufigkeit'- (GLK-) and t-values. Other periods, though less likely, are also presented, but may have weaker t-values and/or GLK. Some relatively good dating statistics, such as for the period 1089 to 1118, are less plausible. Given the low altitudinal position (temperate water) and the trophic state of the lake (promoting potentially fast decomposition), the good quality of the alder sample material suggests that the trees were submerged only for a shorter period but not for almost 1000 years (for an opposite, high-elevated and cold-lake dendrochronological record see e.g. (Kleppe et al. 2011).

Furthermore, the graphical comparison with the regional reference chronology also suggests that the period 1923 to 1952 is the most likely due to the synchronisation of several pointer years, such as the peak around the mid-1920s and the low in the 1930s (Supplement 2).

KS site

The number of tree rings found in the samples ranged from 10 to 75, while the diameter of the samples ranged from 10 to 90 cm. The larger tree stumps showed rather straight surfaces, indicating previous cuts by means of hand or chain saws. Four oak and nine beech samples could be dated, since they contained enough datable tree rings, that is, 30 to 82 years (**Figure 2-3**). The other samples were not datable due to rotten wood or small amounts of tree rings visible.

The samples cover a growth period of 84 years, 1895 to 1979. The period of die-off or felling of the trees covers 20 years, 1959-1979 (**Figure 2-3**). The growing period indicates drier site conditions in the past. Otherwise tree growth would have been impossible. A good indicator of the extent of the water-level fluctuations at this lake is the fact that the water depth at sample KRU1 and at samples UW1 to UW6 is currently c. 3 to 5 m. Since the trees were growing at these sites between 1879 and 1969, it is certain that this location must have fallen dry permanently during this period. Since the lake has a maximum depth of 7 m, and most of the lake is less than 3 m deep, it can be derived that most of the basin must have almost dried out during the last third of the 19th century and first half of the 20th century.

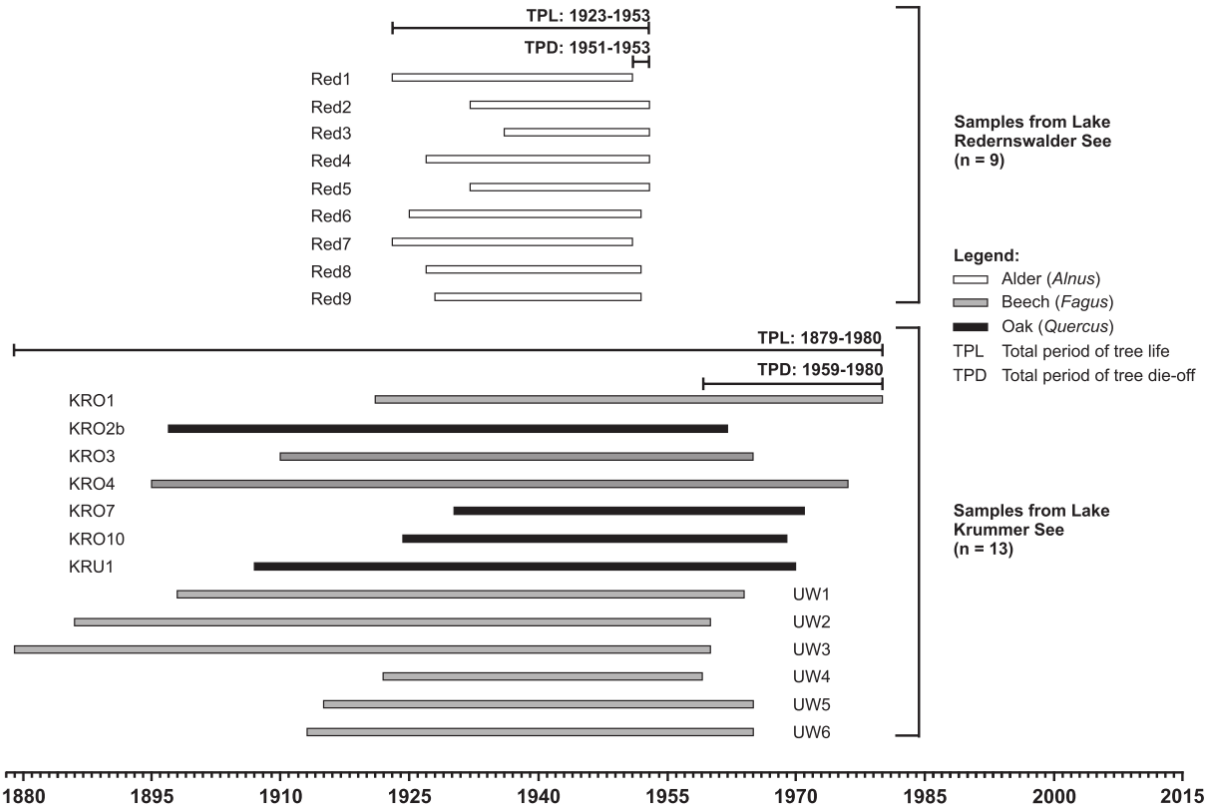

Figure 2-3: Overview of the dendrochronological records in the basins of Lakes Redernswalder See and Krummer See.

2.4.3 Aerial Photos and Topographic Maps

Lake levels in the aerial photos/DOPs (**Figure 2-4**) were estimated by merging the shorelines with the DEM. The results were ranges of height (i.e. lake-level) values due to a number of cumulative inaccuracies. **Figure 2-5** shows an example for the spatial distribution along the shoreline and the range of water-level values for RS (2012-05-24) and KS (2014-01-14). The DOP of 2012-05-24 has a wider range of values than the GPS measurement on 2014-01-14. At KS, the outliers with very high lake levels are concentrated on one part of the shoreline. At RS, outliers with extraordinary small values area concentrated to one area as well, but in general the estimated range of lake levels is distributed over the entire shoreline and not significantly clustered in one part of the area.

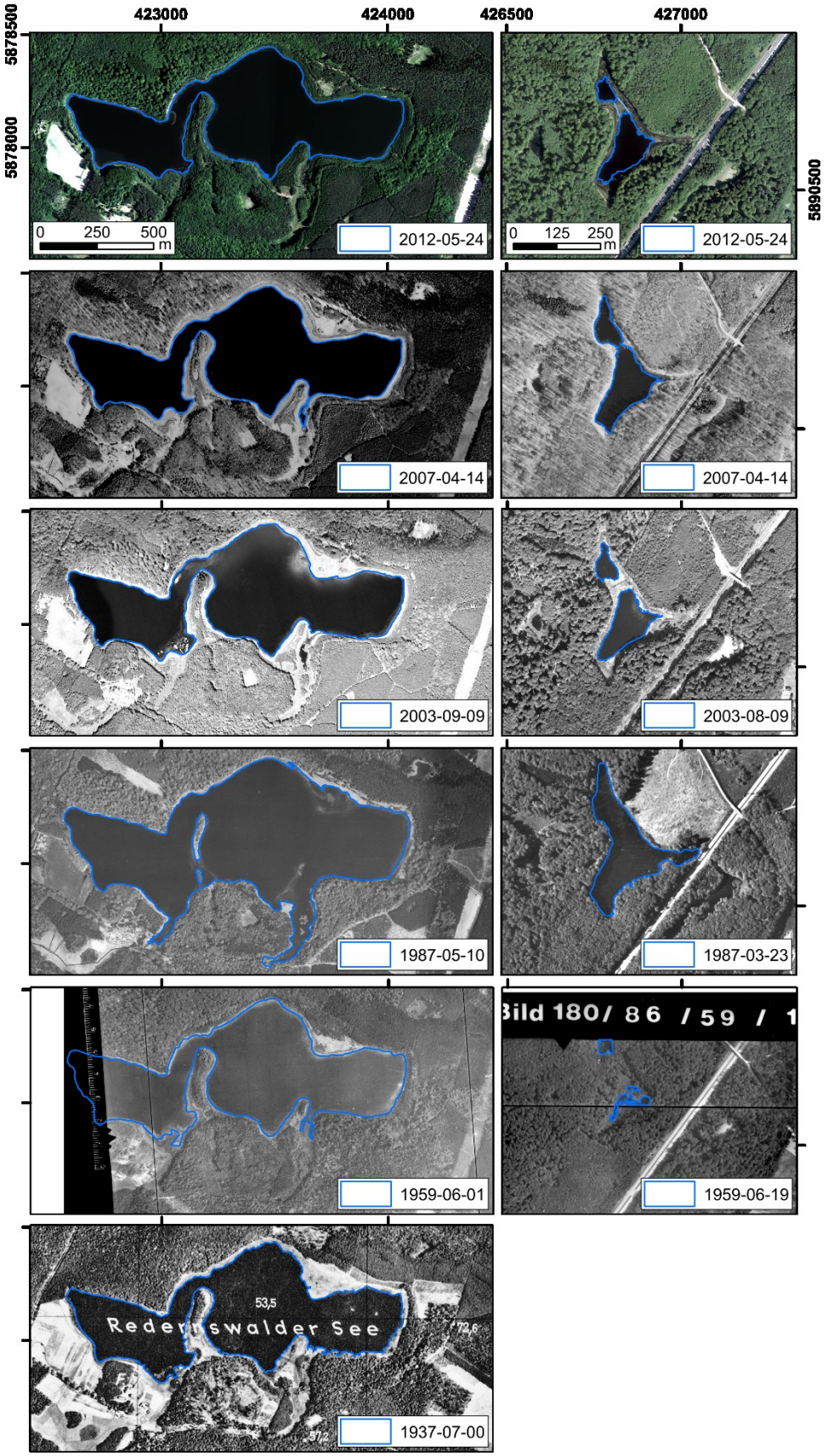

Figure 2-4: Selected aerial photos of Redernswalder See (left) and Krummer See (right). The blue lines represent the shorelines of the lakes that were extracted from the aerial photos. At Lake Krummer See we digitised a land bridge based on the digital orthophoto 2012-05-24. However, fieldwork in summer 2012 showed that it was only dense vegetation in and on the water. Thus the corrected shoreline based on this additional knowledge is illustrated

in light blue.

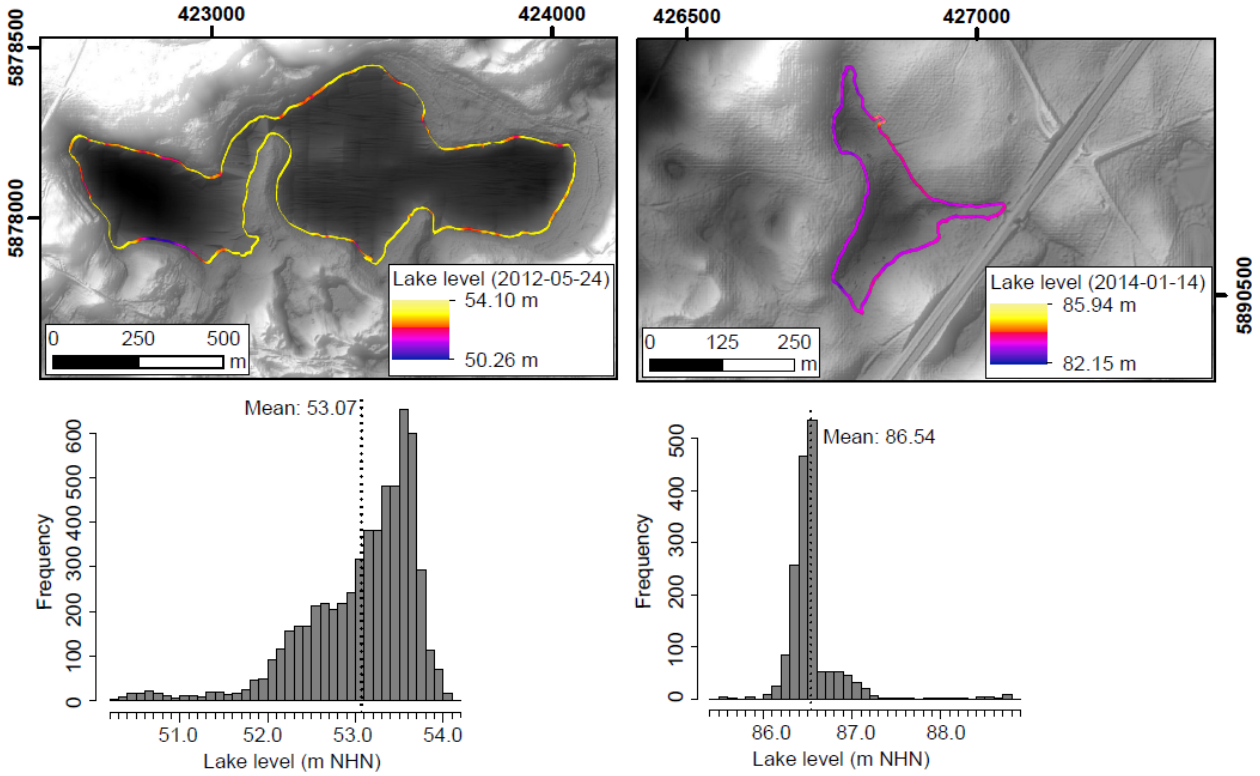

Figure 2-5: Range of lake-level values for Lake Redernswalder See on 2012-05-24 (left) and Lake Krummer See on 2014-01-04 (right) gained by merging the manually digitised shoreline with the high-resolution digital elevation model (DEM). Above – Shoreline height values. The 1-2 pixel broad line is enlarged for illustration purpose. Below – Histograms of the height values with resulting mean lake levels.

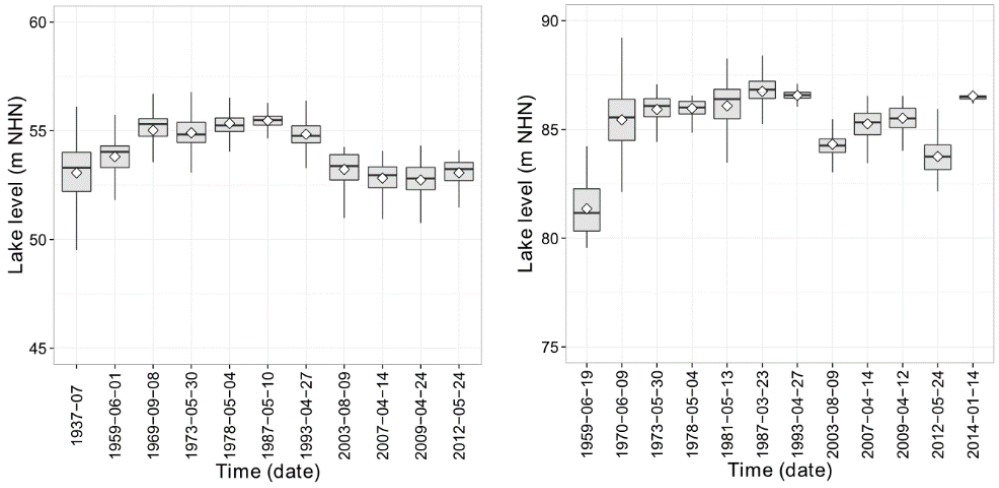

Figure 2-6: Ranges of height (i.e. lake-level) values gained by merging the extracted shorelines with the high-resolution digital elevation model (DEM) for Lake Redernswalder See (left) and Lake Krummer See (right). The shoreline of Lake Krummer See on 2014-01-14 was measured by GPS device. The rhomb illustrates the mean value, the dark line the median. The grey box is the interquartile range (IQR) that is the range in which 75 % of the lake-level values of each date fall. The whiskers in the boxplot mark values within 1.5 IQR. Extreme outliers are not plotted.

Figure 2-6 shows the ranges of the lake-level values of each date of RS and KS as boxplots. For the following analysis of the lake level, we used the mean lake level calculated from the

range of height values of each date. The quality of the estimated lake levels can be evaluated based on the interquartile range (IQR). The largest IQR ranges (c. 2 m) are illustrated for the oldest aerial photos (RS 1937; KS 1959 and 1970). The DOPs of the last decade have an IQR of c. 1 m. The aerial photo of RS 1987 and that of KS 1993 exhibited the smallest IQR range with less than 0.5 m. The GPS derived shoreline of KS 2014 has an IQR of only few centimetres.

The maps of RS and KS have, only a limited spatial and temporal reliability (cf. (Suchozebrska & Chabudziński 2007); Supplement 3) and could only be used for a very rough estimation of historic lake levels. The 'Schmettausche Karte' that was produced from 1767 to 1787 shows a maximum extension of RS. In that map the peninsula which is now visible in the south, was then an island. Three nowadays dry bays in the southern part of the lake were actually flooded. Using the DEM, modelled lake levels of RS between 55.5 m and 57 m NHN results in lakes which resemble the shape of RS drawn in the 'Schmettausche Karte' (see (Grandke 2009)). However, the development of a very similar shape showing an island and three flooded bays is not possible based on the DEM. The island is either flooded at one point or one bay is dried out. The map of 1954 (DDR-TK25) of KS shows the lake as a wet area but not as a lake (Supplement 3). Such a complete dry out of KS occurs only when the water level falls below 79.5 m NHN.

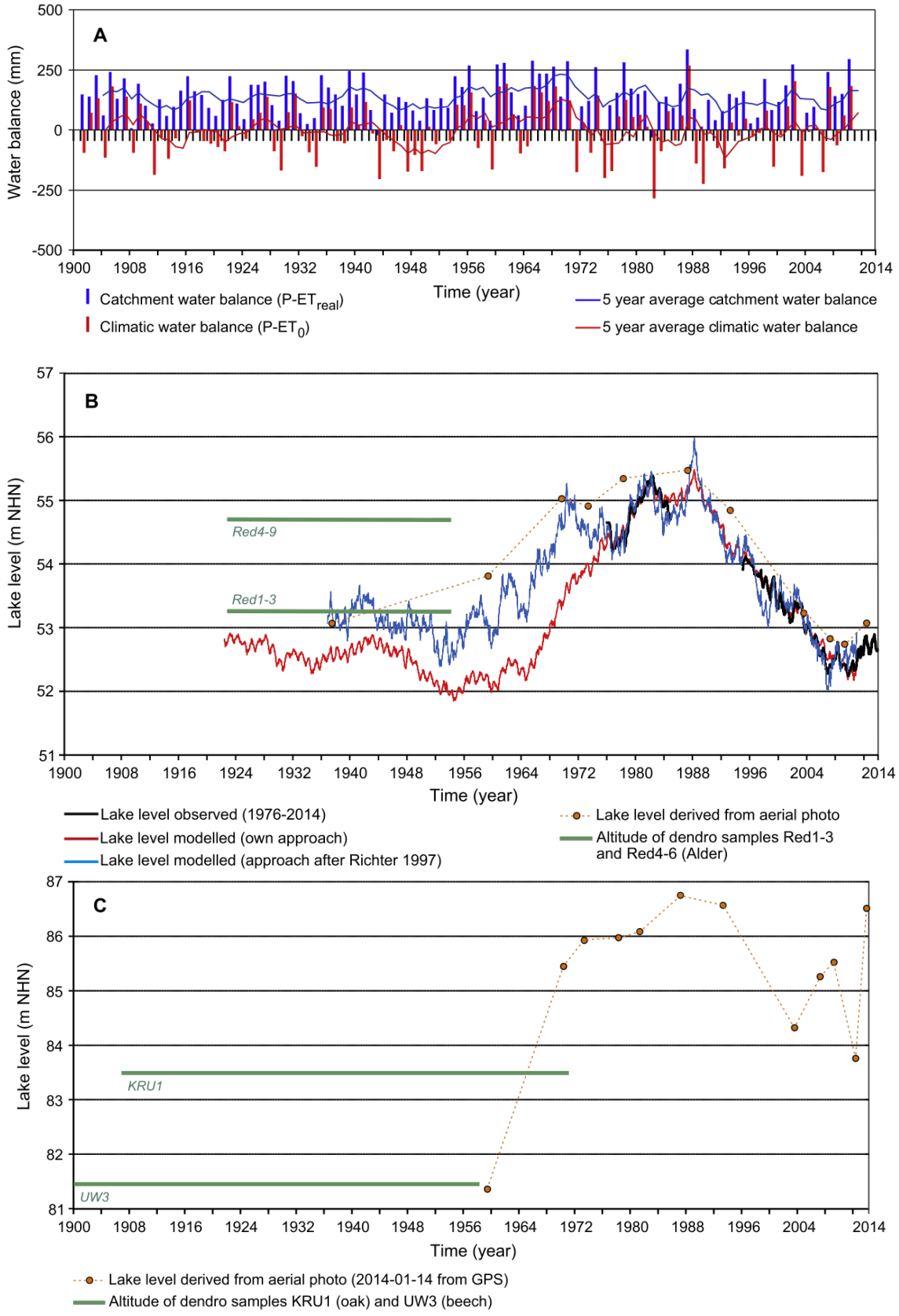

Figure 2-7: Synoptic overview on multi-decadal climatic and lake-level dynamics in the study area. **A –** Catchment water balance und climatic water balance for Lake Redernswalder See and Angermünde meteorological station, respectively. **B –** Lake-level dynamics of Lake Redernswalder See according to different evidence. **C –** Lake-level dynamics of Lake Krummer See according to different evidence.

Figure 2-7B shows the estimated lake-level changes ('mean', cf. **Figure 2-6**) of RS between 1937 and 2012 using aerial photos/DOPs. The comparison of the estimated lake levels of RS obtained from aerial photos with the gauging data shows that both lake-level curves have the same tendency to fluctuations. For validation we calculated the difference between the estimated and the measured lake levels with a maximum time difference of one week because seasonal lake-level changes might be significant. The differences regarding the level range from -0.83 m to -0.24 m. On average, lake-level estimations based on aerial photos/DOPs underestimate the measured lake level by -0.41 m[1].

The estimated lake level of KS between 1959 and 2012 shows a similar trend as RS (**Figure 2-7C**), with a very low lake level in 1959 and a high lake-level period between 1970 and 1993. The GPS measurement on the 2014-01-14 (**Figure 2-5**, **Figure 2-6**) illustrates a very high level again (86.5 m NHN).

Supplement 3 demonstrates the lake-area changes. RS has its maximum lake area in 1987 with a total area of c. 62 ha and its minimum lake area in 2009 with c. 42 ha. KS is much smaller with a lake area of 4.1 ha in 1987. In 1959 the lake nearly dried out with an area of c. 0.1 ha.

2.4.4 Lake-Level Modelling of Lake Redernswalder See

The water-balance dynamics of both the catchment and the wider region were simulated from 1901 to 2010 (**Figure 2-7A**). Distinct periods of relatively negative (e.g. 1940s/50s) and positive values (1960s) occurred parallel to low/decreasing and high/increasing lake levels (**Figure 2-7B**), respectively. The time period 1976-2010 was primarily chosen for calibrating the model due to the availability of gauging data. Additionally, estimated lake levels from four aerial photos (1937, 1959, 1969, 1973) were used for calibration (**Figure 2-7B**). These four lake levels were corrected by a systematic lake-level shift of -0.43 m, derived as the mean difference between data from aerial photos and gauging. Application of shorter time periods for model calibration (e.g. 1995-2011) resulted in unrealistically high lake levels in the past, e.g. 6 m higher than observed. By the recursive use of the previous water level (W_{i-1}) in our approach, the preliminary lead time decreased from 33 to 21 years, compared to the approach of Richter (Richter 1997). Thus, the lake level could be modelled over 12 more years until 1922. The goodness of fit was slightly higher in our approach (Supplement 4). But generally, both modelled lake-level time series are very similar at least over the observation period. Our approach operates in a smoother fashion compared to the approach of Richter (Richter 1997). Its short time dynamics are less distinct with intra-annual lake-level amplitude of 0.23 m *versus* 0.45 m (against 0.30 m of the observed gauging record). Furthermore, but not resolved in **Figure 2-7**, the approach of Richter (Richter 1997) shows lake-level maxima in May and ours in March. Annual minima are passed in December and in September, respectively. During the late 1940s/early 1950s, significantly low values of the climatic water balance led to the lowest modelled lake levels over the whole record. This is also reflected in the approach of Richter (Richter 1997), which produced relatively higher lake levels throughout the pre-observation period. This may have been an outcome of the model's more pronounced response to fluctuations in the climatic water balance, neglecting the delay and damping caused by the catchment.

According to our approach, the lake level until the mid-1960s amounts to around 52.5 m NHN and is characterised by markedly small amplitudes as compared to the later period (**Figure**

[1] The algebraic signs of the difference are reversed. The difference, gauged level minus reconstructed level, results in positive values and thus, the reconstructed lake levels overestimate the in situ measured values.

2-7B). In this period the approach of Richter (Richter 1997) models higher amplitudes, but this can also be found in the observed period after 1995. The following pronounced lake-level rise lasting till the late 1980s is obviously induced by the positive water balance before 1970. In the 1980s the lake level fluctuates around the peak position of c. 55 m NHN, indicating the damping effect of a delayed recharge from the groundwater storage of the catchment (Natkhin 2010). The absolute lake-level maximum of the model record was calculated to be 55.5 m NHN in 1988 according to our approach and 56.0 m NHN after Richter (Richter 1997). This peak follows the absolute maximum of the climatic water balance in 1987. Unfortunately, there is no observation to validate this absolute lake-level maximum. Following the course of relatively dry years starting in the early 1990s, the lake level decreased more or less continually by more than 3 m until summer 2006 (52.5 m NHN). Starting with the wet year 2007, the catchment water balance shows positive values again, resulting in a persistence of the lake level at a low position (c. 52.5 m NHN) so far.

2.5 Discussion

2.5.1 Comparison with Long-Term Regional Gauging Records

Further gauges, located both in the same groundwater catchment as RS and in the whole Schorfheide area as well as beyond, verify a negative water-level trend for closed lakes since the mid-1980s and a positive trend from c. 2010 onwards (Natkhin 2010; Germer et al. 2011; Brothers et al. 2014; Kaiser, Friedrich, et al. 2012); **Figure 2-2**, **Figure 2-8A**). Probably unique is the record from Lake Peetschsee, lying c. 50 km northwest of RS, which began in 1958 (Richter, 1997; Kaiser et al., 2014a). It shows that periods of relatively high and low lake levels regularly alternated in the last c. 50 years. If one includes the modelled lake-level from 1909 to 1957 (Richter 1997), this periodicity becomes evident for the whole 20th century (**Figure 2-8B**). Other lakes in the region suggest that periodic lake-level fluctuations with amplitudes of c. 1 to 3 m are characteristic for groundwater-fed (closed) lakes (e.g. (Kaiser, Koch, et al. 2014; Natkhin et al. 2012). These dynamics primarily depend on climatic impacts, i.e. the periodic occurrence of wet and dry periods (Richter 1997; Kaiser, Küster, et al. 2014). The long-term record of Lake Müritz (c. 11,700 ha), the largest lake in the German lowlands and located c. 80 km to the northwest, however, reveals other dynamics. This (open) lake, having several in- and outlets which are steered by weirs, is clearly controlled by water-level management, largely superimposing the climatic signal (**Figure 2-8C**).

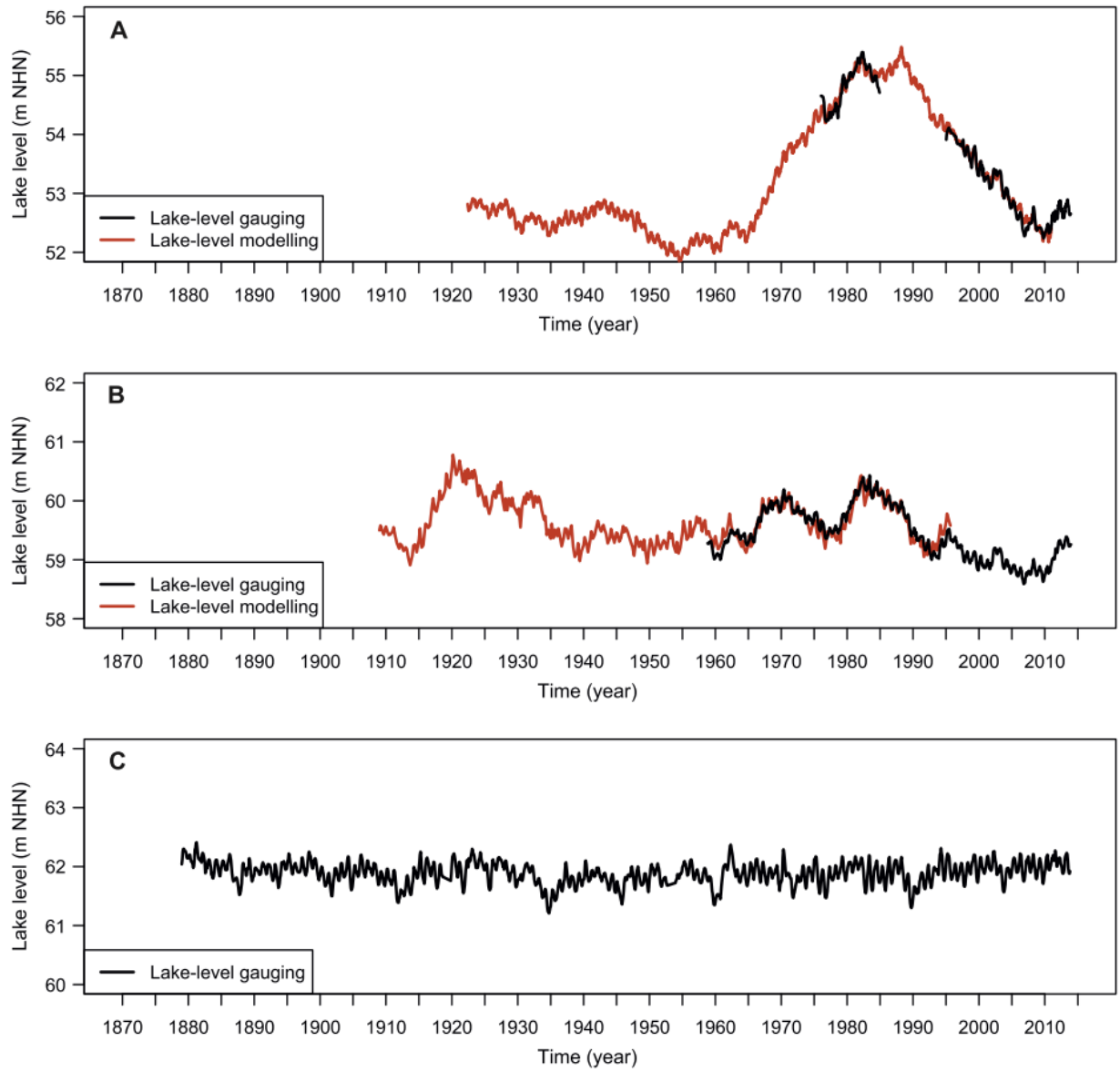

Figure 2-8: Multi-decadal lake-level records from north-eastern Germany. **A** – Lake Redernswalder See with gauging data since 1976 and lake-level modelling since 1922 after the own approach introduced in this study. **B** – Lake Peetschsee with gauging data since 1958 (data provided by Anke Pingel, Potsdam) and lake-level modelling from 1908 to 1997 after Richter (1997). **C** – Lake Müritz with gauging data since 1879 (data provided by Peter Stüve, Neustrelitz). Unlike Redernswalder See and Peetschsee which are (groundwater-fed) closed lakes, Müritz is an open lake having several in- and outlets that are controlled by weirs.

2.5.2 Drowned Trees and Peatlands as Lake- and Groundwater-Level Recorders

From an international perspective, several successful studies using both drowned (dead) and living trees for dendrohydrological studies were performed (Biondi & Strachan 2012). With respect to groundwater- and lake-level fluctuations both short-term (e.g. (Bégin 2001; Xiao et al. 2005)) and long-term dynamics (e.g. (Loaiciga et al. 1993; Gunnarson 2001; Hunter et al. 2006; Meko 2006; Quinn & Sellinger 2006; Wiles et al. 2009; Kleppe et al. 2011; Perez-Valdivia & Sauchyn 2011; Jones et al. 2001)) were the foci of the studies.

Drowned trees, as analysed in RS and KS, however, were rarely described in regional inland lakes or used as bioarchives thus far. One exception are small pine stumps (dating 1876-1893) that were found just below the present-day water level of Lake Kulowsee, c. 50 km northwest of RS (unpublished data). By contrast, submarine oak remains (*in situ* stems and stumps) were discovered along the German and Polish Baltic Sea coast, forming well-investigated geo-/bioarchives (e.g. (Lampe 2005; Uścinowicz et al. 2011)). Furthermore, a multitude of archaeological construction wood exists which was retrieved from both inland lakes (e.g. (Bleile 2008)) and terrestrial sites including river valleys and peatlands, contributing to long chronologies for different tree species (e.g. (Brose & Heussner 2002; Büntgen et al. 2011)).

Our results on lake-level dynamics in RS and KS can be confronted with results from peat stratigraphy and wetland ecology of the nearby Barschpfuhl kettle-hole mire, located only c. 1 km north of RS. Here a high-resolution palaeoecological study was performed (van der Linden et al. 2008), using a 60 cm-thick peat layer from the surface (c. 60 m NHN). The peat chronology is based on radiocarbon wiggle-match dating and covers the time interval from AD 1705 to 2003, comprising c. 300 years. The peat stratigraphy at Barschpfuhl bears a noticeable layer of extremely decomposed peat (25-35 cm) that is encompassed by low and medium decomposed peat. As this layer comprises a time interval from 1790 to 1960, it might represent a dry phase similar to what we reconstructed at least for the 1870s to 1960s for RS and KS. Furthermore, local water-table reconstruction by using testate amoebae (i.e. microfaunal fossils) indicates periods of lower (e.g. 1950, 2003) and of higher (ground-) water levels (e.g. 1964, 1990) at Barschpfuhl. However, all fluctuations are in a range of 5 cm only, and no long-term trends in the data exist. Considering the peatland type (i.e. kettle-hole mire) with its ecological and hydrological characteristics (Timmermann & Succow 2001), obviously a hydraulic buffer effect is present which decouples the very local (peatland-) from the supra-local (ground-) water level. Indeed, the surface of a kettle-hole mire is often partially 'floating' on a subsurface water lens (i.e. a perched aquifer; (van der Linden et al. 2008)). This peatland geoarchive hardly reflects the hydrological changes in the wider groundwater catchment that includes RS and the Poratz groundwater well. Both show maximal water-level amplitudes of c. 3 m from the 1980s to 2000s and 1960s to 2000s, respectively.

For the last c. 20 years kettle-hole mires around RS, including Barschpfuhl, have revealed different reactions of the local groundwater levels, depending from the hydrogeological setting (Luthardt et al. 2010). According to these observations, one can conclude that there is no spatially uniform hydrological cause-response relationship at present, pleading for a careful interpretation even of records of the past.

2.5.3 Aerial Photos and Topographic Maps

Aerial imagery is the only remote sensing data category that has a high resolution and remained consistent from the 1930s/1950s to the present (e.g. (Gerard et al. 2010). Therefore, it is ideal for the long-term monitoring of the landscape dynamics, including lake-level and lake-area changes. Aerial photos were already used successfully for the distinction of former shorelines of lakes, in synthesis with tree ring and lake sediment analysis (Shapley et al. 2005), and for the analysis of lake-area changes due to climatic change (e.g. (Klein et al. 2005; Papastergiadou et al. 2007)).

The retrieval of a water level based on the extracted contours of a water body from a DEM were mostly used for the estimation of flood-water levels so far (e.g. (Puech & Raclot 2002)). Our study shows that the approach applied here is also valuable for the estimation of lake levels. The accurate geo-referencing of the aerial photos is time consuming, but the quality difference

between the lake levels extracted from DOPs and aerial photos seems not as large as was first expected. Dense vegetation along the shoreline is the challenging obstacle for an accurate estimation of the lake level. For example, the DOP of RS (2012-05-24) has high pixel position accuracy, but nevertheless shows a wide range of lake level values (**Figure 2-5**, **Figure 2-6**). For KS, fieldwork in summer 2012 revealed a strong influence of vegetation on the analysis of remote sensing data. The corrected shoreline based on this expert knowledge can be noted in the corresponding subset of DOP (2012-05-24) in **Figure 2-4**. Thus, the lake level of KS (2012-05-24) is of limited reliability. A much higher water level (c. 86 m NHN) would be realistic. The continuous increase of the lake level of RS in 2012 supports this reasoning.

The smallest IQR was assigned to the GPS measurement of KS 2014. None of the indirect reconstructed shorelines reaches its precision. However, it must be considered that a longer shoreline potentially has a wider range of lake-level values: RS is much larger than KS and an increasing lake level results in a longer shoreline. For studies at other lakes we recommend the use of subsets of the shoreline with shallow topography and without interfering vegetation to ensure a reliable digitisation of the shoreline for the lake-level estimation.

Maps are a valuable tool to trace earlier landscape changes. In the region their records reach back to the 16th century at the earliest for certain small areas (Cordshagen 1986) and to the second half of the 18th century for the entire area (Kressner 2009). However, spatial and temporal inaccuracies limit their use as a precise hydrological proxy (e.g. (Marszelewski & Adamczyk 2004; Choiński 2009). The changing appearance of peninsulas, islands and dried out bays/wet areas are good indicators for lake-level changes, but this evidence is of only limited suitability for quantitative estimations. Spatial inaccuracies can be bypassed partly by the modelling of historic lake levels based on the shape of lake areas drawn in a map (e.g. (Grandke 2009). However, this method provided only very rough results for RS, probably due to an altered topography since the 18th century.

2.5.4 Lake-Level Modelling of Lake Redernswalder See

So far, several studies to model the water-balance and lake-level of closed lakes were performed throughout the world (e.g. (Legesse et al. 2004; Vallet-Coulomb et al. 2006; Troin et al. 2012). Our approach to calculate lake levels for RS based on water-balance modelling was the most comprehensive applied in the region so far. The combination of a sophisticated model for calculating the catchment water balance (WaSiM-ETH; (Schulla & Jasper 2007)) and an empirical approach to model the lake-level dynamics is innovative for the analysis of closed lakes interconnected with groundwater in central Europe.

The model approach after Richter (Richter 1997) shows a good fit to the observed lake levels of RS, as good as Richter (Richter 1997) showed for Lake Peetschsee. Nevertheless, our own approach performs better for RS (Supplement 4). A general methodical advantage of our approach is its proximity to the full water balance equation and the connection to the lake level of the previous time step (Supplement 4). The adaptability and modelling quality for different lakes was clearly not in the focus of this work. But for further application the local complexity in coupling between meteorology, hydrogeology and hydrological lake dynamics as well as land use/land cover characteristics must be carefully considered.

However, the results obtained for RS are accompanied by some obstacles. The first one is the relatively short period of the gauging record, comprising a lack of data from 1985 to 1994. Secondly, with a view to the completeness of meteorological data, an imbalance exists in the gauging record, leading to uncertainties in the calibration of the parameters used for the

empirical model approaches. The extrapolation of an empirical model into the past without any observation data generally increases uncertainty (Refsgaard & Henriksen 2004). Some modelled lake-level extremes of RS occur in periods without gauging record. Based on a short-term calibration period (1995-2010) high lake levels in the beginning of the reconstruction period and a lake-level decrease over most of the time afterwards were confirmed. But insufficient observation data were available for periods of a predicted lake-level rise. To solve this problem, the lake-level data retrieved by some aerial photos were additionally used for calibration. In addition, detailed information on historical land use (i.e. a changing forest structure) could not be obtained. Thus the land-use change before 1950 could not be implemented into the model.

There are some further uncertainties caused by methodological shortcomings pertaining to the regional hydrology of groundwater dominated systems. Most of them were recently evaluated and discussed for the wider study region by Thomas et al. (Thomas et al. 2012). In particular, the problem of correctly quantifying the local climatic water balance still exists. There are well-proven empirical procedures for correcting measured precipitation (e.g. (Richter 1995)). But, calculation of the daily evapotranspiration still remains difficult due to the low density of meteorological stations with the full set of input data. In addition, there are different approaches for calculating the actual evapotranspiration. They differ especially for forested catchments, lakes, riparian vegetation or groundwater-dependent systems, which are abundant in the RS catchment.

2.5.5 Synthesis

Compiling all the lake-level evidence from RS, the varying conformity of the records for certain periods becomes evident (**Figure 2-7B**). The best match of the records is from 1976 to the present where the lake-level curves tend to merge. Prior to that the lake-levels derived from modelling and aerial photos were (correctly) widely below the level defined by the dendro-record of samples Red1-3. This dendro-record generally reflects a maximal possible lake level for the period 1923-1952. In comparison with aerial photos and with lake-level modelling after the approach of Richter (Richter 1997), our modelled lake-level before 1976 is constantly lower in a range of 0.25 to 1.6 m. A systematic deviation is also found between observed lake levels and lake levels derived from aerial photos.

The same general dynamics with low lake levels in the first half of the 20th century, a rise afterwards up to the mid-1980s and a following decline is proven by the KS proxy record (**Figure 2-7C**), consisting of dendrochronologically dated tree remains and lake-level reconstruction by means of aerial photos. Thus two consistent multi-decadal lake-level records of different temporal resolution were established.

The dimension of the local hydrological and ecological changes and, consequently, of the suitability/sensitivity of the geo-/bioarchive (i.e. preservation potential for submerged tree remains) clearly differ, depending from a faster reaction time and larger amplitude of the lake level in KS compared to RS (**Figure 2-9**).

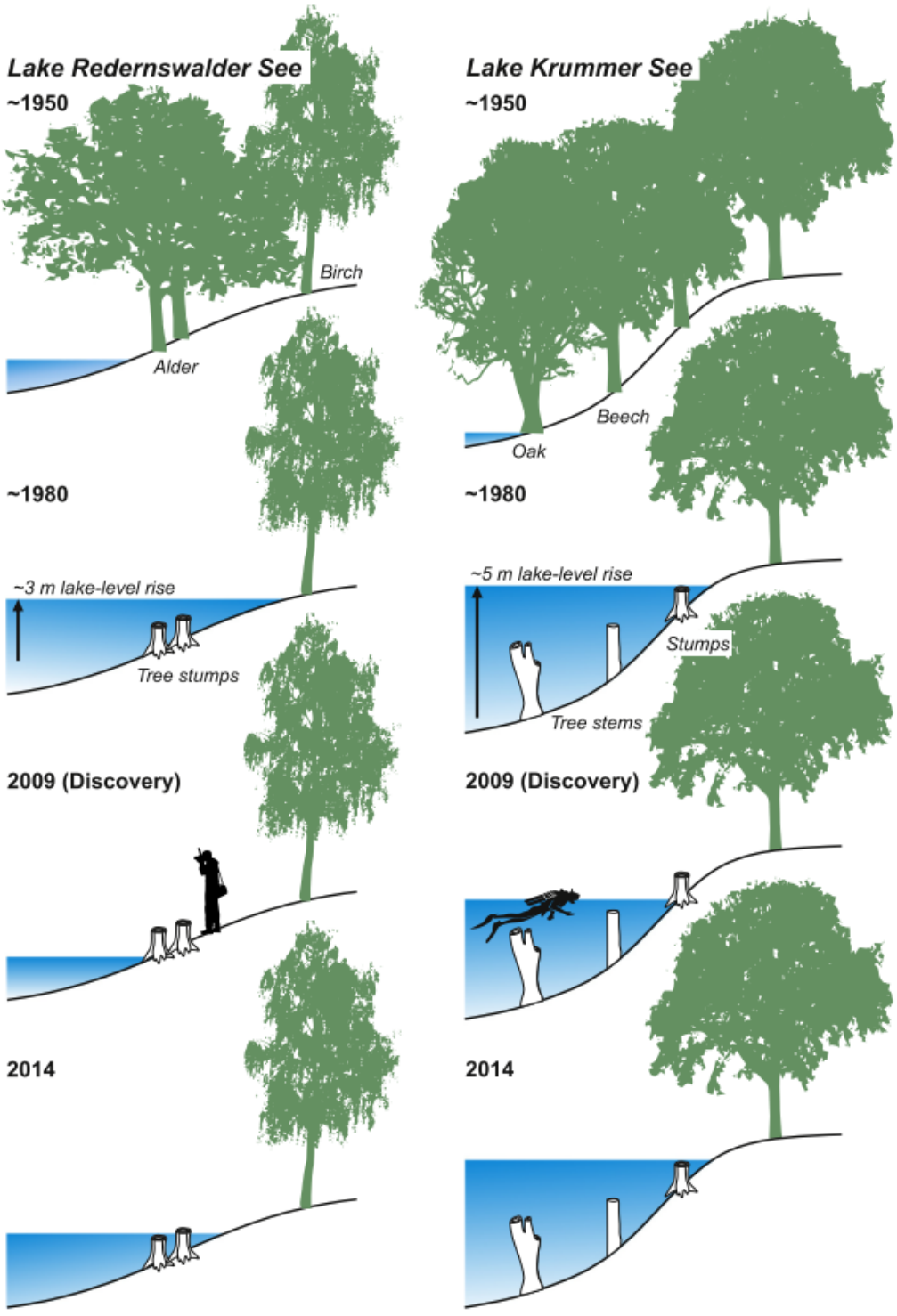

Figure 2-9: Synoptic sketch showing the local water-level dynamics at Lakes Redernswalder See and Krummer See for selected years with related vegetation changes at the shoreline and taphonomic processes of the tree remains investigated.

Thomas et al. (Thomas et al. 2012) found that the long-term dynamics of precipitation and evapotranspiration do not differ significantly at distances as short as in this study. In spite of that, time series of groundwater or lake levels can differ substantially even for adjacent sites. Lischeid et al. (Lischeid et al. 2010) analysed time series of various groundwater wells and lakes in the study area, though a much shorter time period was covered. They could assign most

of the spatial variance of the observed dynamics to different degrees of damping of deep seepage. This in turn seems to be related to a differing depth to the groundwater and to different soil substrates. The same was found for another data set, measured about 50 km further to the southeast (Lischeid et al. 2012).

Our study revealed drastic changes of lake levels that were rarely reported from natural lakes for other parts of northern central Europe. In fact, the study region is sensitive to minor changes of the water balance. In general, plants are very effective in ensuring their need of water, resulting in fairly stable annual rates of evapotranspiration in spite of substantial interannual fluctuations of precipitation. Consequently, groundwater recharge can be regarded as the residual of precipitation minus plant water uptake and evaporation. In the study region groundwater recharge amounted to 83 mm/year on average for the 1983-2007 period, which was only 16 % of the mean annual precipitation of 529 mm/year (Natkhin et al. 2012). Thus, the low groundwater recharge would be drastically reduced even by an only slight decrease of annual precipitation, resulting in a drastic change of groundwater and lake levels.

Broadening the perspective, scenario analyses that assess the effect of single anthropogenic measures (e.g. land-use change, construction of barrages) or of climate change on landscape hydrology are usually based on the implicit assumption that stationarity is the norm for remote, undisturbed (i.e. near-natural) hydrosystems. Only recently have scientists challenged this, showing a multitude of anthropogenic effects on hydrological processes (e.g. (Milly et al. 2008). Our results clearly revealed that in addition to seasonal lake-level dynamics fluctuations at a scale of decades need to be considered in this region. In fact, clear evidence exists that low-frequency fluctuations have always been an intrinsic property of the climate and related hydrological conditions and should be taken into account for further hydroclimatic and hydrological studies (Clarke 2007).

2.5.6 Conclusions and Outlooks

Knowledge on multi-decadal lake-level and groundwater-level dynamics is very much helpful to understand the long-term landscape water budget and its effects in northern central Europe and beyond. Incorporating not only present and future perspectives, but also focus on historic hydrology and palaeohydrology, resulted into new insights concerning the dynamics and thus assisted us with both hydrological process understanding and the evaluation of hydrological proxy data.

For the first time evidence from a geo-/bioarchive and remote-sensing were jointly exploited in the region, revealing their high potential for lake-level studies. By applying a combined approach of gauging and proxy-data analysis and of retrograde modelling we were able to establish two consistent lake-level records that cover the last c. 90 years in maximum. Thus a quasi-continuous, c. 40 years long time series of observation data could be extended c. 50 years further into the unobserved past. In general, our results reveal non-stationarities of the landscape water budget at a scale of decades that should be taken into account for future hydroclimatic, hydrological and climate impact studies in the region.

This study also contributes to the question how centennial- to millennial-scale lake-level records can be interpreted, using the dynamics of the recent past as a key to understanding. As the last c. 100 years for RS show, there are several low-magnitude fluctuations with amplitude of c. 1 m and one high-magnitude fluctuation with amplitude of c. 3 m. Further multi-decadal records from the region reveal considerable variability, depending on the hydrological lake type which modifies water feeding and water level.

Ongoing work in the surroundings of the lakes examined aims, on the one hand, to realise a detailed study of structures (landforms, soils, vegetation) along shorelines that have been affected by water-level changes over the last decades. On the other hand, an analysis of sub-littoral sediment cores is under way for the same lakes, and this aims to generate millennial-scale lake-level records. Combining all evidence, i.e. monitoring data, proxy-data analysis and further modelling efforts, we aspire to establish a long-term lake-level history for the region, covering the whole Holocene.

Acknowledgements: This research was performed largely within the TERENO project (http://teodoor.icg.kfa-juelich.de/overview-de) and the ICLEA project (http://www.iclea.de/en/home/) of the Helmholtz Association. Some research had already been carried out within the NEWAL-NET project funded by the German Ministry of Education and Research (Grant No. 0330562A). We express our warm gratitude to Heike Mauersberger (Angermünde) and Rüdiger Mauersberger (Templin) who directed our interest to Lakes Redernswalder See and Krummer See. The authority of UNESCO Biosphere Reserve Schorfheide-Chorin granted easy access to the protected lakes. Rüdiger Michels (Angermünde), Anke Pingel (Potsdam) and Peter Stüve (Neustrelitz) assisted through provision of some gauging records. The sonar investigation of Lake Krummer See, providing bathymetric data, we owe to Jürgen Becker (Greifswald). The diving trip for sampling subaquatic tree remains in Lake Krummer See were kindly performed by Siggi Hauke, Michael Jablonski, Frank Kroll, Silke Oldorff and René Pastor (all Tauchclub Nehmitzsee, Rheinsberg). Thankfully, we could use the modelling approach and the advice given by Dieter Richter (Berlin). We would like to thank Raphael Ganzenmüller (Marburg) for the preparation of some figures and Ross Beveridge (Berlin) for improving the English. Finally, we owe two anonymous reviewers and the guest editor David M. Meko (Tucson, Arizona) very helpful comments on an earlier version of the manuscript.

Supplements: Supplements 1-5 associated with this article can be found, in the online version, at http://dx.doi.org/10.1016/j.jhydrol.2014.12. 057. The supplement 3 on remote sensing is also included in this thesis (**Supplementary Materials on Chapter 2**).

3 Reconstruction of Long- and Short-Term Lake Level Changes Using RapidEye Satellite Imagery

Heine, I., Stüve, P., Kleinschmit, B., & Itzerott, S. (2015). Reconstruction of Lake Level Changes of Groundwater-Fed Lakes in Northeastern Germany Using RapidEye Time Series. Water, 7(8), 4175–4199*, doi:10.3390/w7084175*.

Received: 2 April 2015 / Revised: 21 July 2015 / Accepted: 23 July 2015 / Published: 31 July 2015

Abstract

Groundwater-fed lakes in northeastern Germany are characterized by significant lake level changes, but for only a few lakes are *in situ* water level measurements available. In this study, we test the potential of RapidEye satellite images for indirectly reconstructing lake level changes. The lake levels are derived by intersecting water-land borders with a high-resolution digital elevation model (DEM). Based on Lake Fürstenseer (LF), we define requirements and limitations of the method. Water-land borders were extracted automatically from the 37 RapidEye images available for the period between 2009 and 2014. *Otsu*'s threshold was used for the NIR band and for the normalized difference water index (NDWI). The results were validated with *in situ* gauging, contour lines from the DEM, and *in situ* Differential Global Positioning System (DGPS) measurements of the shoreline. Using an ideal shoreline subset, the lake levels could be reconstructed with decimeter accuracy using the NIR water-land border, but the levels were systematically underestimated by 0–20 cm. The accuracy of the reconstructed lake level retrieval strongly depends on the precision of the water-land border retrieval, on the accuracy of the DEM, and on the lake level itself. A clear shift of the water-land border with increasing lake level is also essential for the unambiguous reconstruction of different levels. This shift needs to be several times larger than the pixel size. The biggest challenges for lake level reconstruction are the presence of vegetation at the shorelines, the quality of the topographic data in the underwater area, the slope of the shoreline, and shadows in combination with low solar angles.

3.1 Introduction

The glacial landscape of the northeastern Central European lowlands in Germany and Poland is characterized by a high number of natural lakes. Most are groundwater lakes whose water levels are linked to the local uncovered aquifer. Groundwater and precipitation determine the inflow, evapotranspiration the outflow (Kaiser, Friedrich, et al. 2012; Mauersberger 2006). These processes affect the natural dynamic of the lakes and lake level changes. Previous studies showed that groundwater-fed lakes are characterized by small seasonal fluctuations and large perennial changes in lake levels (Kaiser, Friedrich, et al. 2012; Mauersberger 2006). In addition to natural level fluctuations, human interference such as land use and hydromelioration, as well as climate change, influence lake levels (Germer et al. 2011; Kaiser, Koch, et al. 2014). Lake level changes influence the lakes' physics, chemistry and biology. Lakes in the northeastern Central European lowlands play an important role in ecosystem functions (Kaiser, Friedrich, et al. 2012). The most important services of lakes are the protection of biodiversity, water and carbon storage as well as their recreational value (tourism) (Kaiser, Koch, et al. 2014).

In the last few years, field measurements at selected lakes in Germany and Poland showed a significant increase in their lake levels after a long period of continuous sinking (Kaiser, Friedrich, et al. 2012; Heine et al. 2014). A lake level decrease leads to the drying out of the shallow water areas at the shoreline, up to the appearance of sandy sediments. As a reaction, macrophytes, reed, and macrozoobenthos move to deeper water areas. If the change is abrupt the existing flora and fauna vanish (van de Weyer et al. 2009). The (temporal) loss of typical underwater and shallow water vegetation is a serious problem because of its contribution to water filtering processes and its function as habitat for fauna (Brauns et al. 2008; Landesamt Brandenburg 2008). Large macrophyte stocks help to stabilize clear water conditions (Landesumweltamt Brandenburg 2004; Kaiser, Friedrich, et al. 2012; Schmieder et al. 2004). Their loss can cause a transition from macrophyte-dominated states of lakes with clear water conditions to murky plankton-dominated states (Hilt et al. 2010). This affects specifically

shallow lakes as the smaller lake volume and depth accelerate biological processes and increase eutrophication (Hupfer & Nixdorf 2011). Additionally, the loss of vegetation and the drying out of shorelines lead to an increased mineralization of organic matter. If the water level rises and those sediments are flooded again, the mineral substance again dissolves and increases the nutrient content of the water (Ulrich 1998).

So far, lake level and shoreline changes have only been monitored at selected lakes. As field monitoring is time consuming and expensive, most lakes in northeastern Germany and Poland are not gauged and their lake level fluctuations could only be estimated. In future, the aim should be to monitor a large number of lakes to build a database for trend analysis. Remote sensing images can be used for lake monitoring and reconstructing past oscillations. Multispectral remote sensing data have been successfully used in the past to monitor and map lakes (Verpoorter et al. 2012; Muster et al. 2013; Maillard et al. 2012; Wang et al. 2014) and to monitor coastline changes (Alesheikh et al. 2007; White & El Asmar 1999; Lipakis & Chrysoulakis 2008; Li & Damen 2010; Gens 2010; Pardo-Pascual et al. 2012). Lake levels can be measured directly by radar altimetry (Baup et al. 2014; Maillard et al. 2015; Abarca-Del-Rio et al. 2012; Da Silva et al. 2012) or indirectly by combining topographic data and water–land boundaries (Gupta & Banerji 1985; Smith 1997; Brakenridge et al. 2005; Alsdorf et al. 2007; Hostache, Matgen, Schumann, Member, et al. 2009; Maillard et al. 2012; K. Kaiser et al. 2015). Indirect reconstruction of lake volumes or levels has been accomplished using aerial photos (K. Kaiser et al. 2015) and medium-resolution data (Gupta & Banerji 1985; Maillard et al. 2012). It has also been used to reconstruct water surface elevations during inundations using various types of remote sensing data (Smith 1997; Brakenridge et al. 2005; Alsdorf et al. 2007; Hostache, Matgen, Schumann, Member, et al. 2009).

As radar altimeters are profiling tools and their orbital spacing misses too many lakes (Alsdorf et al. 2007), we use in this study an indirect method to reconstruct lake levels: we test the potential of high-resolution multi-spectral satellite images (RapidEye) for the indirect measurement and reconstruction of small and short-term lake levels changes. The short-term analysis of small lake level changes and high-resolution satellite image data leads to new methodological challenges: in this study, we discuss in detail the influence of shorelines slopes, vegetation and shadows on the accuracy of lake level reconstruction. The large data set for LF, including daily gauging and a shoreline measured *in situ*, enables absolute validation, whereas previous studies could only compare water-land borders or levels extracted at different times (Gens 2010; Li & Damen 2010). In order to assess the transferability of this lake level reconstruction approach, we examine the attainable accuracy and define requirements and limitations.

3.2 Study area

Our test site, LF, is a well-researched groundwater-fed lake located near Neustrelitz in Mecklenburg-Vorpommern, Germany (**Figure 3-1**). The lake is part of the Mecklenburg Lake District and the geology of its catchment is sandur from the last ice age (Germer et al. 2010). The mean annual precipitation at the closest climate station, Carpin-Serrahn (Wetterdienst n.d.), is 656 mm (reference period: 1988–2014). The distribution of the annual precipitation is bimodal with maxima in July (mean: 75 mm) and December (mean: 58 mm) and minima in April (mean: 35 mm) and October (mean: 48 mm).

LF is representative of a large number of groundwater-fed lakes in northeastern Central Europe and it has a heterogeneous shoreline, which is essential for analyzing shoreline slope and vegetation.

The lake does not have an active inlet or outlet and is characterized by significant seasonal and inter-annual lake level changes (Kaiser, Friedrich, et al. 2012; Germer et al. 2010). The range of annual lake level oscillation is in the range of 0.2 m (reference period: 1988–2014) with a local maximum level in April and a local minimum in October in a typical annual cycle. Periods with high lake levels over 83.8 m a.s.l. (1988/1988, 1995/1996 and 2012/2013) are followed by low water periods with an absolute minimum in 2007 (63.2 m a.s.l.). Consequently, the water surface area of LF varies between 2.1 km^2 am 2.6 km^2 (GIS analysis based on DEM and *in situ* level measurements). Between 2009 and 2014, there is a positive trend in lake level due to extraordinarily high precipitation. The gauge data since 1988 and the decomposition of the time series are illustrated in detail in Figure S1.

The average depth of the lake is 8.0 m; the maximum depth is 24.5 m at a lake level of 63.5 m a.s.l. (bathymetric survey). The lake is a mesotrophic clear water lake characterized by water stratification (Landesamt für Umwelt Naturschutz und Geologie Mecklenburg-Vorpommern 2011). The maximum sight depth, measured via secchi disk between 2004 and 2012, ranges from 4–8 m (MLUV M-V 2014). In winter, the lake is on average completely covered with ice on 51 days and partly covered on 14 days (reference period: winter 2009/2010–winter 2013/2014) (Stalu-MV 2015).

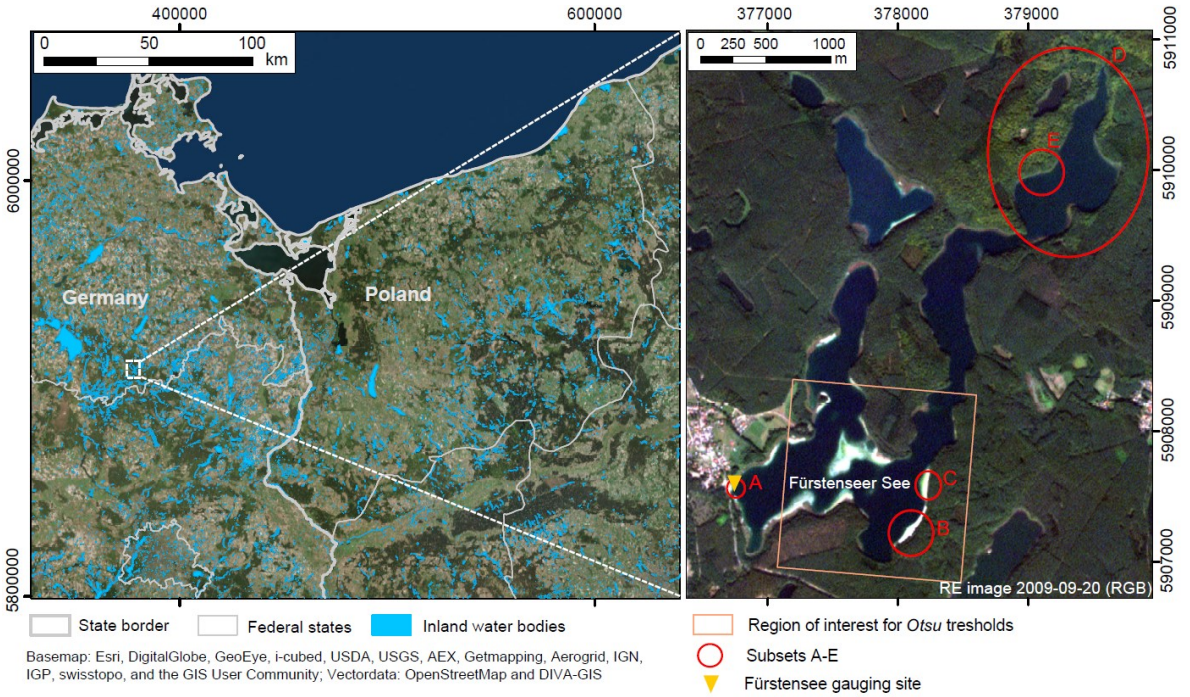

Figure 3-1: The northern Central European lowlands are characterized by a large number of water bodies. Lake Fürstenseer (LF) is located near Neustrelitz in Mecklenburg-Vorpommern, Germany. The close-up shows a RapidEye satellite image of LF in September 2009 (low lake level). The orange rectangle marks the region of interest for calculating the *Otsu* thresholds. The red circles mark different subsets of the shorelines (A–E), and the yellow triangle shows the position of the Fürstensee gauging station.

3.3 Materials and Methods

3.3.1 Data Acquisition and Preparation

The LF database includes *in situ* lake levels, a digital surface model of the terrestrial area adjacent to the lake, bathymetric point data for the lake, and Differential Global Positioning

System (DGPS) measurements of the shoreline in August 2014 (**Table 3-1**). A workflow of the preparation of the topographic data and the RapidEye images is illustrated in Figure S2.

The Fürstensee gauging site is located at the new public beach (**Figure 3-1**, subset A). The processing of the lake level data includes the transfer of the measured relative lake level (in cm) to absolute level values in m above sea level (a.s.l.). The transfer is based on height information provided by the Staatliches Amt für Landwirtschaft und Umwelt Mecklenburgische Seenplatte (Stalu-MV 2015).

Digital surface models with 1 m resolution, locally only 2 m resolution, are available nationwide from German government agencies. The digital surface model with 1 m resolution (ATKIS-DGM1) covering LF is based on two LIDAR acquisitions in winter 2010.

The bathymetric survey took place on 7 October 2002. Despite the time since the survey, the bathymetry is assumed to be still representative because of the closed basin and thus very low levels of erosion and sedimentation at the lake. The survey was conducted by a surveying company on behalf of Landesamt für innere Verwaltung Mecklenburg Vorpommern (LaiV-MV 2013). In a boat, the surveyors navigated in rows over the lake and measured the relative depth (z) from the lake bottom to the water surface. For the transformation to absolute height values, the z values were subtracted from the *in situ* gauged lake level in October 2002 (63.53 m). *Ca*. 46,000 points were measured on the 2.4 km^2 lake surface. The distance between rows was 50 m and the shoreline was not mapped *in situ*. Based on the *in situ* measured level, the shoreline was reconstructed as a contour from the ATKIS-DGM1. The shoreline was added to the points of the bathymetric survey as points with zero depth. Then, the underwater surface model was calculated as a Triangulated Irregular Network (TIN). The TIN was resampled to a raster with 1 m pixel grid size. The accuracy of the underwater surface model is highly dependent on the density of measured points.

Table 3-1: Overview of the available data.

Data	Abbreviation	Method/Device	Acquisition Date	Resolution (Accuracy)	Source
In situ measured lake level		Manual reading at gauging site	monthly since 1987, daily since 2006	1 cm	Staatliches Amt für Landwirtschaft und Umwelt Mecklenburgische Seenplatte (MS) (Stalu-MV 2015)
Digital surface model	ATKIS-DGM1	Pre-processed LiDAR	1 November 2010 and 15 December 2010	1 m (vertical: 0.15–0.2 m)	Landesamt für innere Verwaltung Mecklenburg-Vorpommern (LaiV-MV 2013)
Bathymetric point data		Sonar via SIMRAD-Echolot	7 October 2002	(Horizontal: 1 m, vertical: 0.1 m)	Ministerium für Landwirtschaft,Umwelt und Verbraucherschutz M-V (MLUV M-V 2014)
In situ measured water-land border		Differential Global Positioning System via Triumph-VS Receiver	12 August 2014	(Horizontal RMSE <1 m)	

Finally, an over- and under-water digital elevation model (DEM) of LF was generated by merging the ATKIS-DGM1 and the bathymetric data. Below 63.53 m, the DEM was based on

the bathymetric survey and above 63.53 m on the ATKIS-DGM1 (*cf.* Figures S3 and 6). The DEM has a 1 m resolution.

The water–land borders of LF were extracted from RapidEye (RE) satellite images. The data were provided by BlackBridge AG, Berlin, Germany (www.blackbridge.com). RapidEye images were chosen because of their high spatial resolution of 6.5 m, their high temporal resolution, the large size of the archive including data collected since 2009, and the free-of-charge availability for German research projects using the RapidEye Research Archive. Five micro-satellites have provided products since February 2009 with a theoretical temporal resolution of one day (off-nadir) or 5.5 days (at nadir). The sensors on the satellites acquire five spectral bands at wavelengths between 440 and 850 nm, including the red edge band (band 1: 440–510 nm, band 2: 520–590 nm, band 3: 630–685 nm, band 4: 690–730 nm, and band 5: 760–850 nm) (Sandau 2010). For this study the images were provided in processing level 3A, delivered as rectangular image tiles. Level 3A processing includes orthorectification and resampling to 5 m × 5 m pixels, as well as radiometric, geometric, and terrain correction of the images (RapidEye 2013).

A total of 108 scenes are available showing LF between April 2009 and October 2014. However, 71 scenes were excluded from further analysis due to ice cover, snow or a closed cloud cover above the lake. The remaining 37 suitable RapidEye images collected between April 2009 and October 2014 are listed in **Table 3-2**. The further preprocessing of the images included the calculation of the top of atmosphere reflectance (TOAR) (RapidEye 2013), the co-registration of the stack of images, and cloud masking.

Table 3-2: Available RapidEye archive data showing LF between April 2009 and October 2014, including the metadata for the acquisitions. The lack of data for 2013 is due to the scarcity of acquisitions because of cloud cover and ice.

Acquisition Date	Satellite	Sensor	Sensor Viewing Angle (°)	Sun Elevation Angle (SEA) (°)	Lake Levels (m a.s.l.) *measured in situ*
2009-04-04	RE-1	MSI	0.06	42.59	63.37
2009-04-13	RE-1	MSI	13.43	45.81	63.36
2009-04-21	RE-4	MSI	6.69	48.72	63.34
2009-08-31	RE-2	MSI	−3.05	45.31	63.18
2009-09-20	RE-3	MSI	−2.90	37.75	63.15
2010-06-03	RE-2	MSI	17.03	59.12	63.4
2010-06-17	RE-2	MSI	20.46	60.06	63.39
2010-07-03	RE-3	MSI	3.68	59.74	63.34
2010-07-19	RE-5	MSI	10.38	57.56	63.29
2010-09-22	RE-3	MSI	3.53	37.05	63.32
2010-10-04	RE-1	MSI	13.16	32.40	63.31
2011-04-20	RE-3	MSI	−2.94	48.26	63.54
2011-05-07	RE-1	MSI	3.49	53.54	63.51
2011-05-11	RE-5	MSI	−3.18	54.59	63.5
2011-05-30	RE-5	MSI	−2.95	58.50	63.52
2011-06-04	RE-5	MSI	−9.79	59.11	63.51
2011-06-27	RE-5	MSI	13.60	60.10	63.53
2011-09-24	RE-3	MSI	6.88	36.34	63.7
2011-10-02	RE-1	MSI	−2.96	33.05	63.7
2011-10-13	RE-3	MSI	7.07	29.00	63.7

2011-10-17	RE-2	MSI	3.91	27.42	63.7
2011-10-22	RE-2	MSI	−6.11	25.52	63.7
2011-11-13	RE-5	MSI	−6.21	18.63	63.68
2012-04-05	RE-1	MSI	−9.61	43.05	63.92
2012-05-01	RE-4	MSI	10.25	52.08	63.94
2012-05-23	RE-2	MSI	10.24	57.48	63.91
2012-06-18	RE-4	MSI	−2.95	60.21	63.84
2012-07-24	RE-2	MSI	7.03	56.53	63.83
2012-10-12	RE-1	MSI	10.00	29.07	63.77
2012-11-14	RE-5	MSI	−6.25	18.14	63.77
2014-03-10	RE-5	MSI	−5.87	32.77	63.86
2014-03-20	RE-1	MSI	6.69	36.70	63.86
2014-04-25	RE-3	MSI	−13.11	49.95	63.87
2014-05-01	RE-5	MSI	0.31	51.93	63.86
2014-05-20	RE-5	MSI	0.34	56.82	63.84
2014-08-06	RE-2	MSI	3.54	53.44	63.76
2014-09-05	RE-3	MSI	−9.77	43.52	63.72

To analyze changing water–land borders, precise locating of the RapidEye images is required. We chose a well-positioned master RapidEye image based on a comparison with digital orthophotos. All RapidEye slave images were co-registered to this master image using the script of Behling *et al.* (Behling et al. 2014). Co-registration was based on 100 points per image tile. The maximum root mean squared error (RMSE) of the co-registered slave images to the master image ranges from 0.04–1.46 m and is on average 0.75 m. Finally, clouds were masked using two thresholds in band 1 (blue) and band 3 (red) improved by an additional buffer area of 50 m.

Finally, we measured *in situ* the shoreline in August 2014 via DGPS. The DGPS measurement of the water–land border took place on 12 August 2014, close to the RapidEye acquisition on 6 August 2014. Additionally, a description of the vegetation at the shoreline and in the water was acquired. The correction of the GPS signal was performed online by the Landesamt für innere Verwaltung Mecklenburg-Vorpommern via SAPOS-HEPS during the field measurement (Amt für Geoinformation n.d.). However, high vegetation at the northern part of the lake led to gaps in the mobile phone network and to inaccuracies in the online correction of the DGPS signal. We removed all points with a horizontal root mean square error >1 m to maintain high accuracy.

3.3.2 Method

The lake's water level was reconstructed by intersecting the water–land border with a digital elevation model (DEM), which results in the absolute height of the lake surface (=the lake level) (Maillard et al. 2012; Hostache, Matgen, Schumann, Member, et al. 2009; K. Kaiser et al. 2015). The principle is demonstrated in **Figure 3-2**. **Figure 3-2b** also illustrates the challenges caused by vegetation and steep slopes that reduce the distances between contour lines. In practical application, inaccuracies in the extraction of the water-land borders or in the DEM must also be considered. While in the ideal case the water-land border lies on one contour line, in practice the water-land border cuts through several contour lines. Thus, the intersection of the water-land border and DEM results in a range of height values for each date. After a

statistical analysis of the height values, the mode value (=most frequent value) for each date is taken as the according reconstructed lake level.

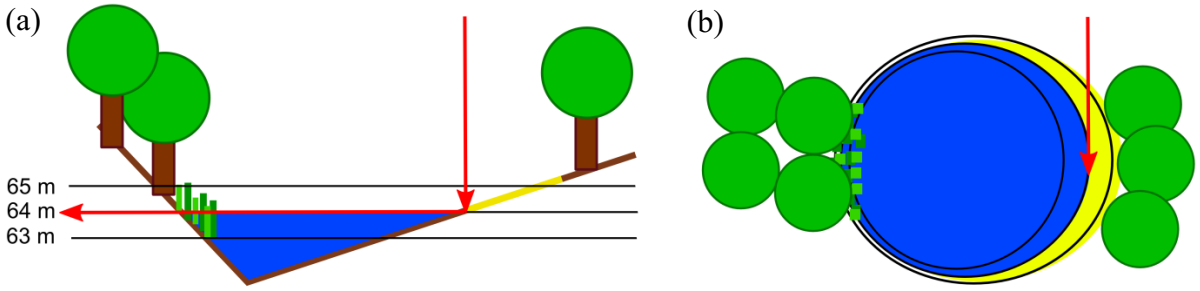

Figure 3-2: (a) Scheme of the side view of a lake including its topography; **(b)** scheme of the top view of a lake including its topography (contour lines). The top view illustrates a satellite image in which the water-land border is delineated. In an ideal case, the water-land border lies on one contour line, in this example at 64 m. This height of the water-land border (=contour line) equals the lake level.

Two state-of-the-art approaches for distinguishing water-land borders in multispectral images are thresholds in the NIR band (Arbor et al. 1976; Muster et al. 2013; Kropáček et al. 2012) and the use of the Normalized Difference Water Index (NDWI) by McFeeters (Roessler et al. 2013; Ji et al. 2009; Lu et al. 2013; Li et al. 2013). The formula for calculating NDWI according to McFeeters (1996) (McFeeters 1996) is:

$$NDWI = \frac{Ref(green) - Ref(NIR)}{Ref(green) + Ref(NIR)} \quad (1)$$

where *Ref* is Reflectance.

To delineate the water-land border in the RE images and reconstruct former levels we tested and compared both approaches, the thresholding of the NIR band and the use of NDWI. To avoid subjectivity in the choice of the threshold and to maximize the level of automation, we used the automatic *Otsu* threshold (Li et al. 2013; Lu et al. 2011). In a bimodal histogram, the *Otsu* algorithm calculates the optimum threshold separating the two classes by minimizing the intra-class variance or maximizing the inter-class variance (Otsu 1979). To calculate the *Otsu* thresholds, we selected a subset of the southern part of LF and its surroundings (**Figure 3-1**). The histograms of NIR and NDWI for this region of interest showed a clear bimodal distribution with the two classes water and land. Based on this threshold, the entire RapidEye image was classified and the shoreline of LF converted to vectors. To reconstruct the lake level, only the longest water-land border of LF was selected and small misclassified polygons were removed.

The extracted water-land borders (NIR and NDWI) from the RapidEye image of 6 August 2014 were validated by the water-land border determined *in situ* with the DGPS signal. As a degree of precision, we calculated the minimum distances between each DGPS point and the extracted RE water-land borders. Additionally, in the time series we compared all extracted RapidEye water-land borders to the corresponding contour line from the DEM and the *in situ* gauged lake level. For the evaluation, we separated each RapidEye water-land border into a row of points with 1 m distance and based on this separation calculated from the DEM the minimum distance to the corresponding contour lines.

The final step was the intersection of the extracted RapidEye water-land border with the high-resolution DEM for the lake level reconstruction. As the shoreline is very heterogeneous with

respect to land cover and shoreline topography, we selected and compared different subsets, as recommend by Kaiser *et al.*, 2015 (K. Kaiser et al. 2015). The subsets were selected based on shoreline slope and vegetation. The slope of the shoreline of LF is defined as the slope (in percent) between 63 m a.s.l. and 64 m a.s.l. The range from 63 m a.s.l. to 64 m a.s.l. represents the rounded range of lake level changes in the last decade. The selected subsets were approximately 40 m wide to have a minimum size for a statistical analysis of the reconstructed level values.

The entire processing chain of water classification and level reconstruction was implemented using the free software R (version 3.0.1) and is illustrated as a workflow in Figure S2.

3.4 Results

3.4.1 Automatic Water-Land Border Extraction

The comparison of measured DGPS points and the extracted water-land borders (NDWI and NIR) in August 2014 are illustrated in **Figure 3-3**. The boxplots in **Figure 3-3a** represent the calculated minimum distances between the DGPS points and the extracted water-land borders using NDWI and NIR. Negative distances imply that the extracted water-land border is inside the *in situ* determined boundary (underestimation of the water extent); positive distances imply that the extracted water-land border is outside the *in situ* determined boundary (overestimation of the water extent).

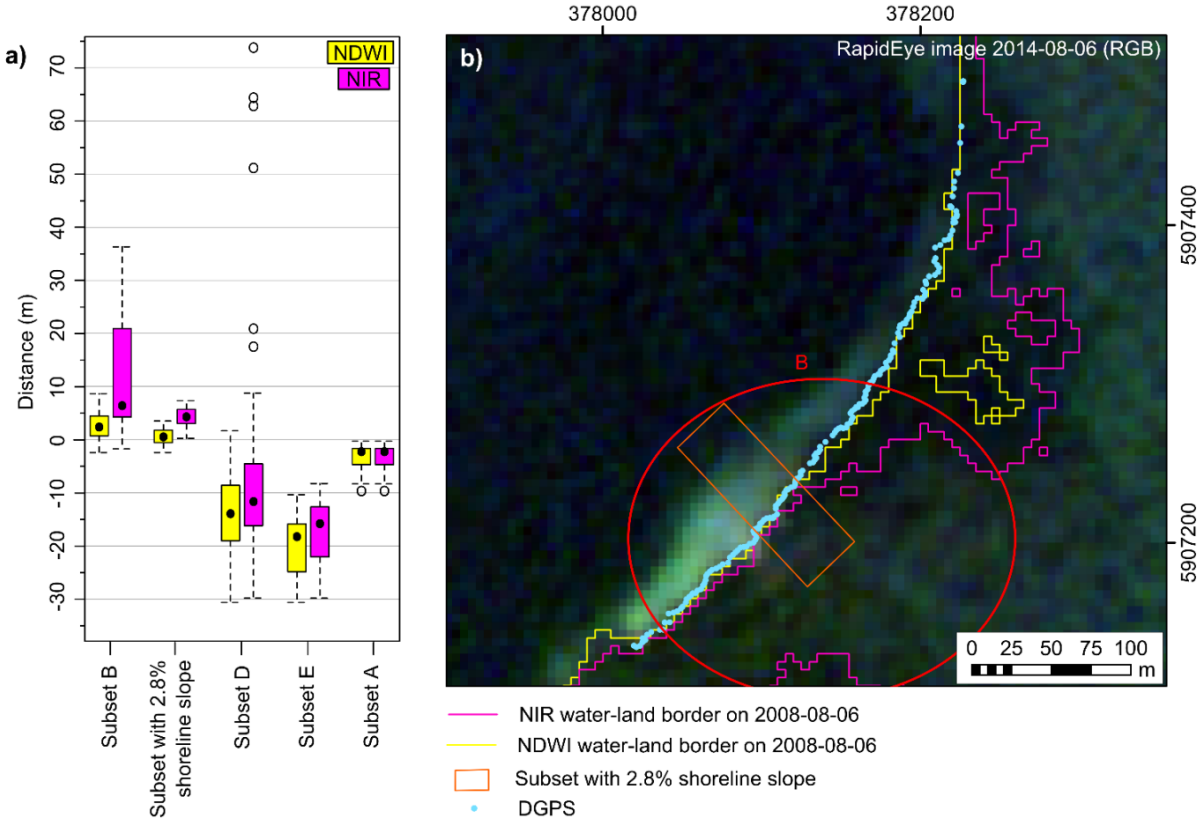

Figure 3-3: (a) shows the minimum distances between the DGPS points and the extracted water-land borders (NDWI and NIR) at different subsets (cf. **Figure 3-1**). Negative distances show an underestimation of the extracted water-land border, meaning that the extracted water-land border is inside the in situ determined boundary. Positive distances show an overestimation, meaning that the extracted water-land border is outside the in situ determined boundary. The black dots represent the median value. **(b)** illustrates the reconstructed and in

situ determined water-land borders at the southeastern part of LF. The reconstructed water-land borders were mapped in the RapidEye image using Otsu's threshold in the NIR (pink line) and the NDWI (yellow line) images. The in situ determined water-land border was measured via DGPS (light blue dots).

Eye-catching in **Figure 3-3a** are the ranges of negative and positive deviations. High deviations for NIR in subsets B and D result from misclassifications caused by the dark cloud shadows in the RapidEye image (6 August 2014). The NIR water-land border spreads massively into the land area with deviations up to 80 m. The NDWI water-land border also shows misclassifications in the land area, but the lake shoreline remains intact. Large negative deviations are caused by dense reed and overhanging trees (subset E). Subset B is not completely free of vegetation as reed grows there sparsely (mapped in summer 2014). There are beech trees growing around the lake. In summer 2014, at a level of 63.77 m, the water was close to, but not yet under the trees. Here, the deviations between DGPS and NIR/NDWI water-land borders are caused by inaccuracies in water extraction. The overestimation of the NIR water-land border at subset B is mainly caused by cloud shadow, but also in the smaller subset without direct cloud shadow the NIR water-land border is overestimated on average by 4 m (range: 0 m–7 m). The NDWI water-land border at the subset with 2.8% slope differs on average by 1 m from the DGPS-derived shoreline. The height differences between the DGPS-derived shoreline and the RapidEye water-land borders range from 0.05 to 0.25 m (NIR) and 0 to 0.20 m (NDWI) at the subset with 2.8% slope.

The new public beach (subset A) is only 50 m wide, with a very small sandy stripe (*ca.* 2.5 m in August 2014) and lawns behind. Here, the extracted water-land borders using NDWI and NIR are identical, with an underestimation of 0 m–10 m. The height difference between the DGPS shoreline and the NDWI/NIR water-land borders is between 0 and 0.25 m.

Not only cloud shadow, but also shadows behind rows of trees and buildings caused misclassifications using the NIR image. These small misclassified polygons were removed for the reconstruction of the lake level and only the longest line was taken as the water-land border.

3.4.2 Shoreline Changes

In addition to the validation using DGPS measurements, the extracted water-land-borders (NDWI and NIR) were compared to the according contour lines at different lake levels**. Figure 3-4** illustrates the water-land borders and the contour lines at minimum level (63.15 m a.s.l.) on 20 September 2009, two intermediate levels, and the near-maximum level (63.91 m a.s.l.) on 23 May 2012 (*cf*. Figure S1). The changes of the water-land border at the southeastern beach of LF are illustrated in smaller scale in Figure S4. The lake levels on 1 May 2012 (63.94 m a.s.l., maximum level) and 5 April 2012 (63.92 m a.s.l.) were slightly higher, but clouds covered large parts of LF.

The contour lines from the DEM (**Figure 3-4**c) show clear changes of the shoreline with increasing lake level. In the southwestern very shallow area (slope: 0%–3%), the contour lines move up to 150 m between the minimum and maximum extent. The sandbank that is visible in the RapidEye image is, however, not detected. This error is caused by the large gap of bathymetric points in the shallow water area and the resulting significant underestimation of the height in this area (*cf*. Figure S3).

On the vegetation free southeastern beach, the NIR water-land borders (**Figure 3-4a**) clearly show the changes in lake level. The NIR water-land border moves up to 35 m between the minimum and maximum extent, whereas the NDWI water-land borders (**Figure 3-4b**) are clearly overestimated at the low and intermediate lake levels (*cf*. the close-up in Figure S4).

The position of the NDWI water-land border at low water levels (20 September 2009) fits neither the GIS analysis nor photos from 2009 that show a wide sand beach (Figure S5).

The sandbank in the middle of the southern part of LF is detected via NIR and NDWI. In the NIR image it has a size of *ca.* 3300 m^2 at minimum water level (20 September 2009) and shrinks with increasing levels to *ca.* 300 m^2 on 21 April 2009. In the NDWI image it is at *ca.* 300 m^2 also much smaller than in the NIR water-land border and only detected at the minimum level.

Due to the importance of topographic data for lake level reconstruction, **Figure 3-5** illustrates the NIR water-land borders and the according contour lines at low and high levels as well as the topographic data. The underwater surface model is based on bathymetric points and the contour line on the day of the bathymetric survey. The gap between the point data and the contour line ranges in the shallow water area from *ca.* 15 m to *ca.* 40 m, depending on the slope of the shoreline. It is unavoidably larger in the shallower subsets.

Whereas the low lake level falls in the area of the underwater surface model, the high level falls in the area covered by ATKIS-DGM1. Thus, these two quality levels of the topography need to be kept in mind for the further analysis. The distance between the contour line and the NIR water-land border at low lake levels is larger than the distance between both at high lake levels (*cf.* **Figure 3-6**). In the subset with 2.7% slope the high deviation between the extracted NIR water-land border and the contour line sticks out. This deviation is caused by flooded trees. It must also be considered that there is a deviation between the NIR water-land borders and the contour lines because of the different resolutions of the RapidEye image and the DEM.

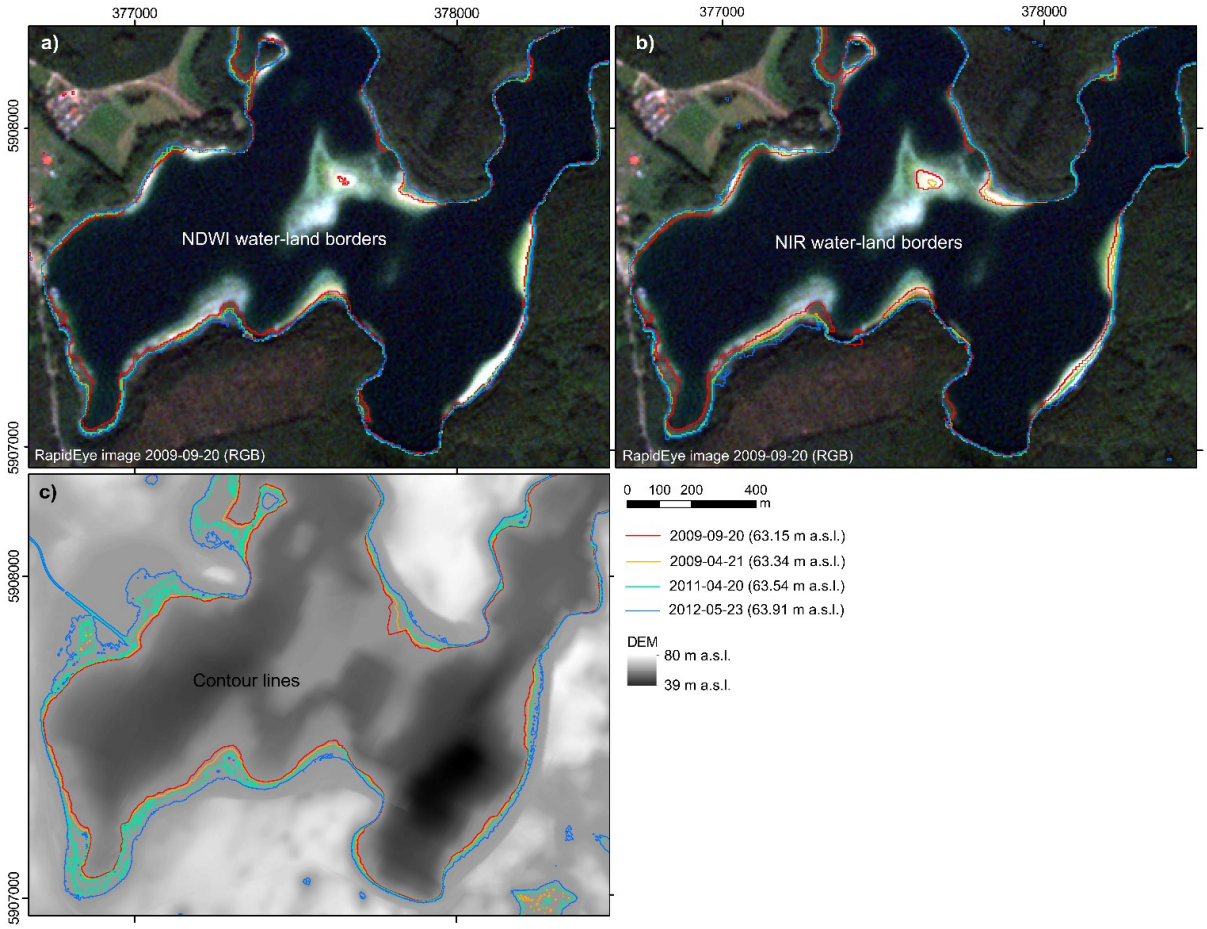

Figure 3-4: Illustration of the water-land borders on 21 April 2009, 20 September 2009, 20 April 2011, and 23 May 2012. **(a)** shows the water-land borders extracted from the RapidEye images using the NDWI; **(b)** shows the water-land borders extracted from the RapidEye images using the NIR; **(c)** represents the GIS analysis with contour lines: The levels measured in situ on the four dates are delineated as contour lines in the DEM. The minimum level (63.15 m a.s.l.) between 2009 and 2014 was measured on 20 September 2009, the maximum level on a cloud free image (63.91 m a.s.l.) on 23 May 2012.

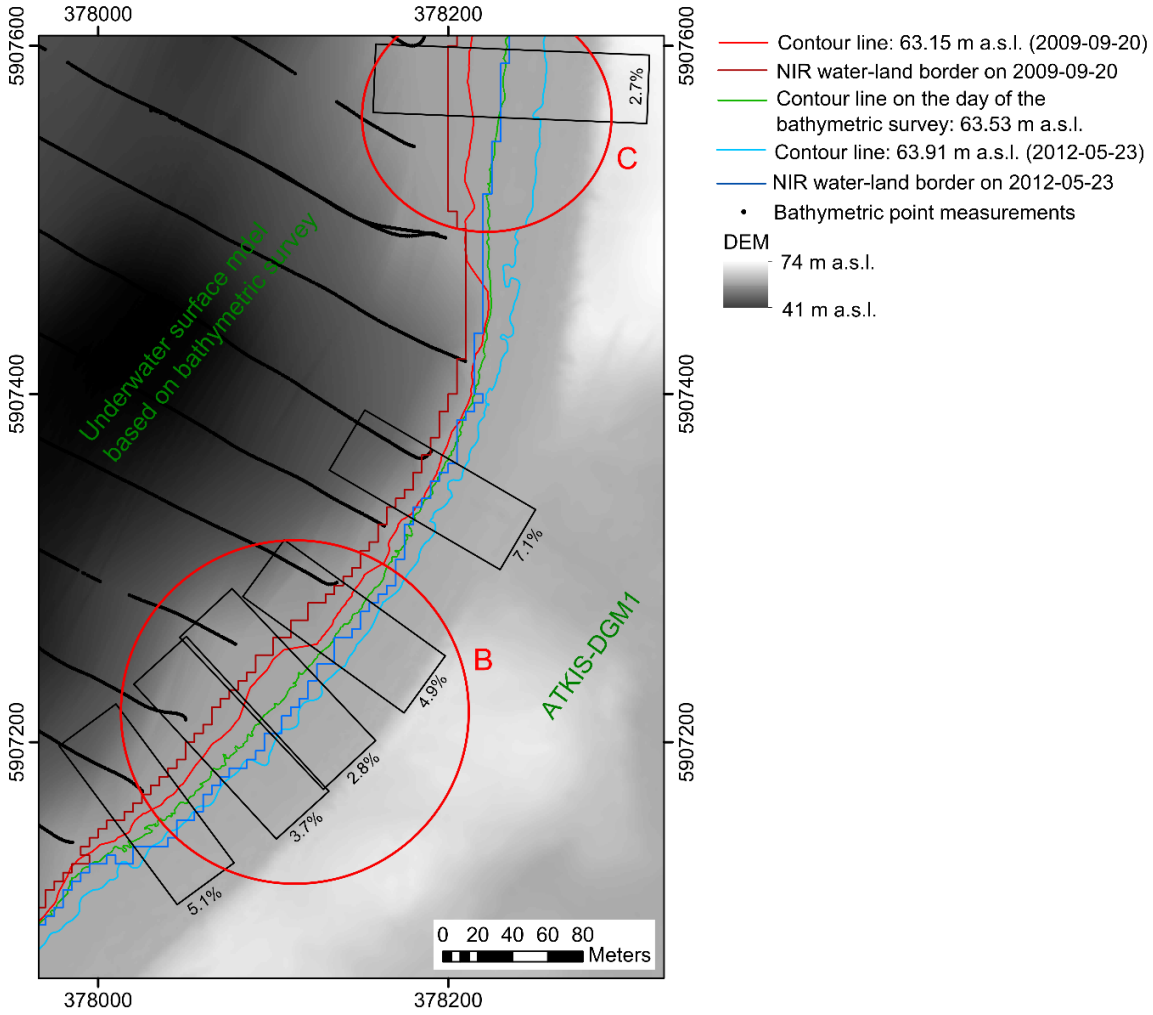

Figure 3-5: Digital elevation model, NIR water-land borders and corresponding contour lines at the southeastern part of LF (subsets B and C). The red and blue lines illustrate the deviation between the reconstructed water-land borders and the contour lines at the minimum lake level (20 September 2009, 63.15 m a.s.l.) and its maximum level in a cloud free image (23 May 2012, 63.91 m a.s.l.). The toothed shorelines (dark red and dark blue) were extracted from the RapidEye NIR image. The smoother lines (bright red and bright blue) are the contour lines from the DEM based on levels measured in situ. The green line illustrates the contour line on the day of the bathymetric survey (63.53 m a.s.l.). The measured bathymetric points are the black dots. Different subsets and their slopes (in percentage) are noted.

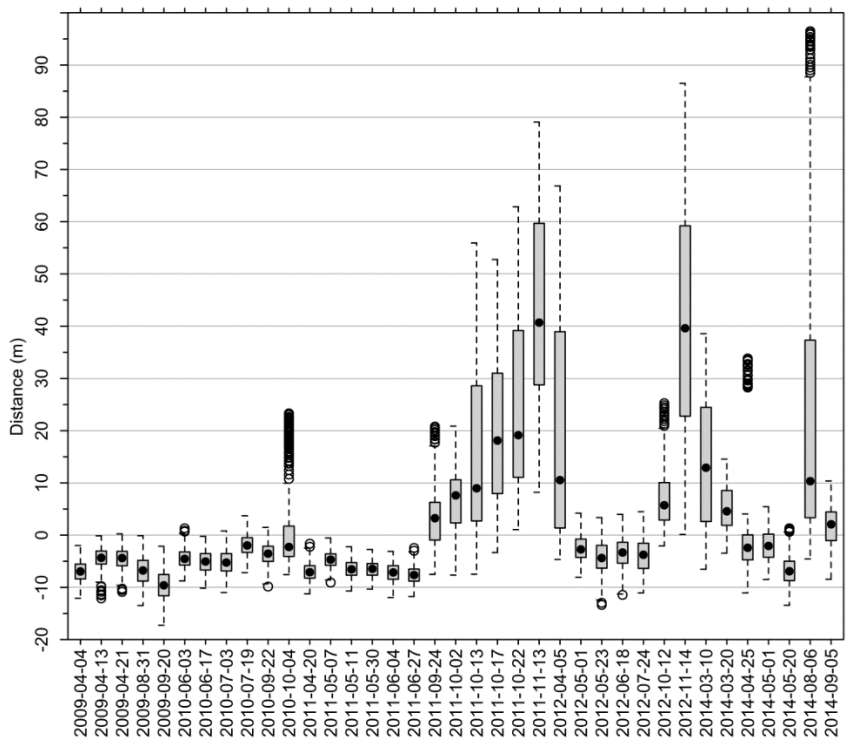

Figure 3-6: Boxplot of the minimum distances (in m) between the RapidEye water-land borders (NIR) and the according DEM contours at subset B. The black dots represent the median. The root mean squared error (RMSE) for all dates is 21.1 m. The RMSE is reduced to 10.8 m when dates with a very low sun elevation angle (SEA) below 30° and dates with a SEA angle below 45° in cases of high lake levels (≥63.7 m a.s.l.) are excluded.

A comparison of the contour lines from the DEM with the extracted NIR water-land borders of the entire time series is illustrated in **Figure 3-6**. It is based on subset B. On 24 of the 37 dates the RapidEye water-land border (NIR) compared with the median of the distances to the according DEM contour line is negative, in the range of −2 m to −10 m. At near-maximum lake level on 23 May 2012 the NIR water-land border is underestimated on average by −4.1 m, at the minimum lake level on 20 September 2009 by −9.7 m. Thirteen dates of the time series are characterized by (high) positive median distances up to several tens of meters. One of those outliers is 6 August 2014, the date of the field campaign with misclassifications due to cloud shadow. Data collected on 5 April 2012 is heavily disturbed by cloud shadow, data for 19 July 2010 only slightly. The six images between 12 October and 15 November are all characterized by a low sun elevation angle (SEA) <30°. Due to the higher noise in those images, the automatic classification fails and the classification spreads into a dark clearing in the surrounding forest (*cf*. Figure S6). The remaining images that overestimate the water surface area are dated 24 September 2011, 2 October 2011, 5 April 2012, 10 March 2014, 20 March 2014, and 24 September 2014. These dates have in common a SEA of 30° and 45° and a high lake level ≥63.7 m a.s.l. At this high lake level, the sandy beach is completely flooded. By contrast, images with a sandy beach (4 April 2009, 20 September 2009, 22 September 2010, and 4 October 2010) and a SEA between 30° and 45° underestimate the water surface area. A comparison of the contour lines with the extracted NIR water-land borders using the subset with 2.8% slope (ideal subset) can be found in Figure S7. Using the ideal subset the root mean squared error (RMSE) for all dates is 13.5 m. After excluding the 12 images with low SEA, the RMSE sinks to 5.0 m.

3.4.3 Subset Selection for Lake Level Reconstruction

A precise extraction of the water-land border is essential for an accurate reconstruction of the lake level. Another requirement for lake level reconstruction is the visibility of a water-land border change. **Table 3-3** illustrates the shift of the water-land border at the minimum lake level to the water-land border at the maximum lake level in subsets with different slopes. The position of the subsets at the southeastern shoreline is shown in **Figure 3-5**. The subset with 8.7% slope is located at the new public beach (*cf.* **Figure 3-1**). With shallower slope the distance between the minimum and maximum water-land border increases for the extracted water-land borders and for the contour lines from the DEM. The small shift of 5 m (=1 pixel) is too small for a reliable result, as intermediate lake extents cannot be delineated unambiguously. A shift of 10 m (=2 pixels) at least is theoretically required for the reconstruction of intermediate levels. At LF this means that only subsets with slopes ≤7.1% are suitable for lake level reconstruction.

Table 3-3: Average distances (in m) between the water-land borders at the minimum lake level (20 September 2009, 63.15 m a.s.l.) and the maximum level of a cloud-free image (23 May 2012, 63.91 m a.s.l.) in subsets with various slopes (in percent).

Slope (%)	Distance between Minimum and Maximum NIR Water-Land Border (m)	Distance between Minimum and Maximum Contour Lines (m)	Location (*cf.* **Figure 3-1** and **Figure 3-3**)	Notes
2.7	30.1	40.2	Subset C	Trees flooded in August 2014, high lake level
2.8	29.6	29.0	Subset B	
3.7	29.1	21.6	Subset B	
4.9	21.7	19.1	Subset B	
5.1	22.2	16.3	Subset B	
7.1	10.2	10.8	Subset B	
8.7	5.3	8.9	Subset A	

As this study aims at defining the most attainable accuracy, we conducted the reconstructed lake levels based on an "ideal" subset. The largest distances between the minimum and maximum water surface area are in the two shallowest subsets with 2.7% and 2.8% slopes (*cf.* **Table 3-3**). However, only the subset with 2.8% slope is more or less free of vegetation. Thus, this subset was selected as the ideal subset.

3.4.4 Lake Level Reconstruction

Although validation via DGPS showed more accurate results for the NDWI then for the NIR water-land border extraction, the time series analysis revealed an overestimation of the NDWI lake extent at low lake levels (**Chapters 3.4.1** and **3.4.2**). Thus, the following lake level reconstruction is based on the NIR water-land-borders and the ideal subset (*cf.* **Chapter 3.4.3**).

Even in the case of the ideal subset, the intersection of the water-land border and the DEM results in a range of height values for every image/date. This is due to the different spatial resolutions of DEM and RapidEye images and small inaccuracies in the delineation of the water-land border. The range of height values per date is illustrated in **Figure 3-7**. A comparison of the mean, median and mode height values shows that the mode value is the most

robust parameter. The mode value best represents the lake level, even in cases of misclassification of the water-land-border (*cf.* dates 13 October 2011, 5 April 2012 and 10 March 2014). Thus, the mode value of the height values for one date is considered to be its lake level.

The reconstructed lake level is underestimated for 28 of 37 dates. The underestimate ranges from −20 to −2 cm, the average being −11 cm. For three dates the precise *in situ* lake level is reconstructed (19 July 2010, 2 October 2011, and 6 August 2014); however, two of those images are disturbed by cloud shadow (yellow highlighting in **Figure 3-7**). For six dates (17 October 2011, 22 October 2011, 13 November 2011, 12 October 2012, 14 November 2012, and 20 March 2014) the reconstructed lake levels are overestimated in the range of 6 cm to 79 cm. The overestimations are caused by misclassifications in the extraction of the water-land border. As discussed before, the automatic detection of the water-land border has a reduced accuracy for images acquired at very low SEA <30° and for images with a SEA <45° in cases of high lake level (*cf.* **Table 3-2**). In **Figure 3-7**, all these images are highlighted in red**.** With removal of the 12 images, the RMSE between *in situ* measured and reconstructed levels is reduced from 22 cm to 12 cm, and the absolute mean error from 14 to 11 cm.

In a second step, we analyzed the relative level changes $\Delta h = h(t) - h(t+1)$ of dates without misclassifications in the ideal subset in **Figure 3-8**. For the monitoring period, the absolute mean of difference of $\Delta h(in\ situ)$ and $\Delta h(reconstructed)$ is 5 cm, the RMSE 6 cm. In 2009 and 2010, the lake level is so low that there is a wide sandy area between the lake and surrounding vegetation. At those times, the *in situ* measured and the reconstructed lake level changes are very similar: the difference between $\Delta h(in\ situ)$ and $\Delta h(reconstructed)$ ranges only about ±5 cm (absolute average = 3 cm, RMSE = 3 cm). The only larger deviations on 19 July 2010 and 22 September 2010 can be explained by cloud shadows on image 19 July 2010 and the resulting overestimation of the water level. In 2011 the lake level increases significantly and the sandy beach is flooded. Also, in 2011 the deviations between $\Delta h(in\ situ)$ and $\Delta h(reconstructed)$ grow larger (absolute average 5 cm, RMSE = 6 cm), with a maximum delta of −13 cm. However still, the reconstructed level changes are close to the trends of the changes determined by *in situ* measurement. Since 2012, the year with the highest lake level, the accordance of reconstructed and *in situ* measured level changes decreases significantly. The difference of $\Delta h(in\ situ)$ and $\Delta h(reconstructed)$ ranges from −7 cm to +19 cm (absolute average 6 cm, RMSE = 8 cm). Several times the reconstructed and the *in situ* measured lake levels show opposite lake level changes. The most conspicuous outlier (6 August 2014) is caused by cloud shadow.

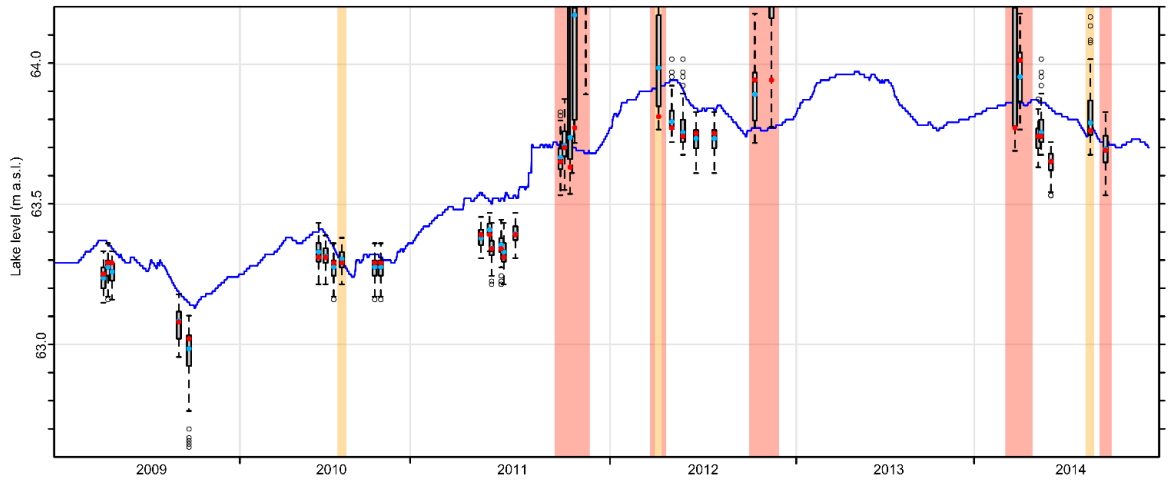

Figure 3-7: Illustration of the in situ measured and reconstructed lake levels at LF. The boxplots show the range of height values based on the intersection of the water-land border in the ideal subset with 2.8% slope with the high-resolution DEM. The mode value of a boxplot is considered to be the lake level at the according date. The blue line shows the in situ measured lake level ranges between January 2009 and November 2014. The red dots are the mode value, the light blue dots the median value for each date. Red highlighted are all dates with a very low sun elevation angle (SEA) below <30° and dates with a SEA angle below <45° in cases of high lake levels (≥63.7 m a.s.l.). Yellow highlighted RE images are disturbed by significant cloud shadows.

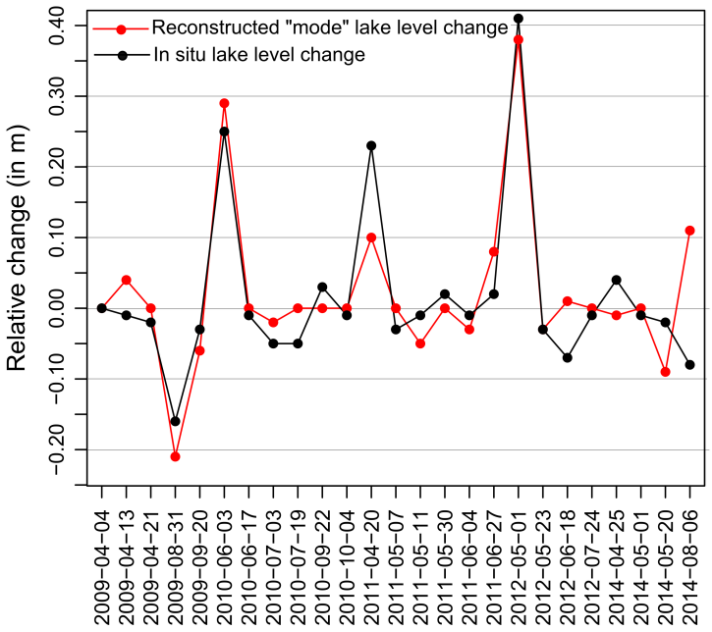

Figure 3-8: The black line shows the relative changes $\Delta h(in\ situ)$ of the in situ measured level, the red line the relative changes $\Delta h(reconstructed)$ of the reconstructed "mode" levels. Twelve dates were removed because of low sun elevation angles.

Finally, we compare the relative changes of the ideal subset with the results of the five other subsets with various slopes (*cf.* **Figure 3-5**). The results are depicted in **Figure 3-9**.

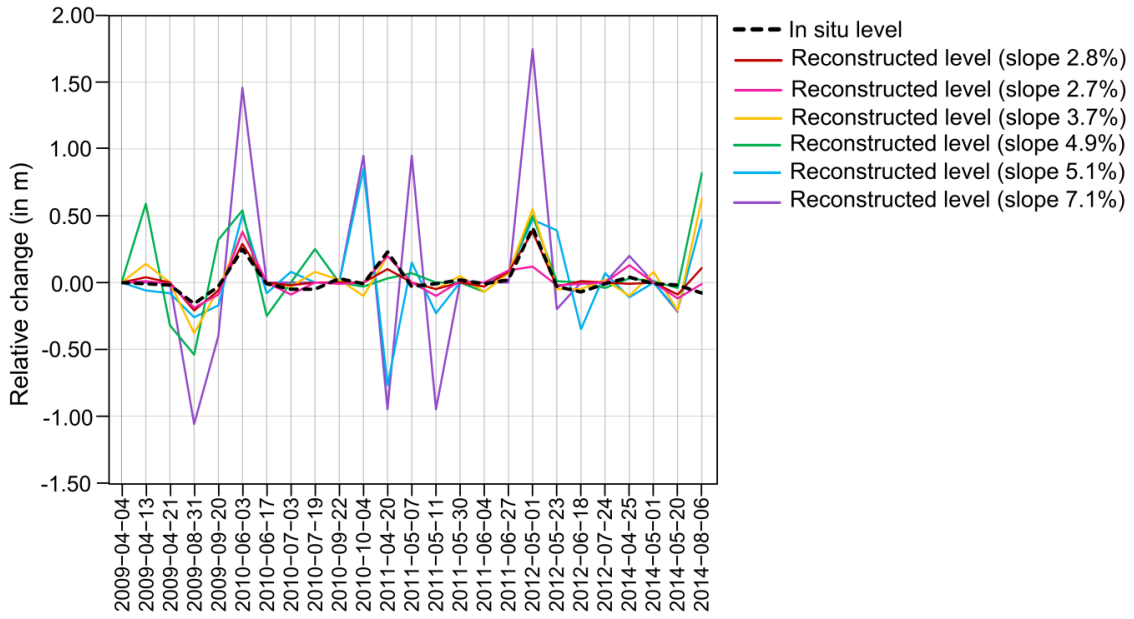

Figure 3-9: Relative changes ($\Delta h = h(t) - h(t+1)$) of the reconstructed lake levels ("mode values"). The black dashed line is the relative change of the level measured *in situ*. The colored lines represent the relative changes of the reconstructed lake levels.

As expected, the shallower the slopes, the higher the precision in the reconstruction of the lake level changes: the level changes using the two shallowest subsets are very similar until the end of 2011. After 2011, the shallowest subset (2.7% slope) shows larger deviations and partly contrary changes. As stated above, the inaccuracies in the shallowest subset are most likely caused by vegetation that covers the water surface. The subset with 3.7% slope still shows the same ups and downs as the lake level change measured *in situ*, but generally has larger deviations and outliers in 2014. The three steepest subsets (slopes of 4.9%, 5.1% and 7.1%) are all characterized by large deviations and outliers, most eye-catching at 20 April 2011.

3.5 Discussion

This study suggests that high-resolution RapidEye archive data are a valuable source for reconstructing former lake levels. It also demonstrates the importance of the shoreline slope, vegetation, and shadows (and thus solar angle) for accurately reconstructing the lake level.

Under ideal conditions, the lake levels can be measured indirectly with the NIR water-land borders in decimeter resolution. This is a significant improvement compared to previous lake level retrievals based on medium resolution data with only one-meter precision (Maillard et al. 2012). Annual and seasonal fluctuations as well as short-term (within two weeks) jumps in lake level were detected. However, for a very high-resolution temporal monitoring of daily changes or changes within one week, the changes in lake level were too small. The maximum level changes within one week are only in the range of ±5 cm, with small changes in the water-land border. The decimeter accuracy (RMSE 12 cm, absolute mean error 11 cm) of the indirect lake level reconstruction is in line with the accuracy of flood level estimations based on high-resolution data (Puech & Raclot 2002; Hostache, Matgen, Schumann, Puech, et al. 2009) and even better than a previous study in northeastern Germany using aerial photos (K. Kaiser et al. 2015). However, the levels were systematically underestimated in the range of −20–0 cm (excluding images with sever misclassification of the water-land border). The underestimation of the lake levels is caused by the underestimation of the water extent in the automatic

extraction of the water-land border. Due to this systematic underestimation of absolute lake levels, an analysis of relative changes is preferred. The accuracy of the relative changes is generally high (RMSE = 6 cm), but difference between times with sandy beaches and times with flooded beaches became visible: whereas the accuracy in 2009 and 2010 with a sandy beach was very high with (RMSE = 3 cm), it declined massively to approx. ±20 cm (RMSE 6 cm) with higher lake levels and a flawless transition of water to vegetation. This shows that the accuracy of the lake level retrieval depends on terrain and vegetation cover on the lake shore. Thus, the accuracy of the lake level retrieval can change over the monitoring period due to changing shoreline conditions at different dates and lake levels.

Essential for an accurate lake level reconstruction is the precise delineation of the water-land border and precise topographic data. Other studies just compare their extracted coastline at different times without absolute validation of the shoreline precision (Gens 2010; Li & Damen 2010). We validated the delineated water-land borders with DGPS measurements and with contour lines from the DEM. The water-land borders were extracted from the RE images automatically using *Otsu*'s threshold on the NIR bands and the NDWI images. Whereas the NDWI water-land border had a higher accuracy in the DGPS validation, the time series revealed significate overestimations of the water extent, which fits to the findings of Li *et al.*, 2013 (Li et al. 2013). The extraction of the water-land borders via NIR showed a higher sensitivity to (cloud) shadows, but was also more precise in the delineation of water at low water levels. Thus, we decided to use NIR for the lake level reconstruction.

The sensitivity of NIR and NDWI to shadows is a well-known problem and causes misclassifications (Bochow et al. 2012; Verpoorter et al. 2012; Maillard et al. 2012; Ji et al. 2009; Lira 2006; Qiao et al. 2012). Shadows of trees and buildings caused small misclassifications that were easily filtered by only taking the longest line as the water-land border. Analysis of the NIR water-land borders and the reconstructed lake levels showed that cloud shadows, such as in the RapidEye image contemporary to the field campaign with the DGPS measurements, could lead to an overestimation of water extent and thus to a relatively higher reconstructed lake level (smaller or no underestimation). This finding confirms the importance of validation with contour lines.

The accuracy of the NIR water-land borders (without misclassified images due to low solar angles) in comparison to the according contour lines at the ideal subset with 2.8% slope is RMSE = 5.0 m; for the subset B the RMSE = 10.8 m. A deviation between the NIR water-land border and the contour line is expected due to the different spatial resolutions of the RapidEye images and the DEM. In a previous study with a very high resolution IKONOS image, the RMSE between the delineation of sandy coastlines and the *in situ* measured water-land border was approx. 6 m (Lipakis & Chrysoulakis 2008). Another study with medium-resolution Landsat data estimates its accuracy as 1.3 pixels (pixel size = 30 m) (Alesheikh et al. 2007). Systematic underestimation of the NIR water-land border is caused by the inherent sensitivity of NIR reflectance in littoral zones with very shallow water columns and by the spectral mixture of water and land (Wang et al. 2014; Davaasuren & Meesters 2012). Underestimation of the water-land border via NIR band is confirmed by Wang *et al.*, 2014 (Wang et al. 2014). However, it needs to be considered that the contour lines in the GIS analysis in this study probably differ from the *in situ* determined water-land borders due to inaccuracies in the DEM, specifically in the area of the underwater surface model and because of the different resolutions of the RapidEye image and the DEM.

Essential for the unambiguous reconstruction of different levels is also a clear shift of the water-land border with increasing lake level. This shift needs to be several times larger than the pixel

size. This study finds that for RapidEye images a 30 m (=6 pixels) shift between minimum and maximum levels (80 cm level difference) is necessary for reconstructing lake levels with decimeter accuracy. A 30 m shift is reached at shoreline slopes <4%. A smaller shift significantly reduced the accuracy of lake level reconstruction, so only a trend in lake level changes could be estimated. The ideal subset for lake level reconstruction at LF has a 2.8% slope.

In summary, the requirements for lake level reconstruction with decimeter accuracy are:

1) The water-land border needs to be delineated precisely. The automatic *Otsu* threshold on the NIR band showed the best results, but the approach is sensitive to shadows and thus to low solar angles. Dense vegetation cover hinders the accurate retrieval of water-land borders.

2) The topographic data needs to be accurate as the lake level reconstruction is only as good as the underlying DEM. This is specifically true for the underwater surface model, which is not of very high quality due to sparse bathymetric point measurements. Due to the different quality levels of the DEM, the accuracy of lake level reconstruction depends here also on the lake level itself.

3) The shoreline subset that is used for the retrieval of the lake level needs to be very shallow, so that the shift of the water-land border with changing lake level is maximized. Using RapidEye images, a decimeter accuracy of lake level reconstruction is only feasible if the shoreline slope is less than 3%.

These requirements are very strict and only very few lakes can fulfill the demands. Suitable lakes with shallow shorelines are, for example, Lake Wittwesee near Reihnsberg, Lake Redernswalder See near Parlow-Glambeck, Lake Briesensee near Poritz, and Lake Stechlin near Neuglobsow. The above-mentioned suitable lake sites are characterized by having little or no vegetation on sandy beaches during low level periods in the time range of the RapidEye acquisitions. However, at high lake levels reed vegetation often colonizes the shallow shorelines.

Another limitation on regular lake level monitoring is the actual temporal resolution of the RapidEye time series, with often less than one image per month and no suitable images from September/October until April. Frequent clouds coverage as well as cloud shadows reduced the temporal resolution of the RapidEye time series massively. Additionally, low solar angles during wintertime result in larger shadows and a worse signal-to-noise-ratio so that land is mistaken for water in the automatic classification. As a consequence, images with a very low SEA <30° and images with a low SEA between 30° and 45° during high lake levels needed to be removed. Thus, at LS only 75% of the RapidEye images in the archive could be finally used for the lake level reconstruction.

Nevertheless, monitoring lake level changes remains a hot topic as only *ca*. 500 of the *ca.* 5000 lakes in northeastern Germany have regular gauging stations (Päzolt 2015; Mathes 2015) and because the RapidEye time series analysis in this study clearly showed the significance of lake level and shoreline changes for ecologic and economic reasons: Within one season, between April 2009 and September 2009, the size of the sandbank decreased by 90% and within one year the sandbank and shallow sandy beaches were completely flooded. This rapid change has high ecological impact on LF. For tourism the vanishing old public beach (subset B) with its wide sandy beach was a loss of attraction and at the new public beach (subset A) a swimming pier needed to be relocated. Also important was the flooding of the land connection of the peninsula

in the southwest and the drowning of trees (subset C). The increase in lake level also influenced the submerged and aquatic vegetation: whereas the drying out of the shallow areas at low lake levels led to a significant reduction in the amount of pondweed and stonewort (Kaiser, Friedrich, et al. 2012); the shallow water areas were again colonized with reed in 2014. It is hoped that with a continuous high lake level the former underwater macrophytes will recolonize to stabilized and secure clear water conditions.

3.6 Conclusions

In this study, we measured lake levels indirectly by combining information on the water-land borders derived from high-resolution multi-spectral satellite images (RapidEye) and high-resolution topographic data. The results showed that the reconstruction of lake level changes worked well even for small and short-term lake levels changes. The RMSE between *in situ* measured lake level changes and reconstructed lake level changes was 6 cm. The absolute lake levels were reconstructed with decimeter accuracy, but they showed a systematic underestimation by −20–0 cm. The RMSE between *in situ* measured lake levels and reconstructed lake levels was 12 cm.

We tested two approaches for retrieval of water-land borders: automatic thresholds (*Otsu*) of the NIR bands and of the NDWI images. This study showed that NIR water-land borders were more precise than NDWI water-land borders, but also more sensitive to shadows. The RMSE between NIR water-land borders and according contour lines was 5.0 m (excluding winter images). Limitations in the accuracy of the delineation of the water-land border are caused by the characteristics of the RapidEye sensors and by the interfering shoreline vegetation. Mixed water and land pixels lead to an underestimation of the NIR water-land border. Due to changing shoreline conditions at different dates and lake levels, the accuracy of the lake level delineation can change over the monitoring period. The sensitivity of the NIR band to shadows causes severe misclassifications in the NIR water-land borders, especially in winter with low SEA angles. Clouds and shadows reduce significantly the repeat interval of usable RapidEye data acquisitions. Possible alternatives to tackle the limitations of the RapidEye optical system could be very high resolution data or Synthetic Aperture Radar (SAR). However, both alternatives bring new challenges. The use of very high resolution data (e.g., Worldview-2, Quickbird, Spot) for higher precision of water-land border determination comes with high cost of the images. SAR sensors are sunlight independent and able to penetrate clouds and light rain (Lillesand et al. 2008). However, the side-looking geometry of the sensors is a disadvantage for spatially precise monitoring of shorelines (Heine et al. 2014).

The time series analysis of the NIR water-land borders at LF showed significant shifts of the shoreline with increasing lake levels. This is essential for the unambiguous reconstruction of different lake levels. The shift needs to be several times larger than the pixel size. For RapidEye images, at least a 30 m (6 pixels) shift between minimum and maximum lake levels (80 cm level difference) is necessary for reconstructing lake levels with decimeter accuracy. Such a 30 m shift results from shoreline slopes <4%. A smaller shift significantly reduces the accuracy of lake level reconstruction, so only a trend in lake level changes could be estimated.

Our results show that the reconstruction of small lake level changes can only be achieved using high resolution topographic data. For better accuracy, LIDAR acquisitions at low lake levels could substitute medium-resolution bathymetric surveys in shallow parts of the lake. As long as erosion and sedimentation rates are low, one-time acquisition of additional topographic data would be sufficient.

For the natural lakes in northeastern Germany and Poland, the transferability of the approach is limited, because of the specific requirements of the method. The very shallow shoreline slopes of the natural lakes often exhibit dense shoreline vegetation. Our experience indicates that the approach can be transferred to lakes with shorelines affected by human activity which keeps the shores free of vegetation such as public beaches or watering places. Additionally, the use of the lakes as reservoirs and fish ponds often introduces significant lake level changes.

Supplements: Supplementary materials can be found online at http://www.mdpi.com/2073-4441/7/8/4175/s1. The materials are additionally included in this thesis: **Supplementary Materials on Chapter 3**.

Acknowledgments: We would like to thank Julian Oeser and Robert Behling for their help in processing the RapidEye images and Christian Hohmann for his help in the field campaign. We are also grateful to our anonymous reviewers for their helpful and constructive comments. This study was funded by the "Helmholtz Association of German Research Centres Initiative—Networking Fund for funding a Helmholtz Virtual Institute" (VH-VI-415). Satellite imagery was provided by ESA (proposal no. 14611) and BlackBridge (RESA Projekt-ID A1274).

Author Contributions: Iris Heine developed the methodological framework, performed programming, and conducted the analysis. Birgit Kleinschmit and Sibylle Itzerott were involved in formulating the research questions, preparing the manuscript, and contributing to critical discussions. Iris Heine, Birgit Kleinschmit and Sibylle Itzerott were involved in the general paper review. Peter Stüve supported the study by providing *in situ* data as well as expert knowledge about the gauging and the study area.

Conflicts of Interest: The authors declare no conflict of interest.

4 Year-Long Monitoring of Reed Belts Using Dual-Polarimetric TerraSAR-X Imagery

Heine, I., Jagdhuber, T., & Itzerott, S. (2016). Classification and Monitoring of Reed Belts Using Dual-Polarimetric TerraSAR-X Time Series. Remote Sensing, 8(7), 552, *doi:10.3390/rs8070552*.

Received: 19 February 2016 / Revised: 20 May 2016 / Accepted: 22 June 2016 / Published: 29 June 2016

Abstract

Synthetic aperture radar polarimetry (PolSAR) and polarimetric decomposition techniques have proven to be useful tools for wetland mapping. In this study we classify reed belts and monitor their phenological changes at a natural lake in northeastern Germany using dual-co-polarized (HH, VV) TerraSAR-X time series. The time series comprises 19 images, acquired between August 2014 and May 2015, in ascending and descending orbit. We calculated different polarimetric indices using the HH and VV intensities, the dual-polarimetric coherency matrix including dominant and mean alpha scattering angles, and entropy and anisotropy (normalized eigenvalue difference) as well as combinations of entropy and anisotropy for the analysis of the scattering scenarios. The image classifications were performed with the random forest classifier and validated with high-resolution digital orthophotos. The time series analysis of the reed belts revealed significant seasonal changes for the double-bounce–sensitive parameters (intensity ratio HH/VV and intensity difference HH-VV, the co-polarimetric coherence phase and the dominant and mean alpha scattering angles) and in the dual-polarimetric coherence (amplitude), anisotropy, entropy, and anisotropy-entropy combinations; whereas in summer dense leaves cause volume scattering, in winter, after leaves have fallen, the reed stems cause predominately double-bounce scattering. Our study showed that the five most important parameters for the classification of reed are the intensity difference HH-VV, the mean alpha scattering angle, intensity ratio HH/VV, and the coherence (phase). Due to the better separation of reed and other vegetation (deciduous forest, coniferous forest, meadow), winter acquisitions are preferred for the mapping of reed. Multi-temporal stacks of winter images performed better than summer ones. The combination of ascending and descending images also improved the result as it reduces the influence of the sensor look direction. However, in this study, only an accuracy of ~50% correct classified reed areas was reached. Whereas the shorelines with reed areas (>10 m broad) could be detected correctly, the actual reed areas were significantly overestimated. The main source of error is probably the challenging data geocoding causing geolocation inaccuracies, which need to be solved in future studies.

4.1 Introduction

The common reed (*Phragmites australis*) is a perennial wetland grass that grows typically in large and dense communities, so-called reed belts (Bogenrieder 1990; Rodewald-Rudescu 1974). The reed belts are important for the erosion protection of shorelines, as a biotope for animals, as carbon storage and as a cleaning filter of the lake water (Bogenrieder 1990; Schmieder et al. 2004). Most of the shallow lake areas in northeastern Germany are covered by reed, but fluctuations of the lake levels can reduce the plant stocks temporarily (Heine et al. 2014). Despite their importance, reed vegetation is not regularly monitored: the last biotope mapping at Lake Fürstenseer was carried out in 1991. The expenditure of time for the field mapping of reed is enormous because of large lake extents, the dense vegetation around the lake, or, in some cases, the limited accessibility of lakes in nature conservation areas. Thus, the monitoring and mapping of reed are performed based on aerial photos and (very) high resolution optical satellite images (Bresciani et al. 2009; Schuster et al. 2015; Csaplovics & Nemeth 2014; Lantz & Wang 2014). However, very high resolution optical images are often expensive and have the inherent disadvantage of weather and illumination dependence: a regular monitoring of lakes in northeastern Germany is not feasible due to frequent cloud coverage and low sun elevation angles in winter (Heine et al. 2015). Synthetic aperture radar (SAR) sensors do not have these limitations and therefore are the method of choice for regular, all-year monitoring. The SAR image is hereby a result of the acquisition geometry and system

parameters as well as the reed scatterer characteristics, in particular its water content and structure (dielectric constant, orientation, distribution and density of scattering elements) (Castree et al. 2009, p.317). Using synthetic aperture radar polarimetry (PolSAR) and polarimetric decomposition techniques allows the physical characterization of the scattering scenario and the involved scatterers (Lee & Pottier 2009). Important for the analysis of the scattering scenario is the penetration depth of the SAR signal which is predominantly a function of its wavelength: for short wavelengths such as X-band and C-band, vegetation leaves are important scattering objects, whereas longer wavelengths such as L- and P-band can penetrate the canopy and branches or trunks are the predominant scattering objects (Castree et al. 2009).

Based on their characteristics, dual- and quad-polarimetric TerraSAR-X and Radarsat-2 images have proven to be useful tools for wetland mapping (Zhao et al. 2014; Smith 1997; White et al. 2015; Betbeder et al. 2014; Schmitt & Brisco 2013). Common classes for wetland monitoring are open water, bare soil, shrubs, forest, and different types of flooded and non-flooded grassland (Betbeder et al. 2014; Zhao et al. 2014; Corcoran et al. 2013; Van Beijma et al. 2014). For short-wavelengths such as X-band, their scattering characteristics can be distinguished as follows: smooth water reflects the SAR signal specularly, whereas bare soil and rough water cause surface backscattering; between two smooth surfaces (e.g., water and trunks) double-bounce scattering occurs and shrubs as well as forest cause volume scattering (Castree et al. 2009). However, it must be considered that in northeastern Germany, deciduous and coniferous forest canopies have significantly different phenologies and, thus, scattering characteristics. Flooded and non-flooded grasslands differ in their scattering behavior due to the considerably different roughness of the soil compared to water. Additionally, different grassland types vary in their density as well as structure and, therefore, also in their scattering mechanisms. Although different grassland types have been included in previous PolSAR wetland monitoring studies, research about reeds is scarce. Only Yajiami et al. monitored reed and lotus plants using X-band and L-band quad-polarimetric PolSAR data at a study site in Japan (Yajima et al. 2008). Reeds have a vertical plant structure, similar to rice or grass. Therefore, PolSAR studies on grassland (Voormansik et al. 2013; Dusseux et al. 2014; Voormansik et al. 2015) and rice monitoring (Lopez-Sanchez et al. 2012; Lopez-sanchez et al. 2011; Lopez-Sanchez et al. 2011; Lopez-Sanchez et al. 2014; Yonezawa et al. 2012; Koppe et al. 2013) are included here. With the following research study, we want to provide new insights about reed monitoring with PolSAR data. The applied data are dual-co-polarized (HH, VV) X-band SAR acquisitions of TerraSAR-X, because the quad-polarimetric mode is only an experimental one for TerraSAR-X (TSX) and acquisitions are only available on a very limited basis. Based on the calculation of 16 dual-polarimetric parameters, the objectives of this study are:

- Gain knowledge about the scattering mechanisms of reed belts during the monitoring period (August 2014 to May 2015) and their exploitation for the phenological monitoring of reeds
- The application of an automatic algorithm for classification of reed areas with recommendations for the best suitable classification input parameters and the most effective acquisition periods for a performant classification.

4.2 Study Area

The Mecklenburg Lake District in northeastern Germany bares the highest density of lakes in Germany. The lake test site, Fürstenseer (FS), is located near Neustrelitz in Mecklenburg-Vorpommern, Germany (**Figure 4-1**). The lithospheric basis of its catchment is sandur from the last ice age (Germer et al. 2010). The lake is fed by groundwater and has no active inlet or

outlet. Like many lakes in the region, it is characterized by seasonal and inter-annual lake level changes (Germer et al. 2010; Kaiser, Friedrich, et al. 2012). Lake FS is well researched (Heine et al. 2015; V. K. Kaiser et al. 2015; Waterstraat & Spiess 2015; Kaiser, Germer, et al. 2012; Kaiser, Friedrich, et al. 2012; Graventein 2013) and representative for many lakes in the region. The lake level and ice coverage are measured daily in the southwestern part of the lake by the State Agency for Agriculture and Environment of the Mecklenburg Lake District. The average depth of the lake is 8.0 m; the maximum depth is 24.5 m, while the lake is located 63.5 m above sea level (a.s.l.) (Heine et al. 2015).

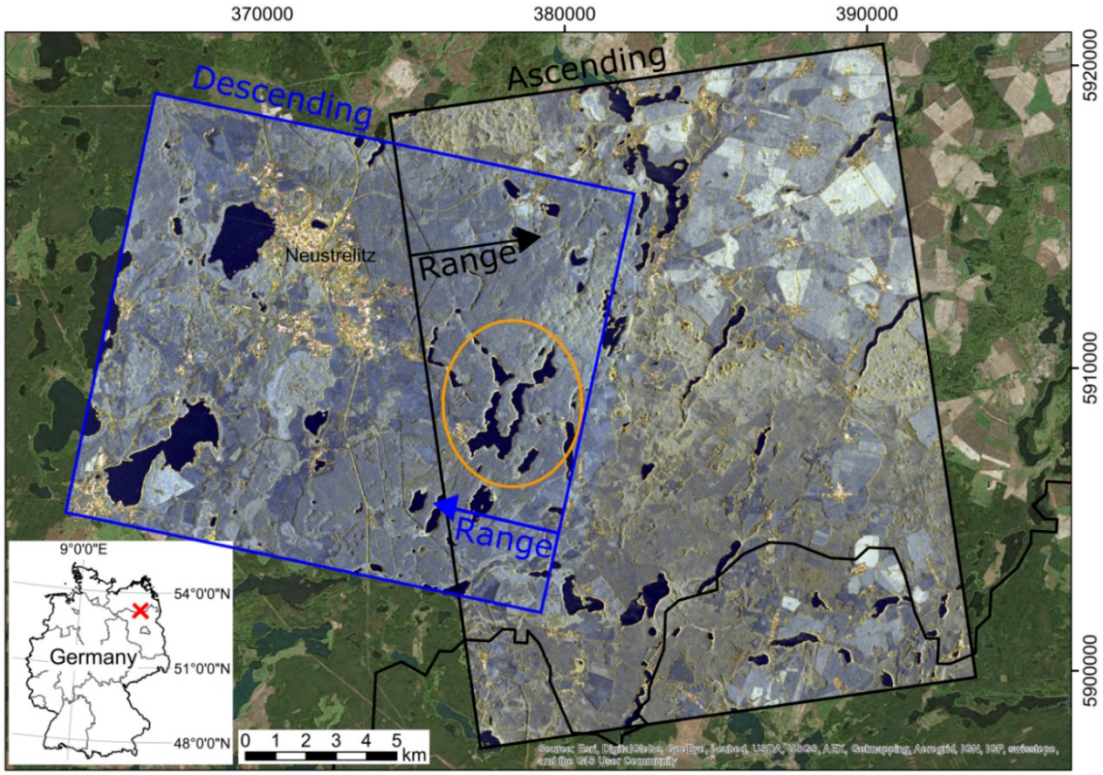

Figure 4-1: Overview of the study area Lake Fürstenseer, near Neustrelitz, Germany. The ascending and descending SAR images are quicklooks of the TerraSAR-X scenes. The quicklook images are RGB composites (δ_{HH}, δ_{VV}, and δ_{HH-VV}) with a reduced pixel size of ca. 25 m. The ascending and descending SAR images were acquired in November 2014 (14 November 2014, 22 November 2014). The look direction (range) of the sensor is indicated by arrows.

The shoreline of the lake is heterogeneous with respect to land cover and shoreline topography, and is little influenced by human activity, except for small bathing sites in the southwest and southeast areas of the lake. The shoreline topography varies with very shallow areas in the southern part and steeper shorelines in the northeastern part of the lake (Heine et al. 2015) (cf. **Figure 4-2**). The shallow shorelines in the southwest of the lake are densely covered with reeds, as is visible in **Figure 4-3**, whereas the southeastern is part only sparsely covered. This difference may be caused by lake level changes in the last decade and the use of the southeastern shoreline as a bathing site. The lake level changes in the last decade ranged around 1 m (cf. **Figure 4-4**): in October 2006 the lake level fell to a local minimum of 63.4 m a.s.l. In 2011 there was a significant increase, causing the level to range around 63.8 m (cf. (Kaiser, Germer, et al. 2012; Germer et al. 2010)). Shallow shoreline areas and a sandbank fell dry during the local minimum in 2006/2007 (Heine et al. 2015). The southeastern shoreline was at this time a sandy beach without reed vegetation. Generally, the reed belts at the shoreline move with the decreasing and rising lake level, as long as the changes are not too abrupt (van de Weyer et al. 2009; Bogenrieder 1990).

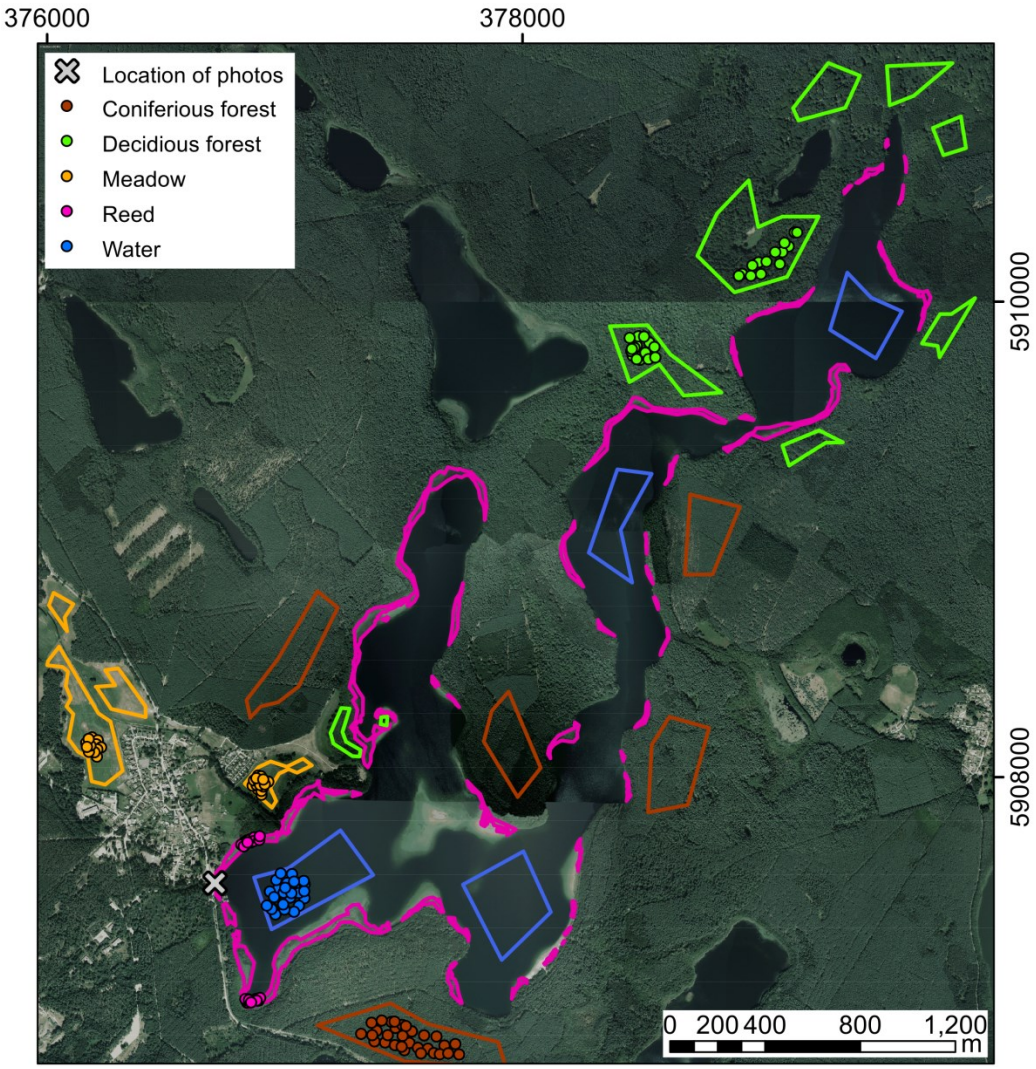

Figure 4-2: Overview of Lake Fürstenseer with the training areas (points) and validation area (polygons) of the five classes. The classes are: reed (pink), water (blue), meadow (orange), deciduous (bright green) and coniferous forest (brown). Base layer is the digital orthophoto with 40 cm resolution (DOP40) from 2013. Photos were taken at the southwestern shoreline (grey cross).

Figure 4-3: Photos of a reed belt at the southwestern part of the lake in June 2014 **(a,b);** November 2015 **(c,d)**; and January 2016 **(e)**. The location of the photos is marked in **Figure 4-2**. Photos **(a,c,e)** were taken in a northwestern direction, the photos **(b,d)** in a southeastern direction.

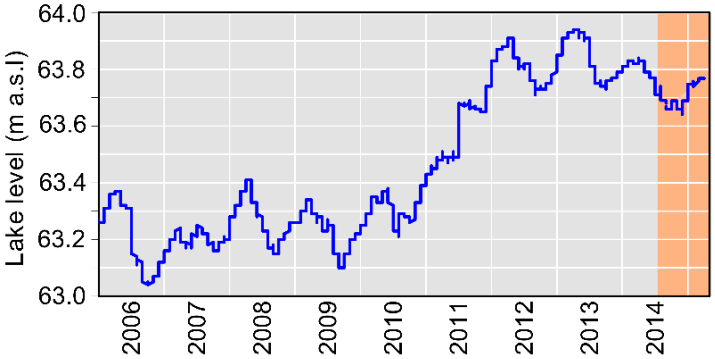

Figure 4-4: Lake level changes of Lake Fürstenseer between January 2006 and March 2015. The monitoring period of this study (August 2014 until May 2015) is highlighted in orange.

4.3 Available Data

4.3.1 Dual-Polarimetric (HH, VV) TerraSAR-X Time Series

For this study, we acquired 19 dual-polarimetric (HH, VV) TSX Stripmap images between August 2014 and May 2015. Four images were acquired in ascending orbit (asc), 15 in descending orbit (desc) (see **Figure 4-1** for coverage). The observation space of polarimetry collapses to a singularity for nadir incidence. In contrast, it widens as the incidence angle increases. Therefore, large incidence angles are preferable in polarimetry, as this maximizes the sensitivity of this observation space (Jagdhuber 2012). Therefore, one of the highest incidence angles in the operational mode of TSX was used with 40° incidence. **Table 4-1** gives an overview on the data of the TSX time series.

The TSX images were delivered in Single Look Slant Range Complex (SSC) format. The pre-processing of the images was implemented in the Interactive Data Language (IDL). First, the images were imported and radiometrically calibrated. Then, intensity-based and polarimetric parameters were calculated according to Equations (3)–(17) (cf. Section 4.4.1). For spatial averaging during the calculation of the 2 × 2 coherency matrix $T_{2\times2}$ in Equation (1), we used a sliding window with a 43 × 7 pixels window size, so that the equivalent number of looks (ENL) exceeds the recommended value of 80 (Lee et al. 2008). The geocoding of the images was performed using the georeferencing points included in the delivered TSX data. The point-based geocoding was chosen as an appropriate processing standard because the study area is flat with very little topography. The ground range resolution of the asc images is 1.7 m and for the desc images it is 1.9 m. The average azimuth resolution of both orbits is 6.6 m. The grid size of the geocoded images is assigned to 3 m × 3 m. Finally, the images were mapped to WGS 1984, UTM 33 N for comparison with orthophotos.

Before classification of the scenes, we estimated the noise empirically on two regions of interest (roi). Therefore, we selected a homogeneous water area (~3300 pixels) and a homogeneous coniferous forest (~3900 pixels). The empirically-based noise equivalent sigma zero (NESZ) is estimated by the mean intensity acquired over the calm lake bodies (in decibel, dB) and is based on the fact that smooth water should have no backscatter signal at the X-band. The NESZ in our images is always smaller than −18.3 dB, which corresponds to the specified NESZ of dual-polarimetric TSX Stripmap images with −19 dB (Eineder et al. 2013). The HH and VV backscattering of the reed areas remains largely above −12.5 dB, and only in winter with ice cover it decreases to −14 dB. The empirically estimated signal-to-noise ratio (SNR), as the mean of the intensity of the forest area divided by the mean of the intensity of the water area, ranges between 7 and 11 dB (**Table 4-1**). Thus, the signal is ~10 times higher than the noise and therefore no significant noise bias is expected.

Table 4-1: Overview of the available TerraSAR-X (TSX) data. The mean incidence angle is extracted from the TSX metadata file, the noise equivalent sigma zero (NESZ) and signal-to-noise ratio (SNR) of the images are estimated empirically (as explained above). Additional information about Lake Fürstenseer, provided by the State Agency for Agriculture and Environment of Mecklenburg Lake District, are listed as well.

Date	Mean Incidence Angle (°)	Orbit	NESZ HH (dB)	NESZ VV (dB)	SNR HH (dB)	SNR VV (dB)	Comments
4 August 2014	38.5	Desc	−20.19	−20.32	10.81	10.80	
7 August 2014	42	Asc	−19.61	−19.74	8.92	9.06	
15 August 2014	38.5	Desc	−20.66	−20.93	9.95	9.82	

6 September 2014	38.5	Desc	−20.47	−20.69	9.54	9.35	
28 September 2014	38.5	Desc	−20.55	−20.91	9.17	8.96	
9 October 2014	38.5	Desc	−20.41	−20.40	10.58	10.21	
20 October 2014	38.5	Desc	−19.56	−18.79	8.76	7.60	
31 October 2014	38.5	Desc	−21.03	−21.38	9.77	9.61	
11 November 2014	38.5	Desc	−21.01	−21.34	9.80	9.52	
14 November 2014	42	Asc	−19.40	−18.36	7.91	6.88	
22 November 2014	38.5	Desc	−21.12	−21.35	9.47	9.23	
25 November 2014	42	Asc	−20.21	−20.10	8.45	8.34	
18 February 2015	38.5	Desc	−19.87	−19.86	9.03	8.54	Lake borders covered by ice
1 March 2015	38.5	Desc	−20.94	−20.80	9.43	8.92	
12 March 2015	38.5	Desc	−21.01	−21.36	9.61	9.53	
23 March 2015	38.5	Desc	−20.87	−21.23	9.91	9.86	
26 March 2015	42	Asc	−19.99	−19.81	8.70	8.45	
3 April 2015	38.5	Desc	−20.54	−20.55	9.78	9.42	
6 May 2015	38.5	Desc	−20.43	−20.85	10.48	10.53	

4.3.2 Validation and Training Data

Based on the different scattering mechanisms of natural vegetation (cf. Section 4.1), we selected five main classes for the study area: open water, deciduous and coniferous forest, meadow, and reed. Bare soil and shrubs are only present in small-scale areas within the study region. Towns and cities are not selected as their own class as the focus is on natural lake regions. The validation areas of reed, water and meadow were digitized based on a digital orthophoto (40 cm resolution, DOP40) from the summer of 2013. For the digitization of the coniferous and deciduous forest validation areas, an additional digital orthophoto (20 cm resolution, DOP20) from winter 2011 was used. The orthophotos were provided by the State Agency for Internal Administration of Mecklenburg-Vorpommern. The validation areas and the training points are illustrated in **Figure 4-2**. The sizes of the validation areas are approximately: 29 ha for open water, 30 ha for deciduous forest, 35 ha for coniferous forest, 11 ha for meadow, and 18 ha for reed. Within those validation areas, we selected 30 points for training of the random forest classifier.

The reed area in the southwestern part of the lake was documented during field campaigns with photos in June 2014, November 2015, and January 2016 (**Figure 4-3**). Since 2015, the northeastern part of the lake was monitored with a time lapse video.

4.4 Methods

4.4.1 Introduction to the Theory of Dual Polarimetry and Its Scattering Parameters

Dual polarimetry is a polarimetric subspace of full or quad polarimetry (HH, HV, VH, VV) (Lee & Pottier 2009; Charbonneau et al. 2010).

In this study, we analyzed 16 dual-polarimetric (HH, VV) parameters with respect to their potential for monitoring reeds (cf. **Table 4-2**). We calculated different indices based on the HH and VV intensities as well as the dual-polarimetric coherency matrix (cf. Equation (1)), including dominant and mean alpha scattering angles, entropy and anisotropy (normalized eigenvalue difference), plus entropy-anisotropy-combinations (*H-A*-combinations).

Table 4-2: Overview of the 16 parameters derived from the dual-polarimetric TSX data.

Parameter	Abbreviation	Unit	Range
Intensity of HH channel	δ_{HH}	Decibel (dB)	−25–5
Intensity of VV channel	δ_{VV}	dB	−25–5
Intensity of HH plus Intensity of VV	δ_{HH+VV}	dB	−25–5
Intensity of HH minus Intensity of VV	δ_{HH-VV}	dB	−25–5
Intensity ratio HH/VV	$\delta_{HH/VV}$	dB	−25–5
Coherence HHVV amplitude	$\lvert\gamma_{HHVV}\rvert$	-	0–1
Coherence HHVV phase	$\angle\gamma_{HHVV}$	radian	−π–π
Intensity XX (pseudo)	$\delta_{XX,pseudo}$	dB	−25–5
Dual-polarimetric mean alpha angle	$\bar{\alpha}_{dual}$	Degree (°)	−180–180
Dual-polarimetric dominant alpha angle	α_{dual}	Degree (°)	−180–180
Entropy	H_{dual}	-	0–1
Anisotropy	A_{dual}	-	0–1
H-A-combination 1	$m1$	-	0–1
H-A-combination 2	$m2$	-	0–1
H-A-combination 3	$m3$	-	0–1
H-A-combination 4	$m4$	-	0–1

A state-of-the-art method for quad-polarimetric decomposition is the mathematically-based entropy/anisotropy/alpha (H/A/α) decomposition by Cloude and Pottier (Cloude & Pottier 1997), which uses eigenvalue/eigenvector analysis of the coherency T matrix for scattering mechanism analysis. The (H/A/α) quad-polarimetric decomposition was later transferred by Cloude to an entropy/alpha (H2α) decomposition for dual-polarimetric data (Cloude n.d.). For this study we use the modified version of the (H2α) decomposition for the 2 × 2 coherency matrix T_{2x2}, as defined in Voormansik et al. (Voormansik et al. 2013):

$$T_{2x2} = \frac{1}{2}\left\langle \begin{bmatrix} (S_{HH}+S_{VV})(S_{HH}+S_{VV})^* & (S_{HH}+S_{VV})(S_{HH}-S_{VV})^* \\ (S_{HH}-S_{VV})(S_{HH}+S_{VV})^* & (S_{HH}-S_{VV})(S_{HH}-S_{VV})^* \end{bmatrix} \right\rangle \quad (1)$$

Based on the eigenvalues λ_1 and λ_2 and the corresponding eigenvector υ_1 of the T_{2x2} coherency matrix, the dual-polarimetric entropy (H_{dual}), the dual-polarimetric anisotropy (A_{dual}), the dominant scattering alpha angle (α_{dual}), and the mean scattering alpha angle ($\bar{\alpha}_{dual}$) are

calculated (Equations (2)–(6)) (Cloude n.d.). P_1 and P_2 are the probabilities, χ_1 is the first coordinate of the first eigenvector, and $|v_1|$ is the length of the first eigenvector (Cloude n.d.):

$$P_1 = \frac{\lambda_1}{\lambda_1 + \lambda_2}, P_2 = \frac{\lambda_2}{\lambda_1 + \lambda_2} \tag{2}$$

$$H_{dal} = -(P_1(\frac{\log_{10} P_1}{\log_{10} 2}) + P_2(\frac{\log_{10} P_2}{\log_{10} 2})) \tag{3}$$

$$A_{dual} = \frac{\lambda_1 - \lambda_2}{\lambda_1 + \lambda_2} \tag{4}$$

$$\propto_{dual} = = \cos^{-1} \frac{|\chi_1|}{|v_1|} \tag{5}$$

$$\overline{\propto}_{dual} = P_1 \propto_{dual} + P_2(\frac{\pi}{2} - \propto_{dual}) \tag{6}$$

Based on the intensities of the HH and VV channels, we calculated different indices (in dB) (Equation (7)–(9)). In Equations (10) and (11), the intensities of the HH and the VV channels (in dB) are expressed as well.

$$\delta_{HH/VV} = 10 \log_{10} \frac{\langle |S_{HH}|^2 \rangle}{\langle |S_{VV}|^2 \rangle} \tag{7}$$

$$\delta_{HH-VV} = 10 \log_{10}(\langle |S_{HH}|^2 \rangle - \langle |S_{VV}|^2 \rangle) \tag{8}$$

$$\delta_{HH+VV} = 10 \log_{10}(\langle |S_{HH}|^2 \rangle + \langle |S_{VV}|^2 \rangle) \tag{9}$$

$$\delta_{HH} = 10 \log_{10}(\langle |S_{HH}|^2 \rangle) \tag{10}$$

$$\delta_{VV} = 10 \log_{10}(\langle |S_{VV}|^2 \rangle) \tag{11}$$

The dual-polarimetric coherence between HH and VV channels is given in Equation (12) as a complex number. Therefore, γ_{HHVV} provides the coherence amplitude $|\gamma_{HHVV}|$ and the coherence phase $\angle\gamma_{HHVV}$ for analysis (Voormansik et al. 2013).

$$\gamma_{HHVV} = \frac{\langle S_{VV} {S_{HH}}^* \rangle}{\sqrt{\langle |S_{HH}|^2 \rangle \langle |S_{VV}|^2 \rangle}} \tag{12}$$

Assuming azimuthal symmetry for volume scattering and reflection symmetry for ground scattering also allows the synthesization of the intensity of the cross-polarization $\delta_{XX,pseudo}$ (in dB) from coherent co-polarization data using the coherence γ_{HHVV} as follows (Jagdhuber et al. 2013; Cloude 2009; Souyris et al. 2005; Voormansik et al. 2015):

$$\delta_{XX,pseudo} = 10 \log_{10}(\frac{1}{4} \cdot (1 - |\gamma_{HHVV}|) \cdot \langle |S_{HH} - S_{VV}|^2 \rangle) \tag{13}$$

Hence, the information quality of the synthesized cross-polarization intensity can only be as good as the symmetry assumptions on the scatterers is valid for the respective resolution cell.

Finally, we calculated dual-polarimetric *H-A*-combinations (Equations (14)–(17)) derived equivalently such as for a quad-polarimetric (H/A/α) decomposition (Lee & Pottier 2009, p.245). For quad-polarimetric images $(1-H)(1-A)$ corresponds to the presence of a single dominant scattering mechanism, AH to the presence of two scattering mechanisms with the same probability, $A(1-H)$ to the presence of two unequally probable scattering mechanisms, and $H(1-A)$ indicates random scattering (Lee & Pottier 2009, p.245). For dual-polarimetric *H-A*-combinations, the interpretation has not been researched yet, as the dual-polarimetric anisotropy is not a measure of secondary scattering mechanisms. Therefore, a direct allocation to the quantity of scattering mechanisms involved in the scattering process is not possible in the moment and the combinations are named as:

$$m1 = (1 - H_{dual})\,(1 - A_{dual}) \tag{14}$$

$$m2 = H_{dual}A_{dual} \tag{15}$$

$$m3 = A_{dual}(1 - H_{dual}) \tag{16}$$

$$m4 = H_{dual}(1 - A_{dual}) \tag{17}$$

4.4.2 Random Forest Classification

The classification of the polarimetric SAR images is performed using the random forest (RF) algorithm (Breiman 2001) implemented in R (Liaw & Wiener 2015). It is a state-of-the-art method for the classification of remote sensing images and has been successfully used for the classification of PolSAR images of wetland regions (Corcoran et al. 2013; Van Beijma et al. 2014; Zhao et al. 2014) and crop type (Deschamps et al. 2012; Sonobe et al. 2014) mapping. RF is an ensemble learning method and is based on the construction of a large number of decision trees based on training data. The RF classifier can be trained on very high dimensional datasets, without significant overfitting, and the classifier is also relatively robust to outliers and noise (Breiman 2001) which is important for the spatially variable SAR data. In this study, we selected 30 points for each class as training data for the RF classifier. The position of the training points is illustrated in **Figure 4-2**. The minimum distance between the points is 5 m to avoid sampling within the same pixel. The classes are open water, deciduous forest and coniferous forest, meadow, and reed (cf. **Chapter 4.3.2**). About two-thirds of the training points are randomly selected and used for the construction of each decision tree. The remaining training points are used, respectively, as input for each decision tree to generate a test classification for error estimation (out-of-bag error) (Breiman 2001; Loosvelt, Peters & Skriver 2012). After a large number of trees is generated (in this study: 500), their different classification results for input are compared and the most popular class ("majority vote") is assigned as the classification output (Breiman 2001).

Another advantage of the RF classifier is the possibility to assess the importance of each classification parameter (variable) in the classification (Breiman 2001; Liaw & Wiener 2015). We chose the "mean decrease in accuracy" as the importance measure as it takes into account the impact of each predictor variable individually as well as its interaction with the other input variables (Loosvelt, Peters & Skriver 2012). The importance of a variable is handed out as the mean decrease in the accuracy of the classification. It is calculated during the out-of-bag error calculation phase of the RF classification and represents the difference between the prediction accuracy before and after permuting the variable of interest. The mean decrease in accuracy is given for each class separately (=local importance of a variable) (Liaw & Wiener 2015). These importance measures have also been used for feature selection in the classification of

polarimetric images (Zhao et al. 2014; Loosvelt, Peters & Skriver 2012; Loosvelt, Peters, Skriver, et al. 2012). In this study, we use the information about the importance of a variable to evaluate and score different polarimetric parameters for the classification of reed. As the importance values of the variables may vary with each run, we run the RF classifier 10 times and average the importance values for the analysis.

To test the accuracy of the different polarimetric SAR parameters, the RF classifier was applied on different combinations of polarimetric parameters:

- Single parameter images: every parameter at every date
- Parameter stacks: stack of all kinds of parameters of a date
- Multi-temporal parameter stacks: stack of all kinds of parameters of multiple dates (with different look directions)
    - all 19 asc and desc images;
    - all 15 desc images;
    - all four asc images;
    - asc and desc winter images without ice (31 October 2014, 11 November 2014, 14 November 2014, 22 November 2014, 25 November 2014, 12 March 2015, 23 March 2015, 26 March 2015);
    - asc winter images without ice (14 November 2014, 25 November 2014, 26 March 2015);
    - desc winter images without ice (31 October 2014, 11 November 2014, 22 November 2014, 12 March 2015, 23 March 2015);
    - two timely matching asc and desc images in November (14 November 2014 and 22 November 2014);
    - two timely matching asc and desc images in March (26 March 2015 and 23 March 2015).

Before the classification of the multi-temporal parameter stacks, the stacks were masked to retrieve the overlaying area of the asc and desc scenes. The polygon is irregular, but the not available (NA) values in the stacked images are not considered within the RF classification.

4.4.3 Evaluation of the Classification

For validation of the reed area, the classification results were cut to match with the lake area and its close surroundings. Therefore, we used the water-land border of the lake plus a 50 m buffer around the lake area. Within this lake area we calculated the intersection of the validation reed area and our classification results as the correct classified reed area. Additionally, we calculated the commission area (false positive classified as reed) and the omission area (missed reed areas, false negative). For better comparison of the time series data, we then calculated the correct classified proportion, the commission error and the omission error in percent (correct classified + commission error + omission error = 100%).

4.5 Results and Discussions

4.5.1 Time Series Analysis of the Validation Areas

Figure 4-5 shows the mean values of each parameter for each validation area (deciduous and coniferous forest, water, meadow, and reed). Additional to the reed validation area, the mean of the "true reed" area is illustrated in dark pink. The "true reed" area is the correct classified reed area that denotes the intersection of the reed area of the RF classification of the parameter stacks (cf. Section 4.5.3) and the validation reed area. The change of the study area in summer and winter is illustrated in **Figure 4-6** with two RGB images ($\delta_{\text{HH-VV}}$, $|\gamma_{\text{HHVV}}|$, and $\overline{\propto}_{dual}$).

First, we will analyze the changes of reed during the year on the basis of **Figure 4-5**. Generally, the "true reed" mean has a similar curve progression as the reed area, but it is shifted and better separated from the other classes. Thus, for the analysis of the phenology, we will concentrate on the "true mean" values because of the less disturbed reed signal.

The phenology of reed is characterized by strong growth in April (mainly stem) and May (stem and leaves). By the end of June the maximum leave area is reached. In August the reed blooms and only the rhizome continues to grow (Geisslhofer & Burian 1970; Rodewald-Rudescu 1974). Between October (Geisslhofer & Burian 1970) and November/December (Rodewald-Rudescu 1974), depending on the literature, the leaves of the reed start to wither and fall off. On 11 November 2015 the leaves were withered, but most were still attached to the stems (**Figure 4-3**). Unfortunately, no photos were taken at the end of 2014, so the actual phenological state of the reed in November 2014 is unknown. The withered stems of the reed keep standing (Bogenrieder 1990; Rodewald-Rudescu 1974) unless they are cut off by moving ice. The cut off of reed is very unlikely in the study area, according to an expert (Peter Stüve) for Lake Fürstenseer See. The time lapse video vaguely shows the development of the first leaves on the reed and the very clear development of the leaves of the deciduous trees between 9 April 2015 and 6 May 2015.

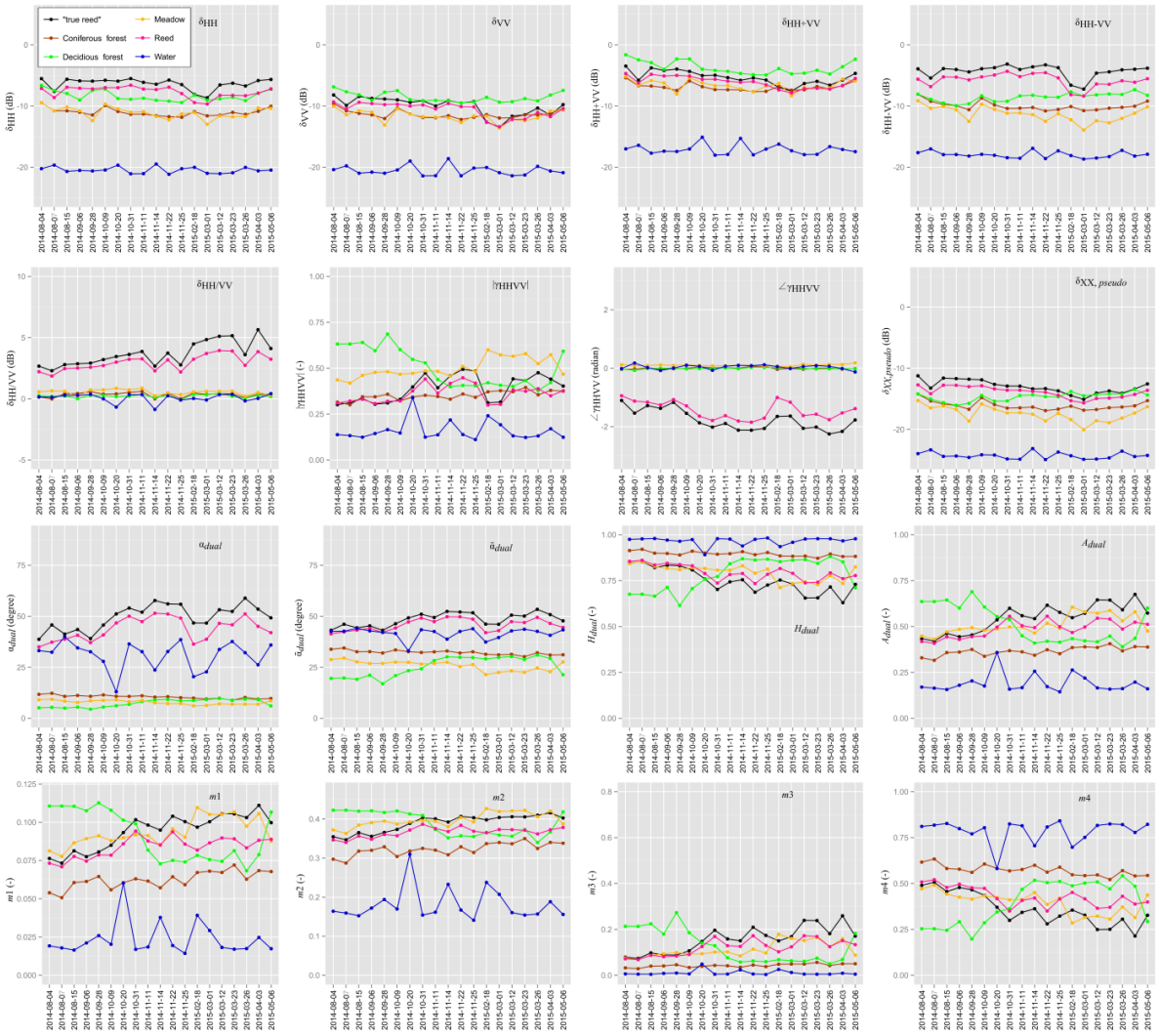

Figure 4-5: Time series of mean values for the 16 parameters from the validation areas (cf. **Figure 4-2** and **Table 4-2**). The mean of the reed area is pink, the "true reed" area is black, meadow is orange, water is blue, coniferous is brown and deciduous forest light green. Acquisitions in asc orbit are noted in grey, dates in desc orbit are in black.

Thus, in summer we expect mainly volume scattering at the X-band coming from the complex structure of the leaves and stems in the reed vegetation (Yajima et al. 2008). In winter and early spring (until early March), we expect predominantly double-bounce scattering from the remaining stems and the lake surface underneath. In May, the development of the reed leaves increases the volume scattering component again. It needs to be considered that our TSX time series does not cover the entire year: there have been no acquisitions in December, January, June, and July.

Generally, the majority of the 16 parameters show a similar trend of high (respectively low) values in August/September, then a decrease (increase) in October, low (high) values in November and March and finally another increase (decrease) in April/May. Outliers are the dates 18 February 2015 and 1 March 2015. On 18 February 2015, the borders of the lake were covered by ice. However, due to the similarity of the polarimetric parameters (e.g., coherences, alpha angles and intensities) on 18 February 2015 and 1 March 2015, we assume that there is still ice coverage on 1 March 2015 on some lake borders. In the following analysis, the acquisitions with ice on 18 February 2015 and 1 March 2015 are excluded due to a very

different scattering behavior. The remaining images are then all ice- and snow-free. The differences between summer (August, September) and winter/early spring (November/beginning of March) are listed in **Table 4-3**. No significant seasonal trend is present in the temporal evolution of the parameters δ_{HH}, δ_{VV}, δ_{HH-VV}, and δ_{HH+VV}.

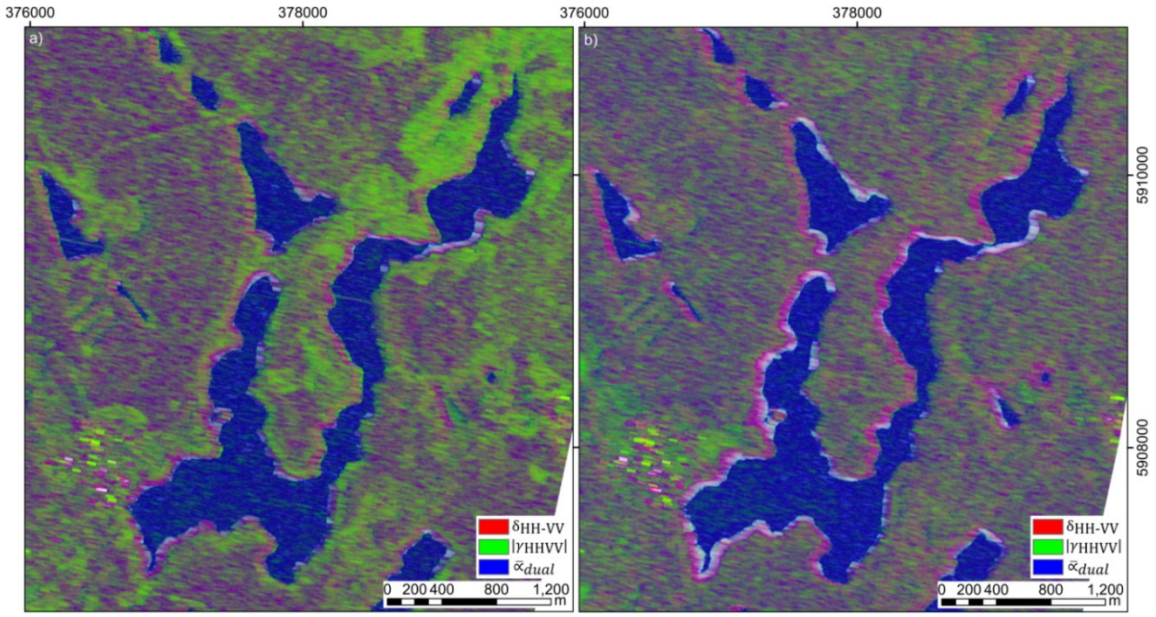

Figure 4-6: RGB images (δ_{HH-VV}, $|\gamma_{HHVV}|$ and $\bar{\propto}_{dual}$) acquired in summer on 4 August 2014 **(a)** and winter on 22 November 2014 **(b)**. The colors are stretched from minimum value to maximum value within the current map extent. Both images are acquired in desc orbit with a western look direction.

Table 4-3: Difference of the mean values and standard deviation of the "true reed" area in summer (August, September) and winter/early spring (November/March).

Parameter	Summer	Winter, Early Spring
$\delta_{HH/VV}$ (only desc images)	2.81 ± 0.09 dB	4.47 ± 0.67 dB
$\delta_{XX,pseudo}$	−11.92 ± 0.69 dB	−13.60 ± 0.39 dB
$\lvert\gamma_{HHVV}\rvert$	0.31 ± 0.01	0.45 ± 0.03
$\angle\gamma_{HHVV}$	−1.29 ± 0.15 rad	−2.07 ± 0.10 rad
$\bar{\propto}_{dual}$	44.4° ± 1.2°	51.4° ± 1.3°
$\propto_{dual}$	41.7° ± 30°	55.2° ± 2.5°
H_{dual}	0.84 ± 0.01	0.71 ± 0.04
A_{dual}	0.44 ± 0.01	0.60 ± 0.04
$m1$	0.08 ± 0.00	0.10 ± 0.00
$m2$	0.36 ± 0.01	0.40 ± 0.01
$m3$	0.09 ± 0.01	0.19 ± 0.03
$m4$	0.48 ± 0.02	0.30 ± 0.04

The phenological changes can be clearly seen in parameters that are sensitive to the double-bounce-scattering mechanism, such as $\delta_{HH/VV}$, $\angle\gamma_{HHVV}$, $\bar{\propto}_{dual}$, and $\propto_{dual}$. However, δ_{HH-VV}, which is also sensitive to double-bounce scattering, does not correlate to the phenological changes, but has high values (mean: −4 dB) during the entire monitoring period. Surprising are also the significant differences between asc and desc images of the parameter $\delta_{HH/VV}$: for desc

images, the $\delta_{HH/VV}$ shows an increase in winter, correlated to more prominent double-bounce scattering. The parameter $\angle\gamma_{HHVV}$ of reed is around −1.3 rad in summer and decreases in winter to values mostly smaller than −2 rad. This would be in line with quad-polarimetric studies that show that a phase shift of about |π| rad indicates double-bounce (Loosvelt, Peters & Skriver 2012). The $\overline{\propto}_{dual}$ of reed ranges between 40° (summer) and 50° (winter, without ice); the $\propto_{dual}$ reaches 60° in winter/early spring. For quad-polarimetric SAR, pure double-bounce as the dominant scatter mechanism is indicated by alpha angles close to 90° (Van Beijma et al. 2014). In this study, we also interpret the increase of the dual-polarimetric alpha angle values in winter as a consequence of an increasing proportion of double-bounce scattering. The parameter $|\gamma_{HHVV}|$ refers to the correlation of HH and VV intensities: here, our study shows that in summer the $|\gamma_{HHVV}|$ of reed belts ("true reed") is lower (~1.5) than in winter without reed leaves. The cross-polarimetric channel predominantly shows vegetation scattering and is sensitive to the amount of biomass (Voormansik et al. 2013; Mohan et al. 2011). The $\delta_{XX,pseudo}$ of reed is therefore lower in winter than in summer, because of the leaf-off period within the reed belts.

The H_{dual} and A_{dual} and, consequently, also $m1$, $m2$, $m3$, and $m4$ values of reed change throughout the year. The A_{dual} and the combination parameters ($m1$, $m2$, $m3$, and $m4$) are new and the interpretation is therefore still speculative: following the interpretation of quad-polarimetric entropy H and anisotropy A, a high H and low A correspond to random scattering, whereas a high H together with a high A correspond to the presence of two equal scattering mechanisms (Lee & Pottier 2009, p.244). In summer H_{dual} is significantly larger than A_{dual}, probably corresponding to volume scattering. In winter both H_{dual} and A_{dual} are characterized by larger fluctuations, which make the interpretation difficult. However, generally, A_{dual} has higher values and is closer to H_{dual} which indicates a change of the scattering mechanism in winter. Our study shows the importance of the mutual use of H_{dual} and A_{dual}, as in a previous PolSAR study of rice with high dual-polarimetric entropy values (~0.9) in spring and which, in the end of the vegetative phase, could not be differentiated. It was suggested that high dual-polarimetric entropy values (~0.9) in spring were a result of the mixed scattering of the surface and double-bounce, and high dual-polarimetric entropy values in the end of the vegetative phase were a result of random scattering generated by the plants' volume (Lopez-sanchez et al. 2011), but for better interpretation the calculation of A_{dual} is useful. For quad-polarimetric images, $m4$ indicates random scattering (Lee & Pottier 2009, p.245), and also for reed, $m4$ decreases in winter, whereas the dual-polarimetric *H-A*-combinations $m1$, $m2$ and $m3$ increase. This could be interpreted as an increase of the presence of single, dominant scattering processes and the two-scattering mechanism because of the double-bounce of reed in winter, but further studies are necessary to validate these purely empirical observations.

As shown above, the phenology of reed changes the polarimetric parameter in winter and summer, but deciduous forest and meadow also show seasonal changes. Additionally, changing environmental conditions such as partial ice coverage of the lake on 18 February 2015 and probably 1 March 2015 influence the separability of the five classes.

The best separation of reed areas from the other classes by the mean values of the observed parameters is achieved in winter by the double-bounce–sensitive parameters δ_{HH-VV}, $\delta_{HH/VV}$, $\angle\gamma_{HHVV}$, $\overline{\propto}_{dual}$ and $\propto_{dual}$. Especially δ_{HH-VV} and $\delta_{HH/VV}$ have proven useful in the classification of flooded vegetation in (Zalite et al. 2013; Lopez-Sanchez et al. 2011). The mean values of $\propto_{dual}$ are more extreme than the mean values of $\overline{\propto}_{dual}$ and the seasonal variation of the parameter $\propto_{dual}$ is more pronounced. Hence, $\propto_{dual}$ appears more suitable for the separation of reed according to the investigations in **Figure 4-5**. Reed has predominantly the highest mean

δ_{HH} values and they are higher than δ_{VV} during the entire monitoring period (cf. (Lopez-Sanchez et al. 2011)). However, δ_{HH} has a high probability of confusion with deciduous forest because, especially in spring, the mean values of δ_{HH} differ only by 2 dB to the ones of reed. The parameter $\delta_{XX,pseudo}$, is an indicator of vegetation scattering (Voormansik et al. 2013; Mohan et al. 2011), and also reacts to reed as well as forest. Thus, δ_{HH} and $\delta_{XX,pseudo}$ are very suitable for the distinction of reed and water (no volume scattering on the lake surface), but not for the distinction of reed and deciduous forest. Another problem is the dependence on the look direction of the co-polarized intensities (HH, VV): in **Figure 4-6** the dependency of the look direction results in higher values near the shorelines in the range direction in channel $\delta_{HH\text{-}VV}$. H_{dual} and A_{dual}, and consequently also the scattering mechanism from the dual-polarimetric *H-A*-combinations, show a high similarity of reed and meadow, probably because of a similar phenology. During leaf fall and growth, confusion with scattering from deciduous forest is also possible. As such, δ_{VV}, δ_{HH+VV}, and $|\gamma_{HHVV}|$ are the parameters that are least distinct in their mean values. They have a high likelihood of confusion of reed with other various classes. Thus, δ_{HH+VV} indicates direct surface or odd-bounce scattering (Lopez-Sanchez et al. 2011) and the mean value for reed is, in winter, nearly identical with the values for scattering from meadows and coniferous forest. In summer, the mean value of reed lies between the mean value of deciduous forest and the values of meadow and coniferous forest, but the probability for confusion is still critical. The parameter $|\gamma_{HHVV}|$ of reed is, in summer, nearly identical with that of coniferous forest; the rest of the year, $|\gamma_{HHVV}|$ of reed is also similar to those of meadow and deciduous forest.

4.5.2 RF Classification: Single Parameter Layer of Every Date

Here, we start with the actual classification, after the analysis of the observed polarimetric parameters by the mean values of the classes. This is important, as the mean values do not represent the spatial variability of these parameters. Therefore, we test the potential of every parameter for reed mapping by classifying every single parameter image using RF classification. The classifications of every parameter at every date result in $6 \cdot 19 = 304$ classifications.

For the evaluation of the classification results, we calculated the correct classified proportion of reed (correct positive), the commission error (false positive) and omission error (false negative) in percent based on the validation reed area. For the temporal evaluation, we stacked the correct classified proportions of each date (**Figure 4-7a**), the commission errors of each date (**Figure 4-7b**), and the omission errors of each date **Figure 4-7b**). The higher the stacks in **Figure 4-7a**, the better the reed classifications of the different parameters are and the more valuable the date is for the classification of reed.

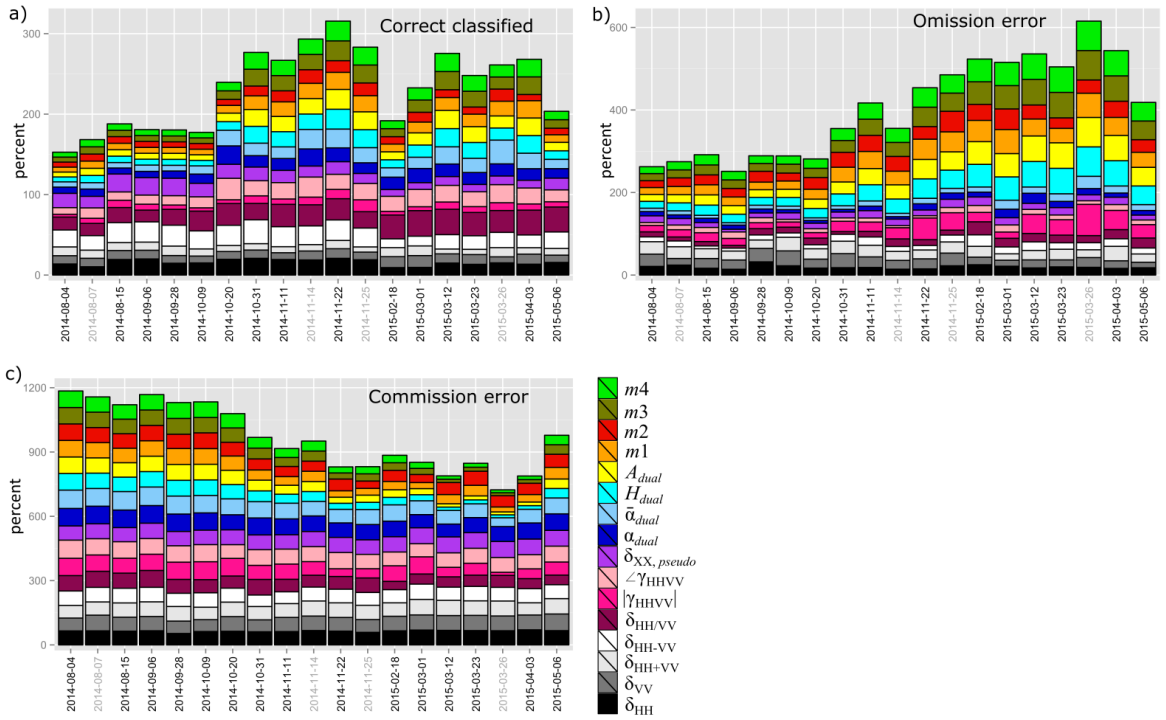

Figure 4-7: Classification accuracies of each observed polarimetric parameter stacked for each date. The proportions within each stack are sorted from the bottom to the top. The correct classified proportion **(a)**; omission error **(b)**; and commission error **(c)** are illustrated seperatedly. The colors of each parameter are the same for all graphs. The labels of the dates are grey for asc images and black for desc images.

In line with the results of Section 4.5.1, there is a significant difference in **Figure 4-7a** between the winter and early spring dates (between 20 October 2014 and 3 April 2015) and the summer and late spring dates (4 August 2014 and 9 October 2014 and on 6 May 2015). The winter and early spring dates have better classification results and the best results are achieved on 22 November 2014. Outliers are, again, 18 February 2014 and 1 March 2014, the dates with (assumed) partial ice cover. A difference between asc images (grey date labels) and desc images (black date labels) is not apparent.

In **Figure 4-7a**, $\delta_{HH/VV}$, δ_{HH-VV}, $\bar{\alpha}_{dual}$, and $\angle\gamma_{HHVV}$ show the best classification results with >25% correctly classified reed areas. The parameter $\delta_{HH/VV}$ achieves the best results, with 32% correctly classified reed area. This result fits with the good separation of the reed mean values from all other classes (**Figure 4-5**). The mean value of α_{dual} was also clearly distinguishable from other classes (**Figure 4-5**), but the RF classification results mainly in low accuracies due to the typically high spatial variability of the parameter (Voormansik et al. 2013), also misclassified as noise in the water area. The $\bar{\alpha}_{dual}$ is not as pronounced as α_{dual}, but it is also less spatially varying and is therefore more suitable for classification. The performances of some parameters vary significantly during the year: δ_{HH-VV} has higher accuracies in summer, $\delta_{HH/VV}$ in winter. The parameters H_{dual}, $\angle\gamma_{HHVV}$, A_{dual}, $m3$, and $m4$ perform better in winter, whereas δ_{HH} and $\delta_{XX,pseudo}$ have a better performance in summer. The different accuracies throughout the year are caused by phenological changes of the reed plants, but also other vegetation classes, and therefore cause greater differences between the mean values of the different classes (**Figure 4-5**).

The graphs of omission and commission error, as well as a visual check of the 304 maps (cf. Supplement 4, Heading 1), show that different parameters have different error behavior: the

intensity parameters have higher commission errors, caused by bright backscatter values around the lake in range directions. Parameters $\overline{\propto}_{dual}$ and $\propto_{dual}$ and $\angle\gamma_{HHVV}$ have high commission errors, mainly caused by misclassified noise in the open water area of the lakes. Additionally, the high spatial variability of $\propto_{dual}$, and also of $\angle\gamma_{HHVV}$, is another source of error. As expected from the comparison of the mean values in Section 4.5.1, H_{dual} and A_{dual}, and consequently also $m1$, $m2$, $m3$ and $m4$, have a high omission error, caused by the confusion of reed with meadows. The same characteristics occur for $|\gamma_{HHVV}|$.

The classification of the single parameter images emphasizes the significant influence of the spatial homogeneity of the parameters on the classification, because a good separation of the mean values from the reed belts and from the main other classes does not automatically come with good classification results for reed. Hence, the high spatial variability of the observed polarimetric parameters is a significant source of error.

4.5.3 RF Classification with Parameter Stacks for One Date

After the analysis of the individual parameters, we now analyze the parameter stacks of each date. **Figure 4-8** presents the correct classified proportion of reed in a stacked way, together with the commission and omission errors of each date. The highest correctly classified proportions (35%–36%) of reed acquisitions were obtained on 14 November 2014, 26 March 2015 (asc images) and 22 November 2014 (desc images). The commission error is mostly over 50%; thus, reed areas are frequently overestimated, and reasons for the overestimation are discussed later in this chapter. On 18 February 2014 and 1 March 2014, the dates with partial ice coverage, the correct classified area is over 30%, but the omission error is high.

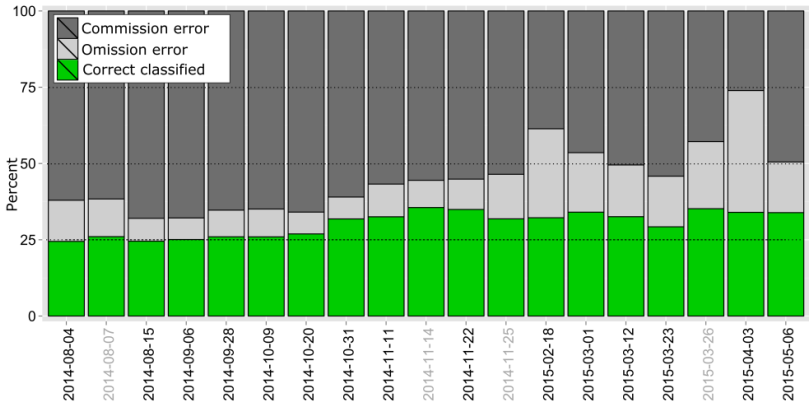

Figure 4-8: Classification accuracies for each acquisition date in percent. Basis for the classification was stacks of all observed polarimetric parameters. For the evaluation the classification result was clipped to the area of Lake Fürstenseer + 50 m buffer. The correct classified proportion is illustrated in green, the commission error (false positive) in dark grey and the omission error (false negative) in light grey. The labels of the dates are grey for asc images and black for desc images.

Figure 4-9 shows the importance of the parameters (concerning the mean decrease in accuracy) for the classification of the reed. A high mean decrease in accuracy means that the parameter is important for the accurate classification of the class "reed". However, it needs to be considered that the RF algorithm aims at the most accurate classification of all classes.

The parameter δ_{HH-VV} is on 15 dates the most important variable, and on the other dates it is one of the five most important variables. Then, $\delta_{XX,pseudo}$ is one of the most important variables in August and September, but it decreases from October onwards in its rank, because other variables ($\delta_{HH/VV}$, $\overline{\propto}_{dual}$, $\propto_{dual}$) become more important. As such, δ_{HH+VV} is, with one

exception, one of the five most important variables in summer. In summer, the dense leaves of the reed cause volume scattering, in addition to double-bounce scattering from the stems. Thus, in summer double-bounce–sensitive parameters are not as valuable in finding reed belts as in winter, and other parameters are chosen by RF classification.

For the 10 ice-free images between 20 October 2014 and 3 April 2015, δ_{HH-VV} is always one of the five most important variables.. δ_{HH} and $\overline{\propto}_{dual}$ are on eight, $\delta_{HH/VV}$ and $\gamma_{HHVV,phase}$ on six, $\delta_{XX,pseudo}$ on four and $\propto_{dual}$ on three dates the most valuable variables. Thus, the variable importance for RF classification is determined by the sensitivity to double-bounce scattering and also by the spatial variability of the parameter: the spatially homogeneous parameters δ_{HH-VV}, $\overline{\propto}_{dual}$ and $\delta_{HH/VV}$ and the spatially variable parameters $\gamma_{HHVV,phase}$, $\propto_{dual}$ reach high importance because they react very well to the double-bounce of reed in winter. However, δ_{HH} and $\delta_{XX,pseudo}$ are spatially homogeneous and partly sensitive to vegetation, and they do not show sensitivity to an increase of double-bounce scattering in the time series.

A high importance of the HV intensity for wetland monitoring was also found in a study by Zhao et al., and in their study, the intensities (HV, HH and VV) were overall more important for accuracy than the quad-polarimetric parameters (Zhao et al. 2014). We conclude that the higher importance of intensity parameters in Zhao et al. and their high importance in our study is caused by the good distinction of many classes via backscattering and backscatter combinations, as well as their spatial homogeneity. However, polarimetric parameters are important, because they are often specific for one scattering type, and thus improve the classification of specific classes (cf., e.g., **Figure 4-5**, $\angle\gamma_{HHVV}$ for the distinction of reed).

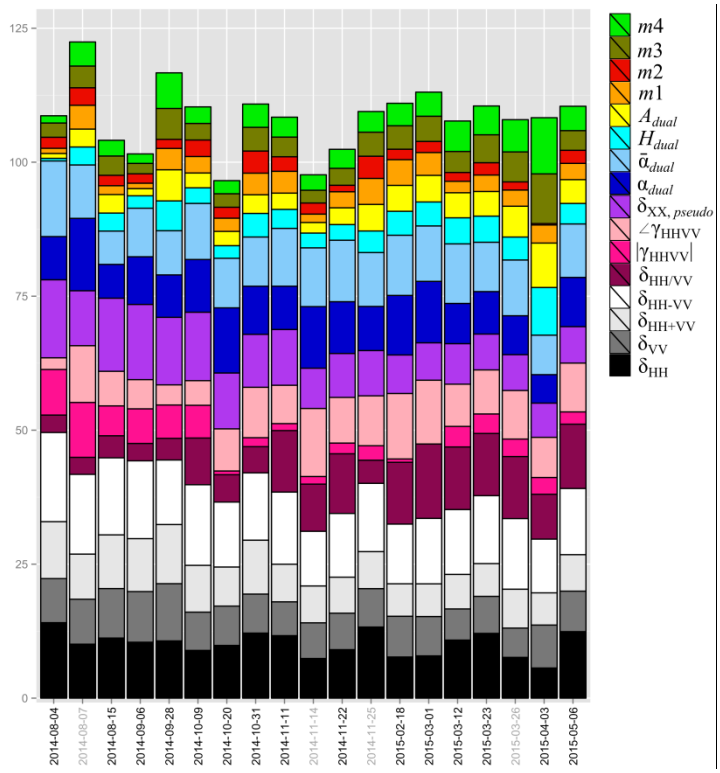

Figure 4-9: Stacked and sorted "mean decrease in accuracy" of the parameters. Basis for the classification were stacks of all parameters. The higher the mean decrease in accuracy, the higher the importance of the variable for classification. The labels of the dates are grey for asc images and black for desc images.

Figure 4-10 and **Figure 4-11** show the RF classification of the four dates, with a desc and an asc image for August and November 2014. The high commission errors (~65%) of the classification result in August are caused by an overestimation of in situ reed areas and false-positive classified reed areas at the shorelines in range directions. Water along with mainly deciduous trees are misclassified as reed. The comparison of the asc and desc images (**Figure 4-10**) reveals that the overestimations of the reed area in comparison to the validation reed area appear generally in the look direction of the sensor (range direction); thus, the classification result of the asc stack goes too far to the east, whereas the result of the desc image reaches too far to the west. The misclassifications of deciduous forest as reed in **Figure 4-10** and **Figure 4-11** are caused by high backscatter values near the shoreline area, similar to the backscatter of reed (cf. **Figure 4-6**), whereas the high commission errors (~60%) of the classification result in November is largely caused by the misclassification of water or deciduous forest located around the reed areas. The overestimation in November is clearly linked to the presence of reed and only locally there are misclassifications related to the sensor look direction. The difference between **Figure 4-10** and **Figure 4-11** is also related to the more prominent double-bounce scattering in winter during the leaf-off season, thus the stronger influence of the double-bounce–sensitive parameters in the classification within this period of the year.

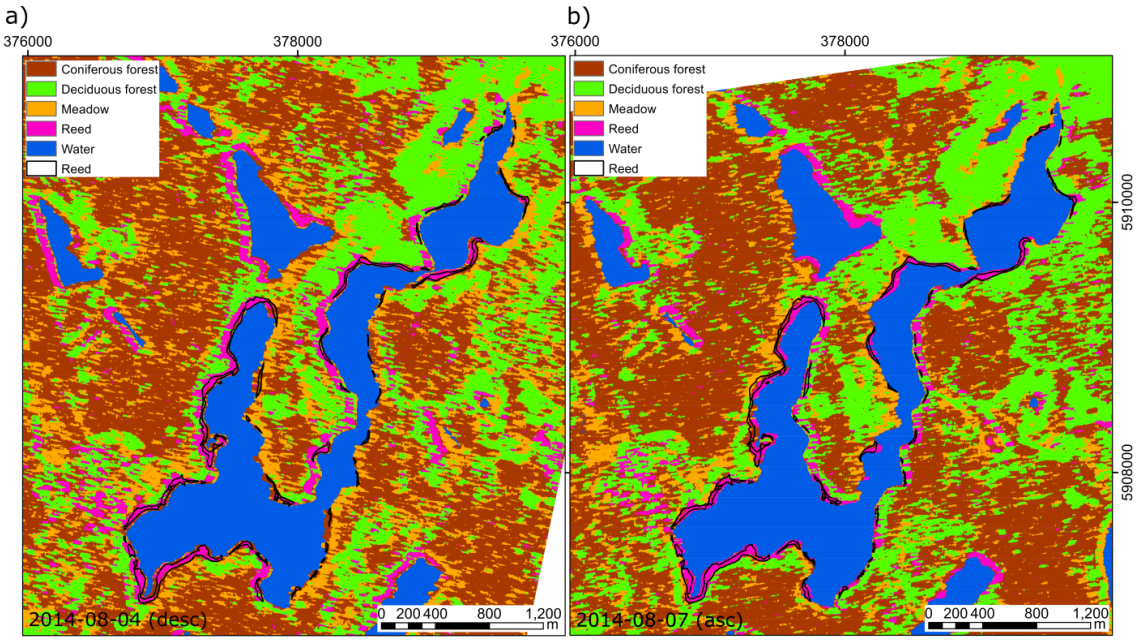

Figure 4-10: RF classification result based on a stack of all parameters on 4 August 2014 **(a)** and on 7 August 2014 **(b)**. The classified reed areas are shown in pink, the validation reed areas are outlined in black. The commission error of reed is very high in the two August images (~65%). The in situ reed areas are overestimated and there are false positive classified reed areas in the desc **(a)** and in the asc **(b)** images at the shorelines in the range direction: On the desc image **(a)** the reed areas are overestimated at western shorelines, in the asc image they are overestimated at the eastern shorelines.

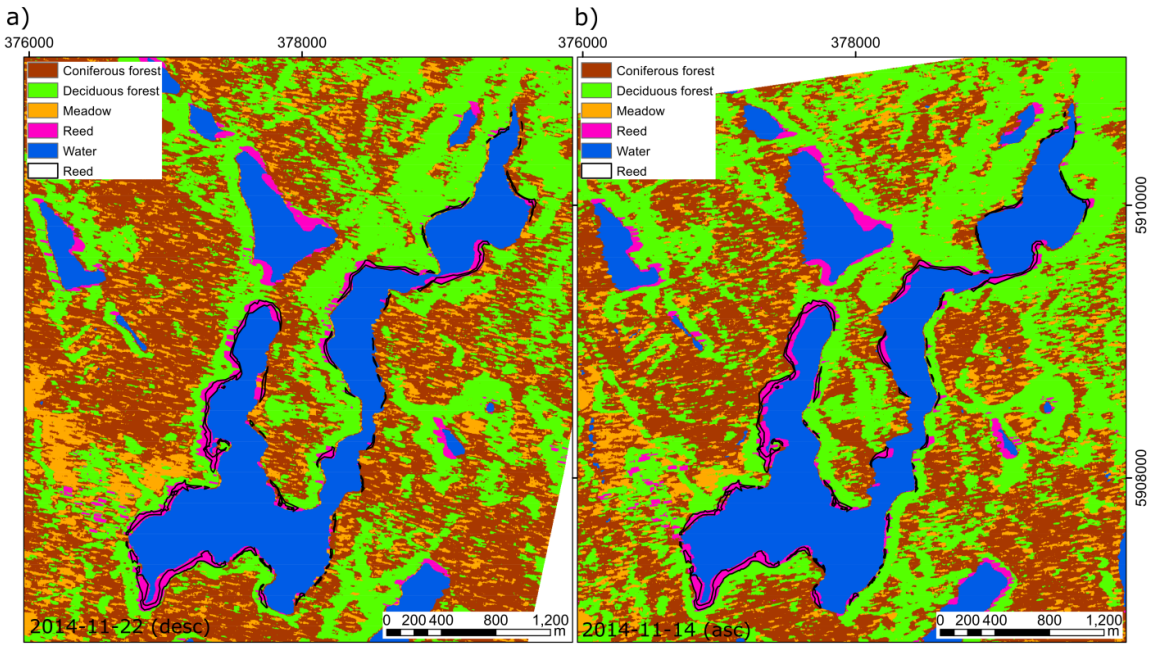

Figure 4-11: RF classification result based on a stack of all parameters on 22 November 2014 **(a)** and on 14 November 2014 **(b)**. The classified reed areas are shown in pink, the validation reed areas are outlined in black. The commission error of reed is still very high in the two November images (~60%). This error is mainly caused by an overestimation of the reed areas.

4.5.4 RF Classification with Multi-Temporal Parameter Stacks

Finally, we tested if the classification accuracy of reed can be improved by using multi-temporal image stacks.

Figure 4-12 illustrated the classification accuracies of the different multi-temporal stacks. All stacks with a combination of asc and desc images perform better than stacks with only desc or only asc images, because it reduces the impact of the looking direction (cf. **Figure 4-10** and **Figure 4-11**). Tests showed that the classification of a multi-temporal stack of asc and desc images has similar (±3% correct classified reed) accuracies as the intersection of the reed areas of the classification results of asc and desc images (cf. Supplement 4, Heading 2). The highest correct classified proportion (45%) is achieved with the multi-temporal stack of ice-free winter images (asc and desc). The corresponding classification is illustrated in **Figure 4-13**. Its confusion matrix is illustrated in **Table 4-4** and the overall accuracy of this classification is 91.90%.

The comparison of **Figure 4-11** and **Figure 4-13** shows that the use of the multi-temporal stack also improves the accuracy of the other classes as compared to single-date classification.

Although, the classification of reed improved through the use of multiple images, the highest correctly classified proportion is only 45%, which is half of the area. For test purposes, we tried a second classification via k-means segmentation. It showed that the k-means classification result of reed is very similar to the one of RF (cf. Supplement 4, Heading 3) and suggests that the error of over 50% is not caused by the choice of the classification method. Another reason potentially leading to a reduced accuracy of the classification may be found in the small number of training points. This might be too few to fully characterize one class. However, tests with five times more training points (150 instead of 30) only led to an accuracy improvement of 1.65%. We explain the high error with various factors:

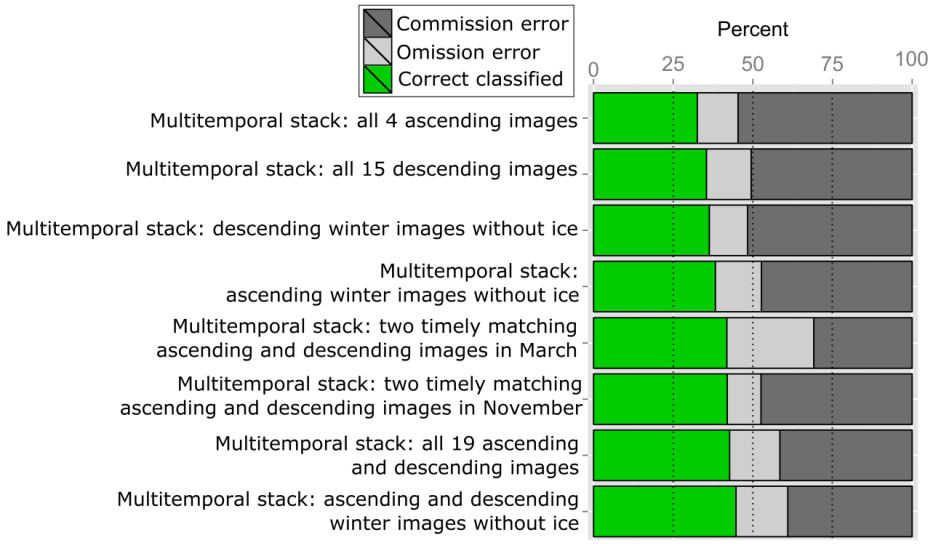

Figure 4-12: Classification accuracies (in percent) of multi-temporal stacks with only asc, only desc images or a combination of both looking directions. For the evalution, the classification result was clipped to the area of Lake Fürstenseer + 50 m buffer. The correct classified proportion is illustrated in green, the commission error (false positive) in dark grey and the omission error (false negative) in light grey.

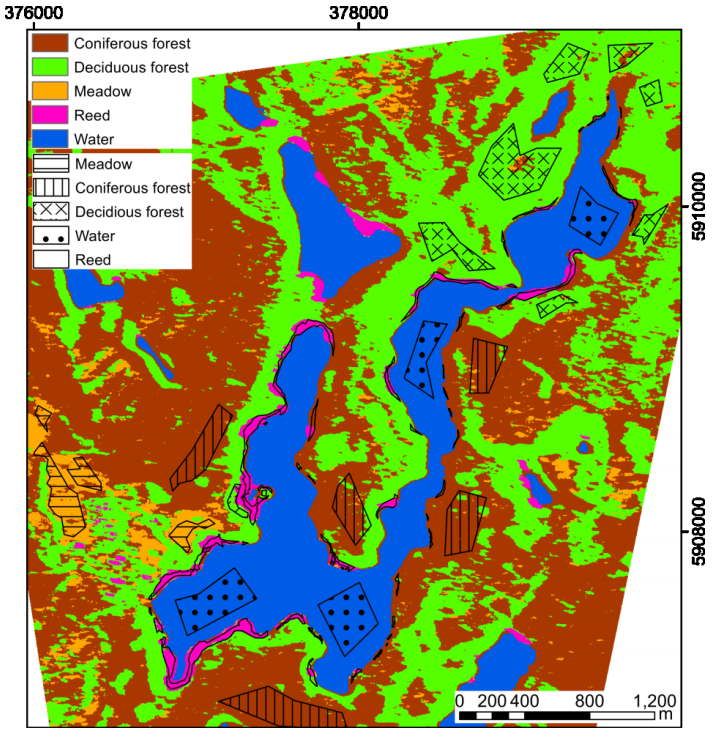

Figure 4-13: Classification result (colors) of the multi-temporal stack of asc and desc winter images (without dates of ice coverage). Overlaid are validation areas (black outlined polygons with different fill pattern) of the five classes: reed, water, meadow, deciduous and coniferous forest.

The reed belts are small and stretched long, sometimes with tree cover, which can lead to a small feature bias. Tree cover might also lead to errors in the manually digitized reed areas that were used for validation. The classification in **Figure 4-13** clearly shows that small reed areas or reed areas with a very small width (<10 m) are not detected using TSX images, but larger and more extended features are. This is also due to the resolution of TSX of 3 m × 3 m after geocoding. Although missed small reed belts are numerous, they have only a small percentage weight for the commission error. The same is valid for the commission error if misclassified

water areas were caused by an expansion of reed areas since 2013. The misclassifications of deciduous forest can be related to the parameter values similar to reed in winter (cf. **Figure 4-5**). Quad-polarimetric images might be beneficial here for improving the distinction with their higher information content. However, the misclassifications could also be caused by spatial deviations between the SAR images and the digital orthophoto. The asc and desc SAR images are acquired with different looking directions and with different incidence angles causing different geocoding challenges. As the comparison of asc and desc images emphasizes, the geocoding of the side-looking SAR is challenging, especially at shoreline areas with a large height difference between high trees and the water surface (Heine et al. 2014). Thus, we think the main sources of errors are spatial inaccuracies due to geocoding.

Table 4-4: Confusion matrix of the random forest classification based on the multi-temporal stack of ice-free winter images (asc and desc). The validation areas used are illustrated in **Figure 4-2**. All numbers represent pixels.

		Predicted by Random Forest				
		Coniferous Forest	**Deciduous Forest**	**Meadow**	**Reed**	**Water**
Actual Class	Coniferous forest	36,807	1527	1503	2528	0
	Deciduous forest	1501	30,931	91	2415	0
	Meadow	453	557	10,597	64	0
	Reed	0	181	0	14,440	0
	Water	0	0	0	247	32,706

4.6 Conclusions

This study investigates the potential of dual-polarimetric TSX data for mapping and monitoring of reed belts: 13 of the 16 calculated parameters (**Table 4-3**) show a significant difference between summer and winter acquisitions caused by the phenology of reed. In summer, the volume scattering of reed belts is high, whereas during the leaf-off season in winter and early spring, double-bounce scattering dominates for the X-band within reed belts. Besides the double-bounce–sensitive parameters ($\delta_{HH/VV}$, $\overline{\propto}_{dual}$, $\propto_{dual}$, and $\angle\gamma_{HHVV}$), also $|\gamma_{HHVV}|$, A_{dual}, H_{dual}, $m1, m2, m3$ and $m4$ reveal seasonal changes for reed in X-band dual-polarimetric SAR data. Changes of the parameters suggest that phenological stages such as the start of leaves growing around the middle of March and the withering and the falling off of leaves starting around October can be monitored as well. However, a more detailed study with a denser time series of TSX images together with a simultaneous in situ documentation of the reed belts and additional measurements, such as the water content of the leaves/stems as well as rain events, is necessary to support this first result. The increase of double-bounce scattering in winter due to the falling-off of leaves enables a better separation of reed and other vegetation (meadow, deciduous and coniferous forest); thus, winter acquisitions (without ice) are preferred for the mapping of reed belts. The five most important parameters for the classification of reed are δ_{HH-VV}, $\overline{\propto}_{dual}$, $\delta_{HH/VV}$, δ_{HH}, and $\angle\gamma_{HHVV}$. Except of δ_{HH}; all these parameters are direct indicators of double-bounce scattering. The $\propto_{dual}$ would be also an appropriate indicator for double-bounce scatting, but it appeared more spatially variable in the analysis than, e.g., $\overline{\propto}_{dual}$. This variability induced classification challenges. Spatial variability seems also to be a problem for $\angle\gamma_{HHVV}$ as a monitoring parameter for reed.

The RF classification is fast, easy to implement, and a preselection of classification parameters is not required because the algorithm automatically selects the best parameters for classification. In the comparison of single-date winter images and a multi-temporal winter stack, the multi-temporal winter stack achieved better results for the classification of reed belts.

The combination of asc and desc images also improved the classification result, as it reduced the influence of the sensor look direction. However, in this study an accuracy of only ~50% correctly classified reed belts was achieved. The overall classification accuracy of all five classes is 91.90%. The following reasons could be identified. Whereas the shorelines with reed areas (>10 m in width) could be detected correctly, the actual areas with reed coverage were significantly overestimated. The main source of error is probably geocoding with spatial inaccuracies. This error could be reduced with better geocoding and additional pre-processing of the SAR data, e.g., an additional co-registration of the SAR images to the digital orthophotos. However, the optimization of the spatial accuracy went beyond the scope of this study. In this study, the focus was on the process of understanding the scattering mechanisms present in reed belts and their exploitation for classification purposes.

Supplements: The following supplementary materials are available online at https://www.mdpi.com/2072-4292/8/7/552/s1. Figure S1: The 16 maps show the classification results of the RF classifier based on the single parameter layers on 22 November 2014. Black outline is the validation reed area. Figure S2: Comparison of the classification results of reed asc and desc winter image stacks (without-ice images). The light blue areas are only classified as reed in the asc stack, the yellow areas only in desc stack. The pink area is the intersection of the reed areas of the classified asc and desc image stacks. Overestimations of the reed area in comparison to the validation reed area (black polygons) appear generally in the look direction of the sensor (range direction). Figure S3: Classification accuracies (in percent) of multi-temporal stacks and intersections of asc and desc classification results. The multi-temporal classification results are based on stacks combining all parameters of different dates. For the intersections of asc and desc images, multi-temporal stacks were classified first and then the intersecting reed area of both looking directions was selected and evaluated. For the evaluation, the classification result was clipped to the area of Lake Fürstenseer + 50 m buffer. The correct classified proportion is illustrated in green, the commission error (false positive) in dark grey and the omission error (false negative) in light grey. Figure S4*:* Reclassified result of the k-means clustering with a multi-temporal stack. The stack consist of the five most valuable parameters in winter (δ_{HH-VV}, $\overline{\propto}_{dual}$, $\delta_{HH/VV}$, δ_{HH}, and $\angle\gamma_{HHVV}$) according to the RF-based ranking of variable importance. The base map is the DOP40 from 2013. Black outlines are the validation reed areas.

Acknowledgments: We would like to thank Peter Stüve for his on-site support and the interesting discussions about the lakes in northeastern Germany. This study was funded by the "Helmholtz Association of German Research Centers Initiative—Networking Fund for funding a Helmholtz Virtual Institute" (VH-VI-415). Satellite imagery was provided by DLR (proposal HYD2636). The investigations were conducted mainly during a research exchange at the Microwaves and Radar Institute of DLR in 2015 under funding of the HGF Alliance HA-310 'Remote Sensing and Earth System Dynamics'.

Author Contributions: Iris Heine developed the methodological framework, performed the analyses, and wrote the article. All authors were involved in the general paper review. Thomas Jagdhuber introduced Iris Heine to polarimetry and its methodologies. He proposed the polarimetric parameters for investigation and supervised the data analyses. He discussed the results and led the path forward during the different development stages of the investigations. Sibylle Itzerott was involved in formulating the research questions and contributing to critical discussions.

Conflicts of Interest: The authors declare no conflict of interest.

5 Long-Term Monitoring of Calcite Precipitation using Multi-Spectral Satellite Imagery

Heine, I., Brauer, A., Heim, B., Itzerott, S., Kasprzak, P., Kienel, U., & Kleinschmit, B. (2017). Monitoring of Calcite Precipitation in Hardwater Lakes with Multi-Spectral Remote Sensing Archives. *Water*, *9*(1), 15*, doi:10.3390/w9010015*.

Received: 4 October 2016 / Revised: 26 November 2016 / Accepted: 13 December 2016 / Published: 3 January 2017

Abstract

Calcite precipitation is a common phenomenon in calcium-rich hardwater lakes during spring and summer, but the number and spatial distribution of lakes with calcite precipitation is unknown. This paper presents a remote sensing based method to observe calcite precipitation over large areas, which are an important prerequisite for a systematic monitoring and evaluation of restoration measurements. We use globally archived satellite remote sensing data for a retrospective systematic assessment of past multi-temporal calcite precipitation events. The database of this study consists of 205 data sets that comprise freely available Landsat and Sentinel 2 data acquired between 1998 and 2015 covering the Northeast German Plain. Calcite precipitation is automatically identified using the green spectra and the metric BGR area, the triangular area between the blue, green and red reflectance value. The validation is based on field measurements of $CaCO_3$ concentrations at three selected lakes, Feldberger Haussee, Breiter Luzin and Schmaler Luzin. The classification accuracy (0.88) is highest for calcite concentrations ≥0.7 mg/L. False negative results are caused by the choice of a conservative classification threshold. False positive results can be explained by already increased calcite concentrations. We successfully transferred the developed method to 21 other hardwater lakes in Northeast Germany. The average duration of lakes with regular calcite precipitation is 37 days. The frequency of calcite precipitation reaches from single time detections up to detections nearly every year. False negative classification results and gaps in Landsat time series reduce the accuracy of frequency and duration monitoring, but in future the image density will increase by acquisitions of Sentinel-2a (and 2b). Our study tested successfully the transfer of the classification approach to Sentinel-2 images. Our study shows that 15 of the 24 lakes have at least one phase of calcite precipitation and all events occur between May and September. At the lakes Schmaler Luzin and Feldberger Haussee, we illustrated the influence of ecological restoration measures aiming at nutrient reduction in the lake water on calcite precipitation. Our study emphasizes the high variance of calcite precipitation in hardwater lakes: each lake has to be monitored individually, which is feasible using Landsat and Sentinel-2 time series.

5.1 Introduction

Calcite (or calcium carbonate) precipitation events in lakes are a common phenomenon in calcium-rich hardwater lakes. They are also described as “whiting”, “milky water phenomenon” or “seasonal clouding” (Strong & Eadie 1978; Thiemann & Koschel 2001; Koschel et al. 1987). The complex process of calcite precipitation has been intensively studied (Weidemann et al. 1985; Proft 1984; Koschel et al. 1987; Koschel et al. 1997; Kempke et al. 2008; Hamilton et al. 2009; Kelts & Hsü 1978; Kronberg 1985; Fan 2014; Dittrich & Koschel 2002; Brunskill 1969; Gal et al. 1996; House 1987; Koschel 1997; Stabel 1986; Strong & Eadie 1978; Thompson 1990; Romero et al. 2006).

Calcite precipitation is the consequence of the supersaturation of the lake water with respect to calcite. Principally, two possible mechanisms can lead to supersaturation: (1) physical-chemical, through seasonal temperature effects on the solubility of carbon dioxide and calcite (i.e., the solubility of calcite decreases with increasing temperature); and (2) biogenic induction through assimilation of carbon dioxide by plankton blooms of photosynthesizing algae and bacteria in the phototrophic upper water column (Thiemann & Koschel 2001; Kelts & Hsü 1978) with impact on the carbonate equilibria of the water, which varies with pH, alkalinity, and total dissolved carbon. Aside from that, cells of algae and cyanobacteria can act as surface catalysts for calcite precipitation well before supersaturation is reached (Stabel 1986; Thompson 1990). In line with that, calcite precipitation events in lakes are recorded after peak

phytoplankton blooms (Koschel 1997; Stabel 1986; Brunskill 1969). Calcite precipitation was found to intensify in relation with the trophic state (based on the concentration of dissolved P) from oligotrophic towards weakly eutrophic conditions, but became weaker towards hypereutrophic/polytrophic conditions because of the inhibition of the precipitation by increased P concentration (Koschel 1997; House 1987; Gal et al. 1996).

The Northeast German Plain is a region dominated by many hardwater lakes (Koschel et al. 1987). Studies concerning these lakes showed that calcite precipitation is an important variable impacting on both the water quality and the ecology of these ecosystems (Proft 1984; Koschel et al. 1987; Koschel et al. 1997). Calcite precipitation reduces the nutrient concentration and, consequently, phytoplankton productivity and therefore is a natural protection mechanism of hardwater lakes against eutrophication (Proft 1984; Koschel et al. 1987). The reduction of nutrient concentration ("self-cleaning") is caused by the co-precipitation of soluble inorganic phosphorus and the flocculation of particles containing phosphorus, which are eventually transported to the sediment at the bottom of a respective lake (Koschel et al. 1987; De Vicente et al. 2006). In times of climate change, also the storage of CO_2 in the sediments might be an important factor. A study at lake Breiter Luzin in Mecklenburg-Vorpommern, Germany, specified sedimentation rates of 300 g $CaCO_3/m^2$/day (Koschel et al. 1987) and Koschel et al. estimate a calcite production and sedimentation of 150–900 ton/km^2 per year for seven lakes in Mecklenburg-Vorpommern (Koschel et al. 1997). Whereas precipitated calcite resuspends to some extent, the majority sinks to the lake bottom (Dittrich & Koschel 2002) and is, without mixing, accumulated in calcite layers. Those calcite sediments have been used for the reconstruction of past precipitation events in other regions (Romero-Viana et al. 2008; De Vicente et al. 2006). However, although the ecological importance of calcite precipitation is recognized, neither the number of lakes with calcite precipitation in the Northeast German Plain nor worldwide is known, because only individual lakes are monitored regularly (Proft 1984; Koschel et al. 1987; Koschel et al. 1997). Additionally, calcite precipitation varies both within and among lakes: intensity, frequency and duration of calcite precipitation events can vary from year to year (Koschel et al. 1997). Thus, calcite precipitation events may easily be missed during one-time observations or short-term monitoring of lakes. Here, remote sensing archives of optical satellite missions such as Landsat or Sentinel offer a great potential for a satellite-based long-term monitoring of lakes with high temporal and spatial resolution and for the synoptic monitoring of a larger region like the Northeast German Plain.

However, only few studies have used remote sensing for the monitoring of calcite precipitation. In southwest Florida and Great Bahama Bank whitings have been monitored using medium-resolution MODIS imagery (Long et al. 2014; Dierssen et al. 2008) and photographs from the NASA manned spacecraft program (Robbins et al. 1997). Two studies have been conducted on the spatial distribution of calcite precipitation within large lakes (the Great Lakes, and Lake Constance) with Landsat imagery (Strong & Eadie 1978; Pulvermüller et al. 1995) and Thiemann and Koschel classified calcite precipitation in 21 lakes in the Northeast German Plain using one hyperspectral airborne data set (Thiemann & Koschel 2001).

In our study, we exploit the multi-spectral long-term remote sensing archive of Landsat and test the applicability for the recently started Sentinel-2 for the long-term monitoring of calcite precipitation in the Northeast German Plain. In this context, the objectives of this study are:

- To develop a robust automated remote sensing-based approach for retrospective long-term multi-temporal calcite precipitation monitoring based on a multi-sensor remote sensing time series.

- To characterize calcite precipitation in terms of frequency and duration to deepen the process understanding.

5.2 Study Area

The lakes of the Northeast German Plain were formed during the late Weichselian glaciation (Koschel et al. 1987). We selected three representative study areas: Feldberg Lake District, the Klocksin Lake Chain, and Rheinsberg Lake Region which are located in the federal states of Mecklenburg-Western Pomerania and Brandenburg in Germany (**Figure 5-1**). These regions are covered by the Landsat acquisition tiles 193023 and 194023. We chose three lakes with regular in situ measurements in the Feldberg Lake District (Feldberger Haussee, Breiter Luzin, and Schmaler Luzin) for the development of a calcite precipitation classification approach and its validation. Then, the applicability has been tested on the other two regions, the Klocksin Lake Chain and Rheinsberg Lake Region.

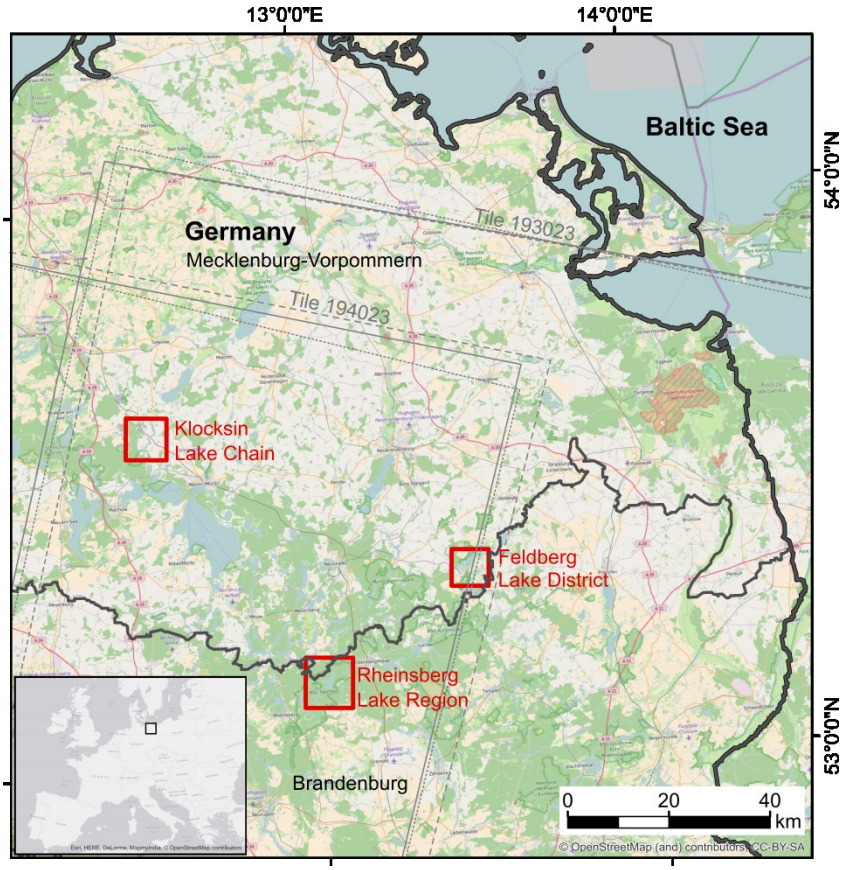

Figure 5-1: Study area with three selected regions: Feldberg Lake District, the Klocksin Lake Chain, and Rheinsberg Lake Region. The gray lines illustrate the Landsat footprints of the acquisition tiles 193023 and 194023. The gray dashed line shows the footprint of Landsat 5, the solid gray line shows the footprint of Landsat 7, the dotted gray line the footprint of Landsat 8.

5.2.1 Feldberg Lake District

Figure 5-2 shows the Feldberg Lake District with its well-researched lakes: Feldberger Haussee (FH), Breiter Luzin (BL) and Schmaler Luzin (SL). All three lakes are hardwater lakes with regular in situ measurements since 1998. The topography, morphology and limnological characteristics of the lakes are summarized in **Table 5-1**.

FH potentially used to be a mesotrophic lake, but nutrient input by sewage (phosphorus and nitrogen) and surface runoff since the 1960s until 1980 caused strong eutrophication (Koschel et al. 1981). In 1980, the sewage discharge was stopped decreasing the external nutrient loading of the lake by 90%. However, because of the tremendous amounts of nutrients (especially phosphorus) stored in the sediment the lake did not respond with a substantial improvement of water quality for decades (Kasprzak et al. 2003). Therefore, phosphorus inactivation by treating the lake with poly-aluminum chloride as a flocculation agent was implemented in April 2011. The following drastic reduction of average total phosphorus concentration in the mixed layer from 0.060 mg/L (2006–2010) to 0.017 mg/L (2011–2015) resulted in an improvement of the trophic status from eutrophic to mesotrophic (Leibniz-Institute of Freshwater Ecology & Inland Fisheries (IGB) 2016; Nixdorf et al. 2013).

BL is located immediately downstream of FH. BL is known for calcite precipitation (Koschel et al. 1987; Proft 1984; Koschel et al. 1997). Its LAWA trophic index of 1997 is mesotrophic, and its potential natural trophy is oligotrophic (Nixdorf et al. 2004a). An unpublished study of the Leibniz-Institute of Freshwater Ecology & Inland Fisheries (IGB) classified BL in 2015 as mesotrophic.

SL is potentially oligotrophic, but nutrient input lead to a moderate eutrophic state since the 1950s (Nixdorf et al. 2004a). Since the 1980s the catchment was restored by reducing the nutrient input from the catchment (Nixdorf et al. 2004a), but only a lake restoration in 1996/1997 reduced the eutrophication significantly (Dittrich & Koschel 2002). The lake was restored by artificially triggering calcite precipitation through in-depth aeration and the addition of $Ca(OH)_2$ in the hypolimnion which caused a significant decrease of total phosphorus content (Nixdorf et al. 2004a). SL is classified as mesotrophic since 1995, with oligotrophic phases (Bachor et al. 2006; Nixdorf et al. 2004a).

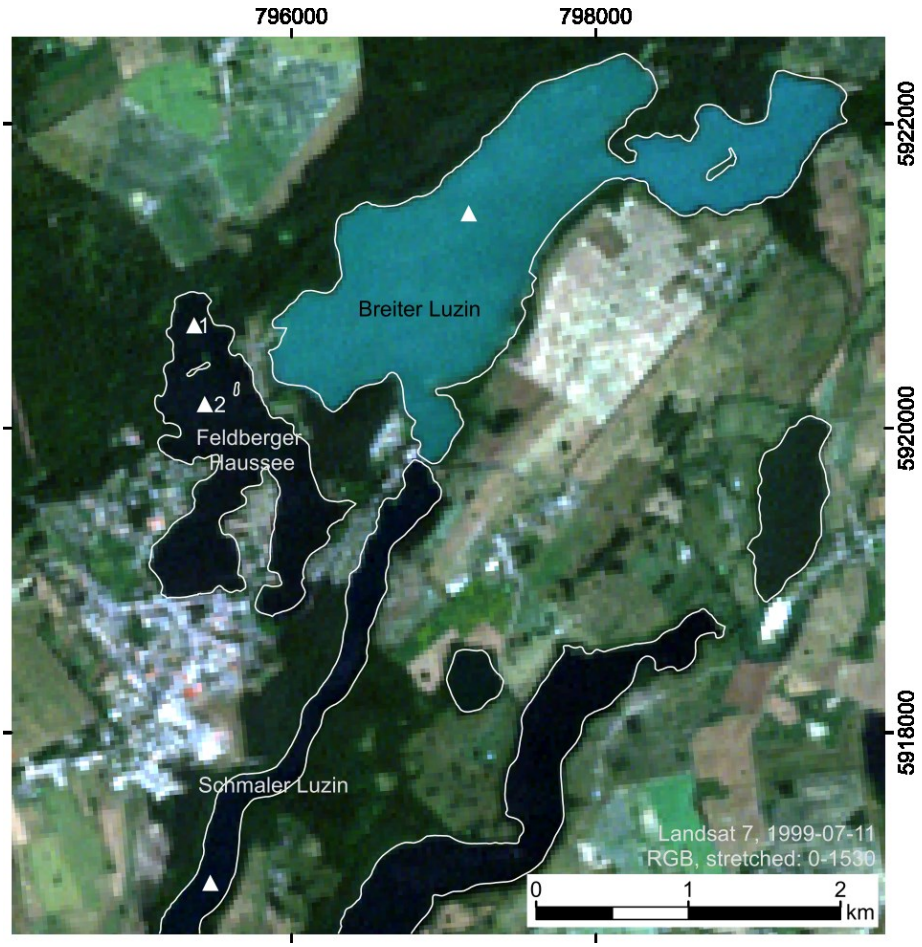

Figure 5-2: Study area of the Feldberg Lake District on 11 July 1999 (Landsat 7, RGB quasi-true color) with Feldberger Haussee (FH), Breiter Luzin (BL) and Schmaler Luzin (SL). BL has a distinct turquoise color whereas FH and SL are dark blue. All lakes are framed with white lines. The sampling sites are illustrated as white triangles.

For FH, regular calcite precipitation events are documented since 1985. Nevertheless, their intensity (i.e., calcite concentration) clearly increased since the year 2006 and remained high ever since. That was the period when FH finally approached mesotrophic conditions. Koschel (1987) concluded that the intensity of calcite precipitation may be highest in moderately nutrient-enriched hardwater lakes, because photosynthesis is high enough to shift the lime-carbonic acid equilibrium to the carbonate side, while the impact of factors to impair the growth of calcite crystals is minimal (Koschel et al. 1987).

Table 5-1: Overview of morphology and limnological characteristics of the lakes FH, BL, and SL. The limnological characterization is based on the Bund/Länder-Arbeitsgemeinschaft Wasser (LAWA) trophic index.

Lake	Area (km^2) (BKG 2011)	Maximum Depth (m) (Nixdorf et al. 2004a)	Mean Depth (m) (Nixdorf et al. 2004a)	LAWA 1997 (Nixdorf et al. 2004a)	Trophic Reference State (Nixdorf et al. 2004a)
FH	1.29	12.5	4.9	Eutrophic	Mesotrophic
BL	3.41	58.3	22.3	Mesotrophic	Oligotrophic
SL (without Carwitzer Becken)	0.84	22.5	12.2	Mesotrophic	Oligotrophic

5.2.2 Klocksin Lake Chain

The second case study area is the Klocksin Lake Chain with Flacher See (FS), Tiefer See (TS), Hofsee (HS), and Bergsee (BS) as shown in **Figure 5-3**. There are no regular in situ measurements of $CaCO_3$ concentrations in the lakes, but measurements in 1996 in TS, FS, and BG show high Ca concentrations (Nixdorf et al. 2004a). The sediment record of TS shows calcite layers in each year and in some years, even two sub layers can be detected during thin section inspection. The calcite layers of the years 1998, 1999, 2003, 2004, 2006, 2007, 2011, and 2012 are thinner than those of the other years in the period considered in this study (Kienel et al. 2013). This hints at shorter or less intensive calcite precipitation, but dissolution of calcite particles on their way through the water column may also play a role. Analyses of sediment trap material (since 2012) indicate peak calcite precipitation either in May/June and August/September or centered in July (Kienel et al. 2017). The known topography, morphology and limnological characteristics of the lakes are summarized in **Table 5-2**.

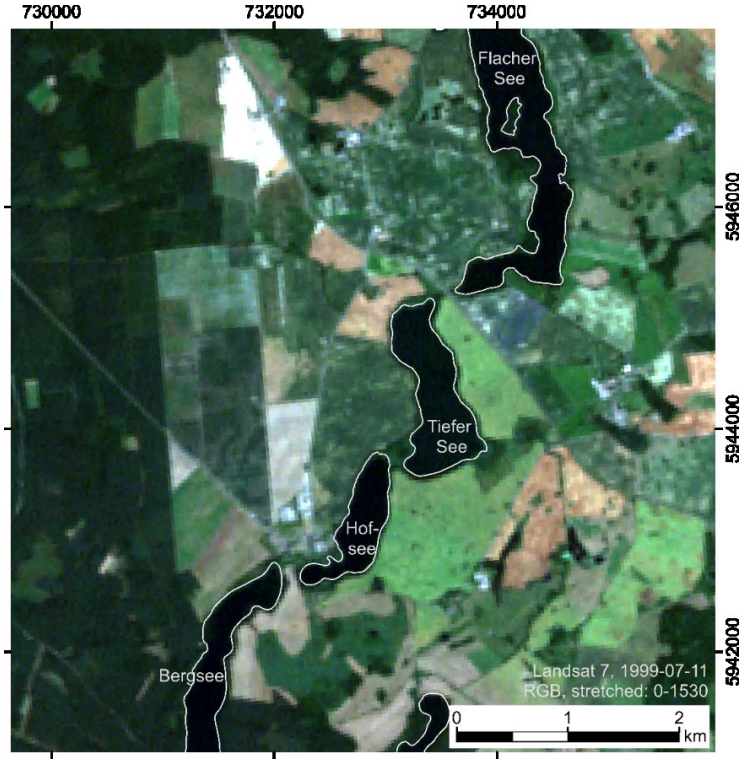

Figure 5-3: Study area of the Klocksin Lake Chain with Flacher See, Tiefer See, Hofsee and Bergsee on 11 July 1999 (Landsat 7, quasi-true color RGB). All lakes appear dark and are framed with white lines.

Table 5-2: Overview of morphology and limnological characteristics of the lakes in the Klocksin Lake Chain.

Lake	Area (km^2) (BKG 2011)	Maximum Depth (m) (Nixdorf et al. 2004a; Müller 2012)	Mean Depth (m)	LAWA 1996 (Nixdorf et al. 2004a; Spieß 2004)	Trophic Reference State (Nixdorf et al. 2004a)
FS	1.25	31.9	9.7	Mesotrophic	Mesotrophic
TS	0.68	62.5	18.5	Mesotrophic	Oligotrophic
HS	0.39	27	-	Mesotrophic	-
BS	0.57	15.0	6.4	Mesotrophic	Mesotrophic

5.2.3 Rheinsberg Lake Region

The third test area is the Rheinsberg Lake Region, with Stechlinsee as the largest lake (**Figure 5-4**). The LAWA trophic state (1998) of Stechlinsee is oligotrophic, which corresponds to the trophic reference state, and the lake has a low phytoplankton biomass (Nixdorf et al. 2004b). Stechlinsee is known for calcite precipitation (Proft 1984; Koschel et al. 1997), and there was an extraordinary intensive event in July 2011 (Leibniz-Institute of Freshwater Ecology & Inland Fisheries (IGB) 2016).

The northern and southern parts of Nehmitzsee have similar chemical and trophic characteristics: the LAWA trophic state in 1997 classify both parts as mesotrophic, which corresponds to the trophic reference state of the lake. Measurements between March and October 2011 showed constant low phytoplankton of ≤0.5 mm^3/L biovolume.

The topography, morphology and limnological characteristics of the lakes, if known, are summarized in **Table 5-3**.

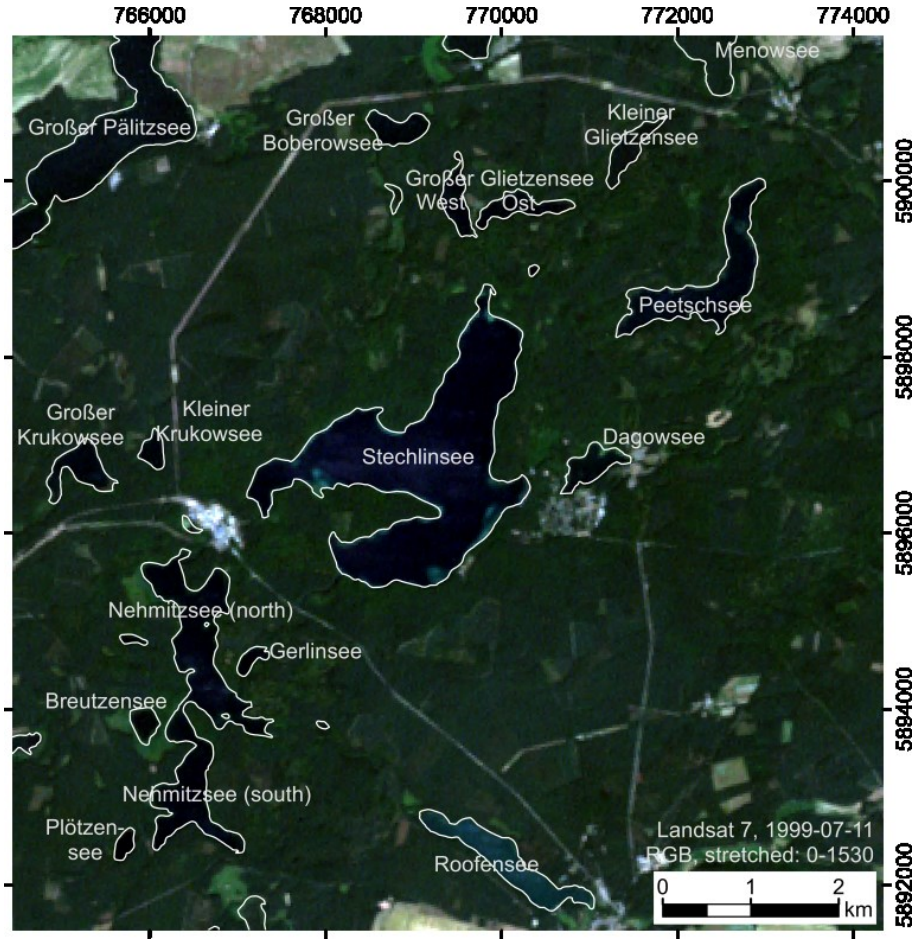

Figure 5-4: Study area of the Rheinsberg Lake Region on 11 July 1999 (Landsat 7, quasi-true color RGB). All lakes appear dark and are framed with white lines.

Table 5-3: Overview of morphology and limnological characteristics of the lakes in Rheinsberg Lake Region.

Lake	Area (km^2) (BKG 2011)	Maximum Depth (m) (Müller 2012; Nixdorf et al. 2004b; Mietz et al. 1995; Koschel 1998)	Mean Depth (m) (Nixdorf et al. 2004b; Mietz et al. 1995)	LAWA 1998 (Nixdorf et al. 2004b; Koschel 1998; Kabus & Wiehle 2013; Wöbbecke & Büro enviteam 2008)	Trophic Reference State (Nixdorf et al. 2004b)
Breutzensee	0.10	3.5	-	Eutrophic	-
Dagowsee	0.20	9.5	5.0	Eutrophic	-
Gerlinsee	0.06	5.5	-	Mesotrophic	-
Großer Glietzensee (Ost)	0.20	13.0	-	Weakly eutrophic	-
Großer Krukowsee	0.25	13.0	-	Mesotrophic	-
Kleiner Krukowsee	0.08	8.5	-	Mesotrophic	-
Nehmitzsee (north)	1.00	18.6	6.79	Mesotrophic	Mesotrophic
Nehmitzsee (south)	0.64	18.6	6.79	Mesotrophic	Mesotrophic
Peetschsee	0.89	21,0	-	Mesotrophic	-
Plötzensee	0.06	9.0	-	Weakly eutrophic	-
Großer Glietzensee (West)	0.16	10.0	-	Weakly eutrophic	-
Großer Boberowsee	0.18	9.5	-	Eutrophic	-
Großer Pälitzsee	2.49	30	-	Eutrophic	Mesotrophic
Kleiner Glietzensee	0.17	4.0	-	Eutrophic	-
Menowsee	0.35	4.5	-	Mesotrophic	-
Roofensee	0.56	19.0	-	Weakly eutrophic	-
Stechlinsee	4.14	68.0	22.8	Oligotrophic	Oligotrophic

5.3 Materials and Methods

5.3.1 Satellite Data and In Situ Data Archive

The multi-temporal satellite remote sensing database comprises data from Landsat 5, 7 and 8 and for 2015 also Sentinel-2 data. The database covers a time span from 1998 to 2015. The repeat cycle of the Landsat satellites is 16 days, the one of Sentinel-2 10 days, but cloud coverage reduces the number of suitable satellite images. The Landsat archives cannot provide a continuous temporal coverage. However, during the years 2003 to 2006 and from 2013 on, high temporal coverage is provided due to the temporal overlap of at least 2 satellite missions. Thus, in this study, the number of suitable Landsat acquisitions varies between 2 and 20 data sets per year with time gaps between 1 day and 160 days between the acquisitions.

In **Table 5-4**, we list the bandwidths of the satellites Landsat 5, 7, 8, and Sentinel 2. The visible bands are blue, green, and red and the infrared wavelengths are near-infrared (NIR) and shortwave-infrared (SWIR) 1 and 2. The bands do not overlay perfectly and there are variations in the bandwidths between the sensors. With exception of the NIR band, the old sensors have

broader bandwidths: for example, the blue bandwidth ranges between 70 nm to 65 nm, the green between 80 nm and 35 nm and the red between 60 nm and 30 nm.

Table 5-4: Overview of the bandwidth of the satellites Landsat 5, 7, 8, and Sentinel-2.

	Band Width of Band (nm)						
Satellite	Blue	Green	Red	NIR	SWIR 1	SWIR 2	Reference
Landsat 5	450–520	520–600	630–690	760–900	1550–1750	2080–2350	(USGS 2011)
Landsat 7	450–515	525–605	630–690	775–900	1550–1750	2090–2350	(Irons et al. 2012)
Landsat 8	450–515	525–600	630–680	845–885	1560–1660	2100–2300	(Irons et al. 2012)
Sentinel-2	458–523	543–578	650–680	785–900	1565–1655	2100–2280	(Drusch et al. 2012)

The Feldberg Lake District region is covered by 200 Landsat images (60 Landsat 5, 115 Landsat 7, 25 Landsat 8; tiles 193023 and 194023) and by two Sentinel-2 images in 2015. The Klocksin Lake Chain and Rheinsberg Lake Region are covered by additional three Landsat images (one Landsat 7 and two Landsat 8 images, all on tile 194023). The data archive is illustrated in **Figure 5-5**.

All the data sets were obtained in the form of orthorectified standard data products to reduce preprocessing efforts. The Landsat images are delivered by U.S. Geological Survey (USGS) as surface reflectance products (including atmospheric correction) (U.S. Department of the Interior & U.S. Geological Survey 2016). The Sentinel-2 satellite images of region Feldberg Lake District were provided by ESA in processing level L1C (European Union & European Space Agency (ESA) for Earth observation 2016). We did the further preprocessing (resampling and atmospheric correction) with sen2cor (version 2.2.1) and Sentinel-2 Toolbox (version 3.0) provided by ESA (European Space Agency (ESA) for Earth observation 2016a; European Space Agency (ESA) for Earth observation 2016b). The spatial resolution of the data sets ranges from 30 m for the Landsat sensors to 10 m for the Sentinel 2 sensors.

As not all lakes are completely cloud-free, the further preprocessing included the cloud and cloud shadow masking. If not noted differently, all processing was implemented and performed in the free software R (version 3.2.2). The clouds and cloud shadow were removed based on the cloud and cloud shadow classifications that are provided with the data. The cloud and cloud shadow masks of Landsat mask generously, thus, at the Feldberg Lake District, we only use the cloud mask with a high confidence and check for cloud shadows manually to keep the density of the time series in accordance to the in situ data. The Sentinel-2 cloud shadow classification fails over lakes, thus, the images have to be checked manually.

Since 1998, there are regular water quality measurements at FH, BL and SL by the Leibniz-Institute of Freshwater Ecology & Inland Fisheries. Besides precipitated $CaCO_3$, Chlorophyll a (*chl-a*), temperature, pH, alkalinity, and ion concentrations (NO_3^-, SiO_3^{2-}, Cl^-, SO_4^{2-}, Na^+, K^+, Mg^{2+}, and Ca^{2+}) are measured. Based on those parameters, the $CaCO_3$ saturation index (SI) was calculated according to Debye-Hückel (Hepperl & Krienitz 1997) using "WinIAP—Software for the Calculation of Ion Activities and Calcite Saturation Index"(Hepperle 2016). The SI shows, depending on the trophic state and the season, if calcite precipitation is possible:

the SI threshold for calcite precipitation in oligotrophic lakes is <5 and in mesotrophic lakes between 5 and 15. In eutrophic lakes, SI values of >15 without calcite precipitation are possible (Koschel et al. 1997). In spring, the thresholds are generally higher than in summer due to the inhibition of calcite precipitation by phosphate (Koschel et al. 1997).

The locations of measurement stations in the lakes are marked in **Figure 5-2**. In FH, $CaCO_3$ is always measured in the northern part of the lake (**Figure 5-2**, Δ1) as the other parameters before 2011. Since 2011, the other parameters are measured at another location further south (**Figure 5-2**, Δ2). All parameters are measured in 0–5 m water depth and multiple measurements versus depth are averaged.

On 68 days there are water quality measurements contemporary to Landsat images, but not at every time all three lakes are sampled. "Contemporary" in this study means that the Landsat images are not acquired more than 3 days before and not more than 5 days after the in situ measurement. These thresholds are set under the assumption that calcite precipitation events appear more suddenly than they vanish.

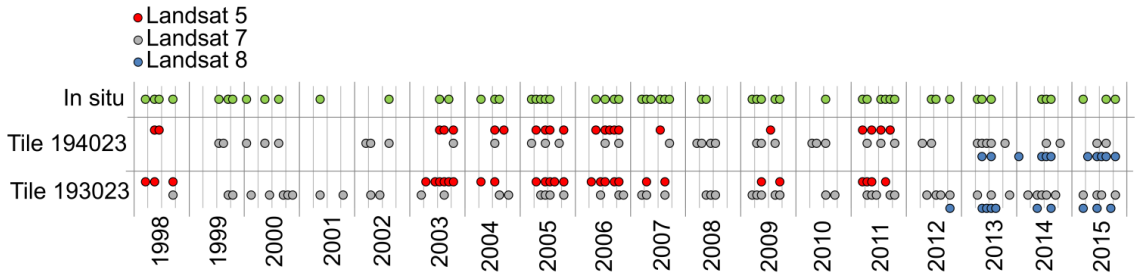

Figure 5-5: Time series of Landsat acquisitions (1998–2015), sorted by tile (cf. **Figure 5-1**) and sensor. "In situ" marks the date of in situ measurements at Feldberg Lake District.

5.3.2 Classification of Calcite Precipitation Using Satellite Imagery

The processing chain is of the classification is illustrated in **Figure 5-6**.

Input data are the preprocessed Landsat and Sentinel images. We manually digitized regions of interest (ROI) for the extraction of lake spectra. For the three lakes of Feldberg Lake District we choose up to 13 ROI per lakes to avoid gaps due to clouds, cloud shadow and the edge of the tile 194023 to keep the density of the satellite data. Thus, those ROI are unevenly distributed in the lakes. At the other lakes we selected one ROI per lake and the ROI are located in the centers of the lakes. All ROI are selected with distance to islands or shallow water areas, which could influence the reflectance spectra. Depending on the lakes, the ROI are differently sized and shaped.

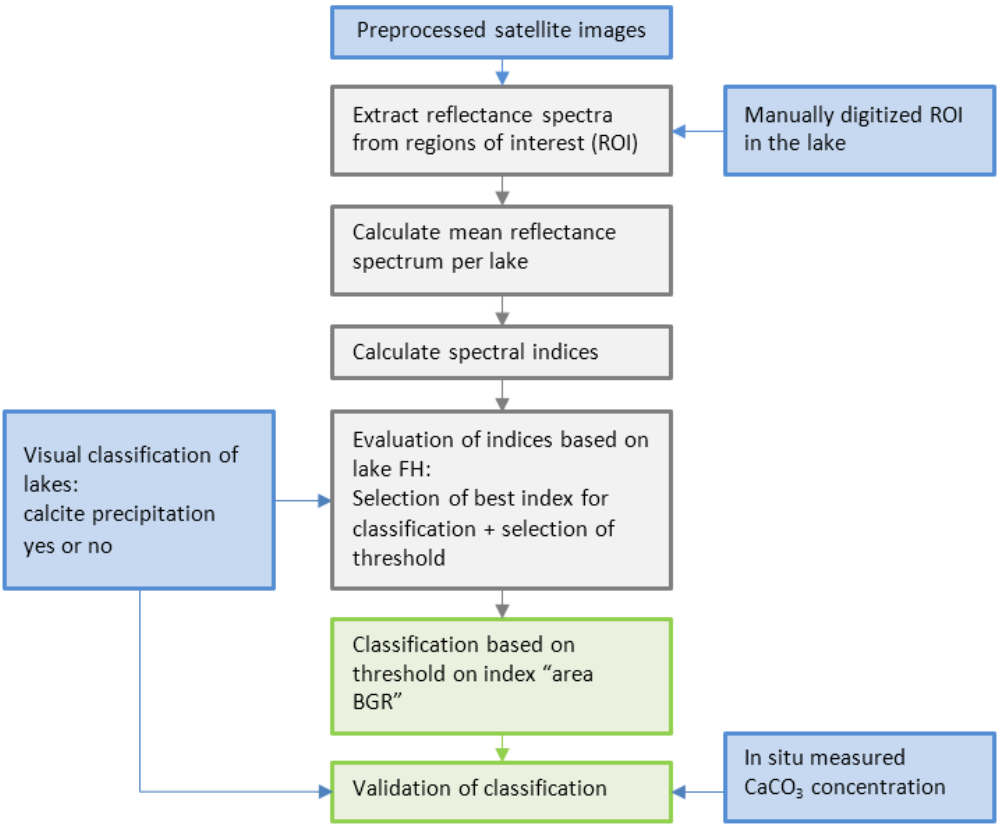

Figure 5-6: Flowchart of the processing steps of Landsat surface reflectance data for the monitoring of calcite precipitation. The blue boxes contain input data, the gray boxes illustrate the development of the robust classification and the green boxes illustrate the classification and validation.

Based on the ROI we extracted the reflectance values of the satellite images. The reflectance values are evaluated: if the standard deviation in any band is high (>100) or if more than 10% of the ROI consist of not applicable (NA) values, the next ROI is tested or, if no next ROI is available, the reflectance values of the lake are set NA. Then, the extracted reflectance values of each band are averaged to get the mean reflectance spectrum of the lake.

The next step is the calculation and evaluation of the spectral indices based on the extracted mean reflectance. The spectral indices are described in **Table 5-5**.

Table 5-5: Overview of the spectral indices.

Index Name	Abbreviation	Formula	Reference
Ratio of the reflectance (Ref.) values of band red and green	Ratio RG	$\text{Ratio RG} = \frac{\text{Ref}_{\text{red}} - \text{Ref}_{\text{green}}}{\text{Ref}_{\text{red}} + \text{Ref}_{\text{green}}}$	(Tucker 1979)
Normalized difference water index	NDWI	$\text{NDWI} = \frac{\text{Ref}_{\text{green}} - \text{Ref}_{\text{NIR}}}{\text{Ref}_{\text{green}} + \text{Ref}_{\text{NIR}}}$	(McFeeters 1996)
Modified normalized difference water index	MNDWI	$\text{MNDWI} = \frac{\text{Ref}_{\text{green}} - \text{Ref(SWIR1)}}{\text{Ref}_{\text{green}} + \text{Ref(SWIR1)}}$	(Xu 2006)
"Area Blue Green Red" as the triangular area in the reflectance values of blue, green and red (using the central wavelength of Landsat 8 for all sensors)	Area BGR	$\text{Area BGR} = 0.5(482 * \text{Ref}_{\text{green}} + 560 * \text{Ref}_{\text{red}} + 655 * \text{Ref}_{\text{blue}} - 560 * \text{Ref}_{\text{blue}} - 655 * \text{Ref}_{\text{green}} - 480 * \text{Ref}_{\text{red}})$	(Braden 1986)
Normalized absorption feature depth of red	NAFD	$\text{NAFD} = 1 - (\frac{\text{Ref}_{\text{red}}}{\text{Ref}_{\text{continumline\_of\_red}}} / \text{Area}_{\text{green,red,NIR}})$	(Curran et al. 2001)
Ratio of bands of an unknown lake and a dark reference lake e.g., lake SL	Ratio RL	$\text{Ratio RL} = \frac{\text{Ref}_{\text{unknown\_lake}} - \text{Ref}_{\text{reference\_lake}}}{\text{Ref}_{\text{unknown\_lake}} + \text{Ref}_{\text{reference\_lake}}}$	This work

The evaluation of the spectral indices is based on the visual classification of "good quality images" of lake FH: we checked visually the image quality and marked images with a low quality. Reasons for low image quality are large cloud coverage, ice and low incidence angles of the sun in winter. Of the 200 images of Feldberg Lake District 114 have a good image quality. Then, greenish-turquoise colored lakes in a quasi-true color Red Green Blue (RGB) image are classified visually as lakes with calcite precipitation. Finally, each index is separated in two groups, dates with and without calcite precipitation, and the groups are compared.

The validation of the satellite-derived classification results of FH, BL and SL is based on the in situ measured $CaCO_3$ concentrations using confusion matrices. Therefore, the dates with in situ $CaCO_3$ concentrations were classified as "calcite precipitation" and "no calcite precipitation". Additionally, we validate the results based on a visual classification in quasi-true color images. At Feldberg Lake District the visual classification itself is validated using the in situ $CaCO_3$ concentrations. In the other two lake regions without in situ measurements, the satellite-derived calcite precipitation events are only validated with the visual classification in quasi-true color images. Instead of confusion matrices for every lake, we summarize all results of each region and show each region in one confusion matrix. The confusion matrices compare true results, in this study the grouped in situ measurements or visual classification results, with predicted results, in this study the satellite-derived classification results. True positive (TP) and true negative (TN) are accurate classification results, where predicted and true results are equal. False positive (FP) are dates in which the true results show no calcite precipitation, but the satellite-derived calcite precipitation shows calcite precipitation. It means the classification overestimated the number of calcite precipitation. False negative (FN) are dates in which the true results shows calcite precipitation, but the satellite-derived calcite precipitation shows no calcite precipitation. It means the classification underestimated the number of calcite precipitation. The accuracy is calculated by dividing the sum of TP and TN by the sum of TP, TN, FP and FN.

Relevant for the validation with confusion matrices is the number of Landsat images with contemporary in situ measurements, the threshold for the grouping of the in situ $CaCO_3$

concentrations on dates with “calcite precipitation” and “no calcite precipitation”, and the relation of dates with calcite precipitation to dates without. FH has 46 dates with Landsat images and field measurements and their $CaCO_3$ concentration ranges from 0 to 3.52 mg/L. BL has 48 dates with Landsat images and field measurements. The $CaCO_3$ concentration ranges from 0.05 to 2.96 mg/L. SL has 31 dates with Landsat images and field measurements and their $CaCO_3$ concentration is always low between 0 and 0.47 mg/L. The number of dates with calcite precipitation varies depending on the $CaCO_3$ that is considered as calcite precipitation. A previous study found that without optical tools, calcite precipitation in the open water is only visible during high calcite concentrations with >1 mg/L (Koschel et al. 1987). Thus, first, we consider all dates with $CaCO_3$ concentration ≥1 mg/L as dates with calcite precipitation. Then, we lower the threshold by 0.1 mg/L steps down to ≥0.5 $CaCO_3$ mg/L, because we suspect a higher sensitivity of the satellite images to calcite precipitation.

As algal blooms are potentially a source for misclassification, we also analyze the lake spectra with high chl-a concentration ≥20 µg/L. The occurrence of considerable algal blooms are related to an chl-a concentration of at least 20 µg/L (Thiemann & Kaufmann 2000).

5.4 Results

5.4.1 In Situ Measurements

The time series of $CaCO_3$ and SI of the three lakes is illustrated in **Figure 5-7**. FH had low $CaCO_3$ concentrations of <1 mg/L before 2006, but exceeded 1 mg/L ten times between 2006 and 2015. BL’s $CaCO_3$ concentrations exceeded 1 mg/L twelve times between 1998 and 2015 and SL remained always <0.5 mg/L $CaCO_3$. The SI values of the three lakes range between 0.7 and 13.7 between 2000 and 2015. Based on their SI values and trophic states, in SL and BL calcite precipitation could have occurred during the monitoring period. The trophic state of FH changes during the monitoring period: before 2011 with eutrophic condition no calcite precipitation is possible, after 2011 the SI values indicate possible calcite precipitation events. The chl-a concentration of SL ranges from 1 to 10 µg/L (average: 3 µg/L) and of BL from 1 to 18 µg/L (average: 3 µg/L). FH has high variation in its chl-a concentration: between 1998 and 2002 its chl-a concentration ranges from 4 to 21 µg/L (average: 9 µg/L), then between 2005 and 28 March 2011 it ranges from 5 to 53 µg/L (average: 19 µg/L). After this chl-a maximum, the concentration declines again to 2–17 µg/L (average: 8 µg/L). On twelve dates FH’s chl-a concentration exceeds 20 µg/L and thereof, five dates exceed 30 µg/L (23 March 2005, 19 April 2005, 30 May 2008, 30 March 2009, and 28 March 2011).

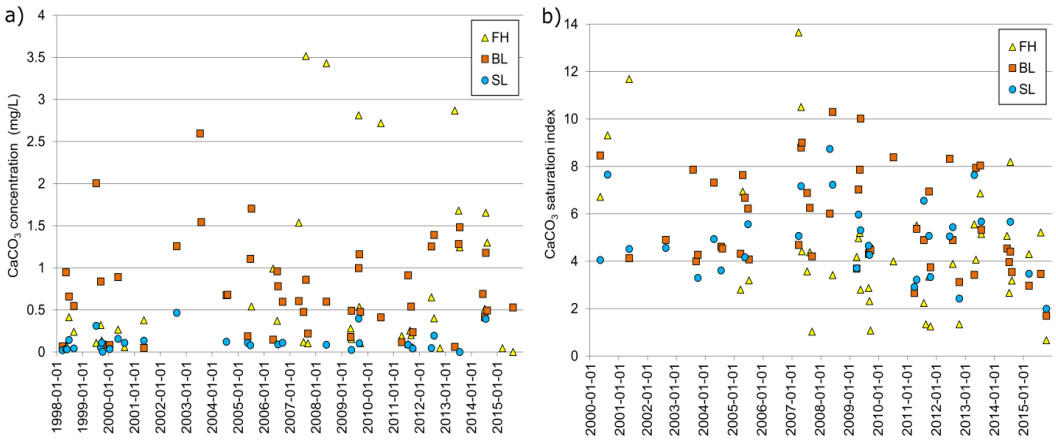

Figure 5-7: Time series (1998 to 2015) of **(a)** in situ measured CaCO3 concentrations (mg/L); and **(b)** the calculated $CaCO_3$ saturation index (SI) in FH, BL, SL lakes.

5.4.2 Calcite Precipitation Visible in Lake Reflectance

The methodological developments aim at the automated multi-temporal mapping of calcite precipitation based on satellite remote sensing time series data. Thus, the approach needs to be able to identify calcite precipitation occurring at different times during the analyzed time span, whereas the determination of the time of calcite precipitation occurrence depends on the length of the time period between two subsequent images contained in the remote sensing time series database.

Figure 5-8 compares two quasi-true color Landsat RGB images, one with (Leibniz-Institute of Freshwater Ecology & Inland Fisheries (IGB) 2016) and the other without calcite precipitation, with photos from contemporary field campaigns. **Figure 5-9** shows a time series of five Landsat RGB images in which BL has different $CaCO_3$ concentrations. The according mean reflectance spectra and the calculation of Area BGR are shown in **Figure 5-10**. On 12 July 1999 the $CaCO_3$ concentration of BL was very high with 2.00 mg/L and the lake is opaque turquoise colored. Until 15 September 1999 the $CaCO_3$ concentrations decreased to 0.84 mg/L, but in the Landsat image the color change is still clearly visible. On 11 October 1999 the calcite precipitation diminished and $CaCO_3$ concentration was very low with 0.09 mg/L and BL appears dark again. The only exceptions are lakes with separated lake basins with narrow passages: On 13 September 1999 the northeastern basin of BL is darker than the main basin (**Figure 5-9d**).

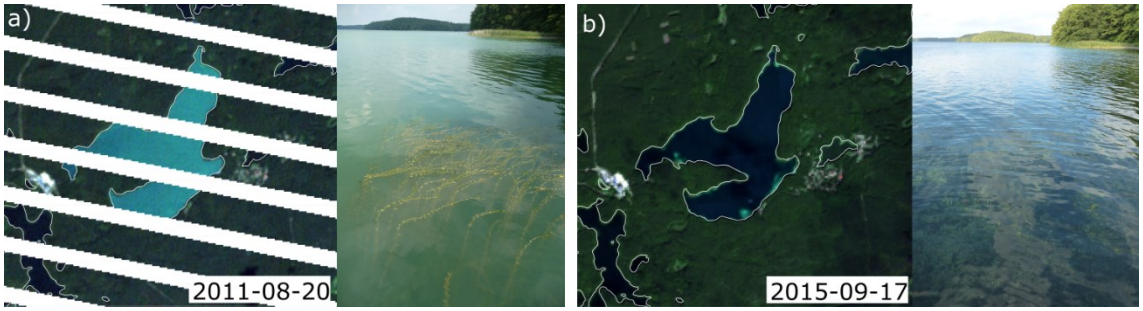

Figure 5-8: Two quasi-true color Landsat RGB of Stechlinsee with photos showing the water surface taken from a boat: **(a)** August 2011, showing the lake with calcite precipitation; and **(b)** September 2015, with clear water. The photos were taken: **(a)** two days before; and **(b)** nine days after the Landsat acquisition.

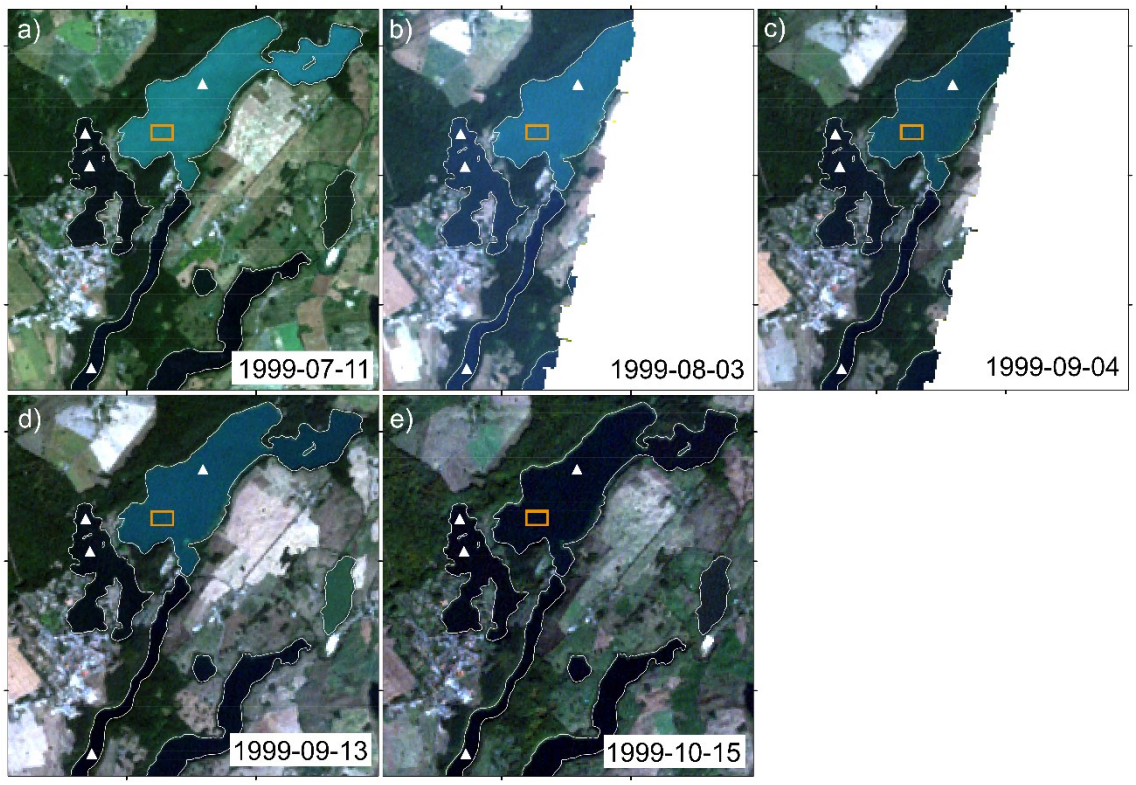

Figure 5-9: Quasi-true color RGB Landsat 7 images of the Feldberg Lake District. The extent is the same as in **Figure 5-2**. All lakes are framed with lines and the positions of in situ measurements are marked with white triangles. The orange rectangle shows the ROI that was used for the extraction of the reflectance spectra. BL is turquoise colored on 11 July 1999 **(a)** due to calcite precipitation. In the following, calcite precipitation diminishes from 3 August 1999 to 13 September 1999 **(b–d)**, and on 15 October 1999 **(e)** BL appears dark again.

The precipitated $CaCO_3$ particles cause a decrease in Secchi depth and an increase of the reflectance (Weidemann et al. 1985; Thiemann & Koschel 2001). According to Thiemann and Koschel the additive effect of calcite precipitation is uniform in the visible (RGB) and near-infrared wavelength range, so that spectral characteristic like absorption bands and reflection maxima are kept (Thiemann & Koschel 2001). **Figure 5-10** illustrates the enhanced reflectance values mainly between blue and NIR caused by calcite precipitation. However, the increase varies by wavelength: the green band shows the strongest increase and has the maximum reflectance values. The reference reflectance spectrum without calcite precipitation on 15 October 1999 has low reflectance values with a maximum blue band. Even though the reflectance spectra of calcite precipitation show higher NIR and SWIR reflectance, an analysis above 800 nm is not recommended as the absorption of clear water superimposes the effect of water components (Thiemann & Koschel 2001; Fan 2014; Strong & Eadie 1978; Pulvermüller et al. 1995). **Figure 5-11** illustrates the variation of lake reflectance spectra with and without calcite precipitation. In the boxplots all mean reflectance spectra of good quality images of BL, SL and FH are combined. With low quality images, the ranges would be even higher. In **Figure 5-11** the mean reflectance values of NIR, SWIR 1, and SWIR 2 do not indicate regular increase of the reflectance, as it could be suspected by the selected reflectance spectra in **Figure 5-10**.

There are twelve dates with high chl-a concentration ≥20 µg/L at FH. Of the twelve dates with high chl-a concentration, only two show a green color: on 12 April 2005 FH appears greenish in the quasi-true color RGB Landsat 12 April 2005 and on 1 June 2008 FH appears green bright. However, 1 June 2008 has in addition to its high chl-a concentration a calcite precipitation event with a high $CaCO_3$ concentration of 3.4 mg/L. The two lake spectra of FH with

greenish/green color are characterized by a steeper increase from blue to green reflectance and a (small) peak in green. The reflectance values of red and NIR are equally high.

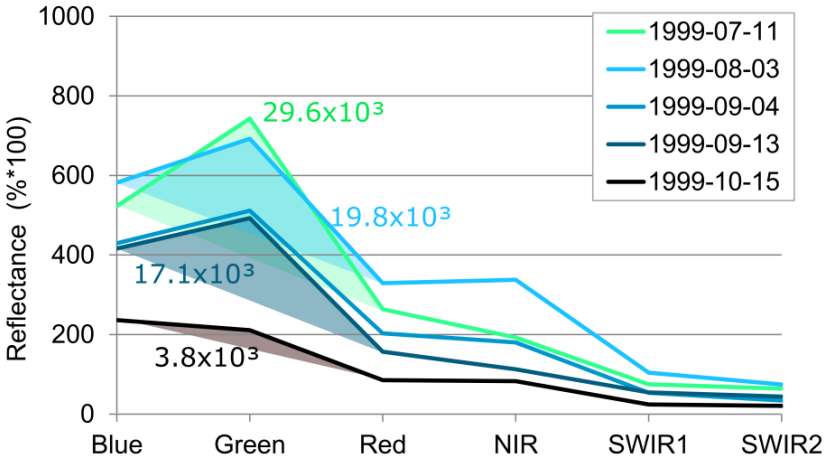

Figure 5-10: Reflectance spectra of BL with calcite precipitation (11 July 1999), diminishing calcite precipitation (3 August 1999 to 13 September 1999), and without calcite precipitation (15 October 1999). The ROI that has been used for the extraction and calculation of the mean reflectance spectra of BL is marked in **Figure 5-7**. The transparent triangles and colored numbers illustrate the "Area BGR".

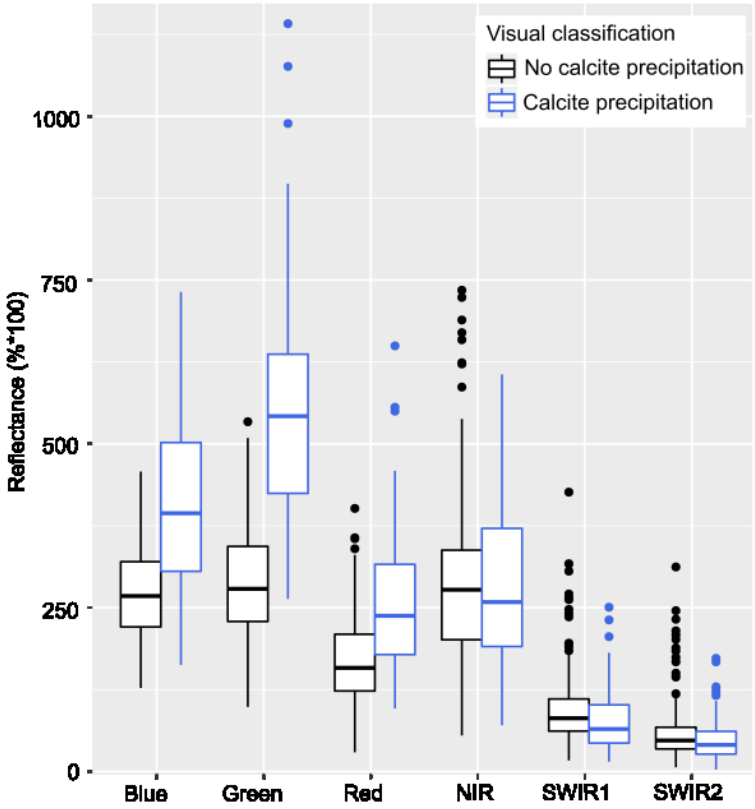

Figure 5-11: Reflectance values in all spectral bands of Breiter Luzin, Schmaler Luzin and Feldberger Haussee of good quality images. All three lakes are visually classified as turquoise (calcite precipitation) or dark (no calcite precipitation).

5.4.3 Best Performing Spectral Indices

The evaluation of the green reflectance and the spatial indices of FH is illustrated in **Figure 5-12**. Area BGR has clearly the best distinction between the two cases with a 74% increase

from 3rd quantile of "no calcite precipitation" to the 1st quantile of the "yes calcite precipitation" boxplot. The next best is the reflectance of green band with 19% increase. We selected a conservative threshold 13 × 10^3 as the maximum value of dates without calcite precipitation of Area BGR.

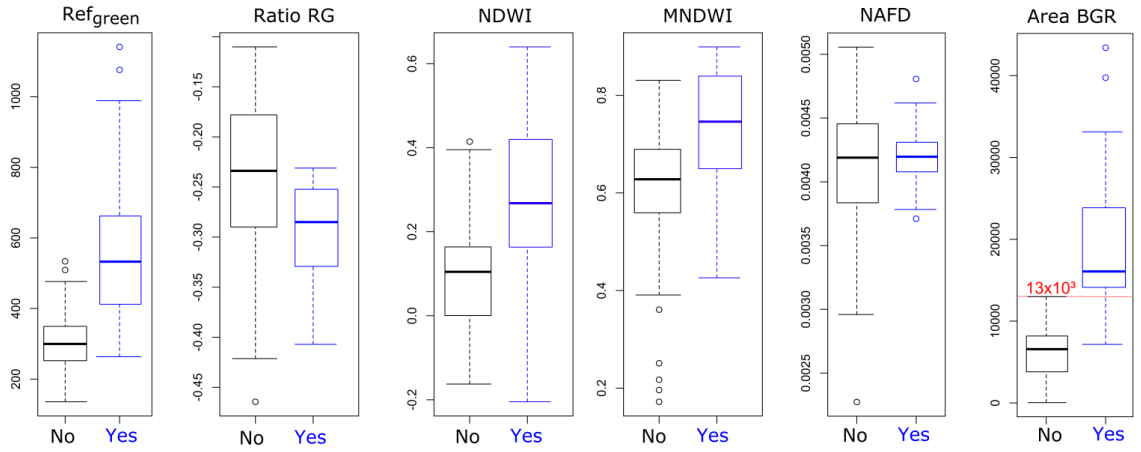

Figure 5-12: Boxplots of the reflectance of green and the indices of FH of good quality images. The indices are separated into dates with calcite precipitation ("Yes") and without calcite precipitation ("No") based on the visual classification of FH. Index "Area BGR" has the best separation of the two classes: the red line marks the conservative threshold 13 × 103 as the maximum value of dates without calcite precipitation.

The calculation of Ratio RL based on SL failed as soon as no reflectance values of the lake could be extracted, because the area of the lake was masked out in the satellite images due to cloud coverage. It was also not possible to derive a universal reference spectrum, because of the variation of reflectance values of SL. **Figure 5-13** illustrates the variation of the mean spectra of SL, grouped by the satellites. There are large variations within the bands, especially in NIR. Additionally, the reflectance values between the satellites vary: between blue and NIR, Landsat 8 has significantly lower reflectance values than Landsat 5, and the reflectance values of Landsat 7 range between the two other satellites.

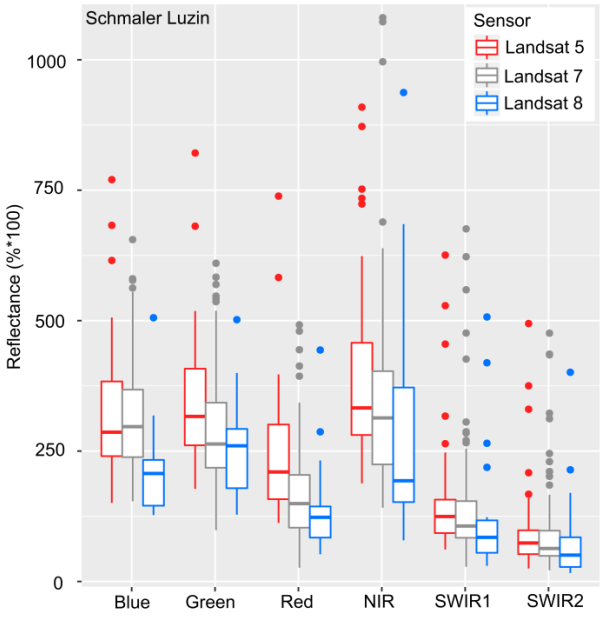

Figure 5-13: Variation of the mean lake spectra of lake SL between 1998 and 2015. The spectra are grouped by the Landsat satellites.

5.4.4 Validation of Landsat-Derived Calcite Precipitation

The satellite-derived calcite precipitation of each region was validated using confusion matrices. **Table 5-6** illustrated the number of accurate classification (TP and TF) and misclassified (FN and FP) results at Feldberg Lake District in comparison to in situ measurements of $CaCO_3$ concentration. The classification accuracy depends on the choice of threshold in $CaCO_3$ concentration: the higher the $CaCO_3$ threshold is set, the higher is the number of FP results and the smaller is the number of FN results. The best accuracy of 0.88 has the comparison with the ≥0.7 mg/L $CaCO_3$. In that case, FN is six (three at FH and three at BL) and the number of FP is nine (all at BL). The nine false positive dates have (slightly) increased $CaCO_3$ concentrations between 0.41 and 0.69 mg/L.

Table 5-6: Confusion matrices of Landsat-derived calcite precipitation with in situ measurements at Feldberg Lake District.

$CaCO_3$ Concentration (mg/L)	TP	TN	FN	FP	Sum	Accuracy
≥1	84	21	4	16	125	0.84
≥0.9	82	24	6	13	125	0.848
≥0.8	82	26	6	11	125	0.864
≥0.7	82	28	6	9	125	0.88
≥0.6	78	31	10	6	125	0.872
≥0.5	71	33	17	4	125	0.832

The accuracy of the visual classification is 0.85 using the threshold ≥0.7 mg/L $CaCO_3$: the sum is 124, with 75 TP, 31 TN, three FN and 16 FP results.

Table 5-7 illustrates the accuracies of Feldberg Lake District, Klocksin Lake Chain and Rheinsberg Lake Region using confusion matrices with visual classifications. The accuracy in the Feldberg Lake District is high with 0.94, but with 28 FN and four FP classification results. The FN results occur at all three lakes (FH: 14, BL: 9, and SL: 5), the FN results only at FH (3) and BL (1). The accuracy in the Klocksin Lake Chain is very high with 0.99, with only two FP (at FS) and two FN classification results (at FS and HS). The accuracy in Rheinsberg Lake Region is also high with 0.97; however, there are 54 false negative results. The FN results are two times at Breutzensee and kleiner Glietzensee, four times at Dagowsee and Großer Boberowsee, six times at Stechlinsee, eight times at Großer Pälitzsee and Roofensee, and 20 times at Menowsee. Even though several calcite precipitation events are missed, the lakes are still classified as lakes with calcite precipitation at other dates during our monitoring period. Extraordinary is the bright green color of Kleiner Glietzensee in March 2014 in the quasi-true color Landsat. Those two dates have been classified as calcite precipitation visually and automatically via Area BGR, but there is no in situ data as evidence available.

Table 5-7: Confusion matrices of Landsat-derived calcite precipitation with visual classifications at Feldberg Lake District, Klocksin Lake Chain, and Rheinsberg Lake Region.

Region	TP	TN	FN	FP	Sum	Accuracy
Feldberg Lake District	429	115	28	4	576	0.94
Klocksin Lake Chain	408	29	2	2	441	0.99
Rheinsberg Lake Region	1862	52	54	0	1968	0.97

5.4.5 Frequency and Duration of Landsat-Derived Calcite Precipitation

Based on the Landsat classification results, we analyzed the frequency and duration of calcite precipitation. The results for each region are illustrated in **Figure 5-14**. A table that lists the classification results of all lakes and dates can be found in the Supplement 5 (Table A1).

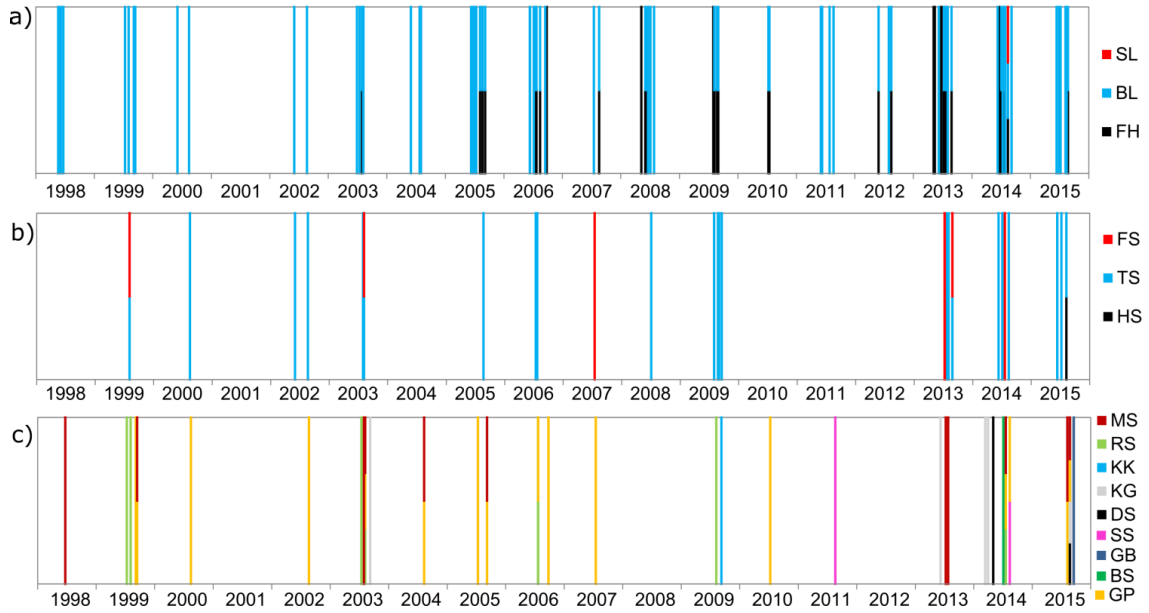

Figure 5-14: Frequency and duration of Landsat-derived calcite precipitation events at the study areas (1998–2015, cf. Supplement 5, Table A1). Images with calcite precipitation are illustrated as bars. **(a)** The Feldberg Lake District with FH, BL, and SL; **(b)** the Klocksin Lake Chain with Flacher See (FS), Tiefer See (TS), and Hofsee (HS); and **(c)** the Rheinsberg Lake Region with Menowsee (MS), Roofensee (RS), Kleiner Krukowsee (KK), Kleiner Glietzensee (KG), Dagowsee (DS), Stechlinsee (SS), Großer Boberowsee (GB), Breutzensee (BS) and Großer Paelitzersee (GP). When more than one lake shows calcite precipitation at the same date, the bars of the lakes are stacked.

Feldberg Lake District

In all lakes in Feldberg Lake District calcite precipitation events are detected (**Figure 5-14a**). All events occur between May and end of September. In FH regular calcite precipitation first occurred in 2005. Between 2005 and 2010 FH had regular calcite precipitation events. In 2011 no calcite precipitation occurred, but in the following three years regular calcite precipitation reoccurred. In 2015, there was only a single calcite precipitation event. BL has calcite precipitation every year except in 2001, but this year only had two Landsat acquisitions on 13 May 2001 and 20 October 2001. At SL one event was detected on the Landsat image on 13 August 2014.

For the calculation of durations, we excluded events which are only detected in one Landsat image, so called “single events”. The maximum duration at FH is then 32 days, with an average duration of 24 days (standard deviation: 11 days). The maximum duration at BL is then 96 days, with an average duration of 57 days (standard deviation: 26 days). An example for a single event is FH in 2013: calcite precipitation was classified on 30 July 2003, but the acquisitions 16 days earlier and 16 days later both show a dark lake without calcite precipitation. This Landsat-derived classification results is equal to the visual classification. Generally, FH and BL show “start–stop–new–start–stop” temporal pattern: Acquisitions with Landsat-derived calcite precipitation are interrupted by acquisition without calcite precipitation, in 2013 in FH, and 2014 for both lakes. However, the visual classification differs

from the Landsat-derived "start–stop–new–start–stop" at FH in 2014: The two of the five dates at FH between 4 July 2014 and 13 August 2014 that are classified as dates without calcite precipitation are classified visually as calcite precipitation and as bad quality images.

Klocksin Lake Chain

In three of the four lakes of the Klocksin Lake Chain, calcite precipitation events are detected (**Figure 5-14b**). At BS no calcite precipitation events were derived from the Landsat-images in the monitoring period. At HS one event was classified on 7 August 2015.

For FS calcite precipitation events are detected on individual Landsat images in 1999, 2003, 2007 and 2014. In 2013 there are three consecutive Landsat-derived events on 8 July 2013, 9 July 2013, and 48 days later, on 26 August 2013. TS shows the most frequent calcite precipitation events (in 11 of the 18 monitored years), whereas sediment analyses show either one or two thinner calcite layers every year. The selection of events in at least two consecutive acquisitions leaves seven years with long-lasting calcite precipitation events: the maximum duration is 56 days, the average is 31 days (standard deviation: 17 days).

Rheinsberg Lake Region

In nine of the 17 lakes in Rheinsberg Lake Region calcite precipitation is derived from Landsat images (**Figure 5-14c**). The lakes without calcite precipitation are Peetschsee, Großer Glietzensee (Ost), Großer Glietzensee (West), Großer Krukowsee, Nehmitzsee (north and south), Plötzensee, and Gerlinsee. In each one image Großer Boberowsee and Kleiner Krukowsee are classified as lakes with calcite precipitaion. Breutzensee, Dagowsee, and Stechlinsee have each two acquisitions that show calcite precipitation events. Only Kleiner Glietzensee, Roofensee, Menowsee, and Großer Pälitzsee show frequent calcite precipitation events on six to 18 dates. However, because of the high number of FN results, we renounced the calculation of durations. Extraordinary are two calcite precipitation events classifications in March at Kleiner Glietzensee (13 March 2014 and 30 March 2014).

5.4.6 Sentinel-2-Derived Calcite Precipitation in the Feldberg Lake District

Finally, we tested the Area BGR classification approach on a Sentinel-2 data set. **Figure 5-15** illustrates the two existing Sentinel-2 images in 2015 and the contemporary Landsat images, together with their lake reflectance spectra.

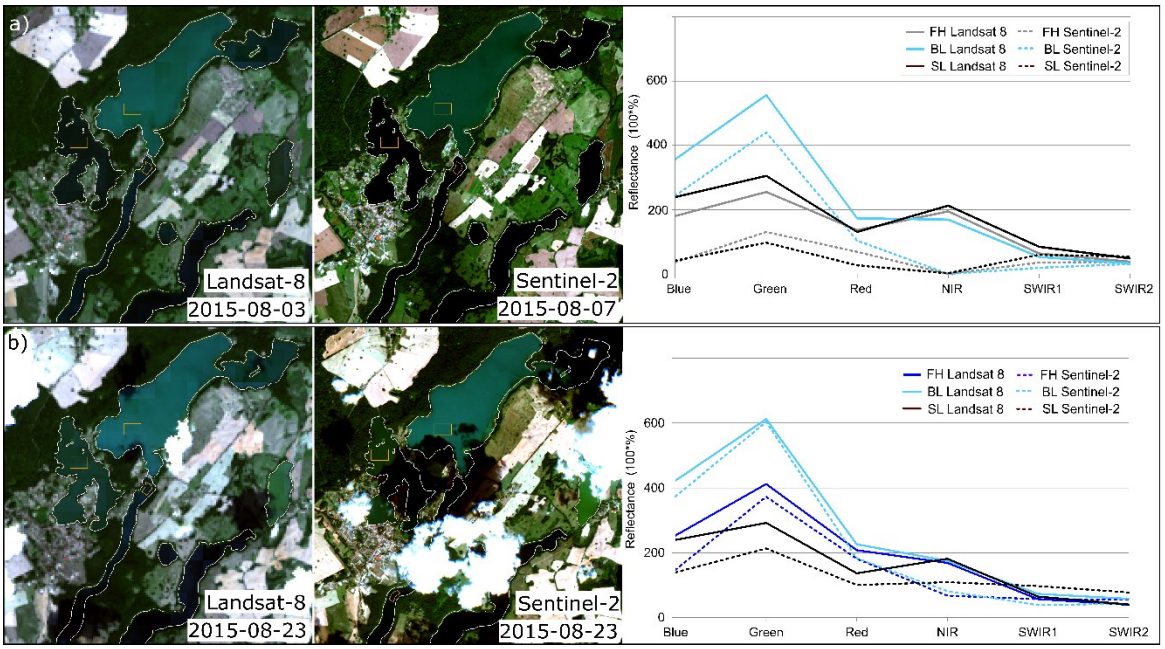

Figure 5-15: Comparison of two contemporary acquired quasi-true color RGB Landsat 8 and Sentinel-2 images of Feldberg Lake District (left and middle) and their according mean spectra (right side). In **(a)**, the Landsat image was acquired on 3 August 2015; and the Sentinel image on 7 August 2015, in **(b)** both images are acquired on 23 August 2015. The orange rectangles in FH, BL and SL illustrate the ROI for the extraction of the mean reflectance spectra. Landsat spectra are illustrated as solid lines, Sentinel spectra as dotted lines.

On 7 August 2015 BH has calcite precipitation, on 23 August 2015 BL and FH. The lakes with calcite precipitation are in the Sentinel-2 images also characterized by a higher reflectance in comparison to the dark lakes without calcite precipitation. On both dates the Sentinel-2 images have lower reflectance values in the visible and NIR wavelength range than Landsat 8. The deviation is largest in the NIR band.

The classification of the Sentinel-2 images via threshold 13×10^3 of Area BGR shows the following results: On 3 August 2015, BL is classified as calcite precipitation with an Area BGR of 22.8×10^3. FH (Area BGR: 7.0×10^3) and SL (5.5×10^3) are classified as lake without calcite precipitation. On 23 August 2015, BL (27.8×10^3) and FH (18.4×10^3) are classified as calcite precipitation, whereas SL (8×10^3) is classified as lake without calcite precipitation. The classification results of the Sentinel-2-derived classifications are equal to the Landsat-derived classification results and the confusion matrices of the Sentinel-2-derived classifications with the Landsat-derived classification and with the visual classification show a perfect accuracy of 1.00.

5.5 Discussion

5.5.1 Visibility of Calcite Precipitation in Multi-Spectral Satellite Imagery (Landsat and Sentinel-2)

The atmospheric correction is the most complex and error-prone processing step in water remote sensing as atmospheric correction models try to remove a large noise (atmosphere) from the small signal of water. However, in time series analysis atmospheric correction is essential for the comparison of different dates and sensors. In this study, we use the Landsat archive (Landsat 5, 7 and 8) and Sentinel-2 imagery, but the focus is the fast and easy applicability of satellite images for the monitoring of calcite precipitation. Thus, we ordered the satellite images in their

highest processing level, including atmospheric correction, or used the state-of-the-art processor (e.g., sen2cor for the atmospheric correction) recommended by the provider of the satellite data. However, the models for the atmospheric correction differ for the different sensors and cause significant variation in the lake spectra (cf. **Figure 5-13**)

Despite the significant variation in the lake spectra, calcite precipitation events are clearly visible in multispectral Landsat and Sentinel-2 images. Whereas lakes without calcite precipitation appear black in quasi-true color RGB images, high $CaCO_3$ concentrations cause an additive effect to the spectra, especially in the green band, resulting in a turquoise color. In addition to calcite precipitation, the lake spectra can be influenced by other suspended minerals, yellow substances ("Gelbstoff"), and phytoplankton (chl-a concentration).

Other suspended mineral particles can increase the reflectance similar to calcite precipitation, but sediment entry is negligible in this study area because of dense vegetation cover, low topography and slow flow velocities that cannot carry sediments (Thiemann & Koschel 2001). In other study areas, however, sediment entry might distort the monitoring of calcite precipitation. Another possible source of error are shallow water areas where the lake bottom can be seen or where wind can resuspend sediments that cause high particle concentrations in the open water (Thiemann & Koschel 2001). Thus, the lake spectra for the analysis are extracted in deep areas of the lakes to avoid misclassifications.

Yellow substances ("Gelbstoff") in the water absorb in ultraviolet and blue (Thiemann & Koschel 2001; Kronberg 1985; Fan 2014), however, as colored dissolved organic matter (CDOM) was not measured in situ, we cannot estimate its influence on our lake spectra.

Whereas lakes with calcite precipitation are mostly turquoise, on some dates, the lake color appears more greenish than turquoise or is even bright green color (e.g., FH on 1 June 2008). Those green colors can be explained by (a mixture of calcite precipitation and) high chl-a concentrations: Phytoplankton scatters diffusely within the algal biomass (additive effect to the spectra), but also absorbs in blue and red (Thiemann & Kaufmann 2000; Kronberg 1985; Schultz & Engman 2000). Lake spectra with high chl-a are characterized by an peak around 700 nm (red edge) (Thiemann & Kaufmann 2000). This peak cannot be detected using Landsat imagery because of the missing red edge band of the Landsat sensors (USGS 2011; Irons et al. 2012). The new Sentinel-2 mission has a red edge band and first tests with Sentinel-2 images showed its potential for the estimation of chl-a (Toming et al. 2016). Thus, we expect that Sentinel-2 will be used in future for additional distinction between calcite precipitation and algal blooms. Even though in this study, the limited amount of Sentinel-2 data and a lack of contemporary in situ measurements hindered a further analysis.

Thus, in this study calcite precipitation and phytoplankton blooms cannot be distinguished clearly. The potential risk of misclassification in the lakes in Feldberg Lake District or Klocksin Lake Chain is very low because the lakes are mostly mesotrophic and considerable algal blooms are most likely in eutrophic lakes with chl-a concentration above 20 µg/L (Thiemann & Kaufmann 2000)). In Rheinsberg Lake Region, several lakes are eutrophic and, whereas calcite precipitation events also occur in eutrophic lakes (cf. Feldberger Haussee), occasional misclassifications of algal blooms cannot be excluded (e.g., March 2014 at Kleiner Glietzensee).

5.5.2 Classification and Validation of Calcite Precipitation Using Multi-Spectral Satellite Imagery

Even though previous studies highlighted the patchiness of calcite precipitation in large lakes (area >20 km^2) (Strong & Eadie 1978; Pulvermüller et al. 1995; Thiemann & Koschel 2001), the lake colors in our study area are homogeneous (cf. **Figure 5-2** and **Figure 5-9**) as the smaller size of the lakes in northeastern Germany supports mixing processes. The only exceptions are different lake colors in separated basins of lakes (cf. BL in **Figure 5-9d** and **Figure 5-15**). Some heterogeneity within the water bodies is smoothed out by the 30-m resolution of Landsat, but there are also artifacts from the atmospheric correction of Landsat 8 images that cause some variation (Department of the Interior & U.S. Geological Survey 2016). Thus, in this study, a classification based on mean lake spectra was chosen to minimize the variation of the lake spectra. In other regions with higher heterogeneity classifications on pixel level might be preferable.

Thiemann and Koschel proposed a classification of calcite concentration based on 800 nm in hyperspectral images and considered more than 3% reflectance at 800 nm as calcite precipitation (Thiemann & Koschel 2001). Although Landsat images do not have an 800 nm band, red is on average 655 nm and NIR is at 865 nm and a comparison with the spectra of BL (**Figure 5-10**) shows that only the strongest calcite precipitation on 11 July 1999 meets their criteria for calcite precipitation. At the other dates the reflectance of red and NIR are below 3% reflectance, even though in situ measurements showed increased $CaCO_3$ concentrations. Therefore, we tested several spectral indices for the classification of calcite precipitation. Best results were achieved with a classification based on the triangular area between the blue, green and red band in the spectra, the "Area BGR". If the Area BGR value is $\geq 13 \times 10^3$, the lake is classified as lake with calcite precipitation. This threshold is suitable for Landsat imagery and Sentinel-2 despite their differences in bandwidth and atmospheric correction.

Before this study, it was unknown which calcite concentrations were detectable from space. Thus, we compared our Landsat-derived classifications with different in situ $CaCO_3$ concentrations. Without optical aid a previous study suggested the limit for the visual detection of calcite precipitation is 1 mg/L (Koschel et al. 1987). Our classification approach was able to detect $CaCO_3$ concentrations ≥0.7 mg/L with an accuracy of 0.88. A higher threshold in the $CaCO_3$ concentration increases the number of FP classification results, whereas a lower $CaCO_3$ concentration increases the number of missed calcite precipitation events (=FN). The accuracy of the automatic classification is hereby also slightly better than the accuracy of the according visual classification of the quasi-true color RGB Landsat images (0.85).

The accuracy of the Landsat-derived classifications is decreased by FN and FP results: Here, FN results can be explained by the conservative threshold that is optimized for the correct classification of lakes without calcite precipitation: Thus, dates with only a slight color change are missed by the threshold. However, the six missed calcite precipitation events all have $CaCO_3$ concentrations between 0.95 and 1.65 mg/L which should have resulted in a visible color change. The visual classification of those dates confirms that four of the six dates indeed showed no or only a slight color change. The other two images have image quality problems and biased lake reflectance spectra because of cloud coverage. The lack in color change despite calcite precipitation might be explained by the heterogeneity of $CaCO_3$ concentrations within the lake or by time gaps of one day between in situ measurement and Landsat images. Thiemann and Koschel already noted the varying $CaCO_3$ concentrations within lakes in northeastern Germany and the possible problems for validation (Thiemann & Koschel 2001). Despite careful work, measurement and transmission errors cannot be excluded for certain.

The nine FP classifications are related to already increased calcite concentrations between 0.41 and 0.69 mg/L and resulting in a turquoise color of the lakes. This applies specifically in the visual classification because of the high sensitivity of the human eye and thus a more sensitive visual classification. Because of the time gaps between in situ measurements and Landsat acquisition, it could also be that the concentration during the Landsat acquisition has already increased. An additional validation of single dates using the SI failed because of: (a) its short term changes as soon as crystallization of $CaCO_3$ starts; and (b) its limitations in case of bio-induced calcite precipitation (Stabel 1986; Thompson 1990) as the occurrence of crystal nucleus, e.g., in form of bacteria (Department of the Interior & U.S. Geological Survey 2016; Koschel et al. 1983), is equally important for calcite precipitation. Considering its SI FH has before 2011 not the potential for calcite precipitation, but in situ $CaCO_3$ measurements and the analysis of Landsat show clear calcite precipitation, whereas SL has high SI values since 2000 and therefore the potential for calcite precipitation, but still calcite precipitation events are very rare.

After the calibration and validation at Feldberg Lake District, the classificaion approach was applied in two other regions without in situ measurements. Here, the validation is based on visual classifications of the lakes. The accuracies are very high (0.99 and 0.97), but whereas Feldberg Lake District has a ratio of calcite precipitation events to normal lake conditions of 1:4, the ratio at Klocksin Lake Chain is already 1:14 and in Rheinsberg Lake Region even higher with 1:36. Thus, the accuracy is biased and in relation to the number of calcite precipitation events, the number of missed calcite precipitations (FN) is high in Rheinsberg Lake Region. The FN results can here also be explained by the conservative classification threshold in combination with the high sensitivity of the human eye and thus a more sensitive visual classification.

The accuracy based on the visual classification at Feldberg Lake District is 0.94. The lower accuracy at Feldberg Lake District in comparison to the other regions is caused by the less strict cloud removal. Especially, haze and missed cloud pixels hinder the accurate classification (FN results).

Whereas FN and FP classification results (e.g., FN results at lake Menowsee) distort the analysis of frequencies and durations, they do not affect the determination of the total area of lakes with calcite precipitation in this study. In comparison to the visual classification, FP are very rare, whereas all FN results occur at lakes that are, at other times, classified as lakes with calcite precipitation.

Overall, calcite precipitation events are detected in 15 of 24 lakes in the study areas and the total lake area of lakes with calcite precipitation is approximately 17 km^2. Thus, our study supports that calcite precipitation is a common phenomenon in the hardwater lakes, but it also emphasized that the durations and frequencies strongly vary so that each lake must be monitored individually.

5.5.3 Time Series: Frequency and Duration of Calcite Precipitation

Remote sensing data and especially, the large Landsat image archive, enable a long-term monitoring of large areas. However, for an accurate monitoring of the duration and frequency of calcite precipitation, a high acquisition density is required. The Landsat archives cannot provide a continuous temporal coverage, due to their limited repetition rate of 16 days and acquisition gaps by cloud coverage.

Whereas in some years with overlapping satellite missions the number of acquisitions is high, other years have only very few acquisitions, e.g., 2001 (cf. **Figure 5-5**). Since 2012, Landsat 7 and Landsat 8 are operating together providing a doubled repetition rate of eight days. However, cloud coverage still reduces the coverage significantly. For example, in 2012 the monitoring of the lakes in the Klocksin Lake Chain is only very irregular, because of the removal of cloud and cloud shadow (cf. Supplement 5) Thus, for a regular monitoring of calcite precipitation at selected lakes a less strict cloud and cloud shadow removal should be considered, even if this comes along with a higher number of misclassification because of cloud and haze (cf. classification accuracy of Feldberg Lake District). Earth observation with the Sentinel-2 satellite(s) will further increase the data density with its higher time resolution and repetition rate of 10 days. However, so far, only two Sentinel-2a images cover the study area, so that the full potential of Sentinel-2 could not yet be studied.

Calcite precipitation is known to be a spatial and temporal very variable process and it is linked to different factors, e.g., trophic state and occurrences of bacteria of the lakes. This causes changing calcite precipitation patterns in time and different calcite precipitation patterns even for adjacent lakes, e.g., in the Feldberg Lake District: even though SL was known for calcite precipitation before 1998, there were no calcite precipitation detected with in situ measurements after the lake restoration in 1996/1997. Whereas the in situ measurements between 1998 and 2015 show $CaCO_3$ concentrations <0.5 mg/L, the Landsat classification shows a clear calcite precipitation event on 13 August 2014 and misses further five visually classified calcite precipitation events. At FH, no calcite precipitation occurred before 2003. This fits to the in situ measurements: The long-term record (1985–2015) of mean seasonal (May–September) $CaCO_3$ concentration of FH indicates low values of <0.5 mg/L until 2005. Afterwards a substantial increase was observed. However, the reasons are not entirely clear. Koschel et al. (1983) have concluded that calcite precipitation might be most intensive in mesotrophic lakes (Koschel et al. 1983). By 2005 the seasonal (May–September) total phosphorus concentration of the mixed layer had dropped to 0.046 mg/L which is still in the eutrophic range but relatively close to mesotrophic conditions (Riedmüller et al. 2014). In 2011, when a second restoration measure has been carried out, calcite precipitation did not occur, while in 2012 a few calcite precipitation events and in 2013 several calcite precipitation events have been observed at FH. In 2014, the duration and frequency of calcite precipitation events is reduced again and in 2015 only one event has been observed. These variations can be explained by the complex process with competing inhibiting factors and supporting factors for calcite precipitation. During eutrophication phases, excess phosphorus has an inhibiting effect on calcite precipitation (Dittrich & Koschel 2002) so that artificial removal of phosphorous through poly-aluminum chloride might increase calcite precipitation. A follow-up monitoring will show if the restoration measures at FH have the same result (absence of calcite precipitation) as the restoration measures at SL.

The three lakes with the most calcite precipitation events are FH, BL, and TS. Their average durations are 24, 57, and 31 days (overall average: 37 day), but all three lakes show start–stop–start–stop patterns. However, the comparison of those patterns with the visual classifications reveals that most of those short-term variations are caused by misclassifications (e.g., FN results at FH between 4 July 2014 and 13 August 2014). Visually validated start–stop–start patterns, e.g., at FH between 24 July 2013 and 26 August 2013, substantiates the results of previous studies that showed calcite precipitation with lower calcite concentrations before and after the main event and non-steady, periodic variations (Proft 1984).

Whereas the validation in Section 5.2 discusses the quality of the Landsat-derived calcite precipitation monitoring, it is still unknown, how many calcite precipitation events are missed

in times without suitable satellite images or in situ measurements. Therefore, we included sediment analyses at TS to discuss the detection rate of calcite precipitation via remote sensing: The Landsat-derived monitoring at lakes in the Klocksin Lake Chain shows calcite precipitation events at TS at 11 of 18 years, whereas sediment analyses show calcite layers every year. A running monitoring study at TS using sediment traps shows high calcite deposition between May and September. The years 2001, 2007, 2010, and 2012 have only one or two Landsat acquisitions during May and September, thus calcite precipitation events were most likely missed. The years 1998, 2004, and 2011 have four, five, and nine acquisitions. However, the acquisitions are not equally distributed with maximum gaps of 55 days (2004 and 2011) to 89 days (1998) days between the acquisitions and thus, still calcite events could have happened in times without Landsat acquisitions. Especially, as the sediment layers in all of the missed years are extraordinary thin (Kienel et al. 2013), which indicates either short-term or weak calcite precipitation events.

At region Rheinsberg Lake Region, eight of the 17 lakes show at least one calcite precipitation event, but the frequency of events is probably higher than our analyses shows, because the validation based on a visual classification reveals approximately as many calcite precipitation events as FN classifications. On the other hand, five lakes are eutrophic, thus, algal bloom may also occur, either contemporary to high $CaCO_3$ concentrations or independent of calcite precipitation. In this region the calcite precipitation on 20 August 2011 at the oligotrophic Stechlinsee has to be highlighted. This calcite precipitation is caused by storm “Otto” in July 2011, which caused the mixing of cyanobacteria populations from 7 m to 8 m depth into the surface water (Leibniz-Institute of Freshwater Ecology & Inland Fisheries (IGB) 2016). The resulting increase of the photosynthesis activity caused an increase of the $CaCO_3$ saturation index and lead to intensive calcite precipitation, still clearly visible in the Landsat image on 20 August 2011.

5.6 Conclusions

In this study, we tested the potential of the Landsat archive and Sentinel-2 for the classification and monitoring of calcite precipitation in lakes. Calcite precipitation due to increased $CaCO_3$ concentrations cause an additive effect to the lake reflectance spectra, especially in the green band, resulting in quasi-true color RGB images in a turquoise color. Thus, we classify calcite precipitation events in lakes based on the calculation of the triangular area between blue, green and red in the mean lake spectra (Area BGR). We chose a conservative threshold, based on the comparison of visually turquoise and dark lake values of one lake (FH) for which a long-term in situ data archive of $CaCO_3$ concentrations is available. Overall, our study area covers 24 lakes. The classification results of FH, BL, and SL are validated with in situ measurements of calcite precipitation, for TS with sediment core data. We detected calcite precipitation with $CaCO_3$ concentrations $\geq$0.7 mg/L in the Feldberg Lake district with a good accuracy of 0.88. Our classification is here better than expected; a previous study suggested a limit of >1 mg/L.

The analysis of the false classified events showed that at some dates the lakes do not show a change of color even though the contemporary $CaCO_3$ concentration is high (FN classifications), whereas other dates with only slightly increased $CaCO_3$ values have a change of color (FP classifications). Important to consider is the time gap between in situ measurement and Landsat acquisition as well as a possible heterogeneous distribution of $CaCO_3$ in the lake.

In a next step, we tested the monitoring approach on 21 other lakes in the regions Klocksin Lake Chain and Rheinsberg Lake Region and validated the classification results based on a visual inspection of the Landsat data. Whereas FN results are relatively frequent in comparison

to the number of detection calcite precipitation events, the overall accuracy in these two regions is still >0.97.

Our study shows that 15 of the 24 lakes covering a total area of approximately 17 km^2 have at least one calcite precipitation event in the observation period. The frequency of calcite precipitation events varies between one detection and regular detections nearly every year. The durations of calcite precipitation events also vary between the lakes, but are for the lakes with regular calcite precipitation (FH, BL, and TS) in average 37 days. The time series for Feldberg Lake District is denser than the one of Klocksin Lake Chain and Rheinsberg Lake Region, but has also a higher risk of misclassifications due to haze and remaining cloud pixels. However, still the effect of lake trophy restoration measures on calcite precipitation can be shown at SL and FH.

The high number of missed calcite precipitation events (=FN results), together with gaps in Landsat time series (e.g., 2001), reduces the accuracy of frequency and duration monitoring. For example, the comparison with sediment data at TS shows that calcite precipitation events have been missed in some years due to low image density in the critical time periods (May to September). In future the image density will increase by acquisitions of Sentinel-2a and coming Sentinel-2b. We tested the application of Area BGR classification method to Sentinel-2 and even although the sensors and the atmospheric correction differ, the classification approach is transferable. Another great potential of Sentinel-2 comes with its red-edge band: We expect that Sentinel-2 can also be used in future for the distinction between algal blooms and calcite precipitation.

Our results emphasized the variety of the lakes and the need to monitor each lake individually. This is due to the complex processes of calcite precipitation, which are influenced by a number of factors including lake trophic state, algae composition and activity, human measures and climate. For the monitoring calcite precipitation in lakes in the entire Northeast German Plain using the large Landsat archive and Sentinel-2 imagery a new method is provided. This is an essential prerequisite, in combination with geochemical analyzes, to investigate the role of permanent CO_2 storage in form of calcite in this region.

Supplements: The following supplementary materials are available (*as Appendix A*) online at http://www.mdpi.com/2073-4441/9/1/15/htm in the online version of the article. Table A1: Calcite precipitation based on the Landsat time series (1998–2015) using the threshold of the area BGR. Lakes with calcite precipitation events are marked with "1" and highlighted in gray. Dark lakes without calcite precipitation are marked with "0". Blank cells are dates without data.

Acknowledgments: This study was funded by the "Helmholtz Association of German Research Centres Initiative—Networking Fund for funding a Helmholtz Virtual Institute" (VH-VI-415).

Author Contributions: Iris Heine developed the methodological framework, performed programming, conducted the analysis and wrote the article; Peter Kasprzak and Ulrike Kienel provided in situ data for and contributed their expert knowledge on the study areas; Birgit Heim supported the analysis of the lake spectra based on her experience of water remote sensing; and Achim Brauer, Birgit Kleinschmit and Sibylle Itzerott were involved in formulating the research questions and contributing to critical discussions. All authors were involved in the general paper review.

Conflicts of Interest: The authors declare no conflict of interest.

6 Synthesis

In this thesis remote sensing imagery was utilized for long-term and large-scale monitoring of lakes within the framework of the interdisciplinary and international virtual institute ICLEA. The aim of this thesis was the development of new remotely-sensed monitoring methods for lakes in the northern Central European lowlands and their application to large-scale areas. The overarching research questions of this work comprise the general potential of archive remote sensing for the long-term monitoring of lakes in the northern Central European lowlands (cf. **Chapter 1.4**) on the basis of specific research questions regarding the development, evaluation, and application of new monitoring methods.

This chapter discusses the joint results of **Chapters 2** to **5** first with respect to the specific research questions (**Chapter 6.1.1**) and then with respect to the overarching research questions (**Chapter 6.1.2**). Finally, the chapter provides an outlook on future applications (**Chapter 6.2**).

6.1 Conclusions

6.1.1 Summary of Results with Respect to the Specific Research Questions

In **Chapters 2** to **5** three new approaches for the long-term monitoring of lakes in the central European lowlands are introduced. Each chapter has specific research objectives (cf. **Chapter 1.4**). The monitoring subjects are lake level changes (**Chapters 2** and **3**), the monitoring of shoreline vegetation (reed) (**Chapter 4**), and the monitoring of calcite precipitation (**Chapter 5**). In this chapter the specific research questions are answered, structured within the different monitoring themes, but still based on the joint results of all four chapters.

6.1.1.1 Lake Level Reconstruction Using Remote Sensing Imagery

Most lakes of the northern Central European lowlands are characterized by significant seasonal and long-term changes (cf. **Chapter 1.2.1**), but only few of them have regular gauging stations or are covered by radar altimeters. Thus, the indirect reconstruction of lake levels was tested based on remote sensing archive data. The reconstruction of lake areas or the comparison of shoreline positions is more common, e.g., (Verpoorter et al. 2012; Muster et al. 2013; Maillard et al. 2012; Wang et al. 2014; Klein et al. 2005; Papastergiadou et al. 2007), but level measurements simplify the synthesis of different data sources.

The reconstruction of the lake levels is based on the extraction of former water-land borders from optical remote sensing archive data and the intersection of (a part of) this reconstructed shoreline with topographic data (cf. **Figure 3-2**). The water-land borders were manually digitized (**Chapter 2.3.3**) in the case of aerial photos, and automatically extracted using the NIR band and Otsu's threshold (**Chapter 3.3.2**) in the case of RE satellite imagery. The topographic data consists of LIDAR based digital surface models of the land area merged with bathymetric measurements of the lake area.

This principle is straightforward and has been used for lake monitoring using medium-resolution optical images (Gupta & Banerji 1985; Maillard et al. 2012). However, the data set at lake Fürstenseer See enabled for the first time the absolute validation of the reconstructed levels with gauged levels and in situ measured GPS shorelines (Gens 2010; Li & Damen 2010).

- How accurately can lake level changes be reconstructed based on optical remote sensing data? What are the advantages and disadvantages for the lake level reconstruction of different optical remote sensing data archives?

Under ideal conditions, the reconstructed lake levels using aerial photos reached meter accuracy and the reconstructed lake levels using RE satellite imagery reached decimeter accuracy. The RE derived results are consistent with the accuracies of flood level estimations based on high-resolution imagery (Puech & Raclot 2002; Hostache, Matgen, Schumann, Puech, et al. 2009). The comparison with in situ measured lake levels showed that the aerial photo-derived lake levels were always overestimated (cf. **Figure 2-7B** and **Footnote 1**), whereas the RE-derived lake levels were systematically underestimated (cf. **Figure 3-7**). The underestimation of the water-land level was caused by an underestimation of the water-land border via the NIR band – a fact known from previous studies (Wang et al. 2014).

In principle, the accuracy of the reconstructed levels depends on the precision of the water-land borders and the topographic data. The thorough analysis of this thesis pointed out more specific factors: high spatial resolution imagery is essential, because lake level changes can only be reconstructed unambiguously if the shift of the water-land border (as a factor of the slope of the lakes' shorelines and its lake level change) is several times larger than the spatial resolution of the remote sensing data (cf. **Chapter 3.5**). A high geometrical accuracy of the remote sensing imagery is also needed. This can be achieved with thorough geo-referencing of aerial photos and co-registration of satellite images. The accuracy of the water-land border was in the thesis reduced by image quality problems (sun glint, cloud shadows, shadows) and shoreline vegetation that covered the water-land border. Thus, shorelines with sparse or no vegetation are preferred. The quality of the topographic data mainly depended on the bathymetric survey, because the LIDAR data has a much higher precision than the bathymetric data. Essential for the bathymetric survey are the measurement accuracy, the point density, and the coverage of points, specifically at the shoreline that was used for the lake level reconstruction (cf. **Chapter 2.4.3**, **Supplementary Materials on Chapter 2**, and **Chapter 3.4**). The topographic inaccuracies must also be considered in the reconstruction of lake areas based on topographic data ("contour lines") (Kaiser, Küster, et al. 2014): the analysis of the lake area of FS shows that contour lines derived from gauged data missed islands, because of gaps in the bathymetric point data (cf. **Figure 3-4**, **Chapter 3.5** and **Supplementary Materials on Chapter 3 (Figure S3)**).

The reconstruction of lake levels requires a high spatial resolution, thus, the number of images is limited, specifically at the beginning of remote sensing for Earth observation. Aerial photos are a good choice for long-term (up to 75 years) monitoring of lakes, but they have long gaps between the acquisitions. This disadvantage was managed in this thesis by the combination with proxy data from geo- and bioarchives, and gauged and modelled lake levels (cf. **Chapter 2**): the fusion of the different data enabled the successful reconstruction and analysis of lake level dynamics during the last century (cf. **Figure 2-7B**). The aerial photo-based lake levels at Redernswalder See have also been used for the cross-validation of the different lake level information and could be used as input parameter for improved modelling.

RE satellite images cover a shorter time series (~5 years), but with much higher temporal resolution (one to two acquisitions per month). Unfortunately, more than two thirds of the archive images were covered by clouds or the lake level reconstruction was hampered by low solar angles in autumn and winter (cf. **Chapter 3.3.1** and **3.5**). This reduced the actual temporal resolution of the RE-derived lake level time series massively.

- Can polarimetric SAR data be used for the extraction of water-land borders at vegetated shorelines?

SAR images are not disturbed by cloud coverage and do not rely on sunlight, thus, they enable a regular monitoring. In addition, PolSAR and polarimetric decomposition techniques enable the discrimination of different scattering mechanisms and have the potential for mapping water below vegetation (cf. **Chapter 1.2.2.2**).

Lake levels are best reconstructed at very shallow shoreline parts, but the shallowest parts of the shoreline tend to be covered by dense vegetation: reed belts grow in the shallow water areas of most lakes in the central European lowlands as long as the lakes are not affected by human intervention or reduced by rapid lake level variations. The dense vegetation covers the water surface, so that the water-land border is not visible in optical images and the shallow shorelines cannot be used for the reconstruction of lake levels. Thus, so far, the RE-based method is only transferable to lakes with vegetation-free shallow shorelines, e.g. with bathing sites and after mechanical removal of reed, or to lakes with very strong lake level changes which balance the influence of the shoreline slope.

The potential of dual-polarimetric TSX imagery for the monitoring of reed covered shorelines was tested to overcome this problem (cf. **Chapter 4)**. The assumption was that the water below the reed would be detectable through double-bounce scattering between the reeds' stems and the smooth water surface. However, the best classification results were achieved with multi-temporal winter image stacks (cf. **Chapter 4.5.4**). Additionally, geometrical inaccuracies due to the challenging side-looking geometry of the sensor hampered the precise extraction of water-land borders.

- What are requirements for the successful application of the developed approaches? What are challenges for the transfer to other lakes?

The accuracy of the lake level reconstruction using RE imagery is influenced by many factors: but specifically, the requirement of a very shallow shoreline without vegetation (**Chapter 3.5**) limits the transferability of the method to other lakes. Additionally, the data availability is not continuous due to frequent data gaps through clouds and image quality problems in autumn and winter. Lake level reconstruction using aerial photos was tested at Redernswalder See and validated with gauged levels, before it was applied at Krummer See. The approach with aerial photos is more robust than the one using RE images, because the spatial resolution of the photos is higher and the lake area changes are more prominent on the longer time scales (cf. **Figure 3-4** (RE) vs. **Figure 2-4** (aerial photos)). However, a transferability to a large number of lakes is not feasible due to the required manual work in the processing of the aerial photos (cf. **Supplementary Materials on Chapter 2**).

- Which specific results can be achieved for northern Central European lowlands and how can the new methods complement in situ measurements and proxy-based monitoring?

The reconstruction of lake levels using aerial photos and RE satellite images was focused on three selected lakes: Redernswalder See, Krummer See (aerial photos), and Fürstenseer See (RE images) (cf. **Figure 1-5**). Fürstenseer See has regular lake level measurements since 1987, Redernswalder See since 1976, but with a large data gap between 1985 and 1994, and Krummer See has never been gauged. As the three lakes are groundwater-fed and endorheic lakes, their lake levels are sensitive to minor changes of the water balance.

Aerial photos have previously been used for the monitoring of shorelines changes, also in synthesis with tree ring and lake sediment analysis (Shapley et al. 2005), and for the analysis of lake-area changes due to climatic change (e.g. (Klein et al. 2005; Papastergiadou et al. 2007)). In this thesis, lake levels derived from aerial photos were combined with in situ gauged, proxy and modelling data for the first time. At Krummer See lake level changes were provided and analyzed for the first time and at Redernswalder See the length of the lake level time series was increased by four decades. The analysis of those lake level reconstructions revealed drastic long-term lake level changes that have rarely been reported from natural lakes for other parts of northern Central Europe. Thus, changes at a scale of decades must be considered in landscape hydrology in addition to seasonal lake-level dynamics fluctuations. This challenges the common implicit assumption of landscape hydrology that stationarity is the norm for remote, undisturbed (i.e. near-natural) hydrosystems (cf. **Chapter 2.5.5**).

Whereas the reconstruction of lake levels at Fürstenseer See via RE images did not add new information to the gauged lake levels, the analysis of the extracted water-land borders illustrates the ecological and economic impact of lake level changes: within one season, the size of the sandbank at Fürstenseer See decreased by 90% and within one year the sandbank and shallow sandy beaches, that were popular among tourists, were completely flooded. The documented increase of the lake level and area also influenced the submerged and aquatic vegetation: shallow water areas were again colonized in 2014 with reed, after a significant decrease of the vegetation in former times with lower lake levels (cf. **Chapter 3.5, Supplementary Materials on Chapter 3 (Figure S4 and S5)**).

Finally, the comparison of the three lakes showed different lake level dynamics (cf. **Figure 2-7B** and **Supplementary Materials on Chapter 3 (Figure S1**) which emphasizes the need for an individual monitoring of lakes.

6.1.1.2 Monitoring of Reed Belts Using Dual-Polarimetric PolSAR Imagery

Reed belts are important habitats for animals and they protect the shorelines from erosion and filter the lake water (Bogenrieder 1990; Schmieder et al. 2004). On a long-term scale they are a sink for greenhouse gases (Brix et al. 2001). However, reed is sensitive to rapid lake level changes (Schmieder et al. 2004) (cf. **Chapter 3.5**). Regular monitoring of reed is also of interest for hydrological measurements at the shorelines, because of the seasonal changes of reed.

Previous studies aiming at the monitoring and mapping of reed are based on aerial photos and high-resolution optical satellite images (Bresciani et al. 2009; Schuster et al. 2015; Csaplovics & Nemeth 2014; Lantz & Wang 2014). However, high-resolution optical images are not suitable for regular monitoring, because of their weather and sunlight dependency and their high cost. Thus, the potential of PolSAR was tested for the regular monitoring of reed at the shorelines of lakes: the PolSAR monitoring of reed is based on 19 dual-polarimetric TSX images, because X-band SAR imagery has proven useful for the distinction of different vegetation types in wetland monitoring (Hong et al. 2015; Betbeder et al. 2014; Van Beijma et al. 2014; Yajima et al. 2008)**.**

The detailed processing of the dual-co-polarimetric TSX images is described in **Chapter 4.4.1** and **Table 4-2** introduces the 16 polarimetric parameters that were derived from the TSX images. The classification of the images is based on the RF classification algorithm (cf. **Chapter 4.4.2**): The RF classification is fast, easy to implement, and a pre-selection of

classification parameters is not required, because the algorithm automatically selects the best parameters for classification.

- Can polarimetric SAR data be used for the short- and long-term monitoring of reed areas? What are the advantages over optical remote sensing imagery monitoring methods? What are disadvantages?

This thesis showed the potential of dual-co-polarimetric X-band SAR imagery for a regular monitoring of reed, because PolSAR decomposition techniques enable the direct measurement of the physical parameters. Additionally, radar allows a regular, year-long monitoring due to its sunlight and near weather independency. Only ice hampers the monitoring of reed (cf. **Chapter 4.5**).

The PolSAR time series analysis showed different scattering mechanisms, caused by seasonal changes of the reed vegetation: 13 of 16 dual-polarimetric TSX derived parameters showed a significant difference between summer and winter acquisitions (cf. **Figure 4-5**). In addition to the double-bounce-sensitive parameters ($\delta_{HH/VV}$, $\bar{\alpha}_{dual}$, α_{dual}, and $\angle\gamma_{HHVV}$), the polarimetric parameters $|\gamma_{HHVV}|$, A_{dual}, H_{dual}, $m1$, $m2$, $m3$, and $m4$ revealed seasonal changes in the reed signal. These changes were caused by the phenology of reed (cf. **Figure 4-3**): in summer, the volume scattering of reed belts is high, whereas during the leaf-off season in winter and early spring, double-bounce scattering dominates for the X-band within reed belts.

The results of this study are consistent with a previous study by Yajiami et al., in which seasonal changes of reed and lotus plants were detected using X-band and L-band quad-polarimetric PolSAR data (Yajima et al. 2008). Dual-polarimetric images have not been used for reed monitoring, but showed comparable results for similarly structured vegetation, specifically rice (Lopez-Sanchez et al. 2012; Lopez-sanchez et al. 2011; Lopez-Sanchez et al. 2011; Lopez-Sanchez et al. 2014; Yonezawa et al. 2012; Koppe et al. 2013). Thus, this thesis presents the first approach for regular phenological reed monitoring using dual-polarimetric SAR imagery. The advantages of dual-polarimetric over quad-polarimetric SAR images are their higher spatial resolution and their higher data availability (cf. **Chapter 1.2.2.2**)

The characteristic scattering mechanisms of reed can be used for a knowledge-based classification of reed: the best distinction of reed from other land cover classes was achieved in winter due to the double-bounce scattering of reed. Three of the five most important parameters for the classification of reed (δ_{HH-VV}, $\bar{\alpha}_{dual}$, $\delta_{HH/VV}$, δ_{HH}, and $\angle\gamma_{HHVV}$) are double-bounce sensitive (**Figure 4-9**). Because of the spatial heterogeneity of the parameters, the classification of stacked images is recommended. The highest classification accuracy of reed was reached using a stack of winter images, combining both sensor flight directions (asc and desc) (cf. **Figure 4-12** and **Figure 4-13**). The overall classification accuracy of all five classes was 92% (**Table 4-4**). Whereas the shorelines with reed areas (>10 m in width) could be detected correctly, the actual areas with reed coverage were significantly overestimated and the accuracy was only ~50%.

This relatively low accuracy of the reed classification was mostly caused by spatial inaccuracies of the images. The geocoding process of side-looking SAR is challenging, specifically at lakes with a significant height difference between water surface and surrounding vegetation (Heine et al. 2014). Nevertheless, the improvement of the spatial accuracy went beyond the scope of this thesis.

Long-term monitoring of reed and change detection related to lake level changes is not yet feasible, despite the potential for short-term monitoring of reed. High-resolution dual-co-polarimetric SAR imagery is only acquired on demand, thus, only small areas and short time

series are covered. Additionally, the measurement of the reed area and furthermore the change detection of reed areas were impaired by problems in the spatial processing of the SAR data.

- What are requirements for the successful application of the developed approaches? What are challenges for the transfer to other lakes?

The PolSAR time series analysis of reed illustrated the characteristic scattering mechanism of reed during the year. Furthermore, the preferable polarimetric parameters for the classification reflects the knowledge about the structural changes of reed during the year. This offers great potential for the transferability of the approach, also for areas without training or validation data. The RF classification requires training points as input, but an additional test with an unsupervised classification approach (k-means clustering) reached nearly the same classification accuracy.

Depending on the spatial resolution of the PolSAR and the geometric accuracy of the images, a minimum width of the reed belts is required. For dual-polarimetric TSX images the minimum width is 10 m (cf. **Figure 4-13**). Additionally, the detection of reed might be influenced by the flight direction of the satellite, the looking direction of the sensor, and the looking angle. In the case of shallow looking angles, topography and high trees could shade reed areas, so that they cannot be detected by the SAR sensor.

The biggest limitation today is the availability of dual-co-polarimetric SAR images. Dual-polarimetric decomposition is only feasible with dual-co-polarimetric, not with dual-cross-polarimetric SAR images. However, the dual-polarimetric decomposition techniques are relatively new and previous monitoring campaigns ordered mostly dual-cross-polarimetric images, because of the depolarizing effect of vegetation (Liebe et al. 2009; Smith 1997; Voormansik et al. 2013). Thus, the application of dual-co-polarimetric images data for the long-term monitoring of lakes is very limited.

The regular monitoring of lakes with dual-co-polarimetric TSX also showed the seasonal changes of deciduous forest. Thus, TSX images might be used for the monitoring of the fall of leaves in autumn and the start of growth in spring. The start and duration time of leave-fall and leave-growth are proxies for climate changes and important input variables for hydrological monitoring.

6.1.1.3 Monitoring of Calcite Precipitation Using Multi-Spectral Imagery

Calcite precipitation is a common phenomenon in hardwater lakes in the northern Central European lowlands, but only individual lakes are monitored regularly (Proft 1984; Koschel et al. 1987; Koschel et al. 1997). The precipitation changes the lake color to a milky turquoise, whereas lakes without calcite precipitation appear dark blue or black (cf. **Figure 5-8** and **Figure 5-9**). Those lake color changes have already been noticed during the analysis of lake levels with multi-spectral RE satellite images at some lakes, but they are also clearly visible in contemporary medium-resolution Landsat imagery. Medium-resolution MODIS imagery (Long et al. 2014; Dierssen et al. 2008) and Landsat imagery (Strong & Eadie 1978; Pulvermüller et al. 1995) has been used before for the monitoring of calcite precipitation in the ocean and in large lakes (the Great Lakes, and Lake Constance). Thus, it was expected that multi-spectral Landsat images have great potential for the long-term monitoring of lakes in the northern Central European lowlands and for the analysis of the distribution of affected lakes.

The analysis of Landsat images and the comparison with in situ measured water parameters at three lakes (SL, BL, and FH) showed clearly the increase in the water reflectance through calcite precipitation in the Landsat images (cf. **Chapter 5.4.2**). The reflectance values between

green and NIR were enhanced by calcite precipitation, but the green band showed the strongest increase and had the maximum reflectance values (cf. **Figure 5-10** and **Figure 5-11**). To balance small-scale heterogeneity within the lakes, their mean lake spectra are calculated from ROIs in the middle of the lakes.

- What are efficient and robust methods to monitor calcite precipitation using multi-spectral remote sensing data?

The potential of the green reflectance values and six spectral indices (cf. **Table 5-5**) was evaluated for the classification of calcite precipitation (cf. **Chapter 5.4.3**). The comparison of reflectance values and spectral indices at lakes with and without calcite precipitation (visual classification) showed that the index "Area BGR" has the best distinction between the two cases (cf. **Figure 5-12**). The "Area BGR" is the triangular area in the reflectance values of blue, green, and red (cf. **Figure 5-10**). The following classification of calcite precipitation events was based on a conservative threshold (Area BGR $> 13 \times 10^3$). The Landsat-derived classification results were validated with in situ measured $CaCO_3$ concentrations and visual classification results: the validation showed that calcite precipitation with $CaCO_3$ concentration $\geq$0.7 mg/L can be detected with a high accuracy of 88% (in situ concentration) and 94% (visual validation) (cf. **Chapter 5.4.4**). The sensitivity of Landsat to the $CaCO_3$ concentration was in this case better than expected as Koschel et al. suggest a visible change of the lake color >1 mg/L $CaCO_3$ (Koschel et al. 1987).

Lake colors can also be influenced by various parameters such as water depth and lake bottom material, suspended minerals, yellow substances, phytoplankton (=high chl-a concentration), and CDOM (cf. **Chapters 1.2.2.1** and **5.5.1)**. Low water depth and suspended minerals could be excluded as source of error and we assumed that the influence of yellow substances and CDOM did not impact the classification result (cf. **Chapter 5.5.1)**. Chl-a concentrations have been measured at three lakes (SL, BL, and FH), but the time series was too irregular for a thorough analysis of calcite precipitation and phytoplankton blooms. The concentration of chl-a could also not be derived from Landsat imagery, because the algorithms for chl-a measurements are sensitive to suspended minerals (cf. **Chapters 1.2.2.1** and **5.5.1**). However, this thesis showed that the "Area BGR" classification is transferable to Sentinel-2 images (**Chapter 5.4.6**). In contrast to Landsat, Sentinel-2 acquires the red edge band, which has the potential for chl-a measurements (Toming et al. 2016). Thus, it is expected that Sentinel-2 can be used in future for a better distinction of phytoplankton blooms and calcite precipitation.

- What are requirements for the successful application of the developed approaches? What are challenges for the transfer to other lakes?

This thesis presented an easy and mostly automatic approach for calcite precipitation monitoring using multi-spectral medium-resolution satellite images. The development of a robust classification ("Area BGR") was based on three lakes with in situ measurements (SL, BL, and FH). The transferability of the approach was successfully tested on further 21 lakes. The Landsat-based classification approach is also applicable for Sentinel-2 imagery (**Chapter 5.4.6**). Thiemann & Koschel mapped 21 lakes in the study area with calcite classification using one hyperspectral airborne data set (Thiemann & Koschel 2001), but this new classification approach enabled for the first time the long-term monitoring of calcite precipitation and a large-scale application based on Landsat and Sentinel-2 images. The Landsat images cover the entire northern Central European lowlands and the archive is immense, despite cloud coverage. Additionally, the new Sentinel-2 mission increases the number of available images.

Challenges of optical remotely-based water quality monitoring are atmospheric disturbances and their correction as well as cloud coverage (cf. **Chapter 1.2.2.1**). In this thesis, preprocessed Landsat surface reflectance images were ordered. The Sentinel-2 images were atmospherically corrected using the sen2cor software that is provided by ESA (cf. **Chapter 5.3.1**). This worked well, despite variation in the lake spectra (**Figure 5-13**), reduced the processing time, and improves the transferability of the approach. Remaining cloud coverage and cloud shadows cause misclassifications, thus, they need to be masked before the classification. Cloud and cloud shadow masks are provided for Landsat and Sentinel-2 images, but the Landsat masks are very wide and the Sentinel-2 cloud shadow classification failed above water surfaces. Thus, the development of individual masking algorithms is recommended. The sensitivity of the mask can be adapted depending on the study area and the research question (cf. **Chapter 5.3.1**). Gaps through cloud coverage must also be considered in the analysis of frequency and duration of calcite precipitation: even though Landsat and Sentinel-2 have regular acquisitions, cloud coverage causes large gaps in some years, so that (short) calcite precipitations are easily missed between two acquisitions (cf. **Chapter 5.5.3**).

Potential sources of error at the lakes are low water depth, high concentration of suspended minerals, yellow substances, or CDOM, or phytoplankton blooms. Those potentials can be reduced or evaluated: the selection of ROIs in the middle of the lakes reduces the possibility of misclassification due to low bathymetry. High concentrations of suspended minerals are mostly caused by sediment entry, e.g., by open soil and heavy rain events. Sediment entry is generally very low in this study area (Thiemann & Koschel 2001), but must be evaluated in other regions to avoid misclassification. Phytoplankton blooms can be misclassified as calcite precipitation, too, but considerable algal blooms are most likely in eutrophic lakes (Thiemann & Kaufmann 2000). Thus, information on the trophic states can be used for the evaluation of the results as well as the time of the events. In this thesis, all except for two classified calcite events occurred between May and end of September, but those two extraordinary events in March appeared green instead of turquoise and are probably misclassified algal blooms (**Chapters 5.4.5** and **5.5.1**).

Additionally, spatial heterogeneity of the lakes has to be considered for the transfer of the method to other regions: in the small lakes in northern Central European Lowlands, the lake colors are homogenous, with the exception of nearly separated lake basins. However, heterogeneous $CaCO_3$ concentrations within lake surface waters are known from large lakes like the Great Lakes and Lake Constance (Strong & Eadie 1978; Pulvermüller et al. 1995).

- Which specific results can be achieved for northern Central European lowlands and how can the new methods complement in situ measurements and proxy-based monitoring?

In this thesis Landsat archive data were used for the long-term monitoring of calcite precipitation at 24 lakes. The Landsat-derived monitoring provided valuable new data as only five of the 24 lakes have been monitored in situ, despite problems with large data gaps in the Landsat time series and occasional misclassifications (cf. **Chapters 5.5.1**, **5.5.2**, and **5.5.3**). The remotely-sensed results were combined with in situ $CaCO_3$ measurements, sediment traps and sediment core analysis (cf. **Chapters 5.4.2** and **5.4.5**): the advantages of Landsat-derived calcite precipitation are the usually high temporal coverage and the spatial monitoring instead of the point information of field measurements.

This study showed that 15 of the 24 lakes have at least one calcite precipitation event in the observation period from 1998 to 2015. The total lake area of the affected lakes is approximately

17 km^2. The frequency of monitored calcite precipitation events varied significantly between one detection and regular detections nearly every year. The duration also varied between the lakes, but was on average 37 days for the three lakes with regular calcite precipitation. At the Stechlinsee and FH, the influence of ecological restoration measures aiming at nutrient reduction in the lake water can be detected (cf. **Chapters 5.4.5** and **5.5.3**). Generally, the results of this thesis emphasizes the high variance of calcite precipitation in hardwater lakes and the need to monitor each lake individually, which is now possible using Landsat and Sentinel-2 imagery.

6.1.2 Overarching Research Question

This chapter answers the overarching research questions of the thesis within the framework of the interdisciplinary and international ICLEA virtual institute. ICLEA aims at the long-term and large scale monitoring of lakes. The purpose of remote sensing imagery is the temporal link between in situ measurements, proxy-based monitoring and the expansion of the monitoring to a large scale. Thus, the following questions arose from the interdisciplinary user perspective:

- What are the requirements for remote sensing data for the monitoring of (specific) lake parameters in the northern Central European lowlands?
- What is the greatest potential and what are the limitations of remote sensing imagery for long-term monitoring?
- What new ecological insights can be found for lakes in the northern Central European lowlands by using remote sensing archives?

6.1.2.1 Demands on Remote Sensing Imagery

In this thesis three remotely-sensed monitoring approaches for lakes in the northern Central European lowlands have been developed and evaluated. Remote sensing generally allows for large scale monitoring, but each of the three monitoring approaches has different demands on remote sensing data. The fundamental demands for the monitoring of lakes using remote sensing data are:

- long time series,
- high temporal resolution, and/or
- high spatial resolution.

The evaluation of the developed monitoring methods in this thesis shows that the successful application of the monitoring approaches is closely linked to the demands and limitations in the usage of remote sensing archive data.

The monitoring of lake level changes requires a (very) high spatial resolution, a long time series, and for the analysis of short-term changes of the lake level, additionally a high temporal resolution. Those demands limit the usable data: the reconstructed time series of lake levels using aerial photos may reach back up to 75 years. However, this time series has gaps of over ten years and lake level changes between the acquisitions are missed. Optical Earth observation satellites on the other hand provide more frequent acquisitions, but the time series are shorter, because of the insufficient spatial resolution of archive data. Old generations of Earth observations satellites and missions have lower spatial resolutions due to technical limitations or their focus on large spatial coverage (e.g., Landsat). On the other hand, very high-resolution

Earth observation satellites (e.g., WorldView-2/3, SPOT 6/7) are not useful for a monitoring with high temporal resolution, because of their limited archive data due to demand acquisitions, and charges for commercial image data. The RE Constellation with five satellites acquired Germany regularly since 2008. They have a high spatial resolution of 6.5 m x 6.5 m (resampled pixel size: 5 m x 5 m), and the image data are available for free for German scientific projects. However, the analysis of reconstructed lake levels using RE imagery shows that their spatial resolution is already challenging for an accurate reconstruction of small lake level changes: for the unambiguous reconstruction of lake levels, the shift of the water-land border has to be several times larger than the pixel size. As the lakes are characterized by seasonal as well as long-term lake level changes a regular monitoring is pursued. However, a regular monitoring is not possible with optical satellite imagery due to their sensitivity to weather (cloud coverage) and low solar angles in winter. The removal of those low quality images massively decreases the number of useful RE images for the reconstruction of lake levels.

Reed is unevenly distributed at the shoreline and the reed belts are long and narrow. Thus, high-resolution PolSAR imagery is essential for the monitoring. The monitoring of the reed phenology also requires a high temporal resolution of the PolSAR images. On the other hand, change detection of reed, related to lake level changes, requires a long time series. The greatest advantage of SAR Earth observation over optical images is the regular annual coverage, which is more robust to atmosphere and also, because only new generations of SAR satellites have (very) high spatial resolutions. Despite several high-resolution SAR missions, including the new Sentinel-1, the data base of images is still very small. SAR images are acquired in different microwave bands and polarization modes: whereas X-band and C-band scatter at the surface of vegetation, L-band penetrates vegetation due to its longer wavelength. The reed monitoring approach is based on dual-co-polarimetric TSX, but it is expect that the approach is transferable to other dual-co-polarimetric X-band or C-band SAR. However, in the past, most Earth observation missions were focused on single-polarimetric (HH or VV), dual-cross-polarimetric or quad-polarimetric SAR and only in recent times the potential of dual-co-polarimetric was recognized. Quad-polarimetric SAR images could be used for the decomposition of the scattering mechanism, and thus, for the monitoring of reed, too, but their higher number of polarimetric channels comes along with a reduced spatial resolution (cf. **Chapter 1.2.2.2**).

Calcite precipitation is an extensive limnological process, thus, medium-resolution imagery is sufficient for the monitoring from space, which allows for the exploitation of the full potential of long term Earth observation missions such as Landsat. The Landsat satellites have been acquiring the Earth regularly since 1972, which enables a long-term monitoring of calcite precipitation on a large spatial scale. Whereas the temporal resolution of the time series is low in the beginning, in recent times with multiple parallel Landsat satellite missions a high temporal resolution has been reached. This temporal resolution is further increased by the Sentinel-2 satellites. A high temporal resolution is important as calcite precipitation events usually last for a short period.

The comparison of the three monitoring approaches shows that the demands on the remote sensing data (long time series, high temporal resolution, and/or high spatial resolution) are critical for the application of the new monitoring approaches. None of the developed monitoring methods can take into account all three requirements at the same time. Thus, trade-offs between different demands are unavoidable and decrease the benefit of the methods (cf. long-time series but low temporal resolution of aerial photos vs. short-time series but high temporal resolution of satellite images). The main limitations are the spatial resolution and the temporal resolution, specifically in the beginning of Earth observation with few available satellites. Thus, the potential of remote sensing archives for the long-term monitoring of lakes

is best exploited if the lake parameter is detectable in medium-resolution imagery as in the case of the monitoring of calcite precipitation. SAR imagery enhances the changes of dense time series. However, older SAR missions are limited to medium-resolution imagery and even though todays SAR Earth observation missions have a high spatial resolution, they often do not fulfill other technical requirements such as polarimetry.

6.1.2.2 Constraints on Multi-Temporal Remote Sensing Imagery

Aside from the demands on remote sensing imagery, the multi-temporal analysis of large archive data sets requires specific processing to ensure the spatial accuracy of the images and the comparability of the measured signals within a time series. Because of the large image data sets the highest possible processing level of optical and SAR imagery was chosen to reduce time consuming processing. However, additional image processing was required for the analysis of the time series data.

The reconstruction of lake levels is very sensitive to spatial errors. Thus, even though the RE images were purchased as pre-processed orthorectified, resampled, radiometric, geometric, and terrain corrected level 3A images, further spatial corrections were required. For the comparison of water-land borders derived from different RE images, the relative accuracy between the images (cf. co-registration) and the absolute spatial accuracy has to be ensured, e.g., through comparison with a DOP (cf. **Chapter 3.3.1**). Validation of the absolute accuracy is only needed for one image, which is then used as master image for the automatic co-registration of all RE images based on Behling et al. (Behling et al. 2014).

The selection of suitable aerial photos from different data resources, the geo-referencing and the manual digitization of water-land borders are very time-consuming, but an automatization of the data processing is not feasible due to the distribution of aerial photos in different (physical) archives and their heterogeneity. The manual work, therefore, limited the use of aerial photos for the analysis of large spatial areas.

The use of dual-polarimetric TSX data for the extraction of water-land borders failed due to spatial inaccuracies, because the side-looking geometry of SAR still poses a significant challenge for the geometric correction. The position errors of the geocoded TSX images also decrease the accuracy of the reed mapping. However, for the monitoring of the phenology the high relative accuracy of the multi-temporal images was sufficient, as the “true reed” area was derived from the intersection of reed areas from the classified TSX image time series (cf. **Chapter 4.5.1**).

The monitoring of calcite precipitations is based on a number of extracted pixel values from ROIs in the middle of the lakes. Those extracted pixels are averaged and the ROIs were digitized manually. Thus, the requirements for absolute and relative spatial accuracy are much lower. Further optimization was not required as the Landsat archive images were delivered with sufficient spatial accuracies, which reduced the general processing time significantly.

Radiometric calibration is essential for multi-temporal optical and SAR images to ensure the comparability of the measured signals within a time series. The optical satellite images, RE, Landsat 5, 7, 8, and Sentinel-2, are already delivered as radiometrically corrected images and only TSX imagery had to be radiometrically calibrated. However, the optical images additionally require the calculation of TOA reflectance values from radiance and for the comparison of reflectance values within a time series or between the at ground reflectance values.

The atmospheric correction is the most complex and error-prone processing step in water remote sensing as the atmospheric correction models try to remove large noise (atmosphere)

from the small signal of water (cf. **Chapter 5.5.1**). The optimization of the atmospheric correction for individual images is challenging and time consuming: thus, in favor of a straightforward application of remote sensing data, the images were ordered according to their highest processing level and state-of-the-art processors were used (e.g., sen2cor for the atmospheric correction of Sentinel-2). For the reconstruction of lake levels using RE images, the calculation of TOA reflectance values is sufficient as each image is classified based on an individual Otsu threshold (**Chapter 3**). The monitoring of calcite precipitation using Landsat and Sentinel-2 images is based on a fixed threshold and validated with in situ measured water quality parameters, thus, an atmospheric correction is required: despite the different sensors and atmospheric corrections, this thesis shows that preprocessed Landsat 5, 7, and 8 surface reflectance images and the sen2cor processed Sentinel-2 images can be successfully used for a joint multi-temporal monitoring of calcite precipitation (**Chapter 5**).

The last challenge for the multi-temporal monitoring within this thesis was the omission of unsuitable images/image parts: for optical images cloud and cloud shadow masking are essential, but snow and ice can also render images for lake monitoring useless. Even though cloud and shadow masks are often delivered with the data, their quality differs: the cloud mask of RE missed too many small clouds, whereas the cloud, cloud shadow, and snow masks of Landsat were too conservative and the Sentinel-2 cloud shadow classification failed above water surfaces. Thus, the development of individual masking algorithms (cf. **Chapters 3.3.1** and **5.3.1**) is necessary for multi-temporal remotely-sensed lake monitoring. TSX imagery was unreliable in winter due to lake ice. An automatic removal of ice images was not possible in this first analysis of reed belts. Instead disturbed images were selected using weather data and information from the daily manual gauging at Lake Fürstenseer See.

6.1.2.3 New Results from Remotely-Sensed Monitoring

This thesis shows that the success of remotely-sensed monitoring methods depends on the properties of the satellite imagery and the demands on the processing: success hereby means the accuracy of monitoring results and the applicability of the method for long time series and large areas. Whereas the lake level reconstruction and the reed monitoring are successful on selected lakes, the remotely-sensed calcite monitoring covers a large time series (two decades) and is applicable on a large scale (cf. **Chapters 2** to **5**, summarized in **Chapter 6.1.1**). Thus, this thesis provides a method for the mapping and inventory of lakes with calcite precipitation using Landsat archive and Sentinel-2 imagery. Additionally, frequency and duration of the precipitation events can be estimated. This is an essential prerequisite, in combination with geochemical analyses, to investigate the role of permanent CO_2 storage in form of calcite in this region.

Generally, the remotely-sensed monitoring of specific lakes in this thesis emphasizes the temporal heterogeneity within lakes and the spatial heterogeneity between the lakes. The ecosystem of each lake reflects their individual flow dynamics, catchment characteristic, human impact, and micro climate. Consequently, monitoring results from one lake, may they be lake levels, reed distribution, or calcite precipitation, cannot be transferred to other lakes. Thus, for a better understanding of landscape and climate dynamics an individual monitoring of a large number of lakes is required. This goal can only be achieved through the use of remote sensing archives, but the demands on the remote sensing data must be considered.

6.2 Outlook

Three new remotely-sensed monitoring methods were developed in this thesis and thoroughly evaluated with different in situ measurements and proxy data. The method development strongly considered the user perspective, anchored in the interdisciplinary context of ICLEA. Based on the three methods, the requirements for remote sensing data and time series analysis were discussed. Additionally, the potential for long-term monitoring and the applicability to large scales was evaluated. Despite the time invested in this work, many aspects and additional research ideas were beyond the scope of this thesis. Thus, this final chapter discusses the prospects of lake monitoring in the northern Central European lowlands. This includes potential methodological developments for the proposed approaches and further applications for lake monitoring using remote sensing imagery.

6.2.1 Lake Level Reconstruction

The large scale application of remotely-sensed indirect lake level reconstruction is limited by its requirements to remote sensing data and the lakes, as well as time-consuming manual work in the case of aerial photos. Nevertheless, for selected lakes aerial photos are an important tool for lake level reconstruction, specifically in combination with proxy-data from sediment or dendrological analysis and modelling. Based on the experience with the analysis of RE imagery, the lake level reconstruction using aerial photos could be optimized by

- the selection of (shallow) shoreline parts without vegetation and a clearly visible water-land border, instead of using the entire water-land border of the lake (cf. **Figure 3-5**)
- taking the mode value of the range of extracted lake level values (cf. **Figure 2-5**) instead of the mean value. The mode value is more robust towards misclassifications of the water-land border and represents the true lake level more accurately (cf. **Chapter 3.4.4**).

Lake level reconstruction is only unambiguously possible if the shift of the water-land border is several times larger than the pixel size of the images. Thus, the method either requires very high-resolution spatial imagery, massive lake level changes or very shallow shorelines (without vegetation) that reflect even small lake level changes. Cloud coverage and low solar angles additionally reduce the temporal resolution. Whereas early Earth observation missions (e.g. Landsat) were strictly limited by the trade-off between high-resolution imagery and large coverage with fast repetition times, the frontiers of technological possibilities are extended with every new satellite. High hopes currently lie with the new European Earth observation mission Copernicus (Malenovský et al. 2012) that aims at closing this gap with large swaths and high spatial resolution: the SAR satellites Sentinel-1a and -1b acquire the Earth's surface with a ~5 m x 5 m resolution (Stripmap mode) and Sentinel-2a acquires the Earth's surface with up to 10 m resolution since 2015. The launch of Sentinel-2b is planned for 2017 (European Space Agency (ESA) for Earth observation 2017b; Drusch et al. 2012) (cf. **Chapter 1.2.2**). The acquisition with each of the two satellites also increases the temporal resolution and, in the case of optical imagery, the chances of cloud-free images. The two Sentinel-1 satellites together have a repeat cycle of 6 days (Sentinel-1 Team 2013), the two Sentinel-2 satellites of 5 days (European Space Agency (ESA) for Earth observation 2017b).

Unfortunately, Sentinel-2 images are probably not suitable for the accurate and unambiguous reconstruction of lake levels (cf. **Chapter 2**), despite their higher spatial resolution. The spatial resolution of the RE band with 6.5 m (5 m resampled) was already challenging, thus, the 10 m

resolution of Sentinel-2's band is expected to be even less accurate. The advantage of the Sentinel-2 satellites are their two SWIR bands for more robust water mapping (Li et al. 2013; Xu 2006). However, their resolution is further reduced to 20 m (European Space Agency (ESA) for Earth observation 2017b). One possible way to improve the extraction of the water-land border from Sentinel-2 images, despite their low resolution, could be the spectral unmixing of pixels at the shoreline (Keshava & Mustard 2002). Spectral unmixing might also be useful for the analysis of RE imagery at shallow shorelines with vegetation.

Another approach to achieve high spatial and temporal resolution is the use of a swarm of high-resolution optical satellites with small coverage each. For example, RE imagery is provided by a swarm of five structurally identical satellites. Planet Labs, Inc., which also bought the RE satellite swarm in 2015, plays a leading role in this area. Their swarm of over 100 tiny CubeSats satellites acquires the Earth's surface in R, G, B, and NIR and provides, with the exception of weather-dependent gaps, daily imagery with 3 m resolution (Planet Labs n.d.). However, their commercial background limits their use for ecological monitoring. Future non-commercial missions may follow their lead.

A year-long continuous monitoring, undisturbed by clouds and low sun angles, can always be achieved by high-resolution SAR imagery. However, single-polarimetric X-band and C-band SAR are scattered by vegetation due to their relative short wavelengths and therefore require more or less vegetation free shorelines (cf. **Chapter 1.2.2.2,** (Heine et al. 2014)) such as optical imagery. High-resolution L-band SAR imagery, is preferred for the monitoring of water below vegetation as it penetrates vegetation due to its long wavelength (Horritt 2003; Smith 1997). So far, only few high-resolution SAR missions use L-band, but ALOS-2 was launched in 2014 and two L-band missions are in planning: the start of the NASA-ISRO SAR Mission (NISAR) is scheduled for 2020 (Jet Propulsion Laboratory & California Institute of Technology n.d.) and Tandem-L is scheduled for 2023 (Eineder et al. 2014).

The acquisition of quad- or dual-co-polarimetric SAR images decreases the spatial resolution of the SAR, but allows the decomposition of the SAR signal (Ji & Wu 2015; Yajima et al. 2008; Cloude n.d.). Thus, PolSAR has potential for the monitoring of water below vegetation. This thesis shows that double-bounce scattering, specifically in winter, indicates water below vegetation in dual-co-polarimetric X-band SAR (cf. **Chapter 4)**. However, the spatial inaccuracies and the low number of high-resolution PolSAR images limit their use for long-term lake level monitoring.

Instead of the indirect extraction of lake levels, in future, the direct measurements via altimeter might be possible for a large number of lakes. So far, direct altimeter-based lake level measurements for lakes in northeastern Germany are not available due to their small sizes or the missing coverage by altimeter tracks (Schwatke et al. 2015; Schwatke n.d.; Alsdorf et al. 2007). However, the number of altimeter satellites increases steadily and with them the chances to cover at least the larger and more compact lakes. The European Earth observation mission Copernicus also covers radar altimetry with their satellites Sentinel-3a (launched 2016), Sentinel-3b (start planned in 2017), and Sentinel-3c (launch planned before 2020) (Sentinel-3 Team 2013) (Sentinel-3 Team 2013).

6.2.2 Reed Belts

The monitoring of reed belts is affected by spatial inaccuracies. Long-term monitoring and transferability to other lakes is limited due to the lack of dual-polarimetric archive data. Whereas TSX intensity images can be ordered as geocoded images, the polarimetric parameters

of this thesis had to be calculated from SSC images and geocoded afterwards. Because of the side-looking geometry, the geocoding is challenging and caused inaccuracies in the monitoring of reed areas and water-land borders. Thus, hopefully in the future, the order of geocoded dual-polarimetric parameters from TSX images will be offered, too. Until then, the (absolute) spatial accuracy of the SAR imagery could be increased by the use of a different geocoding approach in combination with a higher resolution DEM or an additional geo-referencing or co-registration of the images based on optical images.

Because X-band and C-band SAR scatter on leaves of vegetation, it is expected that the TSX-based reed monitoring is transferable to other X-band to C-band satellites. However, high-resolution dual-polarimetric X-band SAR images (TSX, COSMO-SkyMed) and C-band SAR images (Radarsat-2) are mostly acquired on demand. The new Sentinel-1 satellites are C-band SAR and they acquire dual-polarimetric imagery by default, albeit, only dual-cross- and no dual-co-polarimetric channels (European Space Agency (ESA) 2016).

6.2.3 Calcite Precipitation

The monitoring of calcite precipitation proved very useful for long-term and large scale monitoring and this thesis emphasized the importance of an application at the very large scale, because of the heterogeneity of the 24 monitored lakes. Knowledge about the number of affected lakes, their lake area and the frequency and duration of calcite precipitation is important, because the sedimentation of the calcite particles function as carbon and phosphorus sink. Thus, the remotely-sensed monitoring of lakes is, in combination with geochemical analyses, essential for the investigation of the role of calcite precipitation for permanent carbon storage.

The developed monitoring approach for calcite precipitation uses Landsat and Sentinel-2 imagery and is supported by spatial and trophic information on the lakes. The trophic state of the lake can be used for the evaluation of potential misclassifications through phytoplankton blooms (cf. **Chapter 5**). Spatial information on lakes in Germany is available at “Bundesamt für Kartographie und Geodäsie” (cf. (BKG 2011)), but lake polygons for the entire northern Central European lowlands are freely provided by OpenStreetMap (OSM) (OpenStreetMap 2016). The lake polygons are required for the calculation of the lake surface areas, but could also be used for an automatic selection of ROIs for the extraction of mean lake reflectance values. The selection of ROI in this thesis was based on manual work, but an automatization of the process can be achieved, e.g. by a negative buffering of the OSM lake polygons to avoid shallow water areas at the edges of the lakes.

The Landsat satellites allow the construction of a long time series, but its temporal resolution is low in the beginning. In recent times with multiple parallel Landsat satellite missions a high temporal resolution has been reached, which is now further increased by Sentinel-2a and soon also by Sentinel-2b. The Landsat mission will also be continued and the launch of the next Landsat 9 satellite is planned for 2020 (NASA & U.S. Geological Survey 2017). Thus, the effectiveness of optical satellite monitoring for calcite precipitation will be further improved. The increased number of images enhances the chance of cloud-free acquisitions and decreases the possibility of missed calcite precipitation events.

The temporal resolution can be further enhanced by the addition of medium-resolution (200-250 m) satellite imagery. The satellites Terra (launch 1999) and Aqua (launch 2002) with their moderate-resolution imaging spectroradiometer (MODIS) acquire the Earth every one to two days (NASA 2017). MODIS imagery has been used for calcite precipitation monitoring (Long

et al. 2014; Dierssen et al. 2008). The Sentinel-3 satellites are also specifically equipped with an "Ocean and Land Colour Instrument" (Sentinel-3 Team 2013). The Sentinel-3a has a repeat cycle of 27 days, but will be complemented by Sentinel-3b (launch planned for 2017) and Sentinel-3c (launch planned before 2020). Thus, medium-resolution satellites might be an additional lake monitoring opportunity for larger and compactly shaped lakes.

The monitoring approach for calcite precipitation in this thesis is a binary classification, without an estimation of $CaCO_3$ concentrations in the lakes. An estimation of the $CaCO_3$ concentration was not feasible due to the differences in the lake spectra between the multi-spectral sensors and their atmospheric corrections. However, Thiemann et al. proposed an approach for the estimation of $CaCO_3$ concentration using hyperspectral imagery (Thiemann & Koschel 2001). Thus, the use of hyperspectral imagery should be considered for future calcite precipitation monitoring, especially considering the coming hyperspectral Earth observation mission EnMAP (launch planned for 2018) (Guanter et al. 2015).

6.2.4 Chlorophyll-A

Measurement of chl-a is beneficial for remotely-sensed calcite precipitation monitoring, because algal blooms are a potential source for misclassifications. Algal blooms also reduce the water quality and can be harmful (Paerl et al. 2001). Harmful freshwater algal blooms are enhanced by eutrophication and high temperature, thus, regular monitoring is very important in times of climate change (Paerl & Otten 2013; Anderson et al. 2002; O'Neil et al. 2012; Paerl & Huisman 2009). Regular chl-a measurements and the determination of the trophic state of lakes are also required by the Water Framework ("WRRL") aiming at an ecological improvement of European lakes and rivers (cf. **Chapter 1.2.1**).

Chl-a concentration of lakes was measured using hyperspectral remote sensing imagery, in northern Central European lowlands (Thiemann & Kaufmann 2002) and in other regions (Torbick & Corbiere 2015; Kutser 2004; Östlund et al. 2001; Heege & Fischer 2004; Hunter et al. 2010; Moses et al. 2011). Multi-spectral imagery has been used, too, (Brandão et al. 2016; Gholizadeh et al. 2016; Luoheng Han & Jordan 2005; Oyama et al. 2015). The acquisition of the red edge band in multi-spectral imagery significantly improves the accuracy and robustness for ch-a measurement, e.g. in case of high suspended mineral concentrations (Torbick & Corbiere 2015; Weichelt et al. 2014; Wen et al. 2014) (cf. **Chapter 1.2.2.1**). Whereas Landsat images, including the future Landsat 9 mission, do not cover the red edge, the new Sentinel-2 mission does. First tests with Sentinel-2 images showed their potential for the estimation of chl-a concentrations (Toming et al. 2016). It is expected that they can be used in the future for the distinction of calcite precipitation and algal blooms and, thus, improve the proposed calcite precipitation monitoring approach.

6.2.5 Ice Coverage and Wind

Ice coverage, wind speed, and wind direction affect the mixing of the lake water and thus, also the distribution and concentration of phytoplankton in the water, as well as the occurrence of calcite precipitation. This interaction is researched in the northern Central European lowlands at Lakes Tiefer See (Kienel et al. 2017) and Stechlinsee (Leibniz-Institute of Freshwater Ecology & Inland Fisheries (IGB) 2016), but generally in situ measurements are rare.

Near-surface winds over land cannot be measured directly via satellites, but wind speed and direction can be estimated by the analysis of waves. Specifically SAR acquisitions with short wavelengths are sensitive to ripples and waves on the water surface (Martinis 2010) (cf.

Chapter 1.2.2.2) and SAR-based wave and wind retrieval has been frequently used on ocean and coastal areas (Horstmann et al. 2003; Vachon & Dobson 2000; Lehner et al. 2000; Chapron et al. 2001; Mastenbroek 1998). Thus, a transfer of the approaches, at least to large lakes, should be tested.

Because clouds and low solar angles hamper regular optical monitoring, ice monitoring is also mostly based on SAR imagery (Carsey 1992; Rees 2006). Previous studies used single-polarimetric (Yang & Clausi 2012; Soh & Tsatsoulis 1999) and different multi-polarimetric SAR imagery (Scheuchl 2006; Geldsetzer & Yackel 2009; Scheuchl et al. 2005) for (sea) ice monitoring. The use of polarimetric SAR is preferred here (Nghiem & Leshkevich 2007).

So far, the low resolution of old SAR satellites and the limited availability of PolSAR images restricted their use for lake monitoring, but the new Sentinel-1 satellites acquire the Earth's surface regularly and with high resolution. Thus, they offer great new potential for lake ice monitoring and wind retrieval at (large) lakes (Malenovský et al. 2012; Ardhuin et al. 2015).

6.2.6 Water Temperature

Another lake parameter that is often requested in limnological monitoring is the water surface temperature. The lake temperature influences phytoplankton growth and algal blooms (Paerl & Otten 2013), calcite precipitation (Gal et al. 1996; Kienel et al. 2017), and temperature changes can indicate flow dynamics to and within the lake.

Lake surface temperature can be measured from space using thermal infrared (TIR) sensors, e.g. of the Landsat satellites 4-8 (Barsi et al. 2003; Wloczyk et al. 2006; Giardino et al. 2001; Schneider & Mauser 1996; Schott et al. 2001). However, the spatial resolution (Landsat 4-5: 120 m, Landsat 7: 60 m, and Landsat 8: 100 m) limits their use for small lakes and for the mapping of intra lake variability. The new Sentinel-3 satellites acquire TIR, too, with a "Sea and Land Surface Temperature Radiometer" (SLSTR). The SLSTR provides the surface temperature with a very high level of accuracy (better than 0.3 K), but with a very low spatial resolution of 1 km (Sentinel-3 Team 2013). This low resolution limits its use for lake monitoring.

6.2.7 Future Prospects

With the start of the large European Copernicus mission the research community is putting great hopes in its new satellite imagery with high spatial and temporal resolution, available as open data. However, a further aim of the European Union with the Copernicus mission is the extensive application of satellite images beyond research and its use in society, e.g. in state agencies. The application of remote sensing imagery for a broad user base is also the stated goal of other Earth observation missions. However, to exploit the full capabilities of remote sensing, it is essential to connect potential users with the scientific remote sensing community: users interested in utilizing remote sensing imagery may not be familiar with the possibilities and limitations of the technology, whereas the scientific community risks developing new applications that disregard the needs of the end user. Thus, the connection of the two groups is an ongoing challenge of remote sensing. This thesis is a further step in this direction and addresses this challenge with regard to lake monitoring.

Bibliography

Abarca-Del-Rio, R. et al., 2012. Does Lake Titicaca still control the Lake Poopó system water levels? An investigation using satellite altimetry and MODIS data (2000–2009). *Remote Sensing Letters*, 3(March 2015), pp.707–714.

Adrian, R. et al., 2009. Lakes as sentinels of climate change. *Limnology and Oceanography*, 54(6part2), pp.2283–2297. Available at: http://doi.wiley.com/10.4319/lo.2009.54.6_part_2.2283 [Accessed December 16, 2016].

Alesheikh, A., Ghorbanali, A. & Nouri, N., 2007. Coastline change detection using remote sensing. *International journal of Environmental Science and Technology*, 4(1), pp.61–66.

Allen, R. et al., 1998. Crop evapotranspiration-Guidelines for computing crop water requirements-FAO Irrigation and drainage paper 56. *FAO, Rome*. Available at: http://www.academia.edu/download/40878584/Allen_FAO1998.pdf [Accessed December 16, 2016].

Alsdorf, D.E., Rodriguez, E. & Lettenmaier, D.P., 2007. Measuring surface water from space. *Reviews of Geophyics*, 45(2), pp.1–24. Available at: http://www.earthsciences.osu.edu/water/publications/RoG_WATERHM_2007.pdf [Accessed January 14, 2013].

Amitrano, D. et al., 2014. Sentinel-1 for monitoring reservoirs: A performance analysis. *Remote Sensing*, 6(11), pp.10676–10693.

Amt für Geoinformation, V.K., Satellitenpositionierungsdienst-SAPOS®. Available at: http://www.laiv-mv.de/land-mv/LAiV_prod/LAiV/AfGVK/Festpunkte,_SAPOS/SAPOS/index.jsp.

Anders, F. & Byrnes, M., 1991. Accuracy of shoreline change rates as determined from maps and aerial photographs. *Shore and Beach*, 59(1), pp.17–26. Available at: ftp://205.193.112.140/pub/library/2QRU.pdf [Accessed April 4, 2014].

Anderson, D.M., Glibert, P.M. & Burkholder, J.M., 2002. Harmful Algal Blooms and Eutrophication: Nutrient Sources, Composition, and Consequences. *Estuarine Research Federation Estuaries*, 704(4b), pp.704–726.

Annor, F.O. et al., 2009. Delineation of small reservoirs using radar imagery in a semi-arid environment: A case study in the upper east region of Ghana. *Physics and Chemistry of the Earth, Parts A/B/C*, 34(4–5), pp.309–315. Available at: http://linkinghub.elsevier.com/retrieve/pii/S1474706508002222 [Accessed July 18, 2011].

Arbor, A. et al., 1976. Utilization of Satellite Data for Inventorying Prairie Ponds and Lakes. *Photogrammetric Engineering and Remote Sensing*, 42(5), pp.685–694.

Ardhuin, F. et al., 2015. Estimates of ocean wave heights and attenuation in sea ice using the SAR wave mode on Sentinel-1A. *Geophysical Research Letters*, 42(7), pp.2317–2325.

Bachor, A. et al., 2006. *Gewässergütebericht Mecklenburg-Vorpommern 2003/2004/2005/2006: Ergebnisse der Güteüberwachung der Fließ-, Stand- und Küstengewässer und des Grundwassers in Mecklenburg-Vorpommern*, Landesamt für Umwelt Naturschutz und Geologie Mecklenburg-Vorpommern.

Baker, V.R., 2008. Paleoflood hydrology: Origin, progress, prospects. *Geomorphology*, 101(1), pp.1–13.

Barrette, J., August, P. & Golet, F., 2000. Accuracy Assessment of Wetland Boundary Delineation Using Aerial Photography and Digital Orthophotography. *Photogrammetric Engineering & Remote Sensing*, 66(4), pp.409–416.

Barsi, J.A. et al., 2003. Landsat TM and ETM+ thermal band calibration. *Canadian Journal*

of Remote Sensing, 29(2), pp.141–153.
Baup, F., Frappart, F. & Maubant, J., 2014. Combining high-resolution satellite images and altimetry to estimate the volume of small lakes. *Hydrology and Earth System Sciences*, 18(5), pp.2007–2020. Available at: http://www.hydrol-earth-syst-sci.net/18/2007/2014/ [Accessed May 27, 2014].
Bayram, B. et al., 2004. Coast line change detection using CORONA, SPOT and IRS 1D images. In *XXth Congress of the International Society for Photogrammetry and Remote Sensing*. Istanbul, pp. 437–441.
Bégin, Y., 2001. Tree-Ring Dating of Extreme Lake Levels at the Subarctic–Boreal Interface. *Quaternary Research*, 55(2), pp.133–139.
Behling, R., 2016. *Derivation of Spatiotemporal Landslide Activity for Large Areas Using Long-Term Multi-Sensor Satellite Time Series Data*. Technische Universität Berlin.
Behling, R. et al., 2014. Robust automated image co-registration of optical multi-sensor time series data: Database generation for multi-temporal landslide detection. *Remote Sensing*, 6, pp.2572–2600.
Van Beijma, S., Comber, A. & Lamb, A., 2014. Random forest classification of salt marsh vegetation habitats using quad-polarimetric airborne SAR, elevation and optical RS data. *Remote Sensing of Environment*, 149, pp.118–129. Available at: http://dx.doi.org/10.1016/j.rse.2014.04.010.
Benito, G. & Thorndycraft, V.R., 2005. Palaeoflood hydrology and its role in applied hydrological sciences. *Journal of Hydrology*, 313(1), pp.3–15.
Betbeder, J. et al., 2014. Multitemporal classification of TerraSAR-X data for wetland vegetation mapping. *Journal of Applied Remote Sensing*, 8(1), pp.83648-1-83648–16. Available at: http://remotesensing.spiedigitallibrary.org/article.aspx?doi=10.1117/1.JRS.8.083648.
Bierwirth, P.N., Lee, T.J. & Burne, R. V., 1993. Shallow Sea-Floor Reflectance and Water Depth Derived by Unmixing Multispectral Imagery. *Photogrammetric Engineering and Remote Sensing*, 59(3), pp.331–338.
Biondi, F. & Strachan, S., 2012. Dendrohydrology in 2050: Challenges and Opportunities. In *Toward a Sustainable Water Future*. Reston, VA: American Society of Civil Engineers, pp. 355–362. Available at: http://ascelibrary.org/doi/abs/10.1061/9780784412077.ch38 [Accessed December 16, 2016].
BKG, 2011. Geodaten des Bundesamt für Kartographie und Geodäsie (BKG): Digitales Basis-Landschaftsmodell (Basis-DLM), delivered on 27 June 2011. Available at: www.geodatenzentrum.de.
Bleile, R., 2008. Quetzin - Eine spätslawische Burg auf der Kohlinsel im Plauer See. Befunde und Funde zur Problematik slawischer Inselnutzungen in Mecklenburg-Vorpommern. *Beiträge zur Ur- und Frühgeschichte Mecklenburg-Vorpommerns*, 48, pp.1–216.
Blöschl, G. & Montanari, A., 2010. Climate change impacts-throwing the dice? *Hydrological Processes*, 24(3), pp.374–381.
Boak, E.H. & Turner, I.L., 2005. Shoreline Definition and Detection: A Review. *Journal of Coastal Research*, 214, pp.688–703. Available at: http://www.bioone.org/doi/abs/10.2112/03-0071.1 [Accessed March 23, 2014].
Bochow, M. et al., 2012. On the Use of Airborne Imaging Spectroscopy Data for the Automatic Detection and Delineation of Surface Water Bodies. In Y. Chemin, ed. *Remote Sensing of Planet Earth*. InTech, pp. 3–22. Available at: http://www.intechopen.com/articles/show/title/on-the-use-of-airborne-imaging-spectroscopy-data-for-the-automatic-detection-and-delineation-of-surf.
Bogenrieder, A., 1990. Das Schilfrohr (Phragmites australis (Cav.) Trin). *Biologie in unserer Zeit*, 20(4), pp.221–222.

Braden, B., 1986. The Surveyor's Area Formula. *The College Mathematics Journal*, 17(4), pp.326–337.

Brakenridge, G.R. et al., 2005. Space-based measurement of river runoff. *Eos, Transactions American Geophysical Union*, 86(19), p.185. Available at: http://doi.wiley.com/10.1029/2005EO190001.

Brandão, L.P.M., Staehr, P.A. & Bezerra-Neto, J.F., 2016. Seasonal changes in optical properties of two contrasting tropical freshwater systems. *Journal of Limnology*, p.18.

Brauns, M., Garcia, X.F. & Pusch, M.T., 2008. Potential effects of water-level fluctuations on littoral invertebrates in lowland lakes. *Hydrobiologia*, 613, pp.5–12.

Brázdil, R. et al., 2005. Historical Climatology In Europe – The State Of The Art. *Climatic Change*, 70(3), pp.363–430. Available at: http://link.springer.com/10.1007/s10584-005-5924-1 [Accessed December 16, 2016].

Brázdil, R., Kundzewicz, W. & Bentido, G., 2006. Historical hydrology for studying flood risk in Europe. *Hydrological Sciences Journal*, 51(5), pp.739–764. Available at: http://www.tandfonline.com/doi/abs/10.1623/hysj.51.5.739 [Accessed December 16, 2016].

Breiman, L., 2001. Random forests. *Machine learning*, pp.5–32. Available at: http://link.springer.com/article/10.1023/A:1010933404324.

Brekke, C. & Solberg, A.H.S., 2005. Oil spill detection by satellite remote sensing. *Remote Sensing of Environment*, 95(1), pp.1–13.

Bresciani, M. et al., 2009. Monitoring reed vegetation in environmentally sensitive areas in Italy. *Italian Journal of Remote Sensing*, 41(2), pp.125–137.

Brisco, B. et al., 2011. SAR polarimetric change detection for flooded vegetation. *International Journal of Digital Earth*, 6(July 2014), pp.1–12.

Brix, H., Sorrell, B.K. & Lorenzen, B., 2001. Are phragmites-dominated wetlands a net source or net sink of greenhouse gases? *Aquatic Botany*, 69(2–4), pp.313–324.

Brose, F. & Heussner, K.-U., 2002. Zur Klimaentwicklung E. Gringmuth-Dallmer & L. Leciejewicz, eds. *Forschungen zu Mensch und Umwelt im Odergebiet in ur- und frühgeschichtlicher Zeit.*, 60, pp.27–33.

Brothers, S. et al., 2014. A feedback loop links brownification and anoxia in a temperate, shallow lake. *Limnology and Oceanography*, 59(4), pp.1388–1398. Available at: http://doi.wiley.com/10.4319/lo.2014.59.4.1388 [Accessed December 16, 2016].

Brown, A.G., 2002. Learning from the past: palaeohydrology and palaeoecology. *Freshwater Biology*, 47(4), pp.817–829. Available at: http://doi.wiley.com/10.1046/j.1365-2427.2002.00907.x [Accessed December 16, 2016].

Brunskill, G.J., 1969. Fayetteville Green Lake, New York. II. Precipitation and sedimentation of calcite in a meromictic lake with laminated sediments. *Limnology and Oceanography*, 14(6), pp.830–847.

Büntgen, U. et al., 2011. 2500 Years of European Climate Variability and Human Susceptibility. *Science*, 331(6017).

Carsey, F.D., 1992. *Microwave Remote Sensing of Sea Ice*, American Geophysical Union. Available at: http://onlinelibrary.wiley.com/book/10.1029/GM068 [Accessed February 20, 2017].

Castree, N. et al., 2009. *A companion to environmental geography*, Chichester, UK: Wiley-Blackwell, A John Wiley & Sons, Ldt., Publication.

Chapron, B., Johnsen, H. & Garello, R., 2001. Wave and wind retrieval from SAR images of the ocean. *Annales des telecommunications*, 56(11–12), pp.682–699.

Charbonneau, F.J. et al., 2010. Compact polarimetry overview and applications assessment. *Canadian Journal of Remote Sensing*, 36(SUPPL. 2), pp.S298--S315.

Chipman, J.W., L.G.O. and A.A.G., 2009. *Remote sensing methods for lake management: A*

guide for resource managers and decision-makers,
Choiński, A., 2009. Changes in the area of lakes from the Obra River drainage basin taking place from the beginning of the 19th century. *Limnological Review*, 9(4), pp.159–164. Available at: http://www.ptlim.pl/lr2009/pdf/LR2009_16.pdf [Accessed March 12, 2014].
Clarke, R.T., 2007. Hydrological prediction in a non-stationary world. *Hydrology and Earth System Sciences*, 11(1), pp.408–414. Available at: http://www.hydrol-earth-syst-sci.net/11/408/2007/ [Accessed December 16, 2016].
Cloude, S., The dual polarization entropy/alpha decomposition: a PALSAR case study. In *Proc. PolinSAR*. Frascati, Italy, pp. 1–6. Available at: http://adsabs.harvard.edu/abs/2007ESASP.644E...2C [Accessed February 12, 2013].
Cloude, S. & Pottier, E., 1997. An entropy based classification scheme for land applications of polarimetric SAR. *Geoscience and Remote Sensing, IEEE Transactions on*, 35(1), pp.68–78.
Cloude, S.R., 2009. Dual versus quadpol: a new test statistic for radar polarimetry. In *Proc. of "4th Int. Workshop on Science and Applications of SAR Polarimetry and Polarimetric Interferometry – PolInSAR 2009."* pp. 1–8.
Cook, E. & Kairikukstis, L., 1990. *Methods of dendrochronology*, Kluwer, Dortrecht: International Institute for Applied System Analysis. Available at: http://agris.fao.org/agris-search/search.do?recordID=US201300652774.
Corcoran, J., Knight, J. & Gallant, A., 2013. Influence of Multi-Source and Multi-Temporal Remotely Sensed and Ancillary Data on the Accuracy of Random Forest Classification of Wetlands in Northern Minnesota. *Remote Sensing*, 5(7), pp.3212–3238. Available at: http://www.mdpi.com/2072-4292/5/7/3212/.
Cordshagen, C., 1986. Neue Erkenntnisse zum Wirken Tilemann Stellas als Karthograph in Mecklenburg. *Archivmitteilungen*, 36(5), pp.158–160.
Crétaux, J.-F., 2012. Hydrology from Space: a decade of development; A potential for future services. *CNES, Legos, Toulouse, France Geneva, WMO, Nov 2012*.
Crowell, M., Leatherman, S. & Buckley, M., 1991. Historical shoreline change: error analysis and mapping accuracy. *Journal of Coastal Research*, 7(3), pp.839–852. Available at: http://www.jstor.org/stable/4297899 [Accessed March 14, 2014].
Csaplovics, E., 1984. A Practical Application of Colour Infrared Image Interpretation - The Classification of the reed of Lake Neusiedl (Austria). In *ISPRS Archive XXV (A7)*. pp. 143–152.
Csaplovics, E. & Nemeth, E., 2014. Airborne Optical Imaging in Support of Habitat Ecological Monitoring of the Austrian Reed Belt of Lake Neusiedl. In *Proceedings GISScience RSGIS4HQ*. Wien, Austria, pp. 163–167.
Curran, P.J., Dungan, J.L. & Peterson, D.L., 2001. Estimating the foliar biochemical concentration of leaves with reflectance spectrometry: Testing the Kokaly and Clark methodologies. *Remote Sensing of Environment*, 76(3), pp.349–359.
Czymzik, M., Dulski, P. & Plessen, B., 2010. A 450 year record of spring-summer flood layers in annually laminated sediments from Lake Ammersee (southern Germany). *Water Resources Research*, 46(W11528). Available at: https://www.researchgate.net/profile/Ulrich_Von_Grafenstein2/publication/251424732_A_450-year_record_of_springsummer_flood_layers_in_annually_laminated_sediments_from_Lake_Ammersee_(Southern_Germany)/links/0c960533150d224987000000.pdf [Accessed December 16, 2016].
Danklmayer, A. et al., 2008. Analysis of atmospheric propagation effects in Terrasar-X images. In *EEE Geoscience and Remote Sensing Symposium (IGARSS), Boston,*

Massachusetts, USA. p. II-533-II-536. Available at: http://ieeexplore.ieee.org/xpls/abs_all.jsp?arnumber=4779046 [Accessed July 26, 2012].

Davaasuren, N. & Meesters, E.H.W.G., 2012. *Extent and health of mangroves mangroves in Lac Bay Bonaire using satellite data*,

Department of the Interior & U.S. Geological Survey, 2016. *Product Guide - Provisional Landsat 8 surface reflectance product, Version 2.1*, Sioux Falls,SD, USA: U.S. Geological Survey. Available at: https://landsat.usgs.gov/landsat-surface-reflectance-high-level-data-products [Accessed August 17, 2016].

Deschamps, B. et al., 2012. Towards operational radar-only crop type classification: comparison of a traditional decision tree with a random forest classifier. *Canadian Journal of Remote Sensing: Journal canadien de télédétection*, 38(1), pp.60–68.

Deutscher Wetterdienst (DWD), DWD Climate Data Center (CDC): Langjährige Stationsmittelwerte für die Klimareferenzperiode 1961-90.

Dierssen, H.M., Zimmerman, R.C. & Burdige, D.J., 2008. Optics and remote sensing of Bahamian carbonate sediment whitings and potential relationship to wind-driven Langmuir circulation. *Biogeosciences Discussions*, 5(6), pp.4777–4811.

Dietrich, O., Steidl, J. & Pavlik, D., 2012. The impact of global change on the water balance of large wetlands in the Elbe Lowland. *Regional Environmental Change*, 12(4), pp.701–713. Available at: http://link.springer.com/10.1007/s10113-012-0286-5 [Accessed December 16, 2016].

Dittrich, M. & Koschel, R., 2002. Interactions between calcite precipitation (natural and artificial) and phosphorus cycle in the hardwater lake. *Hydrobiologia*, 469, pp.49–57.

Dressler, M. et al., 2007. Multi-proxy Reconstruction of Trophic State, Hypolimnetic Anoxia and Phototrophic Sulphur Bacteria Abundance in a Dimictic Lake in Northern Germany over the past 80 Years. *Journal of Paleolimnology*, 37(2), pp.205–219. Available at: http://link.springer.com/10.1007/s10933-006-9013-x [Accessed January 10, 2017].

Drusch, M. et al., 2012. Sentinel-2: ESA's Optical High-Resolution Mission for GMES Operational Services. *Remote Sensing of Environment*, 120, pp.25–36.

Du, Y. et al., 2016. Water bodies' mapping from Sentinel-2 imagery with Modified Normalized Difference Water Index at 10-m spatial resolution produced by sharpening the swir band. *Remote Sensing*, 8(4).

Dusseux, P. et al., 2014. Combined use of multi-temporal optical and radar satellite images for grassland monitoring. *Remote Sensing*, 6(7), pp.6163–6182.

Eineder, M. et al., 2014. *Tandem-L: Satellite Mission Proposal for Monitoring Dynamic Processes on the Earth ' s Surface*, Available at: http://www.dlr.de/hr/en/desktopdefault.aspx/tabid-8113/14171_read-35837/.

Eineder, M. et al., 2013. *TerraSAR-X Ground Segment, Basic Product Specification Document*,

European Space Agency (ESA), 2016. Copernicus: Sentinel-1 data product. Available at: http://www.esa.int/Our_Activities/Observing_the_Earth/Copernicus/Sentinel-1/Data_products [Accessed December 5, 2016].

European Space Agency (ESA) for Earth observation, 2017a. Copernicus: Mission details of Sentinel-1. Available at: https://earth.esa.int/web/guest/missions/esa-operational-eo-missions/sentinel-1 [Accessed January 1, 2017].

European Space Agency (ESA) for Earth observation, 2017b. Copernicus: Mission details of Sentinel-2. Available at: https://earth.esa.int/web/guest/missions/esa-operational-eo-missions/sentinel-2 [Accessed January 28, 2017].

European Space Agency (ESA) for Earth observation, 2016a. Sen2Cor. Available at: http://step.esa.int/main/third-party-plugins-2/sen2cor/ [Accessed June 6, 2016].

European Space Agency (ESA) for Earth observation, 2016b. Sentinel-2 Toolbox. Available

at: http://step.esa.int/main/toolboxes/sentinel-2-toolbox/ [Accessed June 6, 2016].
European Union & European Space Agency (ESA) for Earth observation, 2016. Sentinels Scientific Data Hub. Available at: https://scihub.copernicus.eu/dhus/#/home [Accessed June 6, 2016].
Evans, T.L. & Costa, M., 2013. Landcover classification of the Lower Nhecolândia subregion of the Brazilian Pantanal Wetlands using ALOS/PALSAR, RADARSAT-2 and ENVISAT/ASAR imagery. *Remote Sensing of Environment*, 128, pp.118–137.
Fan, C., 2014. Spectral Analysis of Water Reflectance for Hyperspectral Remote Sensing of Water Quailty in Estuarine Water. *Water*, (April), pp.19–27.
Feyisa, G.L. et al., 2014. Automated Water Extraction Index: A new technique for surface water mapping using Landsat imagery. *Remote Sensing of Environment*, 140, pp.23–35. Available at: http://dx.doi.org/10.1016/j.rse.2013.08.029.
Fisher, J. & Overton, M., 1994. Interpretation of shoreline position from aerial photographs. *Coastal Engineering Proceedings, Chapter 144*, pp.1998–2003. Available at: http://journals.tdl.org/icce/index.php/icce/article/viewArticle/5088 [Accessed March 12, 2014].
Fritts, H., 1976. *Tree rings and climate*, Caldwell/NJ: Blackburn Press. Available at: https://books.google.com/books?hl=de&lr=&id=mkjsuFdwjeoC&oi=fnd&pg=PP1&ots=jXDgh_jFTG&sig=3pvuLvbFzcbt_oK4UT1KoQt6xsM.
Furnans, J. & Austin, B., 2008. Hydrographic survey methods for determining reservoir volume. *Environmental Modelling & Software*, 23(2), pp.139–146.
Gal, J.Y. et al., 1996. Calcium carbonate solubility: A reappraisal of scale formation and inhibition. *Talanta*, 43(9), pp.1497–1509.
Gebhardt, S. et al., 2008. Simple Image Processing Techniques or near-real time Inundation Monitoring using TerraSAR-X Imagery. In *3. TerraSAR-X Science Team Meeting, Oberpfaffenhofen, Germany*.
Geisslhofer, M. & Burian, K., 1970. Biometrische Untersuchungen im geschlossenene Schilfbestand des Neusiedler Sees. *OIKOS*, 21(2), pp.248–254.
Geldsetzer, T. & Yackel, J.J., 2009. Sea ice type and open water discrimination using dual co-polarized C-band SAR. *Canadian Journal of Remote Sensing*, 35(1), pp.73–84. Available at: http://pubs.casi.ca/doi/abs/10.5589/m08-075.
Gens, R., 2010. Remote sensing of coastlines: detection, extraction and monitoring. *International Journal of Remote Sensing*, 31(7), pp.1819–1836.
Gerard, F. et al., 2010. Land cover change in Europe between 1950 and 2000 determined employing aerial photography. *Progress in Physical Geography*, 34(2), pp.183–205. Available at: http://ppg.sagepub.com/cgi/doi/10.1177/0309133309360141 [Accessed April 10, 2014].
Germer, S. et al., 2011. Water Balance Changes and Responses of Ecosystems and Society in the Berlin-Brandenburg Region – a Review. *DIE ERDE*, 142(1–2), pp.65–95.
Germer, S., Kaiser, K. & Mauersberger, R., 2010. *Sinkende Seespiegel in Nordostdeutschland: Vielzahl hydrologischer Spezialfälle oder Gruppen von ähnlichen Seesystemen?*, Aktuelle Probleme im Wasserhaushalt von Nordostdeutschland: Trends, Ursachen, Lösungen. Scientific Technical Report 10/10. Deutsches GeoForschungsZentrum, Potsdam. Available at: http://www.acatech.de/fileadmin/user_upload/Baumstruktur_nach_Website/Acatech/root/de/Projekte/Laufende_Projekte/Georessource_Wasser/Germer_et_al_STR_2010.pdf [Accessed January 14, 2013].
Gholizadeh, M., Melesse, A. & Reddi, L., 2016. A Comprehensive Review on Water Quality Parameters Estimation Using Remote Sensing Techniques. *Sensors*, 16(8), p.1298. Available at: http://www.mdpi.com/1424-8220/16/8/1298.

Giardino, C. et al., 2001. Detecting chlorophyll, Secchi disk depth and surface temperature in a sub-alpine lake using Landsat imagery. *Science of the Total Environment*, 268(1–3), pp.19–29.

Grandke, M., 2009. Changes in the Breńskie and Białe Miałkie lake area (Sławskie Lakeland) during the period 1778-2008. *Studia Limnologica et Telmatologica*, 3(1), pp.3–24. Available at: http://www.paleolim.amu.edu.pl/SLETT/slett 3 1/slett 03_1_pp_03-24.pdf.

Graventein, H., 2013. *Geomorphologische und sedimentologisch- bodenkundliche Befunde zur Paläohydrologie des Großen Fürstenseer Sees im Müritz-Nationalpark (Mecklenburg-Vorpommern)*. Diplomarbeit, Universität Marburg.

Gregory, K.J. et al., 2006. Past hydrological events and global change. *Hydrological Processes*, 20(1), pp.199–204. Available at: http://doi.wiley.com/10.1002/hyp.6105.

Grosse, G. et al., 2005. The use of CORONA images in remote sensing of periglacial geomorphology: an illustration from the NE Siberian coast. *Permafrost and Periglacial Processes*, 16(2), pp.163–172. Available at: http://doi.wiley.com/10.1002/ppp.509 [Accessed April 3, 2014].

Gstaiger, V. et al., 2012. Multi-sensoral and automated derivation of inundated areas using TerraSAR-X and ENVISAT ASAR data. *International Journal of Remote Sensing*, 33(22), pp.7291–7304. Available at: http://www.tandfonline.com/doi/abs/10.1080/01431161.2012.700421 [Accessed August 22, 2013].

Guanter, L. et al., 2015. The EnMAP Spaceborne Imaging Spectroscopy Mission for Earth Observation. *Remote Sensing*, 7(7), pp.8830–8857. Available at: http://www.mdpi.com/2072-4292/7/7/8830/ [Accessed January 31, 2017].

Gunnarson, B.E., 2001. Lake Level Changes Indicated by Dendrochronology on Subfossil Pine, Jamtland, Central Scandinavian Mountains, Sweden. *Arctic, Antarctic, and Alpine Research*, 33(3), p.274. Available at: http://www.jstor.org/stable/1552234?origin=crossref [Accessed December 16, 2016].

Gupta, R. & Banerji, S., 1985. Monitoring of reservoir volume using LANDSAT data. *Journal of hydrology*, 77, pp.159–170. Available at: http://www.sciencedirect.com/science/article/pii/0022169485902045 [Accessed June 24, 2014].

HAD, 2003. Hydrological Atlas of Germany.

Hahmann, T. et al., 2008. Automatic Extraction of Water Bodies from TerraSAR-X Data. In *Geoscience and Remote Sensing Symposium, 2008. IGARSS 2008. IEEE International*. IEEE, p. III–103. Available at: http://ieeexplore.ieee.org/xpls/abs_all.jsp?arnumber=4779293 [Accessed January 16, 2012].

Hamilton, S.K. et al., 2009. Biogenic calcite–phosphorus precipitation as a negative feedback to lake eutrophication. *Canadian Journal of Fisheries and Aquatic Sciences*, 66(2), pp.343–350.

Hattermann, F.F. et al., 2011. Model-Supported Impact Assessment for the Water Sector in Central Germany Under Climate Change—A Case Study. *Water Resources Management*, 25(13), pp.3113–3134. Available at: http://link.springer.com/10.1007/s11269-011-9848-4 [Accessed December 21, 2016].

Heege, T. & Fischer, J., 2004. Mapping of water constituents in Lake Constance using multispectral airborne scanner data and a physically based processing scheme. *Canadian Journal of Remote Sensing*, 30(1), pp.77–86. Available at: http://www.tandfonline.com/doi/abs/10.5589/m03-056 [Accessed February 20, 2017].

Heine, I. et al., 2014. Monitoring Seasonal Changes in the Water Surface Areas of Reservoirs Using TerraSAR-X Time Series Data in Semiarid Northeastern Brazil. *Journal of*

Selected Topics in Applied Earth Observation and Remote Sensing, 7(8), pp.3190–3199.
Heine, I. et al., 2015. Reconstruction of Lake Level Changes of Groundwater-Fed Lakes in Northeastern Germany Using RapidEye Time Series. *Water*, 7(8), pp.4175–4199. Available at: http://www.mdpi.com/2073-4441/7/8/4175/.
Heinonen, P., Ziglio, G.G. & Van Der Beken, A., 2000. *Hydrological and Limnological Aspects of Lake Monitoring*, West Sussex, England: John Wiley & Sons, LTD.
Hepperl, D. & Krienitz, L., 1997. Phacotus lenticularis (Chlamydomonadales, Phacotaceae) zoospores require external supersaturation of calcium carbonate for calcification in culture. *Journal of Phycology*, 33, pp.415–424.
Hepperle, D., 2016. WinIAP - Software for the Calculation of Ion Activities and Calcite Saturation Index. SequentiX - Digital DNA Processing. Available at: http://www.sequentix.de [Accessed April 29, 2016].
Heremans, R. et al., 2003. Automatic detection of flooded areas on ENVISAT/ASAR images using an object-oriented classification technique and an active contour algorithm. *International Conference on Recent Advances in Space Technologies*, pp.311–316. Available at: http://ieeexplore.ieee.org/lpdocs/epic03/wrapper.htm?arnumber=1303926.
Herrera-Cruz, V. & Koudogbo, F., 2009. TerraSAR-X rapid mapping for flood events. *Proceedings of the International Society for Photogrammetry and Remote Sensing (Earth Imaging for Geospatial Information), Hannover, Germany*, pp.170–175. Available at: http://cmsv021.rrzn.uni-hannover.de/fileadmin/institut/pdf/isprs-Hannover2009/Herrera-Cruz-170.pdf [Accessed January 16, 2012].
Hill, J. & Mehl, W., 2003. Geo- und radiometrische Aufbereitung multi- und hyperspektraler Daten zur Erzeugung langjähriger kalibrierter Zeitreihen. *PhotoGrammetrie –- Fernerkundung –- Geoinformation*, 1, pp.7–14.
Hilt, S. et al., 2010. Can submerged macrophytes influence turbidity and trophic state in deep lakes? Suggestions from a case study. *Journal of Environmental Quality*, 39(2), pp.725–733.
Hilt, S. et al., 2008. Reconstruction of pristine morphology, flow, nutrient conditions and submerged vegetation of lowland river Spree (Germany) from palaeomeanders. *River research and applications*, 24(3), pp.310–329. Available at: http://onlinelibrary.wiley.com/doi/10.1002/rra.1023/full.
Hong, S.-H. et al., 2015. Evaluation of Polarimetric SAR Decomposition for Classifying Wetland Vegetation Types. *Remote Sensing*, 7(7), pp.8563–8585. Available at: http://www.mdpi.com/2072-4292/7/7/8563/.
Horritt, M.S., 2003. Waterline mapping in flooded vegetation from airborne SAR imagery. *Remote Sensing of Environment*, 85(3), pp.271–281. Available at: http://linkinghub.elsevier.com/retrieve/pii/S0034425703000063 [Accessed July 6, 2011].
Horstmann, J. et al., 2003. Global wind speed retrieval from SAR. *IEEE Transactions on Geoscience and Remote Sensing*, 41(10), pp.2277–2286.
Hostache, R., Matgen, P., Schumann, G., Member, S., et al., 2009. Model Calibration Uncertainties Using Satellite SAR Images of Floods. *TRANSACTIONS ON GEOSCIENCE AND REMOTE SENSING*, 47(2), pp.431–441.
Hostache, R., Matgen, P., Schumann, G., Puech, C., et al., 2009. Water Level Estimation and Reduction of Hydraulic Model Calibration Uncertainties Using Satellite SAR Images of Floods. *IEEE Transactions on Geoscience and Remote Sensing*, 47(2), pp.431–441. Available at: http://ieeexplore.ieee.org/xpls/abs_all.jsp?arnumber=4773470 [Accessed October 4, 2012].
House, W., 1987. Inhibition of calcite crystal growth by inorganic phosphate. *Journal of Colloid and Interface Science*, 119, pp.505–511.
Huang, S. et al., 2010. Simulation of spatiotemporal dynamics of water fluxes in Germany

under climate change. *Hydrological Processes*, 24(23), pp.3289–3306. Available at: http://doi.wiley.com/10.1002/hyp.7753 [Accessed December 21, 2016].

Hughes, M.L., McDowell, P.F. & Marcus, W.A., 2006. Accuracy assessment of georectified aerial photographs: Implications for measuring lateral channel movement in a GIS. *Geomorphology*, 74(1–4), pp.1–16. Available at: http://linkinghub.elsevier.com/retrieve/pii/S0169555X05001972 [Accessed April 1, 2014].

Hung, N.N. et al., 2012. Floodplain hydrology of the Mekong Delta, Vietnam. *Hydrological Processes*, 26(5), pp.674–686. Available at: http://doi.wiley.com/10.1002/hyp.8183 [Accessed August 22, 2013].

Hunter, P.D. et al., 2010. Hyperspectral remote sensing of cyanobacterial pigments as indicators for cell populations and toxins in eutrophic lakes. *Remote Sensing of Environment*, 114, pp.2705–2718.

Hunter, R.D. et al., 2006. A multiproxy environmental investigation of Holocene wood from a submerged conifer forest in Lake Huron, USA. *Quaternary Research*, 66(1), pp.67–77.

Hupfer, M. & Nixdorf, B., 2011. *Zustand und Entwicklung von Seen in Berlin und Brandenburg. Materialien der Interdisziplinären Arbeitsgruppen (IAG Globaler Wandel – Regionale Entwicklung)*, Diskussionspapier, 11. Berlin-Brandenburgische Akademie der Wissenschaften.

IPCC, 2014. *Climate change 2014: impacts, adaptation, and vulnerability. Part B: regional aspects. Contribution of Working Group II to the Fifth Assessment Report of the Intergovernmental Panel on Climate Change*, Cambridge: Cambridge University Press. Available at: http://epic.awi.de/37530/.

Irons, J.R., Dwyer, J.L. & Barsi, J.A., 2012. The next Landsat satellite: The Landsat Data Continuity Mission. *Remote Sensing of Environment*, 122, pp.11–21.

Jacob, D. et al., 2008. *Klimaauswirkungen und Anpassung in Deutschland-Phase 1: Erstellung regionaler Klimaszenarien für Deutschland*, Available at: http://pubman.mpdl.mpg.de/pubman/faces/viewItemOverviewPage.jsp?itemId=escidoc:994273.

Jagdhuber, T., 2012. *Soil Parameter Retrieval under Vegetation Cover Using SAR Polarimetry*. University Potsdam. Available at: http://nbn-resolving.de/urn:nbn:de:kobv:517-opus-60519.

Jagdhuber, T., Hajnsek, I. & Papathanassiou, K., 2013. Polarimetric Soil Moisture Retrieval at Short Wavelength. In *Proc. "PolInSAR 6th Int. Workshop on Science and Applications of SAR Polarimetry and Polarimetric Interferometry", in Franscati, Italy*. p. 35. Available at: http://core.kmi.open.ac.uk/download/pdf/11153538.pdf [Accessed July 16, 2014].

Japan Aerospace Exploration Agency / Public Affairs Department, 2014. *ALOS-2 : The Advanced Land Observing Satellite-2 "DAICHI-2,"* Tokyo, Japan. Available at: http://global.jaxa.jp/activity/pr/brochure/files/sat29.pdf [Accessed January 30, 2017].

Jet Propulsion Laboratory & California Institute of Technology, NASA-ISRO Synthetic Aperture Radar. Available at: http://www.jpl.nasa.gov/missions/nasa-isro-synthetic-aperture-radar-nisar/ [Accessed January 30, 2017].

Ji, K. & Wu, Y., 2015. Scattering Mechanism Extraction by a Modified Cloude-Pottier Decomposition for Dual Polarization SAR. *Remote Sensing*, 7(6), pp.7447–7470. Available at: http://www.mdpi.com/2072-4292/7/6/7447/.

Ji, L., Zhang, L. & Wylie, B., 2009. Analysis of Dynamic Thresholds for the Normalized Difference Water Index. *Photogrammetric Engineering & Remote Sensing*, 75(11), pp.1307–1317. Available at: http://essential.metapress.com/openurl.asp?genre=article&id=doi:10.14358/PERS.75.11.

1307.
Johnson, M.R., Andersen, M.J. & Sebree, S.K., 2008. *Hydrographic Surveys for Six Water Bodies in Eastern Nebraska* U.S. Geological Survey & U.S. Department of the Interior, eds., Reston/Virginia.
Jones, R.., McMahon, T.. & Bowler, J.., 2001. Modelling historical lake levels and recent climate change at three closed lakes, Western Victoria, Australia (c.1840–1990). *Journal of Hydrology*, 246(1), pp.159–180.
Kabus, T. & Wiehle, I., 2013. Die Armleuchteralgen (Characeae) in ausgewählten Seen des Naturparks Stechlin-Ruppiner Land (Brandenburg , Deutschland). Ergebnisse der Untersuchungen außerhalb von FFH- und Naturschutzgebieten. *Rostock. Meeresbiolog. Beitr.*, 24, pp.63–74.
Kaiser, K., Friedrich, J., et al., 2012. Aktuelle hydrologische Veränderungen von Seen in Nordostdeutschland: Wasserspiegeltrends, ökologische Konsequenzen, Handlungsmöglichkeiten. In U. Grünewald et al., eds. *Wasserbezogene Anpassungsmaßnahmen an den Landschafts- und Klimawandel*. Stuttgart: Schweizerbart, pp. 148–170.
Kaiser, K., Koch, P.J., et al., 2014. Detection and attribution of lake-level dynamics in north-eastern central Europe in recent decades. *Regional Environmental Change*, 14(4), pp.1587–1600. Available at: http://link.springer.com/article/10.1007/s10113-014-0600-5 [Accessed May 14, 2014].
Kaiser, K., Lorenz, S., et al., 2012. Late Quaternary evolution of rivers, lakes and peatlands in northeast Germany reflecting past climatic and human impact – an overview. *Quaternary Science Journal*, 61(2), pp.103–132. Available at: www.quaternary-science.net [Accessed January 10, 2017].
Kaiser, K., Küster, M., et al., 2014. Littoral landforms and pedosedimentary sequences indicating late Holocene lake-level changes in northern central Europe — A case study from northeastern Germany. *Geomorphology*, 216, pp.58–78.
Kaiser, K. et al., 2015. Multi-decadal lake-level dynamics in north-eastern Germany as derived by a combination of gauging, proxy-data and modelling. *Journal of Hydrology*, 529, pp.584–599. Available at: http://dx.doi.org/10.1016/j.jhydrol.2014.12.057.
Kaiser, K., Germer, S., et al., 2012. Seespiegelschwankungen in Nordostdeutschland: Beobachtung und Rekonstruktion. *System Erde*, 2(1), pp.62–67.
Kaiser, K., 1996. Zur hydrologischen Entwicklung mecklenburgischer Seen im jüngeren Quartär. *Petermanns Geographische Mitteilungen*, 140(5+6), pp.323–342. Available at: http://www.uni-marburg.de/fb19/personal/wiss_ma/kaiser/art_kaiser_pgm_96.pdf [Accessed December 12, 2012].
Kaiser, V.K. et al., 2015. Die hydrologische Entwicklung des Großen Fürstenseer Sees (Müritz-Nationalpark) im letzten Jahrtausend – Ein Überblick. In J. Kobel, M. Küster, & M. Schwabe, eds. *Neue Beiträge zum Naturraum und zur Landschaftsgeschichte im Teilgebiet Serrahn des Müritz-Nationalparks*. Berlin, Germany: Geozon Science Media, pp. 61–81.
Kämpf, L. et al., 2012. Sediment imprint of the severe 2002 summer flood in the Lehnmühle reservoir, eastern Erzgebirge (Germany). *E&G–Quaternary*. Available at: https://www.researchgate.net/profile/Lucas_Kaempf/publication/278007161_Sediment_imprint_of_the_severe_2002_summer_flood_in_the_Lehnmuhle_reservoir_eastern_Erzgebirge_Germany/links/5578260f08ae7521586f16e5.pdf [Accessed December 21, 2016].
Kasprzak, P. et al., 2003. Reduction of nutrient loading, planktivore removal and piscivore stocking as tools in water quality management: The Feldberger Haussee biomanipulation project. *Limnologica*, 33(3), pp.190–204.
Kelts, K. & Hsü, K., 1978. Chapter 9: Freshwater carbonate sedimentation. In *Lakes* -

Chemistry Geology Physics. pp. 295–323. Available at: http://link.springer.com/chapter/10.1007/978-1-4757-1152-3_9 [Accessed March 12, 2014].

Kempke, S. et al., 2008. Biogene Calcitfällung im Bodensee-Prozessverständnis und Modellierung. *WasserWirtschaft*, 98(10), pp.31–33. Available at: http://www.researchgate.net/publication/30019245_Biogene_Calcitfllung_im_Bodensee__Prozessverstndnis_und_Modellierung/file/d912f50ae481c29410.pdf [Accessed March 12, 2014].

Keshava, N. & Mustard, J.F., 2002. Spectral unmixing. *EEE signal processing magazine*, 91(1), pp.44–57.

Kienel, U. et al., 2017. Effects of the mixing duration in spring on diatom deposition in the deep Lake Tiefer See, NE Germany. *Journal of Paleolimnology*, 57, pp.37–49.

Kienel, U. et al., 2013. Recently induced anoxia leading to the preservation of seasonal laminae in two NE-German lakes. *Journal of Paleolimnology*, 50(4), pp.535–544.

Klein, E., Berg, E.E. & Dial, R., 2005. Wetland drying and succession across the Kenai Peninsula Lowlands , south-central Alaska. *Canadian Journal of Forest Research*, 35(8), pp.1931–1941. Available at: http://www.nrcresearchpress.com/doi/abs/10.1139/x05-129 [Accessed December 21, 2016].

Kleppe, J.A. et al., 2011. Duration and severity of Medieval drought in the Lake Tahoe Basin. *Quaternary Science Reviews*, 30(23), pp.3269–3279.

Koppe, W. et al., 2013. Rice monitoring with multi-temporal and dual-polarimetric TerraSAR-X data. *International Journal of Applied Earth Observation and Geoinformation*, 21, pp.568–576. Available at: http://linkinghub.elsevier.com/retrieve/pii/S0303243412001547.

Koschel, R. et al., 1983. Calcite precipitation a a natural control mechanism of eutrophication. *Arch. Hydrobiol.*, 98(3), pp.340–408. Available at: http://agris.fao.org/agris-search/search/display.do?f=2013/US/US201302129541 0410013940.xml;US201302129541 [Accessed March 12, 2014].

Koschel, R. et al., 1981. Eine limnologische Zustandsanalyse des Feldberger Hausssees. *Acta hydrochim hydrobiol*, 9, pp.255–279.

Koschel, R., 1998. Leitbilder eines integrierten Seen- und Landschaftsschutzes. Stechlin-Forum. In *Stechlin-Forum*. Rheinsberg (Brandenburg): Umweltstiftung WWF-Deutschland, pp. 53–62.

Koschel, R., 1997. Structure and function of pelagic calcite precipitation in lake ecosystems. *Verhandlungen der Internationalen Vereinigung für Limnologie*, 26, pp.343–349.

Koschel, R., Kasprzak, P. & Schreiber, A., 1997. Kalzitfällung und Nahrungskettenmanipulation. *Laufener Seminarbeitrag*, 3/97(3), pp.61–76.

Koschel, R., Proft, G. & Raidt, H., 1987. Autochthone Kalkfällung in Hartwasserseen der Mecklenburger Seenplatte. *Limnologica (Berlin)*, 18(2), pp.317–338. Available at: http://scholar.google.com/scholar?hl=en&btnG=Search&q=intitle:Autochthone+Kalkf llung+in+Hartwasserseen+der+Mecklenburger+Seenplatte#0 [Accessed March 12, 2014].

Kowalski, K. & Wilcox, D., 1999. Use of historical and geospatial data to guide the restoration of a Lake Erie coastal marsh. *Wetlands*, 19(4), pp.858–868. Available at: http://link.springer.com/article/10.1007/BF03161788 [Accessed March 12, 2014].

Kressner, L., 2009. *Digitale Analyse der Genauigkeit sowie der Erfassungs- und Darstellungsqualität von Altkarten aus Mecklenburg-Vorpommern – dargestellt an den Kartenwerken von Wiebeking (ca. 1786) und Schmettau (ca. 1788)*. University of Rostock.

Kronberg, P., 1985. *Fernerkundung der Erde. Grundlagen und Methoden des Remote Sensing*

in der Geologie, Stuttgart: Enke Verlag.
Kropáček, J. et al., 2012. Analysis of lake level changes in Nam Co in central Tibet utilizing synergistic satellite altimetry and optical imagery. *International Journal of Applied Earth Observation and Geoinformation*, 17, pp.3–11. Available at: http://linkinghub.elsevier.com/retrieve/pii/S0303243411001449 [Accessed July 15, 2014].
Kutser, T., 2004. Quantitative detection of chlorophyll in cyanobacterial blooms by satellite remote sensing. *Limnology and Oceanography*, 49(6), pp.2179–2189. Available at: http://doi.wiley.com/10.4319/lo.2004.49.6.2179 [Accessed February 20, 2017].
LaiV-MV, 2013. Website des Landesamts für innere Verwaltung Mecklenburg Vorpommern. Available at: http://www.laiv-mv.de/land-mv/LAiV_prod/LAiV/AfGVK/index.jsp [Accessed May 3, 2013].
Lampe, R., 2005. Lateglacial and Holocene water-level variations along the NE German Baltic Sea coast: review and new results. *Quaternary International*, 133, pp.121–136.
Landesamt Brandenburg, 2008. Ökologische Charakterisierung der wichtigsten Brutgebiete für Wasservögel in Brandenburg. *Studien und Tagungsberichte*, 57, pp.1–181.
Landesamt für Umwelt Naturschutz und Geologie Mecklenburg-Vorpommern, 2011. *Gutachtlicher Landschaftsrahmenplan Mecklenburgische Seenplatte*,
Landesumweltamt Brandenburg, 2004. *Leitfaden zur Renaturierung von Feuchtgebieten in Brandenburg*,
Lantz, N.J. & Wang, J., 2014. Object-based classification of Worldview-2 imagery for mapping invasive common reed, Phragmites australis. *Canadian Journal of Remote Sensing*, 39(4), pp.328–340. Available at: http://www.tandfonline.com/doi/abs/10.5589/m13-041.
Lee, J. & Pottier, E., 2009. *Polarimetric Radar Imaging – From Basics to Applications* 1st ed., w York: CRC Press.
Lee, J. Sen et al., 2008. Evaluation and Bias Removal of Multilook Effect on Entropy/Alpha/Anisotropy in Polarimetric SAR Decomposition. *IEEE TRANSACTIONS ON GEOSCIENCE AND REMOTE SENSING*, 46(10), pp.3039–3052.
Leeuwen, B.V.A.N. & Tobak, Z., 2014. Operational Identification of Inland Excess Water Floods Using Satellite Imagery. In *GI_Forum 2014 – Geospatial Innovation for Society*. pp. 12–15.
Legesse, D., Vallet-Coulomb, C. & Gasse, F., 2004. Analysis of the hydrological response of a tropical terminal lake, Lake Abiyata (Main Ethiopian Rift Valley) to changes in climate and human activities. *Hydrological Processes*, 18(3), pp.487–504. Available at: http://doi.wiley.com/10.1002/hyp.1334 [Accessed December 21, 2016].
Lehner, S. et al., 2000. Wind and wave measurements using complex ERS-2 SAR wave mode data. *IEEE Transactions on Geoscience and Remote Sensing*, 38(5), pp.2246–2257. Available at: http://ieeexplore.ieee.org/document/868882/ [Accessed February 20, 2017].
Leibniz-Institute of Freshwater Ecology & Inland Fisheries (IGB), 2016. Unpublished Data.
LGRB, 1997. Geologische Übersichtskarte der Uckermark 1:100.000.
Li, J., Huang, S. & Li, X., 2005. ENVISAT ASAR medium and high resolution images for Near Real Time flood monitoring in China during the 2005 flood season. In *Dragon Symposium "Mid-Term Results", Santorini, Greece*. p. ESA SP-611, 213-226. Available at: http://earth.eo.esa.int/dragon/symp2005/proceedings/papers/s5_3_li.pdf [Accessed January 25, 2012].
Li, W. et al., 2013. A Comparison of Land Surface Water Mapping Using the Normalized Difference Water Index from TM, ETM+ and ALI. *Remote Sensing*, 5(11), pp.5530–5549. Available at: http://www.mdpi.com/2072-4292/5/11/5530/ [Accessed August 5, 2014].

Li, X. & Damen, M.C.J., 2010. Coastline change detection with satellite remote sensing for environmental management of the Pearl River Estuary, China. *Journal of Marine Systems*, 82, pp.S54–S61. Available at: http://dx.doi.org/10.1016/j.jmarsys.2010.02.005.

Liaw, A. & Wiener, M., 2015. *Package " randomForest ,"*

Liebe, J.R. et al., 2009. Suitability and limitations of ENVISAT ASAR for monitoring small reservoirs in a semiarid area. *IEEE Transactions on Geoscience and Remote Sensing,*, 47(5), pp.1536–1547. Available at: http://ieeexplore.ieee.org/xpls/abs_all.jsp?arnumber=4703210 [Accessed January 23, 2012].

Lillesand, T.M., Kiefer, R.W. & Chipman, J.W., 2008. *Remote Sensing and Image Interpretation, 6th ed.*,

van der Linden, M. et al., 2008. Vegetation history and human impact during the last 300 years recorded in a German peat deposit. *Review of Palaeobotany and Palynology*, 152(3), pp.158–175.

Lipakis, M. & Chrysoulakis, N., 2008. Shoreline extraction using satellite imagery E. Pranzini & L. Wetzel, eds. *Beach Erosion Monitoring: Results from BEACHMED-e/OpTIMAL Project*, pp.81–96.

Lira, J., 2006. Segmentation and morphology of open water bodies from multispectral images. *International Journal of Remote Sensing*, 27(18), pp.4015–4038. Available at: http://www.tandfonline.com/doi/abs/10.1080/01431160600702384 [Accessed July 9, 2014].

Lischeid, G. et al., 2010. Assessing coupling between lakes and layered aquifers in a complex Pleistocene landscape based on water level dynamics. *Advances in Water Resources*, 33(11), pp.1331–1339.

Lischeid, G., Steidl, J. & Merz, C., 2012. Funktionalanalyse versus Trendanalyse zur Abschätzung anthropogener Einflüsse auf Grundwasserganglinien. *Grundwasser*, 17(2), pp.79–89. Available at: http://link.springer.com/10.1007/s00767-012-0188-y [Accessed December 21, 2016].

Loaiciga, H., Haston, L. & Michaelsen, J., 1993. Dendrohydrology and long-term hydrologic phenomena. *Reviews of Geophysics*. Available at: http://onlinelibrary.wiley.com/doi/10.1029/93RG00056/full [Accessed December 21, 2016].

Long, J., Hu, C. & Robbins, L., 2014. Whiting events in SW Florida coastal waters: a case study using MODIS medium-resolution data. *Remote Sensing Letters*, 5(6), pp.539–547.

Loosvelt, L., Peters, J., Skriver, H., et al., 2012. Random Forests as a tool for estimating uncertainty at pixel-level in SAR image classification. *International Journal of Applied Earth Observation and Geoinformation*, 19, pp.173–184.

Loosvelt, L., Peters, J. & Skriver, H., 2012. Impact of reducing polarimetric SAR input on the uncertainty of crop classifications based on the random forests algorithm. *IEEE Transactions on Geoscience and Remote Sensing*, 50(10), pp.4185–4200.

Lopez-sanchez, J.M. et al., 2011. RETRIEVAL OF RICE PHENOLOGY BY MEANS OF SAR POLARIMETRY. In *Proc. "PolInSAR 5th Int. Workshop on Science and Applications of SAR Polarimetry and Polarimetric Interferometry", in Franscati, Italy*. pp. 1–8.

Lopez-Sanchez, J.M. et al., 2014. Polarimetric Response of Rice Fields at C-Band: Analysis and Phenology Retrieval. *IEEE Transactions on Geoscience and Remote Sensing*, 52(5), pp.2977–2993. Available at: http://ieeexplore.ieee.org/lpdocs/epic03/wrapper.htm?arnumber=6562759%5Cnhttp://ieeexplore.ieee.org/xpls/abs_all.jsp?arnumber=6562759.

Lopez-Sanchez, J.M., Ballester-Berman, J.D. & Hajnsek, I., 2011. First results of rice

monitoring practices in Spain by means of time series of TerraSAR-X dual-pol images. *IEEE Journal of Selected Topics in Applied Earth Observations and Remote Sensing*, 4(2), pp.412–422.

Lopez-Sanchez, J.M., Cloude, S.R. & Ballester-Berman, J.D., 2012. Rice phenology monitoring by means of SAR polarimetry at X-band. *IEEE Transactions on Geoscience and Remote Sensing*, 50(7 PART 2), pp.2695–2709.

Louet, J. & Bruzzi, S., 1999. ENVISAT mission and system. In *International Geoscience and Remote Sensing Symposium. IGARSS'99 (Cat. No.99CH36293)*. IEEE, pp. 1680–1682. Available at: http://ieeexplore.ieee.org/document/772059/ [Accessed February 15, 2017].

Lu, S. et al., 2013. Lake water volume calculation with time series remote-sensing images. *International Journal of Remote Sensing*, 34(22), pp.7962–7973. Available at: http://www.tandfonline.com/doi/abs/10.1080/01431161.2013.827814 [Accessed April 10, 2014].

Lu, S. et al., 2011. Water body mapping method with HJ-1A/B satellite imagery. *International Journal of Applied Earth Observation and Geoinformation*, 13(3), pp.428–434. Available at: http://dx.doi.org/10.1016/j.jag.2010.09.006.

Luoheng Han & Jordan, K., 2005. Estimating and mapping chlorophyll-a concentration in Pensacola Bay, Florida using Landsat ETM+ data. *International Journal of Remote Sensing*, 26(23), pp.5245–5254. Available at: http://web.ebscohost.com/ehost/pdfviewer/pdfviewer?vid=1&hid=8&sid=18d844b5-e69e-4169-beb7-2cd12013159a%2540sessionmgr13.

Luthardt, V. et al., 2009. Ausgewählte Ergebnisse der Ökosystemaren Umweltbeobachtung in den Brandenburger Biosphärenreservaten. *Fachbeiträge des Landesumweltamtes* , 112, pp.1–23. Available at: https://scholar.google.de/scholar?q=Ausgewählte+Ergebnisse+der+Ökosystemaren+Umweltbeobachtung+in+den+Brandenburger+Biosphärenreservaten&btnG=&hl=de&as_sdt=0%2C5 [Accessed December 21, 2016].

Luthardt, V., Meier-Uhlherr, R. & Schulz, C., 2010. Moore unter Wassermangel - Entwicklungstrends ausgewählter naturnaher Moore in den Wäldern des Biosphärenreservats Schorfheide-Chorin unter besonderer Berücksichtigung ihrer naturräumlichen Einbettung und des Witterungsverlaufs der letzten 16 Jahre. *Naturschutz Und Landschaftspflege in Brandenburg*, 19.

Lyon, J. & Drobney, R., 1984. Lake level effects as measured from aerial photos. *Journal of Surveying Engineering*, 110(2), pp.103–111. Available at: http://ascelibrary.org/doi/abs/10.1061/(ASCE)0733-9453(1984)110:2(103) [Accessed March 13, 2014].

Lyon, J. & Greene, R., 1992. Use of aerial photographs to measure the historical areal extent of Lake Erie coastal wetlands. *Photogrammetric engineering and remote sensing*, 58(9), pp.1355–1360. Available at: http://cat.inist.fr/?aModele=afficheN&cpsidt=5513260 [Accessed March 12, 2014].

Maillard, P., Bercher, N. & Calmant, S., 2015. New processing approaches on the retrieval of water levels in Envisat and SARAL radar altimetry over rivers: A case study of the São Francisco River, Brazil. *Remote Sensing of Environment*, 156, pp.226–241. Available at: http://linkinghub.elsevier.com/retrieve/pii/S0034425714003812 [Accessed January 8, 2015].

Maillard, P., Pivari, M.O. & Luis, C.H.P., 2012. Remote Sensing for Mapping and Monitoring Wetlands and Small Lakes in Southeast Brazil. In Y. Chemin, ed. *Remote Sensing of Planet Earth*. InTech, pp. 23–46. Available at: http://www.intechopen.com/source/pdfs/27092/InTech-Remote_sensing_for_mapping_and_monitoring_wetlands_and_small_lakes_in_southeas

t_brazil.pdf [Accessed February 29, 2012].
Malenovský, Z. et al., 2012. Sentinels for science: Potential of Sentinel-1, -2, and -3 missions for scientific observations of ocean, cryosphere, and land. *Remote Sensing of Environment*, 120, pp.91–101.
Marszelewski, W. & Adamczyk, A., 2004. Changes in the area of the Mazurian lakes in the light of the cartographic materials at the scale 1:25000. *Limnological Review*, 4, pp.167–176. Available at: http://www.ptlim.pl/lr2004/pdf/marszelewski.pdf [Accessed March 12, 2014].
Martinis, S., 2010. *Automatic near real-time flood detection in high resolution X-band synthetic aperture radar satellite data using context-based classification on irregular graphs*. Ludwig-Maximilians-Universität München. Available at: http://edoc.ub.uni-muenchen.de/12373/ [Accessed January 16, 2012].
Martinis, S., Kersten, J. & Twele, A., 2015. A fully automated TerraSAR-X based flood service. *ISPRS Journal of Photogrammetry and Remote Sensing*, 104, pp.203–212.
Martinis, S., Twele, A. & Voigt, S., 2009. Towards operational near real-time flood detection using a split-based automatic thresholding procedure on high resolution TerraSAR-X data. *Nat. Hazards Earth Syst. Sci*, 9, pp.303–314. Available at: www.nat-hazards-earth-syst-sci.net/9/303/2009/ [Accessed February 15, 2017].
Mason, D.C. et al., 2010. Flood Detection in Urban Areas Using TerraSAR-X. *IEEE Transactions on Geoscience and Remote Sensing*, 48(2), pp.882–894.
Mason, I.M. et al., 1994. The response of lake levels and areas to climatic change. *Climatic Change*, 27(2), pp.161–197. Available at: http://link.springer.com/10.1007/BF01093590 [Accessed January 5, 2017].
Mastenbroek, K., 1998. High-resolution wind fields from ERS SAR. *Earth Observation Quarterly*, 59, pp.20–22.
Mathes, J., 2015. *Ministerium für Landwirtschaft, Umwelt und Geologie (Mecklenburg-Vorpommers)*, Available at: http://www.lung.mv-regierung.de.
Mauersberger, H. & Mauersberger, R., 1996. *Die Seen des Biosphärenreservates "Schorfheide-Chorin" – eine ökologische Studie. Untersuchungen zur Struktur, Trophie, Hydrologie, Entwicklung, Nutzung, Vegetation und Libellenfauna*. University of Greifswald.
Mauersberger, R., 2006. Klassifikation der Seen für die Naturraumerkundung des nordostdeutschen Tieflandes. *Archiv für Naturschutz und Landschaftsforschung*, pp.51–90. Available at: http://uckermaerkische-seen.de/PROJEKTE/GROSSPROJEKT/ASSETS-NSGP/Archiv_2006_3_Mauersberger.pdf [Accessed March 4, 2013].
McCurdy, P.G., 1950. Coastal delineation from aerial photographs. *Photogrammetric Enginnering*, 16(4), pp.550–555.
McFeeters, S.K., 1996. The use of the Normalized Difference Water Index (NDWI) in the delineation of open water features. *International Journal of Remote Sensing*, 17(7), pp.1425–1432. Available at: http://www.tandfonline.com/doi/abs/10.1080/01431169608948714 [Accessed January 14, 2014].
Meko, D.M., 2006. Tree-Ring Inferences on Water-Level Fluctuations of Lake Athabasca. *Canadian Water Resources Journal*, 31(4), pp.229–248. Available at: http://www.tandfonline.com/doi/abs/10.4296/cwrj3104229 [Accessed January 5, 2017].
Mertes, L.A.K. et al., 2004. Rivers and Lakes. In S. L. Ustin, ed. *Remote Sensing for Natural Resources Management and Envirnmental Monitoring: Manual for Remote Sensing*. New Jersey: John Wiley & Sons, Inc., pp. 345–358.
Merz, C. & Pekdeger, A., 2011. Anthropogenic changes in the landscape hydrology of the

Berlin-Brandenburg region. *Erde*, 142(1–2), pp.21–39.
Meyer, D., R documentation: Classical Seasonal Decomposition by Moving Averages. Available at: https://stat.ethz.ch/R-manual/R-devel/library/stats/html/decompose.html [Accessed June 15, 2015].
Michael Voltersen, 2011. *Local land cover and water bodies product guide*, Vienna, Austria.
Mietz, O. et al., 1995. *Die Seen im Land Brandenburg. Bericht des Projektes "Seenkataster Brandenburg,"* Seddin, Germany.
Milly, P.C.D. et al., 2008. Stationarity Is Dead: Whither Water Management? *Science*, 319(5863).
MLUV M-V, 2014. Regierungsportal des Ministerium für Landwirtschaft, Umwelt und Verbraucherschutz Mecklenburg-Vorpommern. Available at: http://www.regierung-mv.de/cms2/Regierungsportal_prod/Regierungsportal/de/lm/index.jsp [Accessed December 4, 2014].
Mohan, S. et al., 2011. Monitoring and Retrieval of Vegetation Parameter using Multi-frequency Polarimetric SAR data. , pp.330–333.
Moore, G.K., 1980. Satellite remote sensing of water turbidity. *Hydrological Sciences-Bulletin-des Sciences Hydrologiques*, 25(4), pp.407–422.
Morena, L.C., James, K. V & Beck, J., 2004. An introduction to the RADARSAT-2 mission. *Canadian Journal of Remote Sensing*, 30(3), pp.221–234.
Moses, W.J. et al., 2011. Estimation of chlorophyll- a concentration in turbid productive waters using airborne hyperspectral data. *Water Research*, 46(4), pp.993–1004. Available at: http://digitalcommons.unl.edu/natrespapers [Accessed February 20, 2017].
Müller, J., 2012. GAIA-MV: Tiefenkarten der Seen in Mecklenburg-Vorpommern. Available at: http://www.geodaten-mv.de/ [Accessed September 21, 2016].
Muster, S. et al., 2013. Water Body Distributions Across Scales: A Remote Sensing Based Comparison of Three Arctic TundraWetlands. *Remote Sensing*, 5(4), pp.1498–1523. Available at: http://www.mdpi.com/2072-4292/5/4/1498/ [Accessed July 30, 2014].
NASA, 2017. NASA: MODIS. Available at: https://modis.gsfc.nasa.gov/data/ [Accessed January 31, 2017].
NASA & U.S. Geological Survey, 2017. Landsat Science: Landsat 9. Available at: http://landsat.gsfc.nasa.gov/landsat-9/ [Accessed January 31, 2017].
Nath, R.K. & Deb, S.K., 2010. Water-Body Area Extraction From High Resolution Satellite Images-An Introduction, Review, and Comparison. *International Journal of Image Processing (IJIP)*, 3(6), pp.353–372. Available at: http://www.cscjournals.org/csc/manuscriptinfo.php?ManuscriptCode=67.68.67.74.39.43.42.48.104 [Accessed January 26, 2012].
Natkhin, M. et al., 2012. Differentiating between climate effects and forest growth dynamics effects on decreasing groundwater recharge in a lowland region in Northeast Germany. *Journal of Hydrology*, 448, pp.245–254.
Natkhin, M., 2010. *Modellgestützte Analyse der Einflüsse von Veränderungen der Waldwirtschaft und des Klimas auf den Wasserhaushalt grundwasserabhängiger Landschaftselemente*. University of Potsdam. Available at: http://d-nb.info/1013823567.
Nghiem, S. V. & Leshkevich, G. a., 2007. Satellite SAR Remote Sensing of Great Lakes Ice Cover, Part 1. Ice Backscatter Signatures at C Band. *Journal of Great Lakes Research*, 33(4), pp.722–735.
Nixdorf, B. et al., 2004a. *Dokumentation von Zustand und Entwicklung der wichtigsten Seen Deutschlands (Teil 2)*,
Nixdorf, B. et al., 2004b. *Dokumentation von Zustand und Entwicklung der wichtigsten Seen Deutschlands (Teil 5)*,
Nixdorf, B. et al., 2013. Prozessverständnis als Grundlage für die Gewässerbewirtschaftung -

Fallbeispiele für Limitation, Konkurrenz, Gewässerstruktur und Nahrungsnetzsteuerung. *Korrespondenz Wasserwirtschaft*, 6(12), pp.693–701.

O'Neil, J.M. et al., 2012. The rise of harmful cyanobacteria blooms: The potential roles of eutrophication and climate change. *Harmful Algae*, 14, pp.313–334. Available at: http://www.elsevier.com/copyright [Accessed February 20, 2017].

Oberstadler, R. & Ho, Ã.H., 1997. Assessment of the mapping capabilities of ERS-1SAR Data for flood mapping: A case study in Germany. *Hydrological Processes*, 11(December 1995), pp.1415–1425.

OpenStreetMap, 2016. OpenStreetMap: Data download. Available at: http://download.geofabrik.de/europe.html [Accessed February 29, 2016].

Östlund, C. et al., 2001. Mapping of the water quality of Lake Erken, Sweden, from Imaging Spectrometry and Landsat Thematic Mapper. *The Science of the total environment*, 268(1–3), p.139. Available at: https://www.infona.pl/resource/bwmeta1.element.elsevier-be86f272-2d26-30fc-bb20-0bc6b6ffbcf8 [Accessed February 20, 2017].

Otsu, N., 1979. A threshold selection method from Gray-level. *IEEE Transactions on Systems, Man, and Cybernetics*, SMC-9(1), pp.62–66.

Oyama, Y., Matsushita, B. & Fukushima, T., 2015. Distinguishing surface cyanobacterial blooms and aquatic macrophytes using Landsat/TM and ETM+ shortwave infrared bands. *Remote Sensing of Environment*, 157, pp.35–47. Available at: http://dx.doi.org/10.1016/j.rse.2014.04.031.

Paerl, H.W. et al., 2001. Harmful freshwater algal blooms, With an emphasis on cyanobacteria. *The Scientific World JOURNAL*, 1, pp.76–113. Available at: http://www.hindawi.com/journals/tswj/2001/139109/abs/.

Paerl, H.W. & Huisman, J., 2009. Climate change: a catalyst for global expansion of harmful cyanobacterial blooms. *Environmental Microbiology Reports*, 1, pp.27–37. Available at: http://onlinelibrary.wiley.com/doi/10.1111/j.1758-2229.2008.00004.x/full [Accessed February 20, 2017].

Paerl, H.W. & Otten, T.G., 2013. Harmful Cyanobacterial Blooms: Causes, Consequences, and Controls. *Microbial Ecology*, 65(4), pp.995–1010.

Palmer, S.C.J., Kutser, T. & Hunter, P.D., 2015. Remote sensing of inland waters: Challenges, progress and future directions. *Remote Sensing of Environment*, 157, pp.1–8. Available at: http://dx.doi.org/10.1016/j.rse.2014.09.021.

Papastergiadou, E.S. et al., 2007. Environmental Monitoring of Spatio-temporal Changes Using Remote Sensing and GIS in a Mediterranean Wetland of Northern Greece. *Water Resources Management*, 22(5), pp.579–594. Available at: http://link.springer.com/10.1007/s11269-007-9179-7 [Accessed March 30, 2014].

Pardo-Pascual, J.E. et al., 2012. Automatic extraction of shorelines from Landsat TM and ETM+ multi-temporal images with subpixel precision. *Remote Sensing of Environment*, 123, pp.1–11. Available at: http://linkinghub.elsevier.com/retrieve/pii/S0034425712001174 [Accessed May 29, 2014].

Päzolt, J., 2015. *Landesamt für Umwelt, Gesundheit und Verbraucherschutz (Brandenburg)*, Available at: http://www.lugv.brandenburg.de/.

Perez-Valdivia, C. & Sauchyn, D., 2011. Tree-ring reconstruction of groundwater levels in Alberta, Canada: Long term hydroclimatic variability. *Dendrochronologia*, 29(1), pp.41–47.

Philpot, W.D., 1989. Bathymetric mapping with passive multispectral imagery. *Applied Optics*, 28(8), p.1569. Available at: https://www.osapublishing.org/abstract.cfm?URI=ao-28-8-1569 [Accessed February 14,

2017].
Planet Labs, I., Company website of Planet Labs, Inc. Available at: https://www.planet.com/company/approach/ [Accessed January 31, 2017].
Proft, G., 1984. Die pelagische Calcitfällung und der Carbonatgehalt von Sedimenten pleistozäner Seen. *Acta hydrochimica et hydrobiologica*, 12(1984), pp.321–326. Available at: http://onlinelibrary.wiley.com/doi/10.1002/aheh.19840120314/abstract [Accessed March 12, 2014].
Puech, C. & Matgen, R.H.D.R.P., Estimation of flood water levels by merging DEM and satellite imagery using hydraulics laws through AI to enhance the estimates. , (1), pp.1–7.
Puech, C. & Raclot, D., 2002. Using geographical information systems and aerial photographs to determine water levels during floods. *Hydrological Processes*, 16(8), pp.1593–1602. Available at: http://doi.wiley.com/10.1002/hyp.1023 [Accessed April 7, 2014].
Pulvermüller, A.G., Kleiner, J. & Mauser, W., 1995. Calcite patchiness in Lake Constance as viewed by LANDSAT-TM. *Aquatic Sciences*, 57(4), pp.338–349.
Pulvirenti, L. et al., 2011. An algorithm for operational flood mapping from Synthetic Aperture Radar (SAR) data using fuzzy logic. *Natural Hazards and Earth System Science*, 11(2), pp.529–540. Available at: http://www.nat-hazards-earth-syst-sci.net/11/529/2011/ [Accessed December 9, 2011].
Pulvirenti, L. et al., 2013. Monitoring Flood Evolution in Vegetated Areas Using COSMO-SkyMed Data: The Tuscany 2009 Case Study. *IEEE Journal of Selected Topics in Applied Earth Observations and Remote Sensing*, 6(4), pp.1807–1816.
Qi, Z. et al., 2010. Land use and land cover classification using RADARSAT-2 polarimetric SAR image. *ISPRS TC VII Symposium–100 Years ISPRS*, XXXVIII, pp.198–203. Available at: http://www.isprs.org/proceedings/XXXVIII/part7/a/pdf/198_XXXVIII-part7A.pdf [Accessed February 26, 2013].
Qiao, C. et al., 2012. An Adaptive Water Extraction Method from Remote Sensing Image Based on NDWI. *Journal of the Indian Society of Remote Sensing*, 40(September), pp.421–433.
Quinn, F.H. & Sellinger, C.E., 2006. A Reconstruction of Lake Michigan–Huron Water Levels Derived from Tree Ring Chronologies for the Period 1600–1961. *Journal of Great Lakes Research*, 32(1), pp.29–39. Available at: http://www.bioone.org/doi/abs/10.3394/0380-1330%282006%2932%5B29%3AAROLMW%5D2.0.CO%3B2 [Accessed January 5, 2017].
R Development Core Team, 2006. R: A Language and Environment for Statistical Computing.
RapidEye, 2013. *RapidEye - Satellite Imagery Product Specifications*,
Rees, W., 2006. *Remote Sensing of Snow and Ice*, Taylor & Francis.
Refsgaard, J.C. & Henriksen, H.J., 2004. Modelling guidelines—terminology and guiding principles. *Advances in Water Resources*, 27(1), pp.71–82.
Richter, D., 1997. Das Langzeitverhalten von Niederschlag und Verdunstung und dessen Auswirkungen auf den Wasserhaushalt des Stechlinseegebietes. In *Berichte des Deutschen Wetterdienstes 201*. Offenbach am Main: Selbstverlag des Deutschen Wetterdienstes.
Richter, D., 1995. Ergebnisse methodischer Untersuchungen zur Korrektur des systematischen Meßfehlers des Hellmann-Niederschlagmessers. In *Berichte des Deutschen Wetterdienstes 194*. Offenbach am Main: Selbstverlag des Deutschen Wetterdienstes .
Riedmüller, U., Hoehn, E. & Mischke, U., 2014. *Trophieklassifikation von Seen. Richtlinie*

zur Ermittlung des Trophie-Index nach LAWA für natürliche Seen, Baggerseen,Talsperren und Speicherseen Bund-/Länderarbeitsgemeinschaft Wasser (LAWA), ed., Berlin, Germany: Kulturbuch-Verlag.

Rignot, E.J.M. & Van Zyl, J.J., 1993. Change Detection Techniques for ERS - 1 SAR Data. *IEEE TRANSACTIONS ON GEOSCIENCE AND REMOTE SENSING*, 31(4).

Rinke, K. et al., 2013. Reservoirs as sentinels of catchments: the Rappbode Reservoir Observatory (Harz Mountains, Germany). *Environmental Earth Sciences*, 69(2), pp.523–536. Available at: http://link.springer.com/10.1007/s12665-013-2464-2 [Accessed January 6, 2017].

Ritchie, J.C., Zimba, P. V. & Everitt, J.H., 2003. Remote Sensing Techniques to Assess Water Quality. *Photogrammetric Engineering & Remote Sensing*, 69(6), pp.695–704. Available at: http://essential.metapress.com/openurl.asp?genre=article&id=doi:10.14358/PERS.69.6.695.

Roach, J., Griffith, B. & Verbyla, D., 2012. Comparison of three methods for long-term monitoring of boreal lake area using Landsat TM and ETM+ imagery. *Canadian Journal of Remote Sensing*, 38(4), pp.427–440. Available at: http://www.tandfonline.com/doi/abs/10.5589/m12-035 [Accessed August 12, 2014].

Robbins, L.L., Tao, Y. & Evans, C.A., 1997. Temporal and spatial distribution of whitings on Great Bahama Bank and a new lime mud budget. *Geology*, 25(10), pp.947–950.

Rodewald-Rudescu, L., 1974. *Die Binnengewässer, Band XXVII, Das Schilfrohr*, Stuttgart.

Roessler, S., Wolf, P. & Schneider, T., 2013. Multispectral Remote Sensing of Invasive Aquatic Plants Using RapidEye. In J. M. Krisp et al., eds. *Earth Observation of Global Changes (EOGC)*. Lecture Notes in Geoinformation and Cartography. Berlin, Heidelberg: Springer Berlin Heidelberg, pp. 109–123. Available at: http://link.springer.com/10.1007/978-3-642-32714-8 [Accessed January 14, 2014].

Romero-Viana, L. et al., 2008. Climate signal in varve thickness: Lake la Cruz (Spain), a case study. *Journal of Paleolimnology*, 40(2), pp.703–714.

Romero, L. et al., 2006. Sedimentation patterns of photosynthetic bacteria based on pigment markers in meromictic Lake La Cruz (Spain): Paleolimnological implications. *Journal of Paleolimnology*, 35(1), pp.167–177.

Sandau, R., 2010. Status and trends of small satellite missions for Earth observation. *Acta Astronautica*, 66(1–2), pp.1–12. Available at: http://dx.doi.org/10.1016/j.actaastro.2009.06.008.

Scheuchl, B., 2006. *Sea ice monitoring using spaceborne multi-polarization and polarimetric SAR imagery*, Available at: http://dl.acm.org/citation.cfm?id=1269528 [Accessed January 22, 2013].

Scheuchl, B. et al., 2005. The potential of cross-polarization information for operational sea ice monitoring. In *European Space Agency, (Special Publication) ESA SP*. pp. 2139–2145. Available at: http://sar.ece.ubc.ca/papers/ENVISAT_Symp_2004.pdf [Accessed November 7, 2012].

Schlungbaum, G. & Krech, M., 1999. Klassifizierung und Bewertung von Seen -die Entwicklung vom Seentypensystem bis zur EU-Wasserrahmenrichtlinie. *Rostock. Meeresbiolog. Beitr.*, 7, pp.45–63. Available at: http://www.oekologie.uni-rostock.de/fileadmin/Mathnat_Bio_Oekologie/RMB/RMB_07/RMB_07-02.pdf.

Schmieder, K. et al., 2004. Effects of water level variations on the dynamics of the reed belts of Lake Constance. *Ecohydrology & Hydrobiology*, 4(4), pp.469–480.

Schmitt, A. & Brisco, B., 2013. Wetland Monitoring Using the Curvelet-Based Change Detection Method on Polarimetric SAR Imagery. *Water*, 5(3), pp.1036–1051. Available at: http://www.mdpi.com/2073-4441/5/3/1036/.

Schneider, K. & Mauser, W., 1996. Processing and accuracy of Landsat Thematic Mapper data for lake surface temperature measurement. *International Journal of Remote Sensing*, 17(11), pp.2027–2041.

Schönfelder, I. & Steinberg, C.E.W., 2004. How did the nutrient concentrations change in northeastern German lowland rivers during the last four millennia? - A paleolimnological study of floodplain sediments. *Studia Quaternaria*, 21, pp.129–138.

Schott, J.R. et al., 2001. Calibration of Landsat thermal data and application to water resource studies. *Remote Sensing of Environment*, 78(1–2), pp.108–117.

Schowengerdt, R.A., 2007. *Remote Sensing: Models and Methods for Image Processing, Third Edition*,

Schulla, J. & Jasper, K., 2007. Model Description WaSiM-ETH.

Schultz, G. & Engman, E., 2000. *Remote Sensing in Hydrology and Water Management*, Berlin Heidelberg: Springer.

Schumann, G. et al., 2009. Progress in integration of remote sensing derived flood extent and stage data and hydraulic models. *Rev. Geophys*, 47(4), pp.1–20. Available at: http://www.ecmwf.int/staff/florian_pappenberger/publications/pdf/SchumannEtAl_2009_2008RG000274.pdf [Accessed February 2, 2012].

Schuster, C. et al., 2015. Grassland habitat mapping by intra-annual time series analysis – Comparison of RapidEye and TerraSAR-X satellite data. *International Journal of Applied Earth Observation and Geoinformation*, 34(November), pp.25–34. Available at: http://www.sciencedirect.com/science/article/pii/S0303243414001378.

Schütz, E. & Gruber, E., 2000. *Mythos Reichsautobahn. Bau und Inszenierung der „Straßen des Führers" 1933–1941*, Berlin: Ch. Links Verlag. Available at: https://books.google.com/books?hl=de&lr=&id=V7NLDQ-FUvcC&oi=fnd&pg=PA7&dq=Mythos+Reichsautobahn.+Bau+und+Inszenierung+der+,„Straßen+des+Führers"+1933–1941&ots=AUwhbg7tkw&sig=IEjx_aVhzqDobiWRkGvwDr7ysn8.

Schwarz, G. et al., 2009. Automated information extraction from high resolution SAR images: TerraSAR-X interpretation applications. In *Geoscience and Remote Sensing Symposium, 2009 IEEE International, IGARSS 2009*. IEEE, p. IV–677-680. Available at: http://ieeexplore.ieee.org/xpls/abs_all.jsp?arnumber=5417467 [Accessed February 8, 2012].

Schwatke, C., DAHITI: Database for Hydrological Time Series of Inland Waters. Available at: http://dahiti.dgfi.tum.de/en/request_target/ [Accessed January 20, 2017].

Schwatke, C. et al., 2015. DAHITI – an innovative approach for estimating water level time series over inland waters using multi-mission satellite altimetry. *Hydrology and Earth System Sciences*, 19(10), pp.4345–4364. Available at: http://dahiti.dgfi.tum.de/en/.

Schweingruber, F.H., 1983. *Der Jahrring. Standort, Methodik, Zeit und Klima in der Dendrochronologie.*, Haupt, Bern.

Schweingruber, F.H., 1978. *Microscopic Wood Anatomy*, Birmensdorf, Switzerland.

Sentinel-1 Team, 2013. *Sentinel-1 User Handbook*,

Sentinel-3 Team, 2013. *Sentinel - 3 User Handbook*, Available at: https://sentinels.copernicus.eu/documents/247904/685236/Sentinel-3_User_Handbook [Accessed January 30, 2017].

Shapley, M.D. et al., 2005. Late-Holocene flooding and drought in the Northern Great Plains, USA, reconstructed from tree rings, lake sediments and ancient shorelines. *The Holocene*, 15(1), pp.29–41. Available at: http://hol.sagepub.com/cgi/doi/10.1191/0959683605hl781rp [Accessed April 10, 2014].

Da Silva, J.S. et al., 2012. Water level dynamics of Amazon wetlands at the watershed scale by satellite altimetry. *International Journal of Remote Sensing*, 33(March 2015),

pp.3323–3353.
Smith, L.C., 1997. Satellite remote sensing of river inundation area, stage, and discharge: A review. *Hydrological processes*, 11(10), pp.1427–1439. Available at: http://www.sscnet.ucla.edu/geog/downloads/297/179.pdf [Accessed February 2, 2012].
Soh, L.-K. & Tsatsoulis, C., 1999. Texture Analysis of SAR Sea Ice Imagery Using Gray Level Co-Occurrence Matrices. *IEEE TRANSACTIONS ON GEOSCIENCE AND REMOTE SENSING*, 37(2), pp.780–795. Available at: http://digitalcommons.unl.edu/csearticles [Accessed February 20, 2017].
Solbo, S. & Pettinato, S., 2004. Mapping of flooding in the Alessandria area with ERS. In *IGARSS'04*. IEEE, pp. 4689–4692. Available at: http://ieeexplore.ieee.org/xpls/abs_all.jsp?arnumber=1370204 [Accessed July 26, 2012].
Sonobe, R. et al., 2014. Random forest classification of crop type using multi-temporal TerraSAR-X dual-polarimetric data. *Remote Sensing Letters*, 5(2), pp.157–164.
Souyris, J.-C. et al., 2005. Compact Polarimetry Based on Symmetry Properties of Geophysical Media: The pi/4 Mode. *Geoscience and Remote Sensing, IEEE Transactions on*, 43(3), pp.634–646.
Speer, J.H., 2010. *Fundamentals of Tree-Ring Research*, Tucson, Arizona: University of Arizona Press.
Spieß, H.-J., 2004. Ergebnisse der Untersuchungen submerser Makrophyten in mesotroph-eutrophen Seen Mecklenburg-Vorpommerns. *Rostock. Meeresbiolog. Beitr.*, 13, pp.73–84.
Stabel, H.-H., 1986. Calcite precipitation in Lake Constance: Chemical equilibrium, sedimentation,and nucleation by algae. *Limnology and Oceanography*, 31(5), pp.1081–1094.
Stafford, D.B., 1971. *An aerial photographic technique for beach erosion surveys in North Carolina*,
Stalu-MV, 2015. Staatliches Amt für Landwirtschaft und Umwelt Mecklenburgische Seenplatte: Produkte. Available at: http://www.stalu-mv.de/cms2/StALU_prod/StALU/de/ms/index.jsp [Accessed January 8, 2015].
Strigel, G., Ebner von Eschenbach, A.-D. & Barjenbruch, U. eds., 2010. *Wasser – Grundlage des Lebens. Hydrologie für eine Welt im Wandel*, Stuttgart: Schweizerbart.
Strong, A. & Eadie, B.J., 1978. Satellite observations of calcium carbonate precipitations in the Great Lakes. *Limnology and Oceanography*, 23(5), pp.877–887. Available at: http://ci.nii.ac.jp/naid/10020090969/ [Accessed March 12, 2014].
Strozzi, T. et al., 2012. Glacial lake mapping with very high resolution satellite SAR data. *Natural Hazards and Earth System Science*, 12(8), pp.2487–2498. Available at: http://www.nat-hazards-earth-syst-sci.net/12/2487/2012/ [Accessed March 1, 2013].
Suchozebrska, M. & Chabudziński, L., 2007. Anthropogenic transformations of the hydrographical network in lake catchment areas of the Uściwierz lowering (Łeczna-Włodawa Lake District). *Limnological Review*, (7), pp.225–231.
Tan, H. & NASA, 2016. ASTER website. Available at: https://asterweb.jpl.nasa.gov/ [Accessed January 30, 2017].
Tetteh, G.O., Schönert, M. & Ag, B., 2015. Automatic Generation of Water Masks from RapidEye Images. *Journal of Geoscience and Environment Protection*, 3, pp.17–23.
Thiemann, S. & Kaufmann, H., 2000. Determination of chlorophyll content and trophic state of lakes using field spectrometer and IRS-1C satellite data in the Mecklenburg Lake District, Germany. *Remote Sensing of Environment*, 73(2), pp.227–235.
Thiemann, S. & Kaufmann, H., 2002. Lake water quality monitoring using hyperspectral airborne data - A semiempirical multisensor and multitemporal approach for the Mecklenburg Lake District, Germany. *Remote Sensing of Environment*, 81(2–3), pp.228–

237.
Thiemann, S. & Koschel, R., 2001. Erfassung des räumlichen Verteilungsmusters von Kalkfällung mit Fernerkundungsdaten. *Wasser und Boden*, 53(10), pp.25–28. Available at: http://cat.inist.fr/?aModele=afficheN&cpsidt=1138978 [Accessed July 4, 2014].
Thomas, B. et al., 2012. Regional catchment classification with respect to low flow risk in a Pleistocene landscape. *Journal of Hydrology*, 475, pp.392–402.
Thompson, J.B., 1990. Cyanobacterial Precipitation of Gypsum, Calcite and Magnesitre From Natural Lake Water.Pdf. *Geology*, 18(10), pp.995–998.
Timmermann, T. & Succow, M., 2001. Kesselmoore. In M. Succow & H. Joosten, eds. *Landschaftsökologische Moorkunde*. Stuttgart: Schweizerbart, pp. 379–390.
Tiner, R.W., Lang, M.W. & Klemas, V. V., 2015. *Remote Sensing of Wetlands. Applications and Advances*, Boca Raton, FL, USA: CRC Press.
Toming, K. et al., 2016. First experiences in mapping lakewater quality parameters with sentinel-2 MSI imagery. *Remote Sensing*, 8(8), pp.1–14.
Topouzelis, K.N. & N., K., 2008. Oil Spill Detection by SAR Images: Dark Formation Detection, Feature Extraction and Classification Algorithms. *Sensors*, 8(10), pp.6642–6659. Available at: http://www.mdpi.com/1424-8220/8/10/6642/ [Accessed February 16, 2017].
Torbick, N. & Corbiere, M., 2015. A Multiscale Mapping Assessment of Lake Champlain Cyanobacterial Harmful Algal Blooms. *International Journal of Environmental Research and Public Health*, 12(9), pp.11560–11578. Available at: http://www.mdpi.com/1660-4601/12/9/11560/ [Accessed January 29, 2017].
Townsend, P.A., 2001. Mapping seasonal flooding in forested wetlands using multi-temporal Radarsat SAR. *Photogrammetric Engineering and Remote Sensing*, 67(7), pp.857–864. Available at: http://www.asprs.org/a/publications/pers/2001journal/july/2001_jul_857-864.pdf [Accessed January 17, 2012].
Troin, M. et al., 2012. Rainfall–runoff modeling of recent hydroclimatic change in a subtropical lake catchment: Laguna Mar Chiquita, Argentina. *Journal of Hydrology*, 475, pp.379–391.
Tucker, C.J., 1979. Red and Photographic Infrared Linear Combinations for Monitoring Vegetation. *Remote Sensing of Environment*, 8, pp.127–150.
Twele, A. et al., 2016. Sentinel-1-based flood mapping: a fully automated processing chain. *International Journal of Remote Sensing*, 37(13), pp.2990–3004. Available at: http://www.tandfonline.com/doi/full/10.1080/01431161.2016.1192304 [Accessed February 15, 2017].
U.S. Department of the Interior & U.S. Geological Survey, 2016. USGS website: Earthexplorer. Available at: http://earthexplorer.usgs.gov/ [Accessed February 24, 2016].
Ulrich, K.-U., 1998. *Vergleichende Untersuchungen zur Auswirkungen des Sediments auf die Wasserbeschaffenheit in Trinkwassertalsperren unter Berücksichtigung von Stauspiegelschwankungen*, Cuvillier Verlag, Göttingen.
Uścinowicz, S. et al., 2011. Drowned Forests in the Gulf of Gdańsk (Southern Baltic) as an Indicator of the Holocene Shoreline Changes. In Springer Berlin Heidelberg, pp. 219–231. Available at: http://link.springer.com/10.1007/978-3-642-17220-5_11 [Accessed January 6, 2017].
USGS, 2011. Landsat 7 Science Data Users Handbook. *National Aeronautics and Space Administration*, pp.1–186.
USGS, 2016. USGS Spectral Characteristics Viewer. Available at: https://landsat.usgs.gov/spectral-characteristics-viewer-load [Accessed June 21, 2016].
Vachon, P.W. & Dobson, F.W., 2000. Wind retrieval from RADARSAT SAR images: Selection of a suitable C-band HH polarization wind retrieval model. *Canadian Journal*

of Remote Sensing, 26(4), pp.306–313.
Vallet-Coulomb, C. et al., 2006. Hydrological modeling of tropical closed Lake Ihotry (SW Madagascar): Sensitivity analysis and implications for paleohydrological reconstructions over the past 4000 years. *Journal of Hydrology*, 331(1), pp.257–271.
Verpoorter, C., Kutser, T. & Tranvik, L., 2012. Automated mapping of water bodies using Landsat multispectral data. *Limnology and Oceanography: Methods*, 10, pp.1037–1050. Available at: http://www.aslo.org/lomethods/free/2012/1037.html.
De Vicente, I. et al., 2006. Sedimentary phosphate fractions related to calcite precipitation in an eutrophic hardwater lake (Lake Alserio, northern Italy). *Journal of Paleolimnology*, 35(1), pp.55–64.
Voormansik, K. et al., 2014. Flood Mapping With TerraSAR-X in Forested Regions in Estonia. , 7(2), pp.562–577.
Voormansik, K. et al., 2015. Observations of Cutting Practices in Agricultural Grasslands Using Polarimetric SAR. *IEEE Journal of Selected Topics in Applied Earth Observations and Remote Sensing*, pp.1–15. Available at: http://ieeexplore.ieee.org/lpdocs/epic03/wrapper.htm?arnumber=7360150.
Voormansik, K. et al., 2013. Towards a detection of grassland cutting practices with dual polarimetric TerraSAR-X data. *International Journal of Remote Sensing*, 34(22), pp.8081–8103. Available at: http://www.tandfonline.com/doi/abs/10.1080/01431161.2013.829593.
Wang, J., Sheng, Y. & Tong, T.S.D., 2014. Monitoring decadal lake dynamics across the Yangtze Basin downstream of Three Gorges Dam. *Remote Sensing of Environment*, 152, pp.251–269. Available at: http://linkinghub.elsevier.com/retrieve/pii/S003442571400217X [Accessed July 21, 2014].
Waterstraat, V.A. & Spiess, H., 2015. Zustandsanalyse der Seen in den Einzugsgebieten des Großen Fürstenseer Sees und des Großen Serrahnsees. In J. Kobel, M. Küster, & M. Schwabe, eds. *Neue Beiträge zum Naturraum und zur Landschaftsgeschichte im Teilgebiet Serrahn des Müritz-Nationalparks*. Berlin, Germany: Geozon Science Media, pp. 241–258.
Weichelt, H. et al., 2014. *The RapidEye Red Edge Band*,
Weidemann, A.D. et al., 1985. Particulate and optical properties during CaCO3 precipitation in Otisco Lake. *Limnology and Oceanography*, 30(5), pp.1078–1083.
Wen, X. et al., 2014. Research on the Features of Chlorophyll-a Derived from RapidEye and EOS/MODIS Data in Chaohu Lake. In *IOP Conf. Series: Earth and Environmental Science 17*. pp. 1–6. Available at: http://iopscience.iop.org/1755-1315/17/1/012111 [Accessed January 29, 2017].
Wetterdienst, D., Deutscher Wetterdienst. Available at: http://www.dwd.de/ [Accessed June 20, 2015].
Wetzel, R.G., 2001. *Limnology: Lake and River Ecosystems (3rd Edition)* 3rd Editio., San Diego (California): Academic Pres.
van de Weyer, K. et al., 2009. Flächenbilanzierungen submerser Pflanzenbestände – dargestellt am Beispiel des Großen Stechlinsees (Brandenburg) im Zeitraum von 1962-2008. *Naturschutz und Landschaftspflege in Brandenburg*, 18(4), pp.1–6.
White, K. & El Asmar, H.M., 1999. Monitoring changing position of coastlines using Thematic Mapper imagery, an example from the Nile Delta. *Geomorphology*, 29, pp.93–105.
White, L. et al., 2015. *A Collection of SAR Methodologies for Monitoring Wetlands*, Available at: http://www.mdpi.com/2072-4292/7/6/7615/.
White, L. et al., 2014. RADARSAT-2 Beam Mode Selection for Surface Water and Flooded

Vegetation Mapping. *Canadian Journal of Remote Sensing*, 40(2), pp.135–151.
Wiles, G.C., Krawiec, A.C. & D'Arrigo, R.D., 2009. A 265-year reconstruction of Lake Erie water levels based on North Pacific tree rings. *Geophysical Research Letters*, 36(5), p.L05705. Available at: http://doi.wiley.com/10.1029/2009GL037164 [Accessed January 6, 2017].
Williams, D. & Lyon, J., 1997. Historical aerial photographs and a geographic information system (GIS) to determine effects of long-term water level fluctuations on wetlands along the St. Marys. *Aquatic Botany*, 58(3–4), pp.363–378. Available at: http://www.sciencedirect.com/science/article/pii/S0304377097000466 [Accessed March 12, 2014].
Williamson, C.E. et al., 2009. Lakes and reservoirs as sentinels, integrators, and regulators of climate change. *Limnology and Oceanography*, 54(6part2), pp.2273–2282. Available at: http://doi.wiley.com/10.4319/lo.2009.54.6_part_2.2273 [Accessed February 20, 2017].
Williamson, C.E. et al., 2008. Lakes and streams as sentinels of environmental change in terrestrial and atmospheric processes. *Frontiers in Ecology and the Environment*, 6(5), pp.247–254. Available at: http://doi.wiley.com/10.1890/070140 [Accessed January 6, 2017].
Willmott, C.J., 1982. Some Comments on the Evaluation of Model Performance. *Bulletin of the American Meteorological Society*, 63(11), pp.1309–1313. Available at: http://journals.ametsoc.org/doi/abs/10.1175/1520-0477%281982%29063%3C1309%3ASCOTEO%3E2.0.CO%3B2 [Accessed January 6, 2017].
Wloczyk, C. et al., 2006. Sea and lake surface temperature retrieval from Landsat thermal data in Northern Germany. *International Journal of Remote Sensing*, 27(12), pp.2489–2502. Available at: http://www.tandfonline.com/doi/abs/10.1080/01431160500300206 [Accessed February 20, 2017].
Wöbbecke, K. & Büro enviteam, 2008. *Badegewässerprofil nach Artikel 6 der Richtlinie 2006/7/EG und § 6 der Verordnung über die Qualität und die Bewirtschaftung der Badegewässer vom 06.02.2008 (BbgBadV)*,
Xiao, S.-C. et al., 2005. Lake Level Changes Recorded by Tree Rings of Lakeshore Shrubs: A Case Study at the Lake West-Juyan, Inner Mongolia, China. *Journal of Integrative Plant Biology*, 47(11), pp.1303–1314. Available at: http://doi.wiley.com/10.1111/j.1744-7909.2005.00190.x [Accessed January 6, 2017].
Xu, H., 2006. Modification of normalised difference water index (NDWI) to enhance open water features in remotely sensed imagery. *International Journal of Remote Sensing*, 27(14), pp.3025–3033.
Yajima, Y. et al., 2008. Polsar image analysis of wetlands using modified four component scattering decomposition. *IEEE Transactions on Geoscience and Remote Sensing*, 46(6), pp.1667–1673.
Yang, X. & Clausi, D.A., 2012. Evaluating SAR Sea Ice Image Segmentation Using Edge-Preserving Region-Based MRFs. *IEEE Journal of Selected Topics in Applied Earth Observations and Remote Sensing*, 5(5), pp.1383–1393.
Yayong, S. et al., 2016. Monitoring seasonal changes in the water surface areas of Poyang Lake using Cosmo-Skymed time series data in PR China. In *2016 IEEE International Geoscience and Remote Sensing Symposium (IGARSS)*. IEEE, pp. 7180–7183. Available at: http://ieeexplore.ieee.org/document/7730873/ [Accessed February 15, 2017].
Yonezawa, C. et al., 2012. Growth monitoring and classification of rice fields using multitemporal RADARSAT-2 full-polarimetric data. *International Journal of Remote Sensing*, 33(18), pp.5696–5711.
Zalite, K. et al., 2013. Effects of Inundated Vegetation on X-Band HH–VV Backscatter and

Phase Difference. *IEEE Journal of Selected Topics in Applied Earth Observations and Remote Sensing*, PP(99), pp.1–5. Available at: http://ieeexplore.ieee.org/xpls/abs_all.jsp?arnumber=6588943.

Zhang, Y. et al., 2003. Landsat TM Data and ERS-2 SAR Data in the Gulf of Finland. *IEEE Transactions on Geoscience and Remote Sensing*, 41(3), pp.622–629.

Zhao, L. et al., 2014. Seasonal inundation monitoring and vegetation pattern mapping of the Erguna floodplain by means of a RADARSAT-2 fully polarimetric time series. *Remote Sensing of Environment*, 152, pp.426–440. Available at: http://dx.doi.org/10.1016/j.rse.2014.06.026.

Appendix

Supplementary Materials on Chapter 2

Supplement 3: Supplementary material on remote sensing [2]

Part 1: Detailed description of the pre-processing of aerial photos and topographic maps.

The pre-processing of the aerial photos and topographic maps mainly the assignment of coordinates, called “geo-referencing”. The geo-referencing is based on the two digital orthophotos (DOPs) of 2007 and 2012 with precise geographical information. For the assignment of coordinates common points, so called ground control points (GCPs), are marked in the aerial photo/map and in the DOPs. Functional GCPs that were used for the geo-referencing were street crossings or other characteristic landmarks.

In the aerial photos we set in average 12 GCPs per image (cf. Part 2 and Part 4). In the topographic maps, we set between 14 and 55 GCPs per map (cf. Part 3 and Part 5). Based on the GCPs, the aerial photos and maps are transformed. For the aerial photos, we mostly used a second-order polynomial transformation that ensures the general accuracy of the corrected aerial photos (cf. (Hughes et al. 2006)). In one aerial photo of (1970-6-9) only 6 GCPs could be set, thus, second-order polynomial transformation was not feasible and we used a first-order polynomial transformation instead. For the topographic map, we used the spline transformation, a “rubber sheeting" - method.

The quality of the geometrical correction depends on the distribution and quality of the GCPs, the transformation used, as well as the quality of the aerial photos/maps (cf. (Anders & Byrnes 1991; Hughes et al. 2006)). For evaluation purposes we calculated the total root mean square error (RSME) of the aerial photos as the sum of squares of difference (in meter) between the actual location of a GCP and its predicted location based on the transformation and the residual GCPs. The RSME of the aerial photos are listed in the metadata of the data (cf. Part 3 and Part 5).

Geo-referencing of the aerial photos was reliable with mostly low RSME (< 2 m). Challenging were (1) the small coverage of some photos, with a depiction of only lake and forest areas; (2) the distinct changes of the landscape structure that reduced the number of suitable GCPs and decreases the accuracy of GCPs (e.g. 1959); (3) the blackening of military areas in one photo (1981-05-13, KS); and (4) the significant lens distortion (1973-05-30, RS and KS).

The interpretation of the aerial photos and the clear distinction of the water-land-border are challenged by reed growing in the lake, swimming plants, overhanging trees at the shoreline and, in the case of the image of RS 1993-04-27, sun glint on the water surface. Field observation in 2012 showed a significant floating vegetation cover in KS. Two other specifics were identified, that is, for the lake-level estimation of RS in 1969 only a part of the shoreline was used as the aerial photo does not cover the entire lake. Moreover, for the year 1959 two aerial photos had to be combined to facilitate the extraction of the entire lake area of RS.

[2] Reprinted from Journal of Hydrology, 529 (Part 2), Kaiser et al., Multi-decadal lake-level dynamics in north-eastern Germany as derived by a combination of gauging, proxy-data and modelling, 584–599, copyright (2015), with permission from Elsevier

For the very old historic maps (before 1900) the possible GCPs were so coarse that the actual position of the shorelines could not be extracted. Additionally, the temporal accuracies were low. Old maps were often developed step by step over several years and the date of publication differed from the date of the measurements or the update of old measurements. We noticed that even when maps were published in an updated format, lakes and forests were often just copied out of the old maps.

Part 2: List of the aerial photos and digital orthophotos of Rederswalder See and their metadata.

The metadata of the remote sensing data of Redernswalder See (RS) include the acquisition date of the digital orthophotos (DOPs) and aerial photos, the nominal scale/ resolution and the source of the images. For the aerial photos we listed the number of GCPs and the transformation used, and the resulting root mean square error (RSME) in meter. The RMSE is the sum of deviations between predicted and actual position of the GCPs.

Date	Nominal scale/ resolution	Source	# of GCPs	Trans-formation	RMSE (m)
2012-05-24	20 cm	Landesvermessung und Geobasisinformation Brandenburg (LGB)	DOP	-	-
2009-04-24	20 cm	Landesvermessung und Geobasisinformation Brandenburg (LGB)	DOP	-	-
2007-04-14	40 cm	Landesvermessung und Geobasisinformation Brandenburg (LGB)	DOP	-	-
2003-08-09	100 cm	Landesvermessung und Geobasisinformation Brandenburg (LGB)	DOP	-	-
1993-04-27	1:18000	Landesvermessung und Geobasisinformation Brandenburg (LGB)	14	2nd Order	4.15436
1987-05-10	1:18000	Landesvermessung und Geobasisinformation Brandenburg (LGB)	12	2nd Order	3.66549
1978-05-04	1:12700	Bundesarchiv	12	2nd Order	3.26063
1973-05-30	1:12500	Bundesarchiv	12	2nd Order	5.66798
1969-09-08	1:10500	Bundesarchiv	10	2nd Order	1.48932
1959-06-01	1:10000	Bundesarchiv	9	2nd Order	2.40953
1959-06-01	1:10000	Bundesarchiv	10	2nd Order	4.65904
1937-07-00	1:25000	Landesvermessung und Geobasisinformation Brandenburg (LGB)	DOP	-	-

Part 3: List of the topographic maps of Rederswalder See and their metadata.

The metadata of the topographic maps of Redernswalder See (RS) include the date when the maps were published (and last updated), their name with information about the scale and the source of the maps.

Date	Name	Source
2008 (updated 2005)	TK25 (ATKIS)-2849 Warnitz	vom GFZ (Geo-Basis)
1998 (updated 1994)	TK25-2849 Warnitz	HNE Kartenarchiv
1997 (updated 1994)	TK10- 2849 NW Warnitz	Kartenarchiv Humboldt-Universität
1990 (updated1978)	DDR-TK25 (AS): N-33-100-D-b (Greiffenberg),	Bundesarchiv, Geo-Basis Potsdam

1985 (updated 1981)	DDR-TK25 (AS): N-33-100-D-b (Greiffenberg),	Bundesarchiv, Staatsbibliothek Potsdamer Str.
1981	DDR_TK10-0609_421 Warnitz-Grünheide	Kartenarchiv Humboldt-Universität
1976 (updated 1974)	DDR-TK25 (AS): N-33-100-D-b (Greiffenberg),	Bundesarchiv
1957 (updated 1954)	DDR-TK25 (AS): N-33-100-D-b (Greiffenberg),	Bundesarchiv
1936 (updated 1890)	Messtischblatt 1402 (2849) Polssen	Bundesarchiv
1932 (updated 1890)	Messtischblatt 1402 (2849) Polssen	Staatsbibliothek Berlin, Potsdamer Str.
1924	Militärkarte Angermünde West	Militärgeschichtliches Forschungsamt
1919 (updated1888)	Messtischblatt 1402 (2849) Polssen	Bundesarchiv
1890 (updated 1888)	Messtischblatt 1402 (2849) Polssen	Staatsbibliothek Berlin, Unter den Linden (SBB_IIIC_Kart. N 730), Bundesarchiv
1827	Urmesstischblatt 1402 Polssen	Staatsbibliothek Berlin, Unter den Linden (SBB_IIIC_Kart. N 729)
1767-1787	Schmettausche Karte 36 Tempelin	Staatsbibliothek Berlin, Unter den Linden (Kart. L 5420)
1792	Charte der Uckermark	Deutsches Historisches Museum (Do 2006/508)

Part 4: List of the aerial photos and digital orthophotos of Krummer See and their metadata.

The metadata of the remote sensing data of Krummer See (KS) include the acquisition date of the digital orthophotos (DOPs) and aerial photos, the nominal scale/ resolution and the source of the images. For the aerial photos we listed the number of GCPs and the transformation used, and the resulting root mean square error (RSME) in meter. The RMSE is the sum of deviations between predicted and actual position of the GCPs.

Date	Nominal scale/ resolution	Source	# of GCPs	Trans-formation	RMSE (m)
2012-05-24	20 cm	Landesvermessung und Geobasisinformation Brandenburg (LGB)	DOP	-	-
2009-04-12	20 cm	Landesvermessung und Geobasisinformation Brandenburg (LGB)	DOP	-	-
2007-04-14	40 cm	Landesvermessung und Geobasisinformation Brandenburg (LGB)	DOP	-	-
2003-08-09	100 cm	Landesvermessung und Geobasisinformation Brandenburg (LGB)	DOP	-	-
1993-04-01	1:18000	Landesvermessung und Geobasisinformation Brandenburg (LGB)	9	2nd Order	1.72782
1987-03-23	unknown	Landesvermessung und Geobasisinformation Brandenburg (LGB)	10	2nd Order	0.56343
1981-05-13	1:80000	Landesvermessung und Geobasisinformation Brandenburg (LGB)	9	2nd Order	1.50877
1978-05-04	1:12700	Bundesarchiv	11	2nd Order	1.46313
1973-05-30	1:12500	Bundesarchiv	31	2nd Order	6.13806
1970-06-09	1:7000	Bundesarchiv	6	1st Order	3.43973
1959-06-19	1:10000	Bundesarchiv	7	2nd Order	2.12637

Part 5: List of the topographic maps of Krummer See and their metadata.

The metadata of the topographic maps of Krummer See (KS) include the date when the maps were published (and last updated), their name with information about the scale and the source of the maps.

Date	Name	Source
2008 (updated 2005)	TK25 (ATKIS)-2949 Greiffenberg	vom GFZ (Geo-Basis)
1997 (updated 1994)	TK25 2949 Greiffenberg	HNE Kartenarchiv
1997 (updated 1994)	TK10 2949-SW Wolletz	Kartenarchiv Humboldt-Universität
1990 (updated1978)	DDR-TK25 (AS): N-33-100-D-b (Greiffenberg),	Bundesarchiv, Geo-Basis Potsdam
1985 (updated 1981)	DDR-TK25 (AS): N-33-100-D-c (Parlow-Glambeck)	Bundesarchiv, Staatsbibliothek Potsdamer Str.
1979	DDR_TK25 (AV)_0609-43_Parlow-Glambeck	HNE Kartenarchiv
1976 (updated 1974)	DDR-TK25 (AS): N-33-100-D-c (Parlow-Glambeck)	Bundesarchiv
1957 (updated 1954)	DDR-TK25 (AS): N-33-100-D-c (Parlow-Glambeck)	Bundesarchiv
1936 (updated 1884)	Messtischblatt 14082(2949) Greiffenberg	Bundesarchiv
1928 (updated 1882)	Messtischblatt 14082(2949) Greiffenberg	Bundesarchiv
1924	Militärkarte Angermünde West	Militärgeschichtliches Forschungsamt
1908 (updated 1884)	Messtischblatt 14082(2949) Greiffenberg	Staatsbibliothek Berlin, Unter den Linden (SBB_IIIC_Kart. N 730),
1890 (updated 1884)	Messtischblatt 14082(2949) Greiffenberg	Staatsbibliothek Berlin, Unter den Linden (SBB_IIIC_Kart. N 730),
1826	Urmesstischblatt 1482 Greiffenberg	Staatsbibliothek Berlin, Unter den Linden (SBB_IIIC_Kart. N 729)
1767-1787	Schmettausche Karte 51 Liebenwalde (L5420)	Staatsbibliothek Berlin, Unter den Linden (Kart. L 5420)
1792	Charte der Uckermark	Deutsches Historisches Museum (Do 2006/508)

Part 6: Selected maps of Redernswalder See (left) and Krummer See (right) after the pre-processing.

The dates in brackets are the year of the last update, not the year when the maps were published. 'Gr. Gersdorff See/Gersdorf See' is the name of Lake Redernswalder See in the late 18th to early 19th centuries. Map 'Schmettausche Karte' could not be accurately geo-referenced, thus, the geo-position of the lakes is shifted massively.

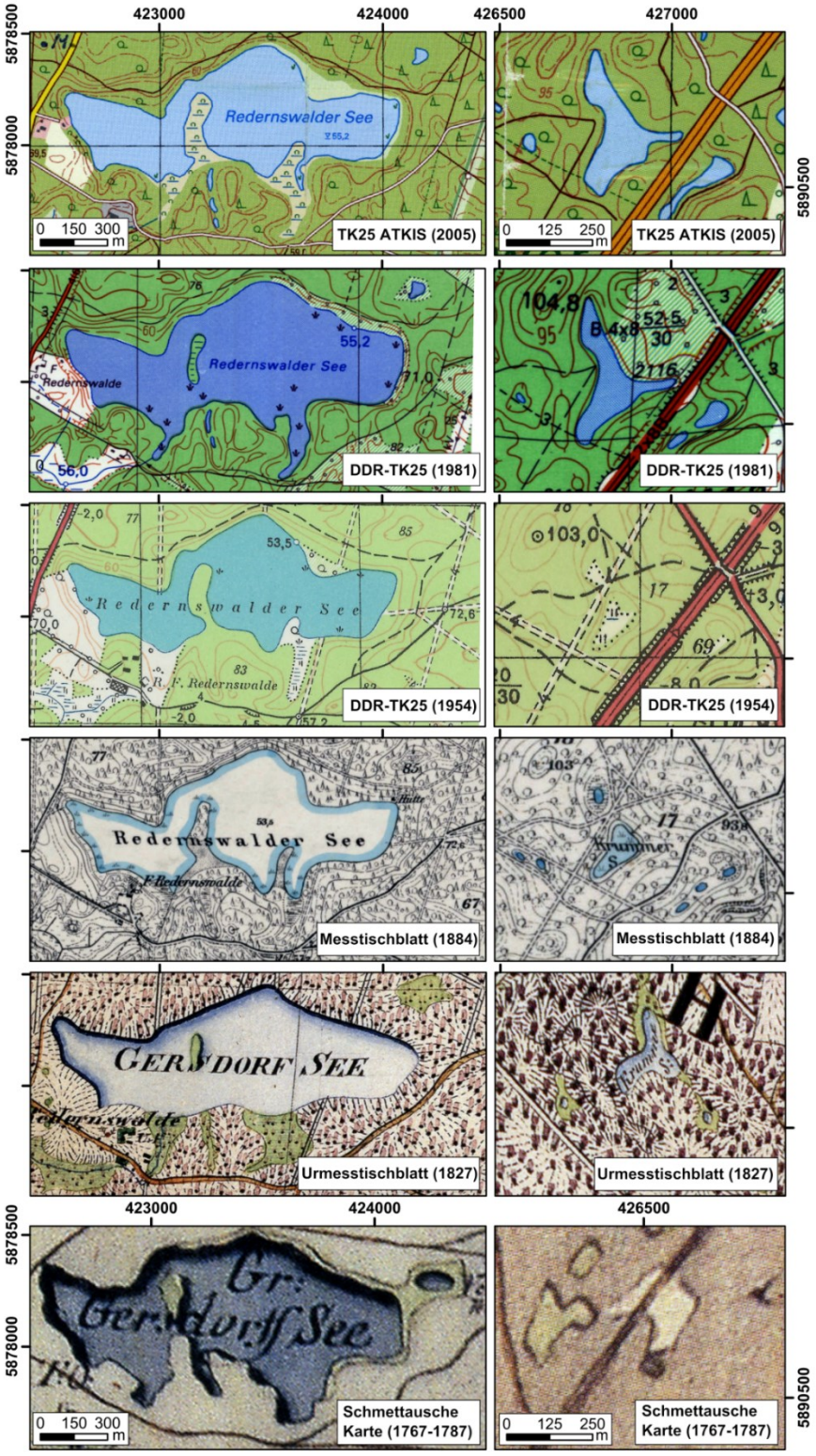
423000
424000
426500
427000
5878500
5878000
5890500
Redernswalder See
TK25 ATKIS (2005)
TK25 ATKIS (2005)
DDR-TK25 (1981)
DDR-TK25 (1981)
DDR-TK25 (1954)
DDR-TK25 (1954)
Messtischblatt (1884)
Messtischblatt (1884)
GERSDORF SEE
Urmesstischblatt (1827)
Urmesstischblatt (1827)
Gr: Gersdorff See
Schmettausche Karte (1767-1787)
Schmettausche Karte (1767-1787)

Part 7: Detailed description of the digital elevation models (DEM) and their pre-processing.

The DEMs of Redernswalder See (RS) and Krummer See (KS) are mosaics of a laser survey DEM and bathymetric data of the lakes. Following data were used for proseccing of the DEM:

Data	Date	Source	Accuracy
DEM of RS with lake surface	2011-01-29/ 20011-02-12	Landesvermessung und Geobasisinformation Brandenburg (LGB), Laserscanning	The resolution is 1 m x 1 m with an vertical and horizontal accuracy of 0.3 m
DEM of KS with lake surface	2011-03-30	Landesvermessung und Geobasisinformation Brandenburg (LGB), Laserscanning	The resolution is 1 m x 1 m with an vertical and horizontal accuracy of 0.3 m
Bathymetric point data of RS	2002-06-11	Landesamt für Umwelt, Gesundheit und Verbraucherschutz (Brandenburg)	The measurements were performed in rows with circa 50 m distance with insufficient distribution of points.
Shoreline of RS	2002-06-00	Not measured at the date of the bathymetric survey, thus, the shoreline was estimated based on the in situ measured lake level (53.38 m NHN at 2002-06-13) plotted in the digital terrain model, supported by an Landsat 7 satellite image (2002-06-01, panchromatic band: 15 m resolution)	
Bathymetric point data of KS	2014-01-14	Measured within the framework of this study	Good distribution and very high number of points in relation to the area of the lake.
Shoreline of KS	2014-01-14	Measured within the framework of this study using a GPS handheld device	

First, we interpolated the bathymetric point data using triangulation. In this interpolation method, triangles are placed between three non-uniformly spaced points and a height gradient is calculated between them. This method is frequently used for the interpolation of bathymetric maps (e.g. (Furnans & Austin 2008; Johnson et al. 2008)). The shorelines are included in the interpolations of the bathymetric point data. Because of the small number of data points of the bathymetric survey of RS and their uneven distribution, the underwater topography of RS shows artefacts and stair-like structures.

The relative bathymetric maps are transformed to absolute height maps using the absolute lake levels at the date of the bathymetric survey. For RS we took the in situ lake level, for KS we used the estimated mean lake level based on the GPS shoreline and the DEM of KS.

The DEMs of the lasersurvey are terrain models and show the bare ground without vegetation. Those DEMs were combined with the interpolated bathymetric maps. The final DEMs of RS and KS illustrate the over- and underwater topography ("terrain") with 1 m resolution.

Part 8: Digital elevation models (DEM) including over- and underwater topography of Redernswalder See and Krummer See.

The digital elevation models (DEM) illustrate the over- and underwater topography of Redernswalder See (left) and Krummer See (right). The blue line represents the shoreline of the lakes (left) extracted from the aerial photo 2012-05-24 (right) measured via GPS device during the field campaign 2014-01-14. The red dots illustrate the dendro sample sites.

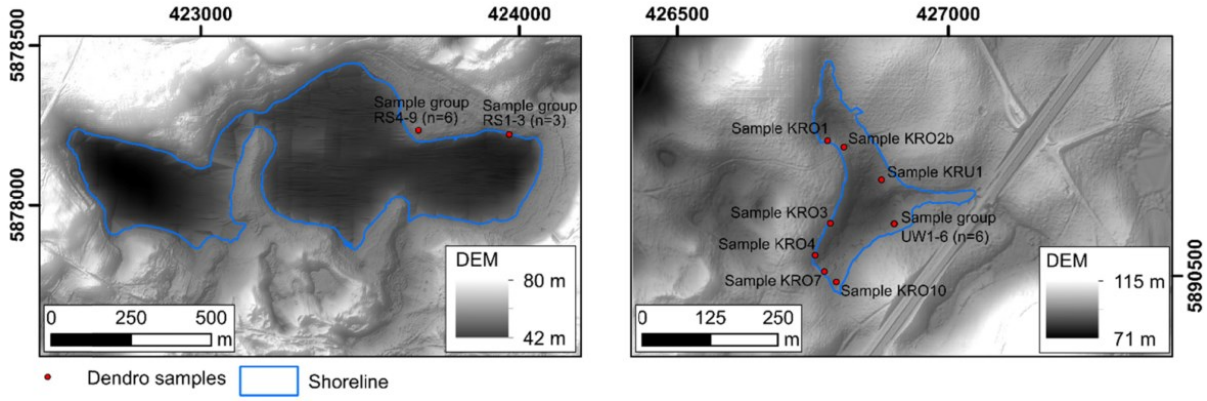

Part 9: Lake areas of Redernswalder See and area changes in percent in comparison to the newest date (2012-05-24).

The table illustrates the absolute lake area of Redernswalder See (RS) in ha and the relative lake area changes in percent in comparison to the newest date (2012-05-24).

Date	Lake area of RS [ha]	Lake area change (%)
2012-05-24	42.58	=100
2009-04-24	41.57	-2
2007-04-14	41.87	-2
2003-08-09	43.55	2
1993-04-27	52.62	24
1987-05-10	61.91	45
1978-05-04	59.84	41
1973-05-30	54.94	29
1969-09-08	46.06	8
1959-06-01	46.06	8
1937-07-15	42.83	1

Part 10: Lake areas of Krummer See and area changes in percent in comparison to the newest date (2014-01-14).

The table illustrates the absolute lake area of Krummer See (KS) in ha and the relative lake area changes in percent in comparison to the newest date (2014-01-14).

Date	Lake area [ha]	Lake area change (%)
2014-01-14	3.63	=100
2012-05-24	1.37	-62
2009-04-12	2.76	-24
2007-04-14	2.55	-30
2003-08-09	1.51	-58
1993-04-27	3.88	7
1987-03-23	4.13	14
1981-05-13	3.49	-4
1978-05-04	3.12	-14
1973-05-30	3.19	-12
1970-06-09	2.75	-24
1959-06-19	0.13	-97

Supplementary Materials on Chapter 3

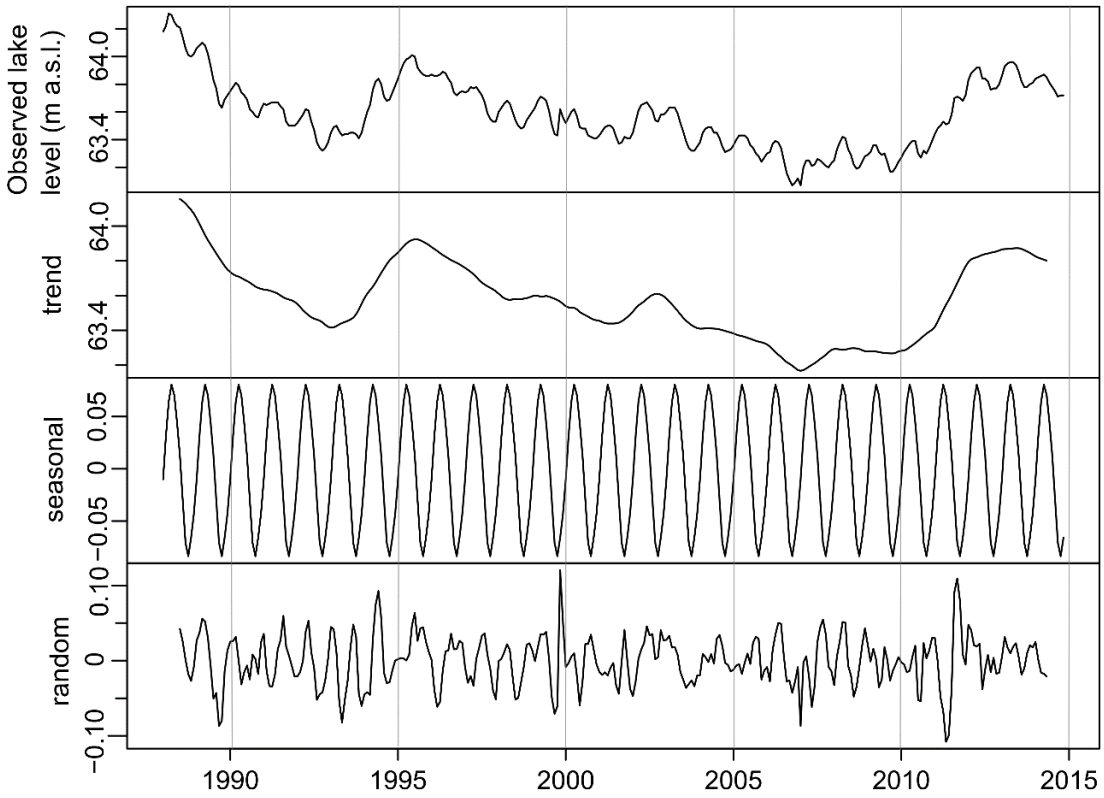

Figure S1. Level changes of LF, including a decomposition of the time series from 1988 to 2014. The observed values are the gauged lake levels. The trend component is calculated by a moving average of the observed data. The seasonal figure is computed by averaging the difference between observed data and trend for each day of all the years considered. The seasonal figure is then centered. The error component ("random") is determined by removing trend and seasonal oscillations from the observed gauging (Meyer n.d.).

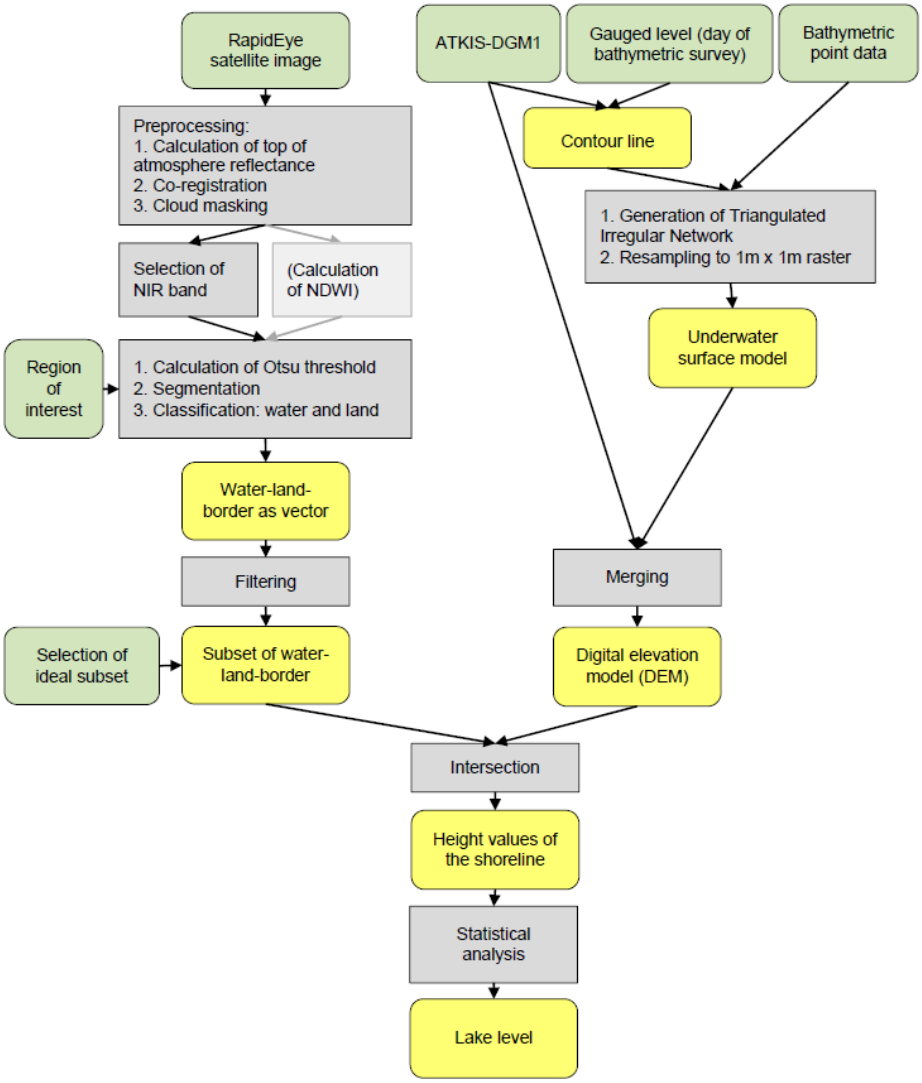

Figure S2. Workflow of the data preparation and the processing chain for the reconstruction of lake levels (*cf.* **Chapter 3, Materials and Methods**).

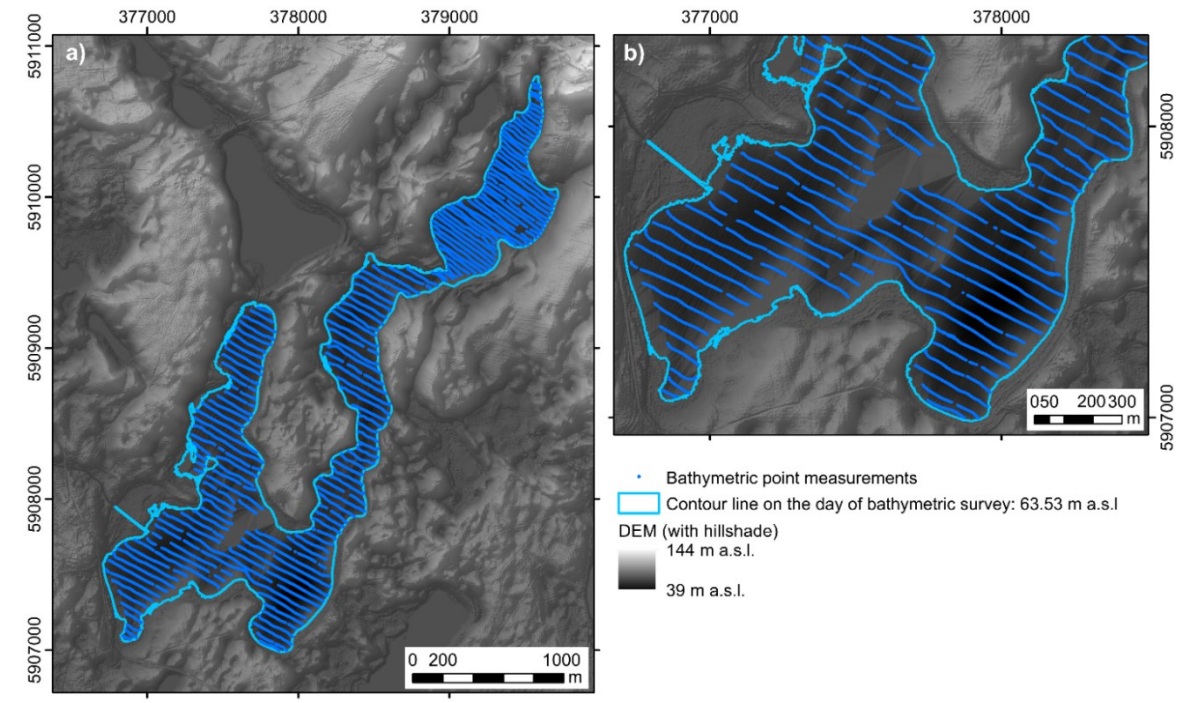

Figure S3. Digital elevation model (DEM) of **(a)** LF and **(b)** its southern part at a smaller scale. The blue dots are the bathymetric point measurements. The light blue line is the contour line from the DEM that illustrates the in situ measured lake level on the day of the bathymetric survey. Points and contour line are used to generate the underwater surface model as a Triangulated Irregular Network. The final DEM is the merged result of the digital surface model (ATKIS-DGM1) and the underwater surface model.

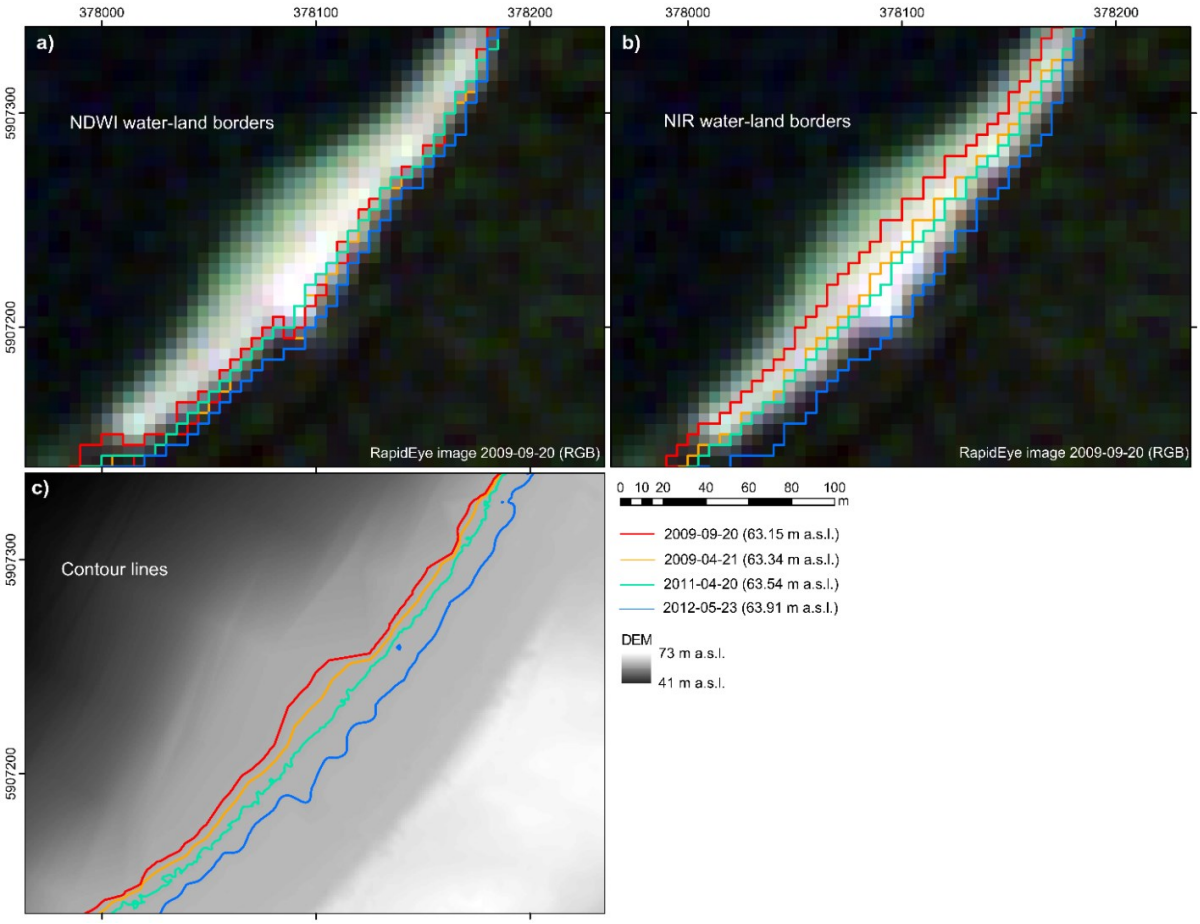

Figure S4. Illustration of the water-land borders and contour lines at the southeastern, shallow beach of LF (subset

B) on 21 April 2009, 20 September 2009, 20 April 2011, and 23 May 2012. Figure (**a**) shows the water-land borders extracted from the RapidEye images using the NDWI. Figure (**b**) shows the water-land borders extracted from the RapidEye images using the NIR. Figure (**c**) represents the GIS analysis with contour lines: The levels measured *in situ* on the four dates are delineated as contour lines in the DEM. The minimum level (63.15 m a.s.l.) between 2009 and 2014 was measured on 20 September 2009, the maximum level on a cloud free image (63.91 m a.s.l.) on 23 May 2012.

Figure S5. Photos of the shallow, southeastern beach in 2009 and 2014 (subset B), looking northwards. In 2009 there is a wide sandy beach, in 2014 the beach is flooded and the water-land border extends to the surrounding trees.

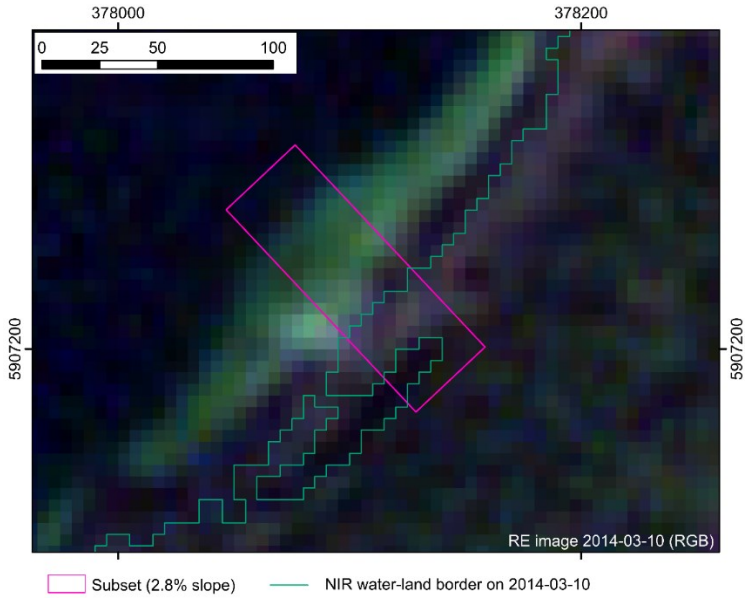

Figure S6. Misclassification of the NIR water-land border on 10 March 2014. The automatic thresholding of the water-land border spreads into a clearing in the surrounding forest. The ideal subset with a 2.8% slope is marked in pink.

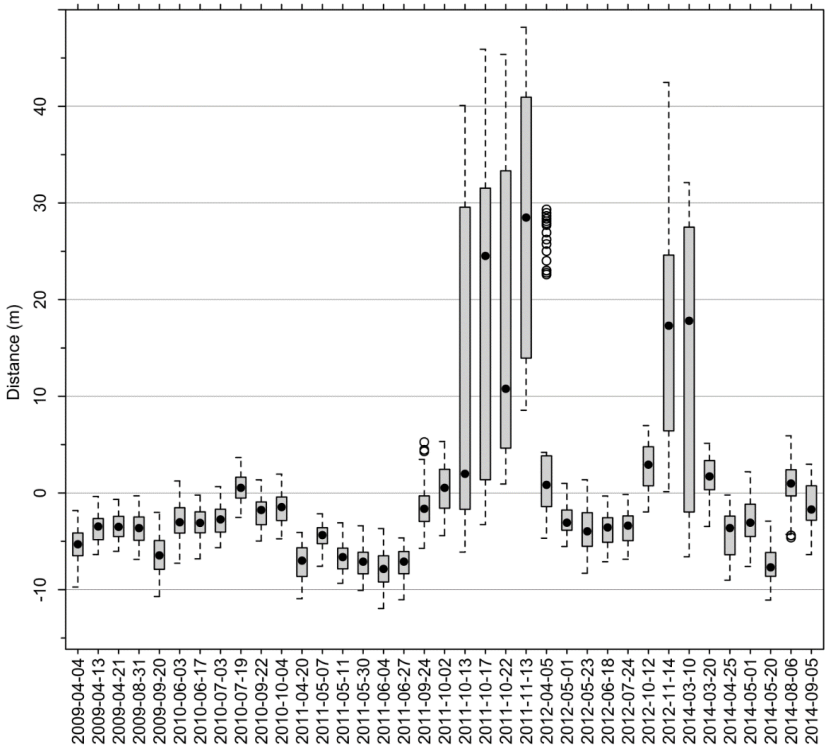

Figure S7. Boxplot of the minimum distances (in m) between the NIR water-land borders and the according contour lines at the ideal subset (subset 2.8%). The black dots represent the median. The RMSE for all dates is 13.5 m. The RMSE is reduced to 5.0 m when dates with a very low sun elevation angle (SEA) below <30°, and dates with a SEA angle below <45° in cases of high lake levels (≥63.7m a.s.l.), are excluded.

Publications Related to the Thesis

The results of this thesis were presented as posters or talks at the following conferences:

- Iris Heine, Julian Oeser, and Sibylle Itzerott (2014): Reconstruction of historic lake levels in NE Germany using remote sensing archive data. Oral presentation at TERENO International Conference in Bonn, Germany.
- Iris Heine, Julian Oeser, Sibylle Itzerott, and Birgit Kleinschmit (2015): Estimating seasonal and annual lake level changes of groundwater-fed lakes in northeastern Germany using RapidEye archive data. Oral presentation at European Geosciences Union General Assembly (EGU) Conference in Vienna, Austria. Geophysical Research Abstracts, Vol. 17, EGU2015-130.
- Iris Heine, Julian Oeser, Sibylle Itzerott, and Birgit Kleinschmit (2015): Reconstruction of shoreline changes at a natural ground-water lake in northeastern Germany using GIS and RapidEye archive data. Poster presentation, ESA Conference Water Mapping from Space (MWBS) Conference, Frascati (Italy).
- Iris Heine, Thomas Jagdhuber, and Sibylle Itzerott (2016): Classification and monitoring of reed belts using dual-polarimetric TerraSAR-X time series. Oral presentation at European Geosciences Union General Assembly (EGU) Conference in Vienna, Austria. Geophysical Research Abstracts, Vol. 18, EGU2016-6209, 2016
- Iris Heine, Thomas Jagdhuber, and Sibylle Itzerott (2016): Monitoring of natural lakes in NE Germany using dual-polarimetric TerraSAR-X. Oral presentation at ESA Living Planet Symposium 2016 in Prague, Czech Republic

Acknowledgments

I would like to take the opportunity to thank all the people who contributed to the completion of my doctoral thesis.

This thesis is part of the Helmholtz Virtual Institute for Integrated Climate and Landscape Evolution Analyses (ICLEA) and was funded by the “Helmholtz Association of German Research Centres Initiative—Networking Fund for funding a Helmholtz Virtual Institute” (VH-VI-415). I am very grateful for the financial support and the opportunity to write my thesis within this inspiring, international, and interdisciplinary project. Special thanks go to my supervisor, Prof. Dr. Achim Brauer, the speaker of the ICLEA virtual institute, and to Dr. Markus Schwab, the coordinator of the ICLEA virtual institute. And many thanks to all my ICLEA colleagues!

The thesis was written at the remote sensing section of the GFZ German Research Centre for Geosciences. My gratitude goes to Prof. Dr. Hermann Kaufmann and Prof. Dr. Luis Guanter, the heads of the remote sensing section during the time of my thesis, for providing a professional and well-structured scientific environment. They gave me the freedom to develop my own ideas and to present and discuss them at international conferences.

I want to thank Prof. Dr. Birgit Kleinschmit for enabling the realization of the thesis at the TU Berlin with her supervision. Thank you, Birgit, for your supervision and your effective comments and advice in the context of writing my thesis and beyond.

My deepest gratitude goes to Dr. Sibylle Itzerott, my supervisor at GFZ, for her continuous support of my PhD study. You always found time for me, even when your calendar was already overloaded and I could always trust on your advice! Sibylle, thank you for that very much!

The colleagues of the remote sensing section always provided a fruitful and inspiring atmosphere with scientific and non-scientific conversations. Many thanks to all of you! A special thanks to Sylvia Magnussen, the technician of the remote sensing section, who always conjured up more disk space when needed.

I also want to thank all my co-authors for contributing with their ideas, advice, and motivation to the presented manuscripts. My special thanks goes to Dr. Thomas Jagdhuber from DLR. Thank you, Thomas, for making it possible to visit you at DLR and for sharing your knowledge about SAR polarimetry. I learned a lot within the few weeks and the time in Oberpfaffenhofen really pushed my motivation.

Special thanks go to all my proofreaders, who helped "optimize" the final thesis. Sibylle, Christian, Katharina, and Ben, thanks for your time, care, and effort.

I would also like to thank my roommate Christian and my lunch break friends for the pleasant time at work, and the colleagues joining the (afternoon) coffee break for off-topic discussions.

Finally, I want to thank my family, my husband Ben, and my friends for moral and emotional support during the long period of my thesis and for taking my mind of it whenever it was necessary. A big thank you goes to my parents for the support during my studies as well as for the freedom and trust in all my life decisions.